UNIVERSITÀ DEGLI STUDI DI MILANO

FACOLTÀ DI SCIENZE E TECNOLOGIE

PhD Course in Chemistry – XXX Cycle

PHOTOACTIVE MATERIALS FOR SOLAR FUELS PRODUCTION

Tutor: Prof. Elena Selli
Co-Tutor: Prof. Lucia Carlucci
Co-Tutor: Dott. Maria Vittoria Dozzi

PhD Student:
Alessandro POMA
R10878

A.A. 2016-2017

Despite everything. And, somehow, somebody

Table of contents

GENERAL INTRODUCTION **1**

I.1 Current energy trends overview 1

I.2 Artificial solar fuels 4

I.3 Aim of the thesis 7

References 9

PART 1 – METAL ORGANIC FRAMEWORKS ***13***

CHAPTER 1 **15**

1.1 Metal organic frameworks 15

1.2 Metal organic frameworks as heterogeneous photocatalysts 18

References 28

CHAPTER 2 – Dipyrrins **31**

2.1 Dipyrrin-based metal complexes as metalloligands 31

References 36

CHAPTER 3 – A Ni-bisdipyrrinato complex complex as a potential sensitizer in MOFs: synthesis and photoelectrochemical characterization **38**

3.1 Introduction 38

3.2 Syntheses 40

3.3 Photoelectrode preparation 42

3.4 Structural and photo(electro)chemical characterization 43

3.5 Synthesis of Ni-bisdpmCOOH 46

3.6 Optical properties 46

3.7 Electrochemical characterization 48

3.8 Photoelectrochemical characterization 50

3.9 Inclusion of Ni-bisdpmCOOH into the UiO-66 framework 54

3.10 Conclusions 57

References 58

CHAPTER 4 – Porphyrins **62**
4.1 Porphyrins as metalloligand 62
4.2 The MTCPP⊂UiO-66-X series 64
4.3 The PCN-222(M) series 69
References 72

CHAPTER 5 – Photophysical characterization and photocatalytic activity of porphyrin containing MOFs **76**
5.1 Photophysical properties of porphyrins 76
5.2 Photophysical characterizations 78
5.2.1 DRS Spectra 79
5.2.1.1 MTCPP Ligands 79
5.2.1.2 MTCPP⊂UiO-66-X series 80
5.2.1.3 PCN-222(M) series 82
5.2.2 Excitation and emission spectra 83
5.2.2.1 MTCPP Ligands 83
5.2.2.2 MTCPP⊂UiO-66 series 87
5.2.2.3 MTCPP⊂UiO-66-NH_2 series 90
5.2.2.4 PCN-222(M) series 95
5.3 Summary of the obtained results 99
5.4 Photocatalytic CO_2 reduction tests with the MTCPP⊂UiO-66-NH_2 series 100
5.5 Photocatalytic CO_2 reduction tests with the PCN-222(M) series 103
References 107

PART 2 – PHOTOELECTROCHEMICAL WATER OXIDATION ***110***

CHAPTER 6 **112**
6.1 Semiconductor electrodes for energy conversion 112
6.2 Photoelectrochemical water splitting 115
6.3 Approaches to form visible-light absorbing oxides 117
References 118

CHAPTER 7 – Understanding the limits: the case of $CuWO_4$ **122**

7.1 Introduction 122

7.2 Materials 124

7.3 Photoelectrode preparation 124

7.4 Optical, morphological and photoelectrochemical characterization 125

7.5 Characterization of $CuWO_4$ multilayer photoanodes 127

7.6 Photoresponse of $CuWO_4$ multilayer photoanodes 128

7.7 Light intensity dependence 136

7.8 Conclusions 140

References 142

PART 3 – THERMAL-ASSISTED PHOTOCATALYTIC METHANOL STEAM REFORMING ***144***

CHAPTER 8 **146**

8.1 TiO_2 in photocatalysis 146

8.2 Basic properties of TiO_2 semiconductor photocatalysts 147

8.3 Loading co-catalysts on TiO_2 150

8.4 Hydrogen generation on TiO_2 photocatalyst through photo-steam reforming of methanol 151

References 154

CHAPTER 9 – Temperature-dependent methanol photo-steam reforming 156

9.1 Introduction 156

9.2 Photocatalyst preparation 157

9.3 Characterisation details 159

9.4 Photocatalytic tests 160

9.5 Photocatalysts characterisation 162

9.6 Effects of gold deposition method and nominal amount 166

9.7 Determination of products and intermediate species 167

9.8 Effects on selectivity of temperature and of deposited Au nanoparticles 172

9.9 Conclusions 178
References 180

CHAPTER 10 182
10.1 Conclusions 182
10.2 The Ni-bisdipyrrinato complex as potential sensitizer 182
10.3 The porphyrin-containing Zr-based MOF series 183
10.4 $CuWO_4$ as water oxidation photocatalyst 184
10.5 The effects of Au nanoparticles and temperature in methanol photosteam reforming reaction 185
10.6 Future perspectives 186

APPENDIX A 188
APPENDIX B 206
APPENDIX C 210
APPENDIX D 224
APPENDIX E 226

List of figures

Figure I.1	Supply of commercially traded primary energy, from BP 2015.	2
Figure I.2	Schematic illustration of heterogeneous semiconductor-based artificial photosynthesis.	7
Figure 1.1	Schematic representation of a MOF structure along with its "building blocks".	16
Figure 1.2	Representation of the MOF-5 structure, with a close look at its metal node (Zn_4O) and organic linker (terephthalate). The yellow sphere represents the volume of the pore	16
Figure 1.3	Rate of aqua ligand exchange for different metal cations as reference for M-L bond dissociation rate in carboxylate-based MOFs.	17
Figure 1.4	UiO-66 framework as a representative robust MOF (left) and its 12-connected Zr_6-cluster node (right)	18
Figure 1.5	Ishitani's Rhenium complex used for CO_2 reduction (left) and TiO_2 semiconductor (right).	19
Figure 1.6	Schematic representation of the photodynamics in a DSSC. Image taken from ref [15].	22
Figure 1.7	Schematic drawing to represent the photodynamic in a MOF structure. In particular, the HER (Hydrogen Evolution Reaction) is shown, with Pt as co-catalyst.	23
Figure 1.8	Different approaches to induce photocatalytic activity in a MOF framework.	24
Figure 1.9	Flat band potential and conduction band position of common metal oxides at pH = 7. Image taken from ref [24].	25
Figure 2.1	Structure of UiO-66: (a) tetrahedral cage; (b) octahedral one and (c) packing of the two.	37
Figure 2.2	XRPD of the (from top to bottom): UiO-66, doped-UiO-66, UiO-66-NH_2, doped-UiO-66-NH_2, UiO-66-$(OH)_2$ and doped-UiO-66-$(OH)_2$ structures.	41
Figure 2.3	Photographs of the different samples.	42

Figure 3.1 Absorption spectrum of Ni-dpmCOOMe (green line), Ni-bisdpmCOOMe (red line) and Ni-bisdpmCOOH (black line) in DMF. 47

Figure 3.2 Anodic (positive potentials) and cathodic (negative potentials) scans of Ni-bisdpmCOOH around the first redox potentials, performed at different potential scanning rates. 48

Figure 3.3 HOMO and LUMO energy levels of Ni-bisdpmCOOH and NiTCPP. 50

Figure 3.4 UV-vis absorption spectra of Ni-bisdpmCOOH adsorbed on a TiO_2-covered electrode, recorded after each adsorption cycle. The absorption spectrum of bare TiO_2 was always subtracted. 51

Figure 3.5 (a) Linear sweep voltammetry curves of Ni-bisdpmCOOH/TiO_2 under irradiation with the 420 nm cut off filter and in the dark; (b) Chronoamperometric analysis of the Ni-bisdpmCOOH/TiO_2 photoanode employing the 420 nm (red thick line) and the 550 nm (black thick line) cut-off filters and of the NiTCPP/TiO_2-based photoanode with the 420 nm cut-off filter (thin line); (c) IPCE and IQE curves obtained with the Ni-bisdpmCOOH/TiO_2 electrode. 53

Figure 3.6 Schematic illustration of the UiO-66 structure (top) and of its doping with Ni-bisdpmCOOH (bottom). 55

Figure 3.7 XRPD pattern of Ni-bisdpmCOOH@UiO-66 (top) and of UiO-66 (bottom). 56

Figure 3.8 Diffuse reflectance spectra of Ni-bisdpmCOOH (bottom) and of the doped framework (top). 57

Figure 4.1 The structure of a porphyrin. 63

Figure 4.2 Schematic illustration of UiO-66 incorporating TCPP (red) as well as the usual Zr_6 cluster (blue) and terephthalic linker (brownish). Yellow sphere indicates the pore cavity. 65

Figure 4.3 Photographs of the different samples. 66

Figure 4.4 Experimental XRPD pattern of (from top to bottom): H_2TCPP⊂UiO-66; CoTCPP⊂UiO-66; CuTCPP⊂UiO-66; NiTCPP⊂UiO-66; FeTCPP⊂UiO-66 and "undoped" UiO-66. 67

Figure 4.5	Experimental XRPD pattern of (from top to bottom): H_2TCPP⊂UiO-66-NH_2; CoTCPP⊂UiO-66-NH_2; CuTCPP⊂UiO-66-NH_2; NiTCPP⊂UiO-66-NH_2; FeTCPP⊂UiO-66-NH_2 and "undoped" UiO-66-NH_2.	68
Figure 4.6	Crystal structure of PCN-222 showing the large 1D channels of the framework.	70
Figure 4.7	Comparison between experimental XRPD patter of (from top to bottom): PCN-222(no metal); PCN-222(Co); PCN-222(Cu); PCN-222(Ni) and PCN-222(Fe) with the simulated one.	71
Figure 5.1	DRS spectra of the porphyrin ligands.	79
Figure 5.2	DRS spectra of the MTCPP⊂UiO-66 series.	81
Figure 5.3	DRS spectra of the MTCPP⊂UiO-66-NH_2 series.	81
Figure 5.4	DRS analysis for the PCN-222(M) series.	82
Figure 5.5	Excitation spectra of MTCPP ligands.	83
Figure 5.6	Excitation spectra of MTCPP ligands (enlarged).	84
Figure 5.7	Emission spectra for MTCPP ligands.	85
Figure 5.8	Emission spectra for MTCPP ligands (enlarged).	85
Figure 5.9	Excitation spectra of MTCPP⊂UiO-66 samples.	87
Figure 5.10	Excitation spectra of MTCPP⊂UiO-66 samples (enlarged).	88
Figure 5.11	Emission spectra of MTCPP⊂UiO-66 samples.	89
Figure 5.12	Emission spectra of MTCPP⊂UiO-66 samples (enlarged).	89
Figure 5.13	Excitation spectra of MTCPP⊂UiO-66-NH_2 samples.	91
Figure 5.14	Excitation spectra of MTCPP⊂UiO-66-NH_2 samples (enlarged).	91
Figure 5.15	Emission spectra of MTCPP⊂UiO-66-NH_2 samples.	92
Figure 5.16	Emission spectra of MTCPP⊂UiO-66-NH_2 samples (enlarged).	92
Figure 5.17	Emission comparison between H_2TCPP⊂UiO-66-NH_2 and UiO-66-NH_2 samples.	94
Figure 5.18	Excitation spectra of PCN-222(M) samples.	95
Figure 5.19	Excitation spectra of PCN-222(M) samples (enlarged).	96
Figure 5.20	Emission spectra of PCN-222(M) samples.	97
Figure 5.21	Emission spectra of PCN-222(M) samples (enlarged).	97

Figure 5.22 Morphological analysis comparison before and after the photocatalytic test of NiTCPP⊂UiO-66-NH_2. 102

Figure 5.23 Photocatalytic CO_2 reduction results of PCN-222(M) series. 104

Figure 5.24 XRPD analysis of PCN-222 sample. 105

Figure 6.1 The formation of a junction between an n-type semiconductor and an electrolyte solution: a) the separate system and b) after equilibration. 113

Figure 6.2 Photogeneration of e^-/h^+ pairs in the bulk and depletion layer of an n-type semiconductor. 114

Figure 6.3 STH efficiency and photocurrent maximum based on band gap and AM1.5G illumination. 107

Figure 6.4 Band structure of oxide semiconductor comparing purely O (2p) to M (s/d) + O (2p) based valence band. 118

Figure 7.1 Absorption spectra of $CuWO_4$ multilayer photoanodes. 127

Figure 7.2 XRD analysis of the $CuWO_4$ thin film coated onto FTO. Bragg reflections from JCPDF 72-0616 are indicated in grey. 128

Figure 7.3 IPCE and IQE analyses of $CuWO_4$ multilayer photoanodes under back-side (a-b) and front-side (c-d) irradiation mode. 130

Figure 7.4 Linear sweep voltammetry of $CuWO_4$ multilayer photoanodes under different irradiation geometries: backside irradiation (left) and front side irradiation (right). 131

Figure 7.5 Product of the IPCE of $CuWO_4$ (5th layer) under backside illumination configuration with the AM1.5 solar spectrum. The dashed vertical line represents the absorption edge of the material found through IPCE analysis. 132

Figure 7.6 Chopped AM1.5 chronoamperometry plots of $CuWO_4$ 5^{th} layer (black line) and typical $BiVO_4$ under backside illumination configuration at 1.23 V_{RHE}. 133

Figure 7.7 Chopped AM1.5 chronoamperometry plots of $CuWO_4$ with (red line) and without (black line) addition of 0.5 M H_2O_2. 135

Figure 7.8 LSV analysis of the multilayer $CuWO_4$ photoelectrode as a function of the irradiation power. 137

Figure 7.9 Photocurrent efficiency dependence (IQE) with respect to absorbed photons at 1.23 $V_{RHE.}$ 138

Figure 7.10 LSV comparison between bare (black line) and Ni/Fe-treated (red line) $CuWO_4$ photoanodes. The LSV scans were recorded at power intensity of 2 mW cm^{-2} at λ = 400 nm. 139

Figure 8.1 Schematic representation of semiconductor activation: (a) general semiconductor, (b) n-type semiconductor and (c) p-type one. Taken from ref [6]. 148

Figure 8.2 Band bending for (a) an n-type semiconductor and (b) a p-type semiconductor, both in equilibrium with a solution. Taken from ref [7]. 149

Figure 9.1 Sketch of the recirculating gas phase system employed for the photocatalytic tests. 160

Figure 9.2 Diffuse reflectance spectra (DRS) of TiO_2 and TiO_2 modified powders with nominal 1% Au nanoparticles loading, obtained by the three different methodologies. In the inset, the magnification of the plasmonic band evidences the red shift in the absorption maximum for the P sample. 163

Figure 9.3 HRTEM images of: a) 1%Au/TiO_2_DP, b) 1%Au/TiO_2_C and c) 1%Au/TiO_2_P samples. 165

Figure 9.4 Overview of the rate of hydrogen production and per cent selectivity to CO_2 and CO obtained with the investigated photocatalysts. Specific reaction conditions: 0.014 g of photocatalyst fed in recirculation mode with 40 mL min^{-1} of 2% CH_3OH/3% H_2O/N_2 (balance) gas mixture. 166

Figure 9.5 Typical gas-phase composition profiles (concentration expressed in mole percent) during irradiation, in the methanol photo-steam reforming reaction. 168

Figure 9.6 Production trend of the gaseous products at different temperatures. Solid lines with filled symbols represent analysis under irradiation, while dashed lines with open symbols represent analysis in absence of irradiation. 173

Figure 9.7	Production rate (a) and selectivity (b) to oxidation products with respect to hydrogen production vs. temperature.	176
Figure 9.8	Hydrogen production ratio over time at different temperatures.	178
Figure A1	^{1}H NMR of the intermediate product.	189
Figure A2	^{1}H NMR of Ligand dpmCOOMe.	193
Figure A3	^{1}H NMR of metalloligand Pd(dpmCOOMe)$_2$.	193
Figure A4	^{1}H NMR of metalloligand Pd(dpmCOOH)$_2$.	195
Figure A5	^{1}H NMR of metalloligand Ni(dpmCOOMe)$_2$.	197
Figure A6	^{1}H NMR of metalloligand Ni-bisdpmCOOMe.	199
Figure A7	^{1}H NMR of metalloligand Ni-bisdpmCOOH.	201
Figure B1	^{1}H NMR spectrum of complex Ni-bisdpmCOOH.	206
Figure B2	Anodic (AC) and cathodic (CA) scans (bold lines) of Ni-bisdpmCOOH complex. Overimposed (thin lines), anodic scan around first oxidation peak (A), cathodic scan around the first reduction peak (C).	206
Figure B3	Effect of the scan rate on the first oxidation peaks of NiTCPP.	207
Figure B4	UV-Vis-NIR absorption spectrum of the TiO_2 paste.	207
Figure B5	Absorption spectrum (difference) of NiTCPP adsorbed onto the TiO_2 paste.	208
Figure C1	^{1}H NMR of the TPPCOOMe ligand.	212
Figure D1	Comparison of IQE analyses for front- and backside irradiation of CuWO4 photoanode (5th layer).	224
Figure E1	Diffused reflectance spectra the Au/TiO_2_C photocatalysts series.	226
Figure E2	Diffused reflectance spectra the Au/TiO_2_DP photocatalysts series.	226
Figure E3	Diffused reflectance spectra the Au/TiO_2_P photocatalysts series.	227
Figure E4	Hydrogen production rate and selectivity for bare P25 TiO_2.	227

List of schemes

Scheme 2.1	Representation of a BODIPY dye and a dipyrrin ligand with the corresponding numbering of its atom.	32
Scheme 2.2	Synthetic procedure for ligand dpmCOOMe.	33
Scheme 2.3	Synthesis of Ni-bisdpmCOOMe complex.	35
Scheme 2.4	Synthesis of Ni-bisdpmCOOH.	35
Scheme 3.1	Synthesis of the 2,2'-bisdipyrrin Ni(II) metalloligand.	46
Scheme 4.1	Synthetic route to the MTCPP "doped" UiO-66 frameworks.	66
Scheme 7.1	Schematic representation of the current doubling effect in the presence of H_2O_2, in which its oxidised form (a superoxide anion) is further oxidised by electron injection into the conduction band of $CuWO_4$.	136
Scheme C1	Three step synthetic route to MTCPP ligand.	210

List of tables

Table 5.1 Soret and Q bands positions of metalloporphyrins. 80

Table 5.2 Excited state lifetimes for MTCPP ligands. 86

Table 5.3 Excited state lifetime for $H_2TCPP \subset UiO\text{-}66$. 90

Table 5.4 Excited state lifetime for $H_2TCPP \subset UiO\text{-}66$. 93

Table 5.5 Excited state lifetime for PCN-222 and PCN-222(Ni) samples. 98

Table 9.1 Methanol oxidation selectivity trends as a function of temperature. 174

Table 9.2 Photocatalytic performance of 1%Au/TiO_2_DP photocatalyst in methanol photo-steam reforming at different temperatures, in terms of production rate and per cent selectivity with respect to hydrogen production. Reaction conditions: 0.015 g of photocatalysts fed in recirculation mode with 60 mL min^{-1} of a 2% CH_3OH/3% H_2O/N_2 (balance) gas mixture. 175

GENERAL INTRODUCTION

I.1. Current energy trends overview

Despite the fact the our society is facing the greatest world economic crisis since the World War II, the actual global energy consumption[1] has reached a value of almost 13 billion ton of oil equivalents (btoe),[2] which corresponds to an average rate of energy consumption of about 12 TW. Although attention towards renewable resources and the seek for other resources than the fossil one largely increased in the last decade (Figure I.1), the latter still provides 87% of the global primary supply, and the renewable resources are less than 10%. Nuclear has slightly increased in the last few years, but this trend will hardly remain the same, because of the decommissioning of many reactors in the US and Europe, which is now taking place[3].

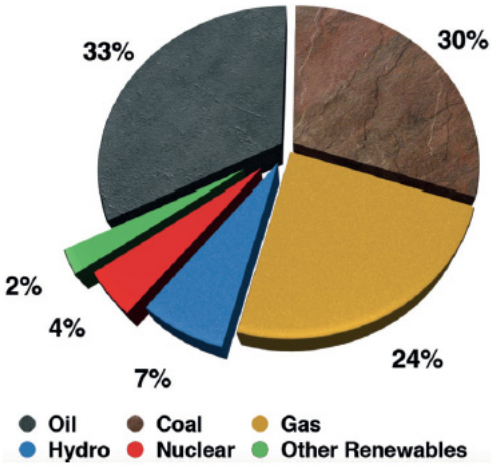

***Figure I.1**. Supply of commercially traded primary energy, from BP 2015, taken from ref [2].*

Therefore, oil represents the first energy source and the largest majority of it (around 80%) is dedicated to the transportation system, while the remaining part is divided in heat, electricity and other petrochemicals, such as asphalt and lubricants.[4] Anyway, the world oil system is now undergoing relevant changes after decades of almost static situation, mainly because of the depletion of now exploited reserves.[5] These changes also include new environmental concerns due to exploration of potential hydrocarbon reservoirs in extreme locations, such as deep offshore and the Artic sea.[6] This trend, for example, led to the catastrophic accident of the Deepwater Horizon platform in the Gulf of Mexico in 2010, which has dramatically affected the economy of a vast coastal region.[7]

On the contrary, a positive change in the world energy landscape can be accounted: the relentless rise of renewable energies. In 2014, in fact, for the first time the global carbon emission associated with energy production remained stable despite the continued economic growth. This is mainly attributable to the growth of developing countries like China, which now produces as much electricity from water, wind and

sunlight as all France and Germany's power plants combining, thus covering 20% of its internal overall demand.[8] In fact, between 2008 and 2012, the investments China did in non-fossil power plants increased by 40%, while those in fossil-fueled facilities were substantially reduced.

Thanks to the remarkable drop of the photovoltaic (PV) module price in the last decade, China has seen a 10-fold increase in their production market. But China is not the only country in which PV electricity is becoming more and more competitive with respect to conventional technologies such as coal and nuclear. Taking into account our country, almost 8% of electricity consumption comes from PV, which is now the largest share in the world.

All the renewable energy sectors are in continuous expansion and growth. The estimated renewable share of final energy consumption is about 19%, with modern technologies and traditional biomass being at 10 and 9%, respectively, while with almost 23% of the overall world's generation, electricity production holds the role of the most important renewable sector. Specifically, at the end of 2014, the hydroelectric global capacity exceeded 1 TW, while wind and PV were 370 GW and almost 180 GW, respectively, thus covering 16.6, 3.1 and 0.9% of the world electricity demand.[9] Although the last two shares appear to be small, these two virtually did not exist up to two decades ago, while hydroelectricity has been an established technology for over 120 years. Moreover, it is estimated that direct and indirect job positions in the field of renewable energies are almost 8 millions, with 1.2 million in EU, and they are in continuous growth.

By considering the above-mentioned data, the transition from fossil fuels to renewable is already ongoing. However, since the energy system is a wide and

complex machine, which is spread all over the planet, it is obvious that it will be a long and a very complex process.[10] In detail, it will offer both great challenges along with great opportunities and it is poised to radically change our way of living.[11]

I.2. Artificial solar fuels

A useful fuel is a chemical reductant that can be transported, stored and used on request by combining it with air-contained oxygen, with consequent energy release. We need this kind of energy source because common energy sources such as oil, gas and coal are poised to be exhausted and their use causes severe damages to human health and environment.[10] Therefore, scientific community has begun to find a sustainable way to efficiently use sunlight in order to produce clean, artificial fuels.[12] To face such a challenge, the complex mechanism of natural photosynthesis has been deeply investigated. The biggest effort is to create an artificial photosynthetic process which is less complicated than the original, natural one and which is capable of producing simple fuels, such as hydrogen and methanol.

The Italian chemist Giacomo Ciamician first exposed the need and the possibility to achieve the production of fuels by non-biological photochemical reactions back to the beginning of the previous century,[13] despite at that time most of the energy was supplied by coal. Later on, coal was progressively replaced by oil and after natural gas become an alternative energy source. When nuclear energy was discovered, people thought that the energy problem was solved forever. In fact, the phrase “too cheap to meter” was coined by Lewis Strauss, chairman of the United States Atomic Energy Commission, who in a 1954 speech to the National Association of Science Writers said:

*“Our children will enjoy in their homes electrical energy **too cheap to meter**... It is not too much to expect that our children will know of great periodic regional famines in the world only as matters of history, will travel effortlessly over the seas and under them and through the air with a minimum of danger and at great speeds, and will experience a lifespan far longer than ours, as disease yields and man comes to understand what causes him to age."*

It is often assumed that Strauss' prediction was a reference to conventional uranium fission nuclear reactors. Indeed, only ten days prior to his “Too Cheap To Meter” speech, Strauss was present at the ground-breaking of the Shippingport Atomic Power Station, where he predicted that "industry would have electrical power from atomic furnaces in five to fifteen years."

Following the energy crisis of the 1970s, scientific world revamped the idea of an artificial photosynthesis,[14] but only in recent years, after full realization of the extensive damages to the biosphere caused by burning fossil fuels[15] and of the intrinsic difficulties of nuclear energy,[10] it has become the object of extensive investigation.

Nowadays, the studies on artificial photosynthesis are currently concentrated on using sunlight to reduce carbon dioxide in aqueous solution to carbon monoxide, ethanol, or methane [Eq. (1)][16] or to split water into molecular hydrogen and molecular oxygen [Eq. (2)]

$$CO_2 + 2\,H_2O + 8\,h\nu\ (\text{sunlight}) \rightarrow CH_4 + 2\,O_2 \qquad \Delta G^\circ = 8.30\ \text{eV} \qquad (1)$$

$$2\,H_2O + 4\,h\nu\ (\text{sunlight}) \rightarrow 2\,H_2 + O_2 \qquad \Delta G^\circ = 4.92\ \text{eV} \qquad (2)$$

Since carbon dioxide reduction is a more difficult process with respect to water splitting from a kinetic point of view and can also be performed by a thermal reaction with molecular hydrogen to yield methanol,[17] the attention of most scientists is currently focused on the reaction (2). Moreover, the electronic absorption spectrum of water does not overlap the emission spectrum of the sun, thus the direct water dissociation by sunlight cannot take place. Therefore, artificial photosynthetic systems must be based on photosensitizers, species capable of absorbing sunlight and using solar energy to produce the desired reaction. From the thermodynamic point of view, the most convenient water splitting process concerns the evolution of molecular oxygen and molecular hydrogen from liquid water [Eq. (3)], the low-energy thermodynamic threshold (1.23 eV) of which allows, in principle, conversion of about 30% of the solar energy. Water splitting entails two multi-electron-transfer reactions [Eqs. (4) and (5)].

$$\tfrac{1}{2}\ H_2O \rightarrow \tfrac{1}{2}\ H_2 + \tfrac{1}{4}\ O_2 \qquad \Delta G^\circ = 1.23\ eV \qquad (3)$$

$$2\ H_2O + 2\ e^- \rightarrow H_2 + 2\ OH^- \qquad E^\circ\ (pH\ 7) = -\ 0.41\ V\ vs\ NHE \qquad (4)$$

$$2\ H_2O \rightarrow O_2 + 4\ H^+ + 4\ e^- \qquad E^\circ\ (pH\ 7) = +\ 0.82\ V\ vs\ NHE \qquad (5)$$

Given that in a photochemical process each photon can transfer only one electron,[18] in a water splitting system two photocatalysts must be present, one to promote electrons for the production of molecular hydrogen, the other one to collect holes (positive charges) for the generation of molecular oxygen.[19]

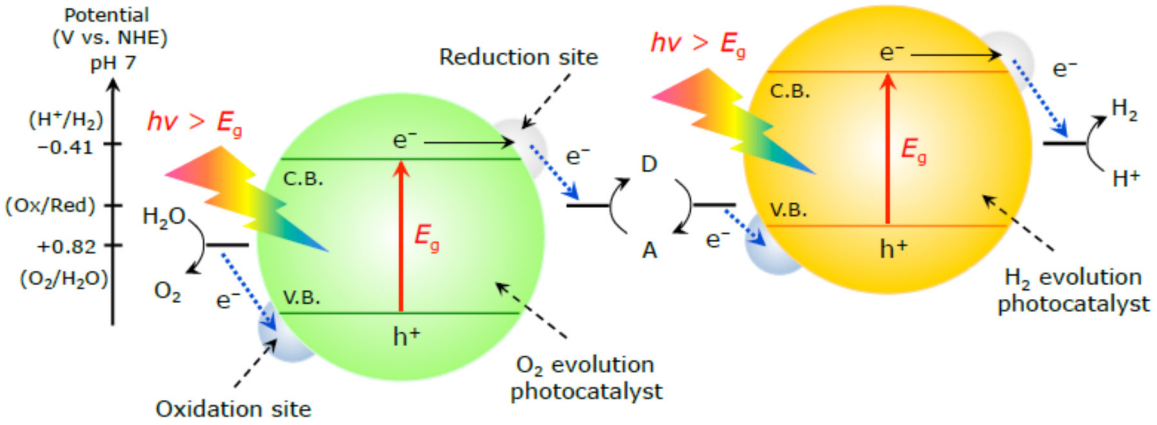

Figure I.2. *Schematic illustration of heterogeneous semiconductor-based artificial photosynthesis.*[20]

Artificial photosynthetic systems for water splitting require a very precise organization of different components in the dimensions of space (location of the components), energy (absorbed photons and redox potentials), and time (rates of competing processes).

Initially it was thought that water splitting could be achieved in homogeneous systems by suitably designed supramolecular arrays of appropriate components.[10] It is now believed, however, that the best approach is photoactivation of solid-state semiconductor materials,[18a] as will be discussed in the next chapters.

I.3. Aim of the thesis

In this thesis project, the main aim was to investigate a new type of photocatalytic materials, the so-called Metal-Organic Frameworks (MOFs), which can be properly tuned to host in their structure active sites able to harvest visible light and to transform it into chemical fuels by CO_2 and/or H_2O reduction. Despite this class of materials has been known since long time,[21] only few years ago they proved to be able to suitable for this application after the discovery of their semiconductor-like behaviour.[22] In our

approach, we took advantage from nature and thus we incorporated porphyrin and dipyrrin moieties into artificial “cages” such as MOFs in order to realize the so-called artificial photosystem with the aid of sacrificial electron donor.

Moreover, we focused our attention to the development of new semiconductor-based photoanodes for water oxidation, which is “bottleneck” half reaction of the overall water splitting process.[23] With this aim, we studied the photoelectrochemical process behind the Oxygen Evolution Reaction (OER) employing a W-based ternary oxide photoanode. The investigated material, which is $CuWO_4$, has been firstly studied in the 80s,[24] but no advanced studies were performed to understand the charge carriers dynamics of photogenerated charge carriers, also in relation to the thickness of the photoactive layer.

Another strategy to produce solar fuels is the one widely employed in photocatalysis, after the first report by Fujishima and Honda, back in 1972,[25] which showed the ability of TiO_2 to produce H_2 from water under irradiation. That is, to modify TiO_2 with different dopants and metals in order to make it a more efficient as catalyst and a better light-harvester. In this frame, we studied the synergistic effect of metal nanoparticles deposited onto the TiO_2 surface, acting as co-catalyst, and the contribution of temperature to the photocatalytic steam reforming reaction of methanol, a type of investigation which has never been done before.

REFERENCES

[1] Key energy data were taken from the BP Energy Statistics 2015.

[2] British Petroleum, BP Statistical Review of World Energy 2015, http://www.bp.com.

[3] United Nations Environment Programme, UNEP Yearbook—Emerging Issues in Our Global Environment, 2012, http://www.unep.org, pp. 35–49.

[4] (a) V. Smil, Oil—A Beginner's Guide, Oneworld, Oxford (UK), 2008; (b) Vennestrøm, P. N. R.; Osmundsen, C. M.; Christensen, C. H.; Taarning, E. *Angew. Chem. Int. Ed.* **2011**, *50*, 10502.

[5] Miller, R. G.; Sorrell, S. R. *Philos. Trans. R. Soc. A* **2013**, *372*, 20130179.

[6] The plain data on oil and gas production evidently do not account for the actual net energy content of these sources and, accordingly, do not offer a comprehensive picture of the energy wealth of a nation.

[7] Kemsley, J. *Chem. Eng. News* **2015**, *93*, 8.

[8] (a) Mathews, J. A. "*Greening of Capitalism. How Asia Is Driving the Next Great Transformation*", Stanford University Press, Stanford, CA (USA), 2015; (b) US Energy Information Administration, International Energy Statistics, 2015, can be found under http://www.eia.gov.

[9] REN 21—Renewable Energy Policy Network for the 21st Century, Renewables 2015 Global Status Report 2015, http://www.ren21.net/.

[10] Armaroli, N.; Balzani, V. "*Energy for a Sustainable World—From the Oil Age to a Sun Powered Future*", Wiley-VCH, Weinheim (Germany), 2011.

[11] Armaroli, N.; Balzani, V. *Angew. Chem. Int. Ed.* **2007**, *46*, 52.

[12] Marshall, J. *Nature* **2014**, *510*, 22.

[13] Ciamician, G. *Science* **1912**, *36*, 385.

[14] (a) Balzani, V.; Moggi, L.; Manfrin, M. F.; Bolletta, F.; Gleria, M. *Science* **1975**, *189*, 852; (b) "*Solar Energy: Chemical Conversion and Storage*" (Eds.: R. R. Hautala, R. B. King, C.Kutal), Humana Press, Clifton (USA), 1979.

[15] Armaroli, N.; Balzani, V. *Chem. Asian J.* **2011**, *6*, 768.

[16] (a) Windle, C.D.; Perutz, R. N. *Coord. Chem. Rev.* **2012**, *256*, 2562; (b) Morris, A. J.; Meyer, G. J.; Fujita, E. *Acc. Chem. Res.* **2009**, *42*, 1983; (c) Habisreutinger, S. N.; Schmidt-Mende, L.; Stolarczyk, J.

K.; *Angew. Chem. Int. Ed.* **2013**, *52*, 7372 (d) Herron, J. A.; Kim, J.; Upadhye, A. A.; Huber, G. W.; Maravelias, C. T. *Energy Environ. Sci.* **2015**, *8*, 126.

[17] Olah, G. A.; *Angew. Chem. Int. Ed.* **2013**, *52*, 104.

[18] (a) Balzani, V.; Ceroni, P.; Bergamini, G. *Angew. Chem. Int. Ed.* **2015**, *54*, 11320; (b) Balzani, V.; P. Ceroni, P.; Juris, A. "*Photochemistry and Photophysics—Concepts, Research, Applications"*, Wiley-VCH, Weinheim (Germany), 2014.

[19] (a) Hammarstrçm, L. *Acc. Chem. Res.* **2015**, *48*, 840; (b) Sartorel, A.; Bonchio, M.; Campagna, S.; Scandola, F. *Chem. Soc. Rev.* **2013**, *42*, 2262.

[20] Maeda, K., *ACS Catal.*, **2013**, *3*, 1486.

[21] Yaghi, O. M.; O'Keeffe, M.; Ockwig, N. W.; Chae, H. K.; Eddaoudi, M.; Kim, J., *Nature* **2003**, *423*, 705.

[22] Silva, C. G.; Corma, A.; Garcìa, H. *J. Mater. Chem.* **2010**, *20*, 3141.

[23] Dau, H.; Limberg, C.; Reier, T.; Risch, M.; Roggqan, S.; Strasser, P. *ChemCatChem*, **2010**, *2*, 724.

[24] Bharati, R.; Shanker, R.; Singh, R. A. *Pramana*, **1980**, *14*, 449.

[25] Fujishima, A.; Honda, K. *Nature* **1972**, *238*, 37.

Part 1

Metal Organic Frameworks

Chapter 1

1.1 Metal-organic frameworks

Metal-organic frameworks (MOFs) are a fascinating class of highly ordered porous and crystalline materials, assembled from metal-containing units (metal cations or clusters) and organic linkers (Figure 1.1 and 1.2).[1] Thanks to their excellent properties, such as high internal surface area, structural diversity and tunable functionality, even if compared to other conventional porous materials, such as activated carbons, mesoporous silica and zeolites, MOFs have received a lot of attention in the past few decades. Due to the forementioned features, MOFs have been intensively studied for their potential application in many different fields, such as gas storage/separation, heterogeneous catalysis, chemical sensing, biomedical applications, drug delivery and others.[2]

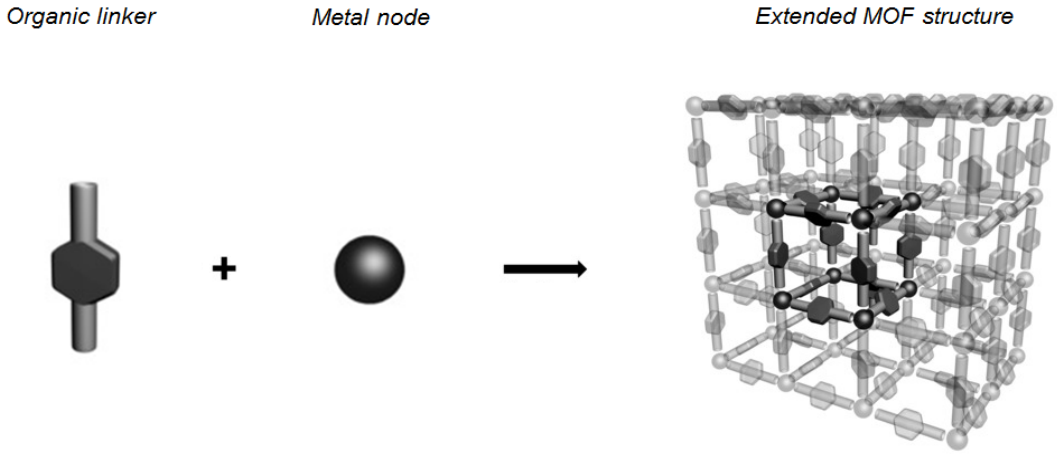

Figure 1.1. *Schematic representation of a MOF structure along with its "building blocks".*[3]

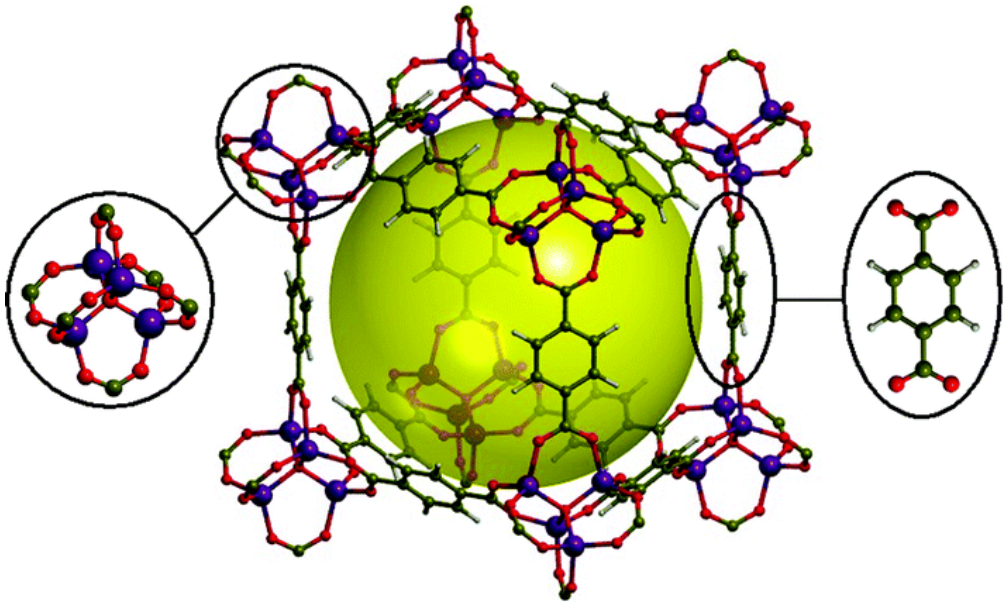

Figure 1.2. *Representation of the MOF-5 structure, with a close look at its metal node (Zn_4O) and organic linker (terephthalate). The yellow sphere represents the volume of the pore.*[4]

When MOFs are used for various applications, it is obviously desirable that the framework itself remains intact throughout the process (*e.g.* in catalytic cycles), thus keeping unchanged its properties and features. However, many reported MOFs suffer of poor stability in aqueous media or at extreme pH values (in both acidic and basic conditions) and this restricts MOFs practical applications only in non-coordinating organic solvents, rather than in water or under harsh conditions.2[f] The stability issues

with many MOFs arise from the “hard/soft acids and bases” theory. In fact, the overwhelming majority of MOFs are assembled from carboxylate-based ligands, addressed as “hard base”, and M^{2+} metal species, addressed as “soft acid”, resulting in weak M-L bonds.[5] Therefore, these MOFs undergo fast dissociation (Figure 1.3) by attack of water, acids or bases. Moreover, when certain functionalities are incorporated into MOF structures, the synthesis of which requires harsh conditions that cannot be sustained by the parent structure, the lack of stability leads to framework collapse, this blocks the accessibility of the functional moieties or results in their dissolution into the homogeneous phase.

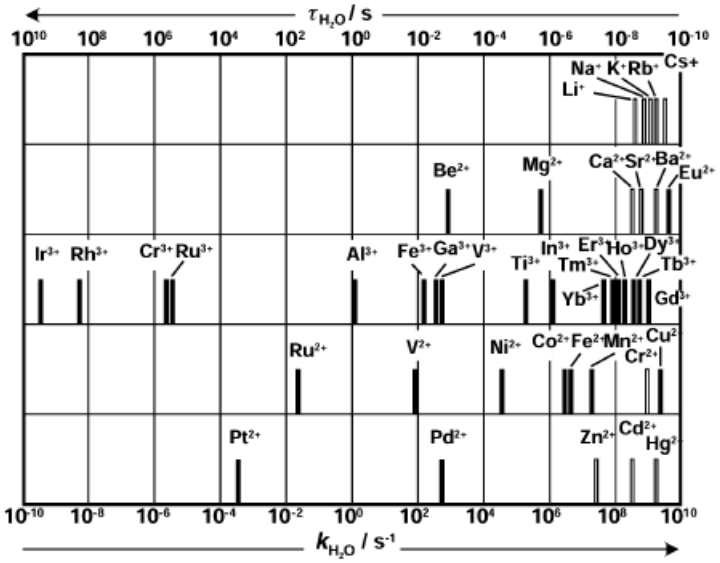

Figure 1.3. *Rate constants of aqua ligand exchange for different metal cations as reference for M-L bond dissociation rate in carboxylate-based MOFs.*[6]

In order to improve MOF stability, high valence metal species has to be selected, due to the stronger electrostatic interaction between them and the carboxylate end of the organic linkers (Figure 1.4). Unfortunately, such type of MOFs are not very common. This can be ascribed to the fact that, in comparison with metal centres with

lower charge density, high valence metal-containing MOFs are particularly difficult to obtain as single crystals, due to the inert coordination bonds between M^{n+} cations and carboxylate anions, making ligand-exchange reactions extremely slow, which is unfavourable for defect repair during crystal the growth.[7]

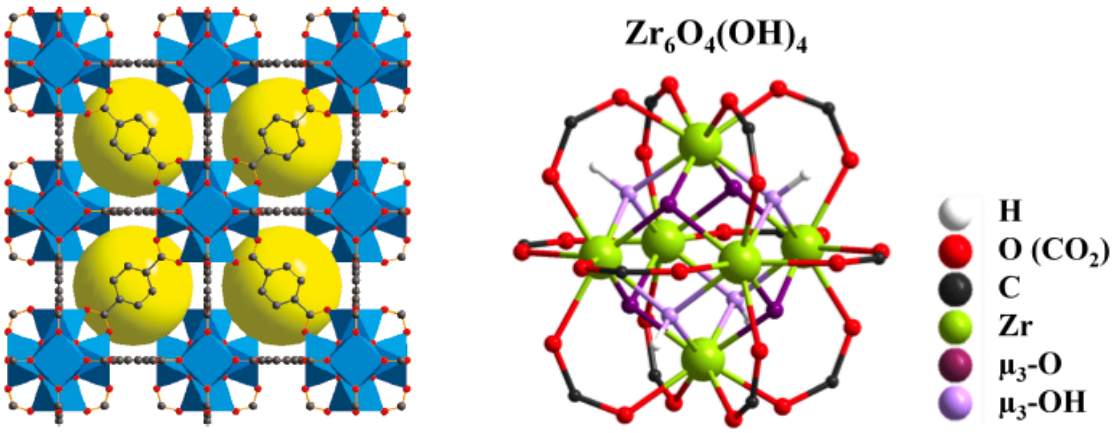

Figure 1.4. *UiO-66 framework as a representative robust MOF (left)[8] and its 12-connected Zr_6-cluster node (right).[9]*

Therefore, in order to exploit the potentialities of MOFs, it is required to synthesize them with high valence metal ions as nodes, in order to impart them high chemical stability under harsh conditions. Moreover, it is mandatory to develop a reliable synthetic methodology, which can allow including particular functionalities inside the MOF framework, to vary the final properties and potential applications of the framework itself.

1.2 Metal organic frameworks as heterogeneous photocatalysts

In the field of *electro-* and *photocatalysis* for solar fuels production, the archetypes of homogeneous and heterogeneous catalysts are, the Re-based complexes

developed by Ishitani *et. al.*[10] for carbon dioxide reduction and the well-known titanium dioxide photocatalyst, along with its modifications (see Figure 1.5).[11]

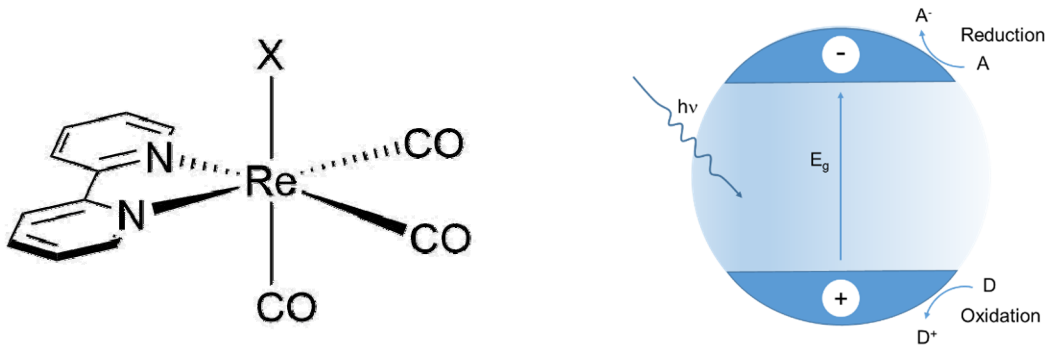

Figure 1.5. *Ishitani's Rhenium complex used for CO_2 reduction (left) and TiO_2 semiconductor (right).*

Obviously, both systems have their advantages and their disadvantages. For the homogeneous system, the advantages are its high efficiency as well as the possibility of using the visible part of the solar spectrum through judicious choice of the nitrogen-based chelating ligand. Moreover, since it is a transition metal complex, the excited state generally derives from a Metal-to-Ligand Charge Transfer (MLCT) process,[12] thus enhancing the electron-hole separation. On the other hand, its main disadvantage consists in being a homogeneous system, which makes the recovering of the catalyst very challenging.

The main advantages of TiO_2, are its recyclability and robustness. This material is stable in a wide range of pH and even in harsh conditions. On the other hand, because of its moderately high band-gap (3.0-3.2 eV), TiO_2 is capable to harvest only the UV part of the solar spectrum, which accounts for ~4% only of the total solar spectrum. Moreover, it undergoes fast electron-hole recombination, which limits the fraction of photogenerated charges effectively capable of electron transfer reaction at the photocatalyst surface. Even though many modifications of the lattice structure of TiO_2

were made, by addition of dopants or by coupling it with other oxide-based semiconductors, the modifications that can be made are not the same with the ones on the molecular materials.[13]

Therefore, if we consider just the advantages of the two systems, the properties that have to be sought in a catalyst are:

1. High efficiency in the targeted reaction;
2. Easy modification of its properties, with special attention to absorption properties;
3. Efficient separation of the electro- or photogenerated electron-hole pair;
4. Chemical stability in harsh conditions;
5. Easy recyclability

A Metal-Organic Framework is a material that can well summarize all of these features. In fact, it possesses a mixed nature, because it is formed by interaction of organic-based linkers and metal-based nodes. This feature is reflected in many aspects. For example, its properties can be tuned by modifying the organic linker in order to add more functionalities or by directly targeting specific ones and the metal node can be changed or modified. In addition, since the light-harvesting unit is the organic ligand, its absorption properties can be tuned as well through ligand modifications. In this regards, the electron-hole separation is enhanced by the mixed nature of the framework itself. Moreover, the careful choice of the binding functionality of the organic linker and the type of the metal node can give raise to an excellent stable material, even under harsh condition. Last, but not least, a MOF is a material which is *insoluble* in any media by definition and therefore it can be regarded as a potential heterogeneous catalyst. In fact, if a MOF is soluble in a certain media, it means that

the frameworks is collapsing and it is releasing its *building blocks* (that is, the organic linkers and metal nodes) into the solution.

In one word, a MOF perfectly satisfies all the criteria required to be a potential catalyst, because it is highly tunable by design, because it possesses a mixed nature (both organic and inorganic) and because it is a heterogeneous system.

The only limitation lies in the first point of the list: simply combining an organic linker with a metal node, even though perfectly tailored in order to satisfy the other criteria, does not assure that it will be also electro- or photocatalytically active. In fact, the photodynamics of the whole framework has to be tailored as well, in order to achieve the desired catalytic effect.

Garcìa and co-workers[14] firstly elucidated the photodynamics of a MOF structure, demonstrating that the electronic structure of a MOF is determined by the interaction of the organic linker and the inorganic node. More precisely, it was demonstrated that a MOF possesses a behaviour similar to that of a semiconductor. From a practical point of view, the photodynamics in a MOF structure does not differ too much from the one of a Dye-Sensitized Solar Cell (DSSC, Figure 1.6).[15]

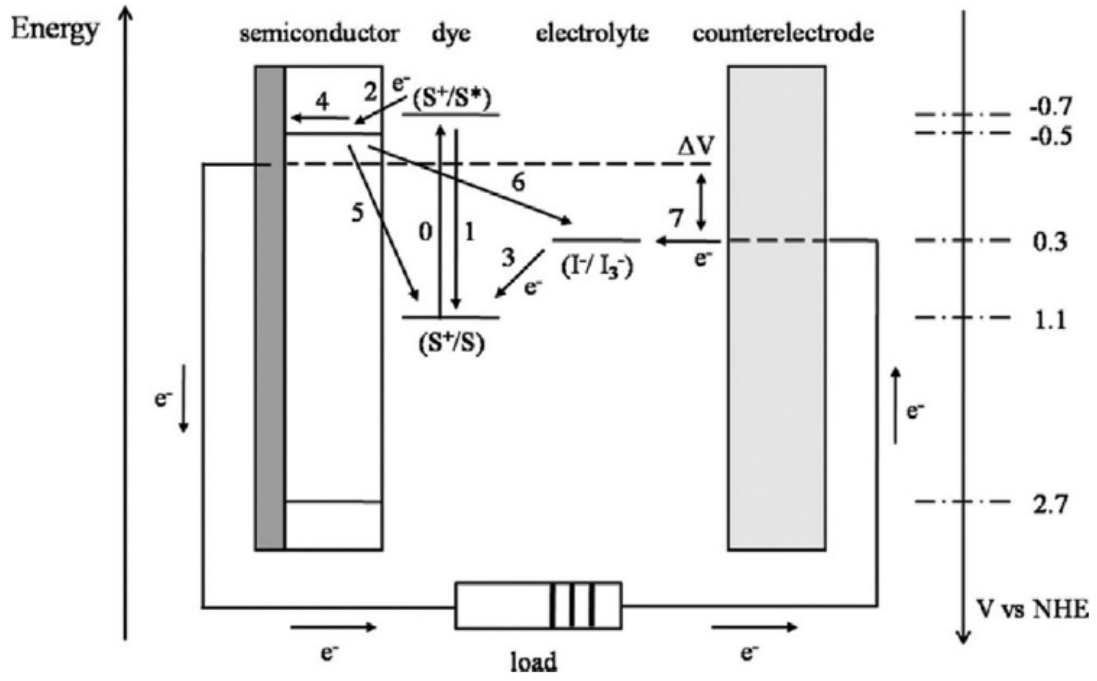

Figure 1.6. *Schematic representation of the photodynamics in a DSSC. Image taken from ref [15].*

In a MOF, the photodynamics has proven to be essentially the same (Figure 1.7). The organic linker acts as light-harvesting unit and so an electron is promoted from the HOMO to the LUMO of the linker. Then, it is injected into the metal node, from which it can potentially reduce species also present in solution with lower (*i.e.* more positive) oxidation potential. Then the cycle is made catalytic (from the MOF perspective) by a molecule which restores the electron “lost” by the MOF species. Differently from the DSSC, this molecule is not a redox couple and generally is not restored. In fact, it is called *Sacrificial Electron Donor* (SED) and it is what limits the mechanism to be fully catalytic.

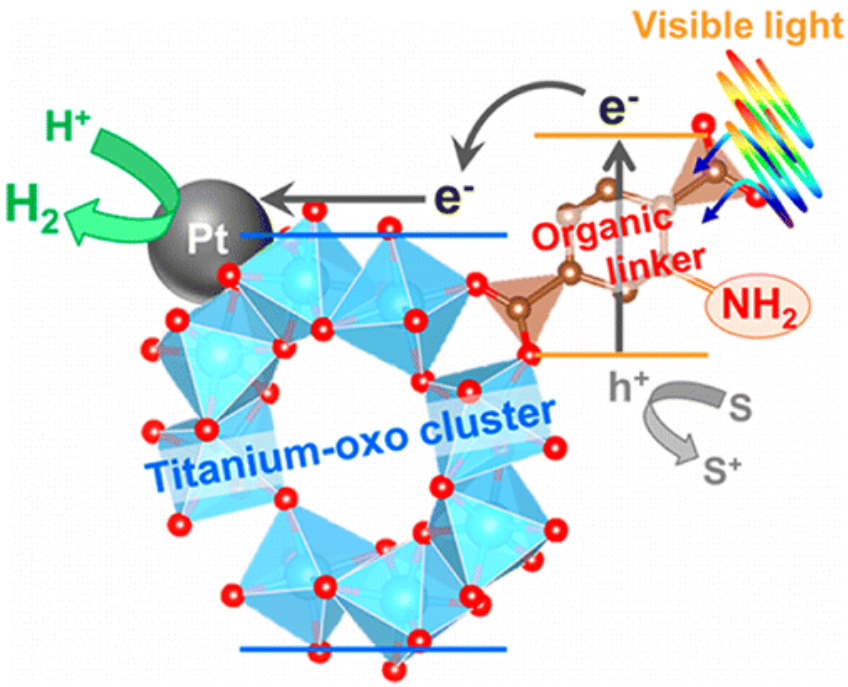

Figure 1.7. *Schematic drawing to represent the photodynamic in a MOF structure. In particular, the HER (Hydrogen Evolution Reaction) is shown, with Pt as co-catalyst.*[16]

Therefore, according to the mechanism described in Figure 1.7, it is mandatory to design a MOF in which the organic linker possesses a LUMO higher in energy with respect to the conduction band of the metal node. Obviously, the latter has to be higher in energy with respect to that of the molecule undergoing the targeted reaction, in order to obtain a downhill reaction. Last, but not the least, the SED has to possess a redox potential higher than the HOMO of the linker, but not too high in energy, in order not to generate competitive pathways for the excited electron. The choice of the proper SED is particularly complicated by the high number of variables present in a particular catalytic system: media, pH, type of reaction, type of catalyst and so on. In the literature, the most used ones are tertiary amines like TEOA and TEA (triethanolamine and trimethylamine, respectively), generally in organic solvents like acetonitrile or *N,N*-dimethylformamide, but even in mixture with H_2O. For aqueous media, especially for lower pH values, EDTA (ethylendiamminetetraacetic acid) is often adopted as SED in

its disodium salt form. Anyway, the optimized parameters that can be used to evaluate the best SED to use still need to be defined.[17]

Anyway, in some cases in the electronic levels of the linker and the metal node do not completely match each other. Therefore, the catalytic properties can be just given by the ligand[18] or there could be a synergistic effect between the ligand and the metal node, for which some of the catalytic activity is directly given by the ligand and some by the abovementioned mechanism.[19] Moreover, this mechanism is not the only one feasible in a MOF framework (Figure 1.8).[20]

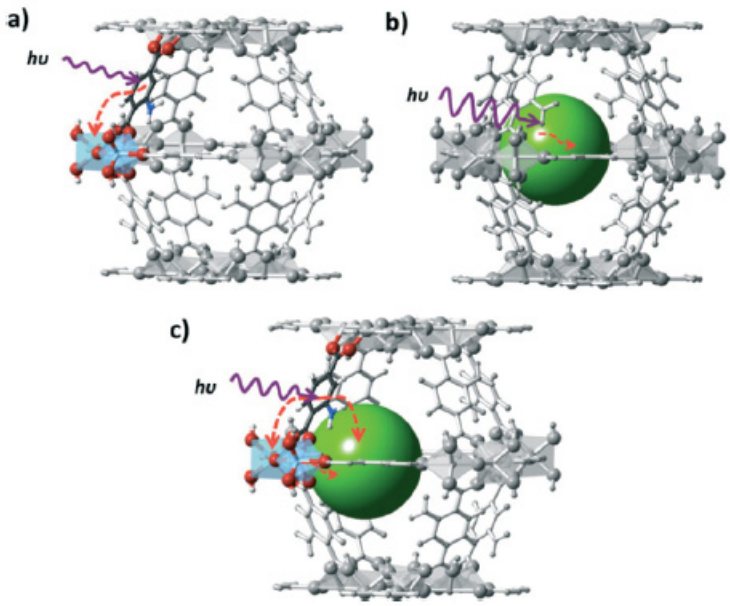

Figure 1.8. *Different approaches to induce photocatalytic activity in a MOF framework.*[21]

The most common approach is mechanism (a), in which the linker acts as a light-harvesting unit and then charge transfer occurs to the inorganic cluster. Generally, for the Hydrogen Evolution Reaction (HER), this mechanism is exploited in the presence of a co-catalyst, as shown in Figure 1.7: the co-catalyst is deposited on the surface of the MOF and “receives” electrons from the metal node.[22] In mechanism (b), the MOF

is used as a scaffold, in which a molecular catalyst is loaded, which can also act as a light-harvesting unit.[23] Mechanism (c) is an in-between one and it resembles mechanism (a) for H_2 production, especially if the Pt co-catalyst is loaded inside the pores of the framework.[22a]

In this part of the thesis, efforts have been devoted to attempt the synthesis of MOFs able to work as photocatalytic systems according to type-a mechanism. As light-harvesting units and linkers, dipyrrin-based metalloligands and porphyrins were selected. Regarding the metal node, the choice had to account for multiple aspects. Knowing that this unit, in a MOF structure, behaves as a semiconductor, taking into account the flat band potential and conduction band position of the common metal oxides at pH = 7 shown in Figure 1.9, then the suitable ones are not too many.[24]

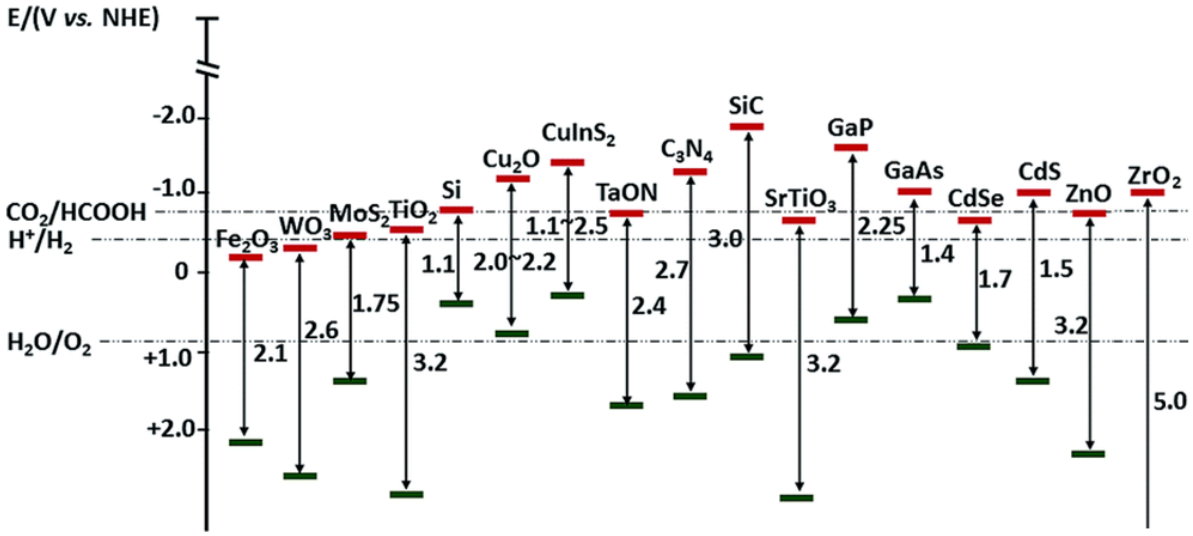

Figure 1.9. *Flat band potential and conduction band position of common metal oxides at pH = 7. Image taken from ref [24].*

In fact, the only one that possesses a conduction band higher than both the H^+ and CO_2 reduction potential is ZrO_2. Moreover, this oxide is made of Zr^{IV}, which is a suitable choice to make a stable framework with carboxylate functionalities, according to the

Hard-Soft Acid-Base (HSAB) theory developed by Pearson.[25] Therefore, our attention was focused on the Zr^{IV} as metal node in the construction of MOF frameworks. A Fe^{III}-based cluster, the Fe_3O one, has been reported to be stable and photocatalytically active for the CO_2 reduction reaction.[26] Therefore, along with the extensive study on the Zr-based MOFs, also the Fe-based ones were explored.

All the requirements that have to be fulfilled in order to induce an effective and efficient catalytic activity in a MOF structure can be summarized as follows:

- **Metal cluster (node)**

1. Hard Lewis acid;
2. CB higher than the H^+ and CO_2 reduction potentials;

- **Organic linker (antennae)**

1. Capable to harvest visible light;
2. LUMO higher than the CB of the metal cluster;
3. Chemically stable

The metal node needs to be a hard Lewis acid in order to generate more stable bonds with the carboxylate linkers, thus achieving a better chemical stability in a wide range of pH. For example, ZnO_2 is known to be unstable in acidic conditions and MOF made with Zn as node are known to be only chemically stable in a small range of pH around neutrality. Moreover, its CB needs to be higher than the reduction potential of the targeted species, since the mechanism adopted for the catalysis requires the electron to be transferred from the linker to the cluster and then to the species which has to be reduced. The linker has to possess an energy gap compatible with the

absorption of visible light, since the UV part of the solar spectrum accounts only for ~4% of the total. Moreover, its HOMO and LUMO positions have to be tailored as well, because the LUMO has to lie above (in terms of energy) the CB of the metal node. Last, the linker has to be chemically stable: that is, once the electron is injected in the CB of the metal node, no photodecomposition has to occur.

With all this in mind, we sought for organic linkers with carboxylate functionalities that could efficiently harvest visible light and transfer the electro- or photogenerated electron to the metal cluster, formed by Zr^{IV} or Fe^{III} ions.

REFERENCES

[1] (a) Yaghi, O. M.; O'Keeffe, M.; Ockwig, N. W.; Chae, H. K.; Eddaoudi, M.; Kim, J., *Nature* **2003**, *423*, 705; (b) Férey, G.; Mellot- Draznieks, C.; Serre, C.; Millange, F.; Dutour, J.; Surblé, S.; Margiolaki, I., *Science* **2005**, *309*, 2040; (c) Horike, S.; Shimomura, S.; Kitagawa, S., *Nat. Chem.* **2009**, *1*, 695; (d) Long, J. R.; Yaghi, O. M., *Chem. Soc. Rev.* **2009**, *38*, 1213; (e) Zhou, H.-C.; Long, J. R.; Yaghi, O. M., *Chem. Rev.* **2012**, *112*, 673.

[2] (a) Horcajada, P.; Gref, R.; Baati, T.; Allan, P. K.; Maurin, G.; Couvreur, P.; Férey, G.; Morris, R. E.; Serre, C., *Chem. Rev.* **2012**, *112*, 1232; (b) Kreno, L. E.; Leong, K.; Farha, O. K.; Allendorf, M. R.; Van Duyne, P.; Hupp, J. T., *Chem. Rev.* **2012**, *112*, 1105; (c) Suh, M. P.; Park, H. J.; Prasad, T. K.; Lim, D.-W., *Chem. Rev.* **2012**, *112*, 782; (d) Sumida, K.; Rogow, D. L.; Mason, J. A.; McDonald, T. M.; Bloch, E. D.; Herm, Z. R.; Bae, T.-H.; Long, J. R., *Chem. Rev.* **2012**, *112*, 724; (e) Yoon, M.; Srirambalaji, R.; Kim, K., *Chem. Rev.* **2012**, *112*, 1196; (f) Cui, Y.; Yue, Y.; Qian, G.; Chen, B., *Chem. Rev.* **2012**, *112*, 1126; (g) Li, J.-R.; Sculley, J.; Zhou, H.-C., *Chem. Rev.* **2012**, *112*, 869; (h) Wu, H.; Gong, Q.; Olson, D. H.; Li, J., *Chem. Rev.* **2012**, *112*, 836; (i) Wang, C.; Zhang, T.; Lin, W., *Chem. Rev.* **2011**, *112*, 1084; (j) Lu, W.-G.; Su, C.-Y.; Lu, T.-B.; Jiang, L.; Chen, J.-M., *J. Am. Chem. Soc.* **2006**, *128*, 34; (k) Umemura, A.; Diring, S.; Furukawa, S.; Uehara, H.; Tsuruoka, T.; Kitagawa, S., *J. Am. Chem. Soc.* **2011**, *133*, 15506; (l) Gao, J.; Maio, J.; Li, P.-Z.; Teng, W. Y.; Yang, L.; Zhao, Y.; Liu, B.; Zhang, Q., *Chem. Commun.* **2014**, *50*, 3786; (m) Lu, H.-S.; Bai, L.; Xiong, W.-W.; Li, P.; Ding, J.; Zhang, G.; Wu, T.; Zhao, Y.; Lee, J.; Yang, Y.; Geng, B.; Zhang, Q., *Inorg. Chem.* **2014**, *53*, 8529.

[3] Image taken from: https://theconversation.com/mof-the-chart-why-a-record-breaking-surface-area-matters-9915.

[4] Civalleri, B.; Napoli, F.; Noël, Y.; Roetti, C.; Dovesi, R., *CrystEngComm*, **2006**, *8*, 364.

[5] Makal, T. A.; Li, J.-R.; Lu, W.; Zhou, H.-C. *Chem. Soc. Rev.*, **2012**, *41*, 7761.

[6] Helm, L.; Merbach, A. E., *J. Chem. Soc., Dalton. Trans.*, 2002, 633.

[7] Jiang, H.-L.; Feng, D.; Wang, K.; Gu, Z.-Y.; Wei, Z.; Chen, Y.-P.; Zhou, H.-C. *J. Am. Chem. Soc.* **2013**, *135*, 13934.

[8] Yang, Q.; Wiersum, A. D.; Jobic, H.; Guillerm, V.; Serre, C.; Llewellyn, P. L.; Maurin, G., *J. Phys. Chem. C*, **2011**, *115*, 13768.

[9] Image taken from: https://www.iycr2014.org/learn/crystallography365/articles/20141212.

[10] Takeda, H.; Koike, K.; Inoue, H.; Ishitani, O., *J. Am. Chem. Soc.*, **2008**, *130*, 2023.

[11] Qu, Y.; Duan, X., *Chem. Soc. Rev.*, **2013**, *42*, 2568.

[12] Turro, N. J., Modern Molecular Photochemistry, University Science Books Ed., 1991.

[13] Tong, H.; Ouyang, S. X.; Bi, Y. P.; Umezawa, N.; Oshikiri, M.; Ye, J. H., *Adv. Mater.*, **2012**, *24*, 229.

[14] Silva, C. G.; Corma, A.; Garcìa, H. *J. Mater. Chem.* **2010**, *20*, 3141.

[15] Hara, K.; Arakawa, H. *Handbook of Photovoltaic Science and Engineering*, **2005**, vol 15.

[16] Horiuki, Y.; Toyao, T.; Saito, M.; Mochizuki, K.; Iwata, M.; Higashimura, H.; Anpo, M.; Matsuoka, M., *J. Phys. Chem. C*, **2012**, *116* , 20848.

[17] Pellegrin, Y.; Odobel, F., *C. R. Chimie*, **2017**, *20*, 283.

[18] Zhang, H.; Wei, J.; Dong, J.; Liu, G.; An, P.; Zhao, G.; Kong, J.; Wang, X.; Meng, X.; Zhang, J.; Ye, J., *Angew. Chem. Int. Ed.*, **2016**, *55*, 14310.

[19] Chen, D.; Xing, H.; Wang, C.; Su, Z., *J. Mater. Chem. A*, **2016**, *4*, 2657.

[20] Nasalevich, M. A.; van der Veen, M.; Kapteijn F.; Gascon, J., *CrystEngComm.*, **2014**, *16*, 4919.

[21] Nasalevich, M. A.; van der Veen, M.; Kapteijn, F.; Gascon, K., *CrystEngComm*, **2014**, *16*, 4919.

[22] (a) Wang, C.; deKrafft, K. E.; Lin, W., *J. Am. Chem. Soc.*, **2012**, *134*, 7211; (b) Horiuchi, Y.; Toyao, T.; Saito, M.; Mochizuki, K.; Iwata, M.; Higashimura, H.; Anpo, M.; Matsuoka, M., *J. Phys. Chem. C*, **2012**, *116*, 20848; (c) He, J.; Wang, J.; Chen, Y.; Zhang, J.; Duan, D.; Wang, Y.; Yan, Z., *Chem. Commun.l,* **2014**, *50*, 7063; (d) Fateeva, A.; Chater, P. A.; Ireland, C. P.; Tahir, A. A.; Khimyak, Y. Z.; Wiper, P. V.; Darwent, J. R.; Rosseinsky, M. J., *Angew. Chem. Int. Ed.*, **2012**, *51*, 7440.

[23] Li, Z.; Xiao, J.-D.; Jiang, H.-L., *ACS Catal.*, **2016**, *6*, 5359.

[24] Zhao, J.; Wang, X.; Xu, Z.; Loo, J. S. C., *J. Mater. Chem.*, **2014**, *2*, 15228.

[25] (a) Pearson, R. G. *J. Chem. Educ.*, **1968**, *45*, 581; (b) Pearson, R. G. *J. Chem. Educ.*, **1968**, *45*, 643.

[26] Wang, D.; Huang, R.; Liu, W.; Sun, D.; Li, Z., *ACS Catal.*, **2014**, *4*, 4254.

Chapter 2

DIPYRRINS

2.1 Dipyrrin-based metal complexes as metalloligand

Boron-dipyrromethene (4,4-difluoro-4-bora-3*a*,4*a*-diaza-*s*-indacene, or BODIPY) fluorescent dyes, a structural parent of the porphyrins, have been the focus of considerable research interest over the last three decades, their synthesis was first described by Treibs and Kreuzer in 1968.[1] The large interest over these molecules relies on the intriguing properties they possess, especially from the spectroscopic point of view, and for their great chemical and photochemical stability. These properties make BODIPY a suitable class of compounds for many applications, such as their use as fluorescent indicators, photodynamic therapy, luminescent devices and energy transfer cassettes. As shown in Scheme 2.1, this family of compounds is based conjugated bis-pyrrolic monoanionic chelating dipyrrinato (dpm) derivative.[2]

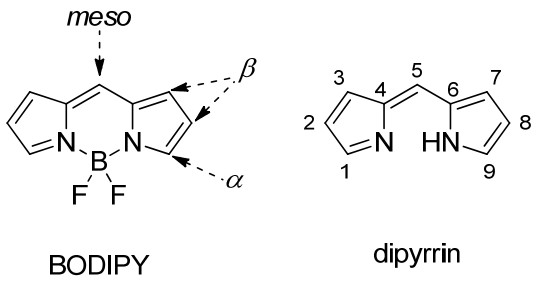

BODIPY dipyrrin

Scheme 2.1. *Representation of a BODIPY dye and a dipyrrin ligand with the corresponding numbering of its atom*

Although the first report of a luminescent dpm-based metal complex is set back in 1979 by Falk and Neufingerl with the $Zn(dpm)_2$ complex,[3] their investigation was mainly focusedon the construction of heterometallic architectures, rather than their luminescent properties. However, several synthetic strategies have been recently proposed for the preparation of stable luminescent dpm-based metal complexes with appreciable luminescence quantum yield and tuneable emission wavelength. In particular, since the emission of the majority of these compounds is ligand-centred, the functionalization of the dipyrrin backbone, either at position 5, equivalent to the *meso* position of a porphyrin, or at positions 1 and 9, has particularly been considered. Both sites allow the introduction of aryl groups with the possibility of bearing extra coordination sites pointing far from the dipyrrin backbone. Moreover, direct linkage at position 1 or 9 can lead to the formation of a bisdipyrrin unit,[4] thus providing a pseudo-macrocyclic character to the resulting ligands.

Despite their high synthetic versatility and their attractive photophysical properties, dipyrrin based metal complexes have not been diffusively incorporated in heterogeneous architectures for photochemical applications as happened for metalloporhyrins.[5] Dipyrrin complexes able to anchor to metal-oxide surfaces, such as

TiO_2, are particularly interesting since they are in principle able to sensitize semiconductor materials, which are not able to harvest visible light.[6] This process is driven by the excitation of the dye upon illumination with visible light and subsequent injection of the excited electron into the CB of the selected semiconductor, as happens in dye sensitized solar cell devices,[7] to obtain electrical work. Inspired by the work of Telfer and co-workers,[8] in which the electron injection from dipyrrin-based complexes into TiO_2 was demonstrated, we targeted the carboxyl-derivative of the dipyrrin ligands as well, in order to satisfy the HSAB theory[9] with hard Lewis acid species such as Zr^{IV} or Ti^{IV} useful for the construction of MOF frameworks.

The synthesis of ligand **dpmCOOMe** is shown in Scheme 2.2, while detailed synthetic procedures are provided in Appendix A.

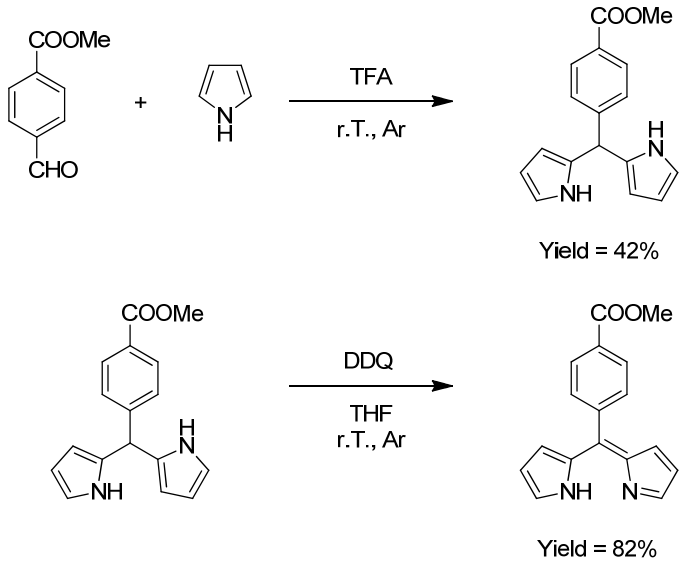

Scheme 2.2. *Synthetic procedure for ligand* ***dpmCOOMe****.*

Briefly, pyrrole and the corresponding aldehyde were stirred at room temperature for three hours in the presence of three drops of TFA (trifluoroacetic acid), under inert atmosphere. Then, the excess of pyrrole was filtered off and the solid washed with

ether and filtered. The obtained white powder was then oxidized with DDQ (2,3-Dichloro-5,6-dicyano-1,4-benzoquinone) at room temperature overnight. The crude product was then purified by means of column chromatography.

The complexes obtained with the use of ligand dpmCOOMe and metal cations such as Ni(II), Cu(II) and Zn(II) were all acid labile (not reported in the thesis), thus they underwent hydrolysis during the saponification step. In order to overcome this weakness, a strategy based on chemical modification of dpmCOOMe ligand was adopted. In particular, the Ni^{II} complex was chosen to target a more rigid structure, which is called bisdipyrrin. The idea was that a more rigid structure can guarantee a better macrocyclic effect and thus better mimic the behaviour of a corrole,[10] so that the metal centre could be maintained in the hydrolysis acidification step. Therefore, following the procedure reported by Baudron ***et. al.***,[11] the Ni-bisdipyrrin derivative was obtained as shown in Scheme 2.4 starting from the $Ni(dpmCOOMe)_2$ complex.

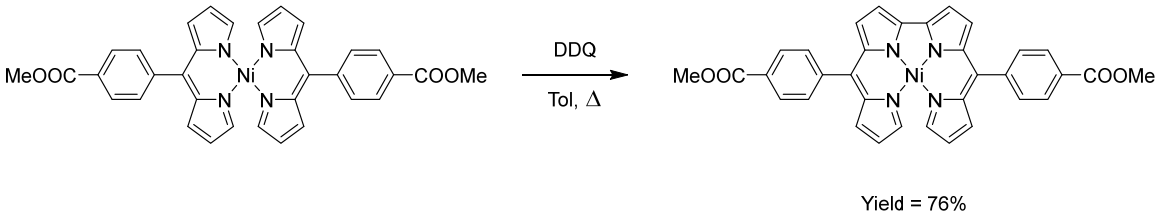

Scheme 2.3. *Synthesis of Ni-bisdpmCOOMe complex*

Briefly, a toluene solution of complex $Ni(dpmCOOMe)_2$ was oxidized with DDQ in toluene at reflux overnight. The targeted compound was obtained in its pure form after purification by means of column chromatography. Subsequent hydrolysis of the ester and careful acidification of the mixture with aqueous HCl gave the corresponding Ni-bisdpmCOOH complex, as shown in Scheme 2.4.

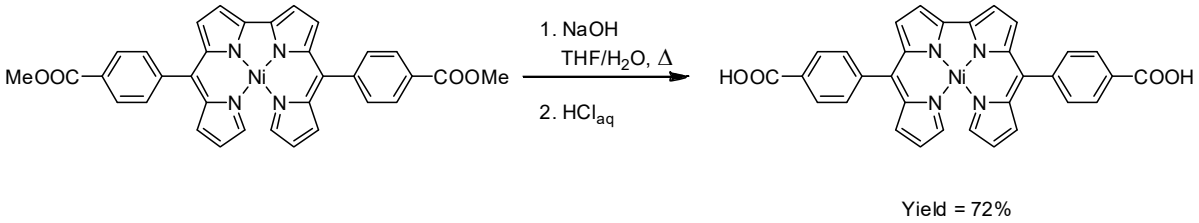

Scheme 2.4. *Synthesis of Ni-bisdpmCOOH*

The key point in this synthesis was the acidification step. In fact, from a homogeneous dark solution up to neutral pH, the compound started to precipitate as soon as few drops of aqueous HCl were added, reaching a pH of ca. 6.5. The aspect of the mixture was a black powder deposited at the bottom of a completely colourless water solution. The compound was thus filtered and washed with water and then collected after drying in oven.

The properties of the Ni-based complex are thoroughly discussed in chapter 3.

REFERENCES

[1] Lu, H.; Mack, J.; Yang, Y.; Shen, Z., *Chem. Soc. Rev.*, **2014**, *43*, 4778 and references therein.

[2] (a) Baudron, S. A., *Dalton Trans.*, **2013**, *42*, 7498 and references therein; (b) Eood, T. E.; Thompson, A., Chem. Rev., 2007, 107, 1831 and references therein.

[3] Falk, H.; Neufingerl, F., *Monatsh. Chem.*, **1979**, *110*, 987.

[4] Gill, H. S.; Finger, I.; Boidarević, I.; Szydlo, F.; Scott, M. J., *New J. Chem.*, **2005**, *29*, 68.

[5] (a) Campbell, W. M.; Burrell, A. K.; Officer, D. L.; Jolley, K. W. *Coord. Chem. Rev.*, **2004**, *248*, 1363; (b) Esswein, A. J.; Nocera, D. G. *Chem. Rev.*, **2007**, *107*, 4022.

[6] Ardo, S.; Meyer, G. J. *Chem. Soc. Rev.*, **2009**, *38*, 115.

[7] Nazeeruddin, M. K.; Gratzel, M. *Comprehensive Coordination Chemistry II*, **2004**, *9*, 719.

[8] Hall, J. D.; McLean, T. M.; Smalley, S. J.; Waterland, M. R. and Telfer, S. G., *Dalton Trans.*, **2010**, *39*, 437.

[9] (a) Pearson, R. G., *J. Chem. Educ.*, **1968**, *45*, 581; (b) Pearson, R. G*., J. Chem. Educ.*, **1968**, *45*, 643.

[10] Orłowsk, R.; Gryko, D.; Gryko, D. T., *Chem. Rev.*, **2017**, *117*, 3102

[11] Baudron, S. A.; Ruffin, H.; Hosseini, M. W., *Chem. Commun.*, **2015**, *51*, 5906.

Chapter 3[1]

A Ni-2,2'-BISDIPYRRINATO COMPLEX AS A POTENTIAL SENSITIZER IN MOFs: SYNTHESIS AND PHOTOELECTROCHEMICAL CHARACTERIZATION

3.1 Introduction

While the most studied class of dyes based on the dipyrrin backbone is that of boron-dipyrromethene (BODIPY) characterized by high chemical and photochemical stability,[2] several examples of luminescent dipyrrin metal complexes have also been recently reported,[3] e.g. dipyrrin complexes containing Rh(III),[4] Cu(I),[5] Pt(II),[6] Ir(III)[7] and

Zn(II).[8] For these systems, the rigidity of the bispyrrolic backbone as well as the steric hindrance of the peripheral aryl groups have been shown to affect their photophysical properties such as the fluorescence quantum yield and the excited state lifetime.[3,7,8] The majority of these compounds is based on ligands with a single dipyrrin moiety functionalized by various groups at the pyrrolic and/or at the meso positions.

2,2'-bis-dipyrrins comprising two dipyrrin fragments connected by a single C-C bond can be regarded as an acyclic analogue of corroles.[9] Even though this class of molecules has been described long ago,[10] so far its use has been mostly limited to the preparation of helicate-type complexes.[11] Although these systems have interesting photophysical and electrochemical properties with potential applications in several fields, a systematic and detailed investigation of such features is still lacking with only few reports published so far.[12] Furthermore, the introduction of such species into more complex architectures and materials was never attempted.

In the present work, we synthesized a novel Ni-based 2,2'-bisdipyrrin complex Ni-bisdpmCOOH and we succeeded to incorporate it into a metal organic framework (MOF). Ni-bisdpmCOOH displays absorption properties extending up to the near infrared (NIR) region of the spectrum. The photophysical and electrochemical characterization of this complex evidenced a suitable positioning of its LUMO energy level with respect to the H^+/H_2 redox couple. It is worth noting that, although dipyrrin complexes were already used as linkers in MOF structures,[13] their incorporation into a Zr-based MOFwas unprecedented.

3.2 Syntheses

All commercial chemicals were used as received from the suppliers (Sigma-Aldrich, TCI Europe and Fluorochem) without further purification. Solvents were dried prior to use. The Ni-dpmCOOMe and Ni-bisdpmCOOMe complexes and demetallated bisdpmCOOH were prepared according to already reported procedures.[11g,14]

Complex Ni-bisdpmCOOH: Ni-bisdpmCOOMe (100.0 mg, 0.164 mmol) was dissolved in a mixture of THF, NaOH 1.0 M and H_2O (3/1/1, 25 mL total volume) and refluxed overnight. After cooling to room temperature (RT), the organic solvent was removed under reduced pressure and the aqueous phase was acidified by addition of a 1.0 M HCl solution down to pH 6.5. This caused the precipitation of Ni-bisdpmCOOH as a black powder which was recovered by filtration and the solid was washed with water and finally dried in air (69.6 mg, 72.5%). ^{1}H-NMR (300 MHz, DMSO-d_6) δ: 8.09 (d, J = 8.1 Hz, 5H), 7.69 (d, J = 8.1 Hz, 5H), 6.83 (d, J = 4.2 Hz, 2H), 6.74 (d, J = 4.4 Hz, 2H), 6.71 (d, J = 4.2 Hz, 2H), 6.56 (d, J = 4.2 Hz, 2H), 6.02 (s, 2H).[15] ESI-MS: m/z = 581.37 [M–H$^+$].

UiO-66 MOF: $ZrCl_4$ (30 mg, 0.129 mmol), 1,4-benzenedicarboxylic acid (BDC, 30 mg, 0.180 mmol) and benzoic acid (500 mg, 4.094 mmol) were dissolved in 3 mL of DMF by ultrasonication in a Pyrex vial. The mixture was heated in an oven at 85 °C for 24 h. The suspension was cooled to room temperature and the white powder was recovered by centrifugation. The solid was first washed three times with DMF to remove unreacted precursors, then washed three times with acetone to achieve solvent-exchange. The resulting UiO-66 MOF was recovered by centrifugation as a white powder and dried in an oven at 80 °C.

Ni-bisdpmCOOH@UiO-66 MOF: $ZrCl_4$ (30 mg, 0.129 mmol), 1,4-benzene-dicarboxylate (BDC, 20 mg, 0.120 mmol), Ni-bisdpmCOOH (5 mg, 0.0086 mmol) and benzoic acid (600 mg, 4.918 mmol) were dissolved in 2 mL of DMF by ultrasonication in a Pyrex vial. The mixture was heated in an oven at 120 °C for 12 h. After cooling to room temperature, the precipitate, characterized by a shiny black colour, was collected by centrifugation, washed three times with DMF to remove unreacted precursors, and then washed three times with acetone. The resulting Ni-bisdpmCOOH@UiO-66 MOF black powder was recovered by centrifugation and dried in an oven at 80 °C.

[5,10,15,20-tetrakis(4-carboxyphenyl)porphyrinato]-Ni(II) (NiTCPP) : Step 1 consisted in the synthesis of [5,10,15,20-tetrakis(4-methoxycarboxyphenyl)porphyrin] (TCPPCOOMe). Pyrrole (3.0 mL, 0.043 mol) and methyl 4-formylbenzoate (6.9 g, 0.042 mol) were added to propionic acid (100 mL) in a 500 mL 3-necked flask and the solution was refluxed overnight in the dark. After cooling to RT, TCPPCOOMe precipitated as a microcrystalline dark powder. This solid was collected by vacuum filtration, first washed with propionic acid, then with water and finally dried in an oven at 80 °C. Yield = 2.5 g (17.5%). ^{1}H-NMR (300 MHz, $CDCl_3$) δ: 8.82 (s, 8H), 8.45 (d, J = 8.3 Hz, 8H), 8.29 (d, J = 8.25 Hz, 8H), 4.11 (s, 12H), -2.81 (bs, 2H).

[5,10,15,20-tetrakis(4-methoxycarbonylphenyl)porphyrinato]-Ni(II) (NiTCPPCOOMe) (step 2), a solution of TPPCOOMe (500.0 mg, 0.59 mmol) and $NiCl_2{\cdot}6H_2O$ (1.80 g, 7.57 mmol) in 60 mL of DMF was refluxed for 5 h. After cooling to RT, the addition of ca. 150 mL of water caused the precipitation of NiTCPPCOOMe as a dark powder. The solid was filtered, and subsequently washed with water and with 1.0 M HCl until the filtrate became colourless. The crystalline powder thus obtained (quantitative yield) was dried in an oven at 80 °C and directly used, without further

purification, in the final step 3, yielding [5,10,15,20-tetrakis(4-carboxyphenyl)porphyrinato]-Ni(II) (NiTCPP).

In step 3, NiTPPCOOMe (500 mg) was stirred in a mixture of THF and methanol (25 mL each), and a solution of NaOH (2.4 g, 60 mmol) in water (25 mL) was added. This mixture was refluxed overnight. After cooling to RT, THF and methanol were removed under vacuum and the volume was restored by addition of water. The mixture was refluxed for ca. 30 min in order to obtain a homogeneous solution, which was acidified with 1.0 M HCl up to complete precipitation. The solid was then filtered, washed with water until the filtrate became colourless and dried in an oven at 80 °C.

3.3 Photoelectrode preparation

The photoanodes were prepared by depositing a commercial TiO_2 paste (Ti-Nanoxide T/SP, Solaronix) on a fluorine tin oxide (FTO) electrode through the so called doctor-blade technique, followed by adsorption of Ni-bisdpmCOOH through electrostatic interaction between the carboxylic groups of the Ni complex and the -OH units on the TiO_2 surface. In detail, the FTO electrode was covered with a scotch tape (3M), thus obtaining a 0.25 cm^2 exposed surface. A small amount of the TiO_2 paste was spread onto the surface with the aid of a microscope slide. The scotch tape was then removed and the electrodes were kept at 70 °C for 1 h and finally annealed at 500 °C for 1 h. A few drops of a Ni-bisdpmCOOH solution in DMF (concentration ca. 10^{-3} M) were deposited on the so-obtained TiO_2 – covered FTO electrodes and left to dry in air. The non-adsorbed dye was removed by washing with DMF and the absorption spectrum of the clean electrode was recorded. This procedure was

repeated until no further increase in absorbance was detected. A total of 10 cycles were performed to attain the final, highest absorbance.

The TiO_2 – covered FTO photoelectrodes modified with NiTCPP were obtained following an identical procedure, using a 0.5 mM solution of NiTCPP in DMF.

3.4 Structural and photo(electro)chemical characterization

Nuclear Magnetic Resonance (NMR) data were collected on a Bruker AVANCE 300 instrument (300 MHz) at room temperature. The chemical shift and coupling constant values are given in ppm and Hz, respectively.

ESI-MS analyses were performed using a LCQ Fleet ion trap mass spectrometer with an electrospray ionization source and an 'Ion Trap' mass analyser. The sample was solubilized in methanol and traces of DMF were added in order to promote its solubility. The MS spectra were obtained by direct infusion of the sample solution under ionization, ESI negative mode. Full-scan mass spectra were recorded in the 50–2000 mass/charge (m/z) range.

UV-Vis-NIR studies were performed on a Perkin-Elmer Lambda 650 S spectrometer with a 2 nm resolution and a 200 nm min^{-1} scanning rate. UV-Vis-NIR reflectance was measured on a Perkin–Elmer Lambda 950 spectrometer (spectra recorded in the reflection mode, using a 150 mm integrating sphere) with a 2 nm resolution and a 200 nm min^{-1} scanning rate.

Cyclic voltammetry was performed in a conventional three-electrode cell using an Autolab PGSTAT 12 (EcoChemie, Utrecht, The Netherlands) potentiostat, controlled by the NOVA (version 2.1) software. The working electrode was a glassy carbon

electrode with a 0.071 cm^2 surface area, a Pt wire was the counter electrode, with Ag/AgCl as the reference electrode.

The observed peak potential (E_p) was expressed with respect to the $Fc^+|Fc$ redox couple by subtracting the $Fc^+|Fc$ half-height peak value, calculated as $E_{p/2}(Fc^+|Fc) = (E_{p,a}(Fc^+|Fc) + E_{p,c}(Fc^+|Fc))/2$, with $E_{p,a}$ and $E_{p,c}$ referring to the anodic and cathodic peaks, respectively. Moreover, E_p values were be converted into the NHE scale by using the following equation: $E_{NHE} = (E_p - E_{p/2}(Fc^+|Fc)) + E°_{Fc+|Fc} - E°_{H+/H2}$, where $E°_{Fc+|Fc}$ is the potential value of the $Fc^+|Fc$ couple referred to vacuum (4.8 V) and $E°_{H+/H2}$ is the potential of the H^+/H_2 couple referred to vacuum (4.44 V).

Photoelectrochemical measurements were performed using a home-made 3-arms cell and the same potentiostat employed for cyclic voltammetry analysis, with the photoelectrode used as working electrode (0.25 cm^2 active surface), a Pt gauze as counter electrode and an Ag/AgCl (3 M NaCl) as reference electrode. The photoelectrodes were tested under backside illumination (through the FTO/TiO_2/Ni-bisdpmCOOH interface). The light source was an Oriel, Model 81172 Solar Simulator with different cut-off filters (420 and 550 nm). The power intensity of the unfiltered AM 1.5G light, measured by means of a Thorlabs PM200 power meter equipped with a S130VC power head with Si detector, was 100 W cm^{-2}. A 0.5 M Na_2SO_3 aqueous solution buffered at pH 7 with potassium phosphate was used in photoelectrochemical measurements. The potential vs. Ag/AgCl was converted into the RHE scale using the following equation: $E_{RHE} = E_{Ag/AgCl} + 0.059\ pH + E°_{Ag/AgCl}$, with $E°_{Ag/AgCl}$ (3.0 M NaCl) = 0.210 V at 25 °C.

Incident photon-to-current efficiency (IPCE) measurements were carried out using a 300 W Lot-Oriel Xe lamp equipped with a Lot-Oriel Omni-λ 150 monochromator and

a Thorlabs SC10 automatic shutter. A 0.62 V bias *vs*. RHE was applied and the current was measured with a 20 nm step, within the 400 to 900 nm wavelength range. The incident light power was measured at each wavelength using the above-mentioned calibrated Thorlabs photodiode and power meter. The IPCE was calculated at each wavelength by the following equation:

$$IPCE = \frac{1240 \cdot j}{P_\lambda \cdot \lambda} \cdot 100$$

where j is the photocurrent density (mA cm^{-2}) and P_λ (nW cm^{-2}) is the power of the monochromatic light at wavelength λ (nm).

The internal quantum efficiency (IQE) at each wavelength was calculated by combining the IPCE spectrum with the absorption (A) spectrum of the photoanode:

$$IQE = \frac{IPCE}{1 - 10^{-A}}$$

X-ray powder diffraction (XRPD) was measured on a BRUKER D8-Focus Bragg-Brentano X-ray Powder Diffractometer equipped with a Cu sealed tube (λ = 1.54178 Å) at 40 kV and 40 mA.

3.5 Synthesis of Ni-bisdpmCOOH

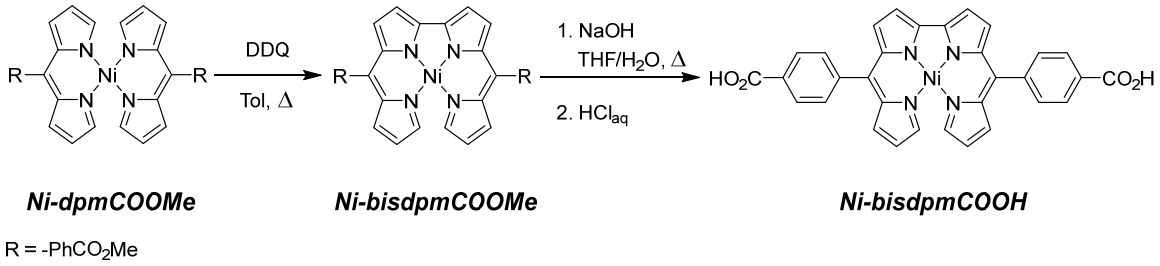

***Scheme 3.1**. Synthesis of the 2,2'-bisdipyrrin Ni(II) metalloligand.*

The synthetic route to Ni-bisdpmCOOH is depicted in Scheme 3.1. The saponification of the Ni-bisdpmCOOMe complex was carried out as described by Brückner *et al.*,[16] with a change concerning the acidification step. Indeed the acid was added until a pH value of *ca.* 6 was reached. Because of the poor solubility of the Ni-bisdpmCOOH complex, the ^{13}C-NMR spectrum could not be recorded. The successful saponification of the ester groups was however confirmed by the absence of the methyl group signals in the upfield region of the ^{1}H-NMR spectrum of complex Ni-bisdpmCOOH (see Figure B1 in Appendix B). On the other hand, evidence of the retention of Ni in the coordinating environment of the molecule was provided by mass spectrometry analysis, which showed a peak at *m/z* = 581.37, corresponding to the desired [M–H^{+}] structure.

3.6 Optical properties

The absorption spectrum of Ni-bisdpmCOOH, recorded in DMF (concentration of $2.92 \cdot 10^{-5}$ M) is shown in Fig. 3.1, together with the absorption spectra of the Ni-dpmCOOMe and Ni-bisdpmCOOMe complexes for comparison. Ni-bisdpmCOOH displays a maximum absorption peak at 416 nm, accompanied by less intense and

broader peaks at 563, 770 and 846 nm. This absorption spectrum is similar to those previously reported for 2,2'-bisdipyrrin based species[11,12] and is comparable to that of the starting Ni-bisdpmCOOMe complex. On the contrary, Ni-dpmCOOMe shows an absorption edge at 570 nm with a strong absorption band peaking at 464 nm and shoulders at *ca.* 440 and 500 nm.

The different absorption properties of Ni-bisdpmCOOH and Ni-bisdpmCOOMe complexes with respect to Ni-dpmCOOMe are clearly related to the increased conjugation and molecular rigidity ensured by the 2,2'-pyrrolic C-C bond. This difference is also evidenced by a comparison between the Ni coordination geometry in the two reported crystal structures.[11g] In fact, while Ni-dpmCOOMe shows a distorted tetrahedral geometry with an angle of *ca* 56° between the two bipyrrolic moieties, in Ni-bisdpmCOOMe the same angle is *ca*. 23°, indicating a distorted square planar geometry.[11g]

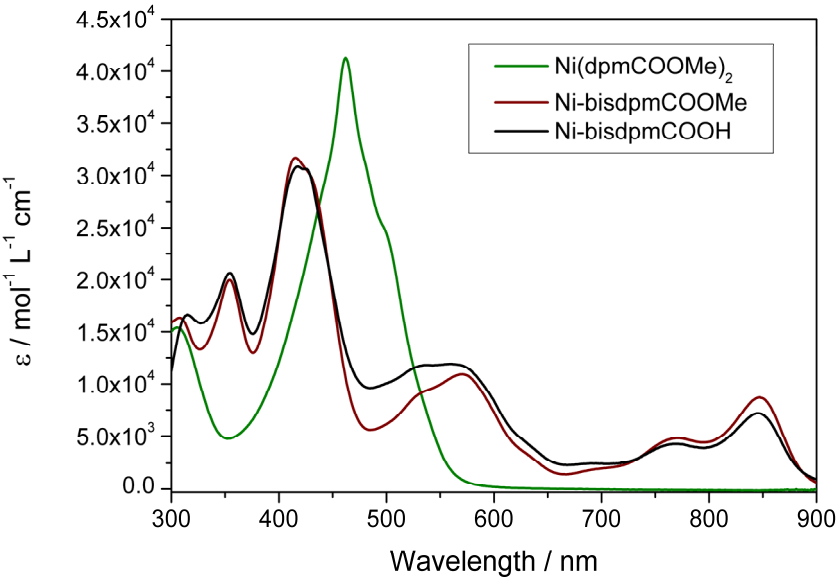

Figure 3.1. *Absorption spectrum of Ni-dpmCOOMe (green line), Ni-bisdpmCOOMe (red line) and Ni-bisdpmCOOH (black line) in DMF.*

3.7 Electrochemical characterization

The redox properties of the Ni-bisdpmCOOH complex were determined by cyclic voltammetry measurements in a DMF solution ($3 \cdot 10^{-4}$ M) containing 0.1 M tetra-*N*-butylammonium hexafluorophosphate ($TBAPF_6$) as supporting electrolyte under an inert atmosphere, obtained by bubbling N_2 in the solution for 10 min. The cyclic voltammetry curves obtained at different potential scanning rate are shown in Fig. 3.2.

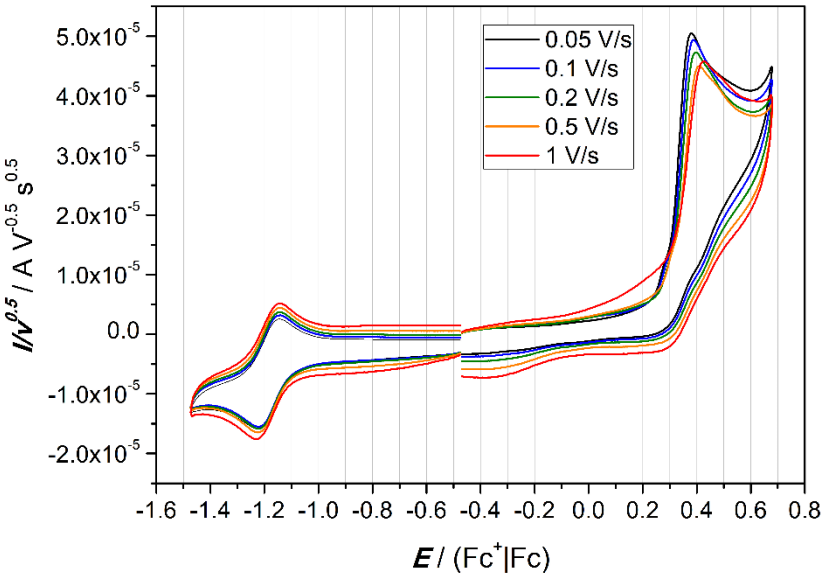

Figure 3.2. *Anodic (positive potentials) and cathodic (negative potentials) scans of Ni-bisdpmCOOH around the first redox potentials, performed at different potential scanning rates.*

The shape of the curve in the anodic part (positive potentials) evidences an irreversible bi-electronic oxidation process at 0.382 V *vs.* $Fc^+|Fc$ for the Ni-bisdipyrrin metalloligand. Moreover, the shift of the anodic oxidation potential with the scan rate implies an electrochemically irreversible electron transfer. Differently, in the cathodic region (negative potentials), the complex displays a chemically and electrochemically reversible one-electron reduction at -1.21 V *vs.* $Fc^+|Fc$. These electrochemical processes are assigned to ligand-centred electron transfer processes, by analogy with

the redox properties already demonstrated for other similar Ni-bisdipyrrin complexes.[12a] Furthermore, with respect to a similar substituted Ni bisdipyrrin complex investigated by Bröring *et al*.,[12b] containing fully alkylated pyrrolic fragments, Ni-bisdpmCOOH displays a significant shift of both cathodic and anodic peaks towards more positive potentials. This effect can be related to the electron depletion induced by the absence of alkyl groups on the bisdipyrrin core,[12b] which usually behave as electron-donating groups.

On the basis of the oxidation and reduction peaks shown in Fig. 3.2, the HOMO and the LUMO energy levels of Ni-bisdpmCOOH are located at 0.74 and -0.85 V *vs.* NHE, respectively, with a HOMO-LUMO gap of 1.59 eV, which is slightly lower than the 1.62 eV calculated for the fully alkylated dipyrrin analogue.[12b] This difference can again be ascribed to the presence of alkyl chains, which make the bisdipyrrin complex investigated by Bröring *et al*.[12b] more electron rich, but less planar and conjugated than Ni-bisdpmCOOH. On the other hand, the presence of electron attracting carboxyl substituents on the phenyl rings of Ni-bisdpmCOOH should not affect its electronic properties, the phenyl groups being twisted with respect to the bisdipyrrin core.[11g]

The cyclic voltammetry curves of nickel tetracarboxyphenyl porphyrin (NiTCPP), which was expressly synthesised in the present work to compare its properties with those of Ni-bisdpmCOOH, displays, in the anodic part, a chemically reversible (at high scan rates) and electrochemically irreversible oxidation peak at 0.66 V *vs.* $Fc^+|Fc$. In the cathodic part, NiTCPP shows a chemically reversible and electrochemically quasi-reversible reduction peak at -1.60 V *vs.* $Fc^+|Fc$ (see Figure B3). The HOMO and LUMO energy levels are at 1.03 and -1.24 V *vs.* NHE, respectively (Fig. 3.3).

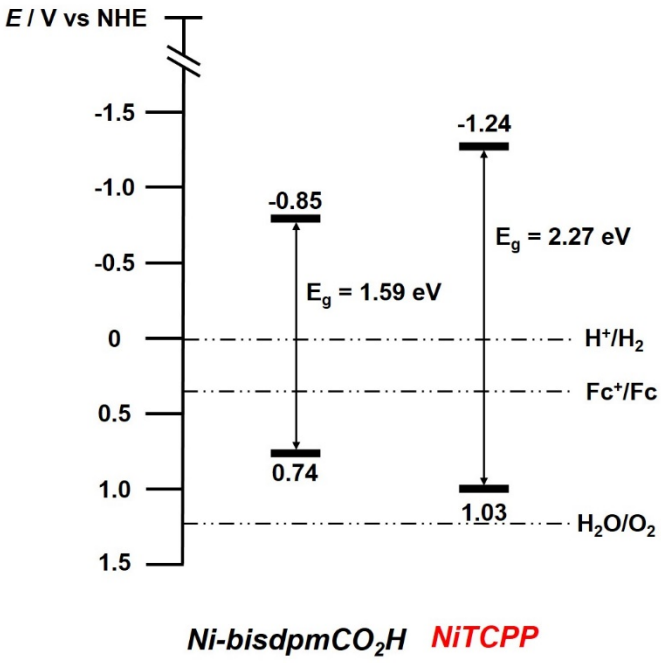

Figure 3.3. *HOMO and LUMO energy levels of Ni-bisdpmCOOH and NiTCPP.*

Interestingly, the LUMO position of both Ni-bisdpmCOOH and NiTCPP are higher in energy with respect to both the TiO_2 conduction band (CB) position (*i.e.* -0.16 V *vs*. NHE)[17] and the H^+/H_2 reduction potential.[18] Therefore, according to the relative energy level positions reported in Fig. 3.3, the electron injection from the LUMO of both photoexcited complexes into the TiO_2 CB is allowed, which makes these systems potentially able to reduce protons from water into hydrogen under visible light irradiation.

3.8 Photoelectrochemical characterization

The UV-Vis-NIR absorption spectra of TiO_2-based electrodes with adsorbed Ni-bisdpmCOOH molecules are shown in Fig. 3.4. Each absorption profile is the difference between the spectrum of the electrode containing the adsorbed dye and that of the electrode containing only TiO_2.

A comparison between these spectra and that reported in Fig. 1 indicates that bisdpmCOOH adsorbed on TiO_2 has an absorption spectrum almost identical to that of the free molecule in solution. The slight blue-shift of the main peak with a maximum at 416 nm could be a consequence of the subtraction procedure of the bare TiO_2 spectrum, having a residual absorption tail up to 450 nm (Figure B4).

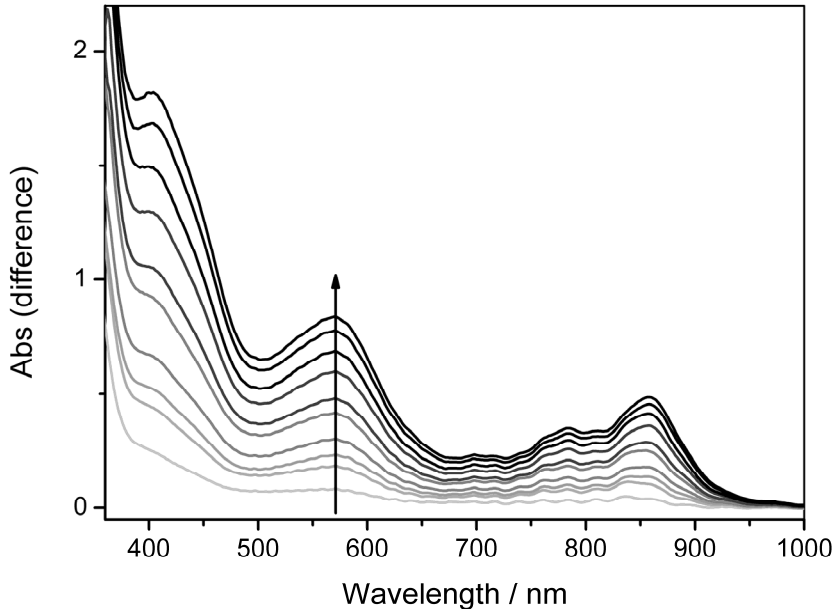

Figure 3.4. *UV-vis absorption spectra of Ni-bisdpmCOOH adsorbed on a TiO_2-covered electrode, recorded after each adsorption cycle. The absorption spectrum of bare TiO_2 was always subtracted.*

The photoelectrochemical (PEC) performance of the modified electrode was explored by means of different photoelectrochemical analyses. Fig. 3.5a shows the linear sweep voltammetry curves recorded with the Ni-bisdpmCOOH on TiO_2 electrode in the 0.22 to 0.62 V *vs.* RHE potential range, demonstrating the onset of photocurrent upon illumination with simulated solar irradiation with the 420 nm cut-off filter. The chronoamperometric curves recorded at 0.62 V *vs.* RHE shown in Fig. 3.5b clearly indicate the presence of photocurrent for the Ni-bisdpmCOOH – sensitized photoanode also when employing the 550 nm cut-off filter, while no photocurrent was

detected with a bare TiO_2 electrode even with the 420 nm filter. By comparison, Fig. 3.5b also shows that when a NiTCPP – sensitized TiO_2 electrode was employed as photoanode under the same conditions, a negligible photocurrent response was detected with the 420 nm cut-off filter, although this molecule absorbs in this spectral region, due to the intense Soret band and the single Q band centred at 532 nm (see Figure B5). The molecular structure and the adsorption conditions of the sensitizer may have a large impact on molecular packing, geometry and aggregation of porphyrin molecules onto the TiO_2 surface, eventually affecting the photocurrent response.[19]

The IPCE curve shown in Fig. 3.5c clearly demonstrates that Ni-bisdpmCOOH adsorbed on TiO_2 is a rather good sensitizer and that electron injection from photoexcited Ni-bisdpmCOOH to the TiO_2 conduction band may efficiently occur up to 620 nm. Moreover, the IQE curve is similar to the IPCE curve, due to the relatively high absorbance of Ni-bisdpmCOOH in the prepared photoanodes (see Fig. 3.4).

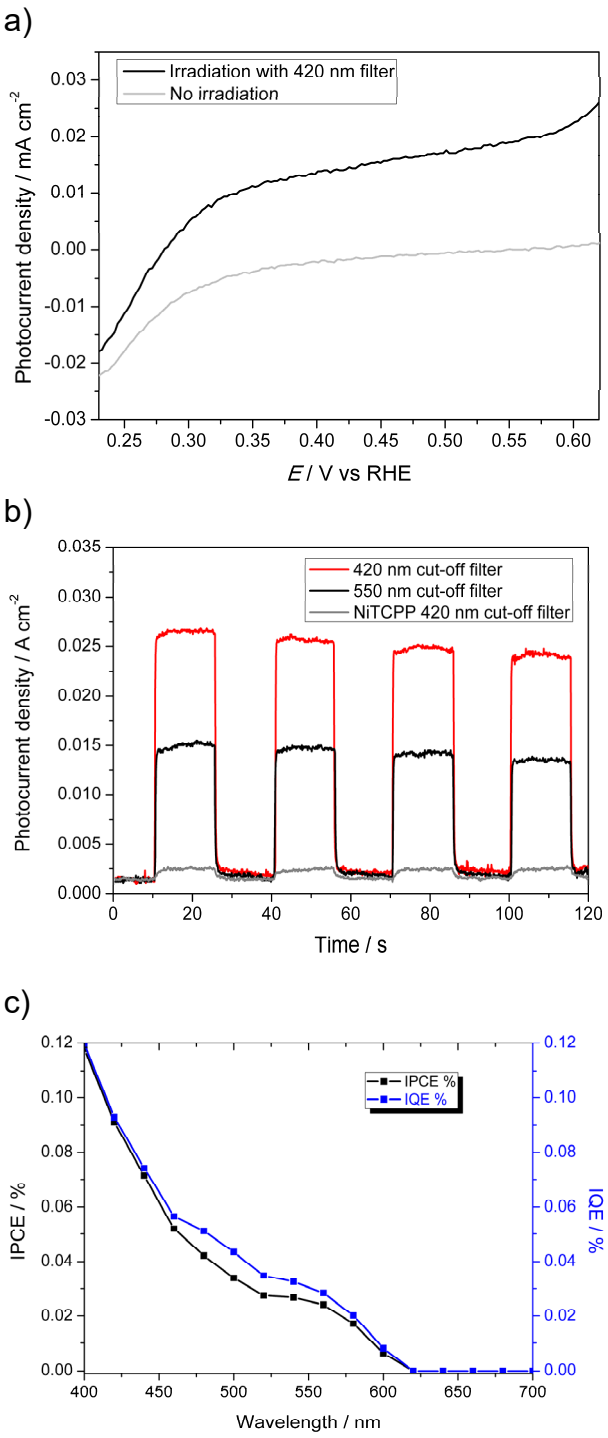

Figure 3.5. *(a) Linear sweep voltammetry curves of Ni-bisdpmCOOH/TiO_2 under irradiation with the 420 nm cut off filter and in the dark; (b) Chronoamperometric analysis of the Ni-bisdpmCOOH/TiO_2 photoanode employing the 420 nm (red thick line) and the 550 nm (black thick line) cut-off filters and of the NiTCPP/TiO_2-based photoanode with the 420 nm cut-off filter (thin line); (c) IPCE and IQE curves obtained with the Ni-bisdpmCOOH/TiO_2 electrode.*

3.9 Inclusion of Ni-bisdpmCOOH into the UiO-66 framework

The integration of multi-functionalities into MOF structures is of great importance to extend the use of these materials to a wide range of applications. The most used method for the synthesis of multifunctional MOFs is still pursued by the mixed-ligand approach, which is based on the partial substitution of the main linker with a different (auxiliary) linker, while preserving the overall MOF structure.[20] Of course, this implies that the auxiliary linker should possess the same geometry and coordinating ability as the "main linker" to make the two linkers "indistinguishable" during the self-assembly process, thus preventing the undesired formation of mixed or segregated phases.

Among the great variety of known MOF structures, it has been established that Zr(IV)-based frameworks show the best chemical stability under a wide range of conditions (temperature, pH, solvents, etc.), making them interesting for many applications.[21]

In the present work, we pursued the idea of exploiting the visible light absorption and electron injection abilities of the Ni-bisdpmCOOH complex by its integration as an auxiliary linker into a robust Zr-based MOF structure. The UiO-66 MOF framework has been chosen, not only because of its high chemical stability and synthetic reproducibility, but also for its conduction band potential which is less negative than the LUMO level of Ni-bisdpmCOOH, the two values being located at -0.60 V and -0.85 V *vs.* NHE, respectively.[22]

The UiO-66 MOF structure is characterized by 12-connected Zr_6-cluster nodes and terephthalic acid as the main linker. In order to substitute part of this latter linker with the Ni-bisdpmCOOH units, we followed the procedure reported by Sun *et al*. who first succeeded to integrate NiTCPP in the UiO-66 framework.[23]

By considering the structural analogy of Ni-bisdpmCOOH with NiTCPP, the introduction of Ni-bisdpmCOOH in the UiO-66 MOF may occur by substitution of the 12-connected Zr_6-cluster node by the 2 connected Ni-bisdpmCOOH, in line with the integration of 4-connected NiTCPP already reported by Sun *et al* (see Fig. 3.6).[23] This is supported by the compatible length of the auxiliary linker evaluated as the distance between the C atoms of two opposite carboxylic acid groups in relation to the maximum extension of the original 12-connected Zr_6-cluster node, which is *ca*. 20.8 Å. The corresponding distance values can be estimated as 18.2 Å for Ni-bisdpmCOOMe,[11g] reasonably similar to that of Ni-bisdpmCOOH, and 18.4 Å in the case of NiTCPP.

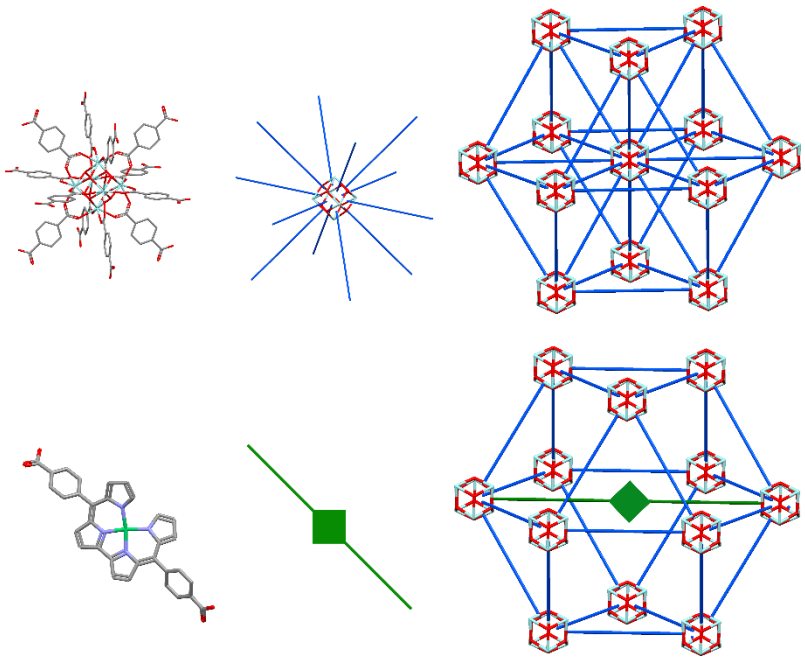

Figure 3.6. *Schematic illustration of the UiO-66 structure (top) and of its doping with Ni-bisdpmCOOH (bottom).*

The successful doping of UiO-66 MOF with Ni-bisdpmCOOH was evidenced by the formation of a black microcrystalline powder, characterized by a unique crystalline phase corresponding to that of the original UiO-66 framework, as shown by XRPD analysis reported in Fig. 3.7.

To demonstrate the effective incorporation of Ni-bisdpmCOOH in the UiO-66 framework, and to rule out any encapsulation of the molecule inside the framework, control reactions were performed. In particular, the use of Ni-bisdpmCOOMe as dopant resulted in a white crystalline material as the bare UiO-66 framework. This demonstrates that the absence of free carboxylic acid coordinating groups prevents the incorporation of such linker into the MOF framework. Similar results were obtained by using as dopant the demetalated bisdpmCOOH molecule, which underlines the key role played by the coordinated Ni centre to give the necessary structural rigidity to the molecule for being successfully incorporated as an auxiliary linker.

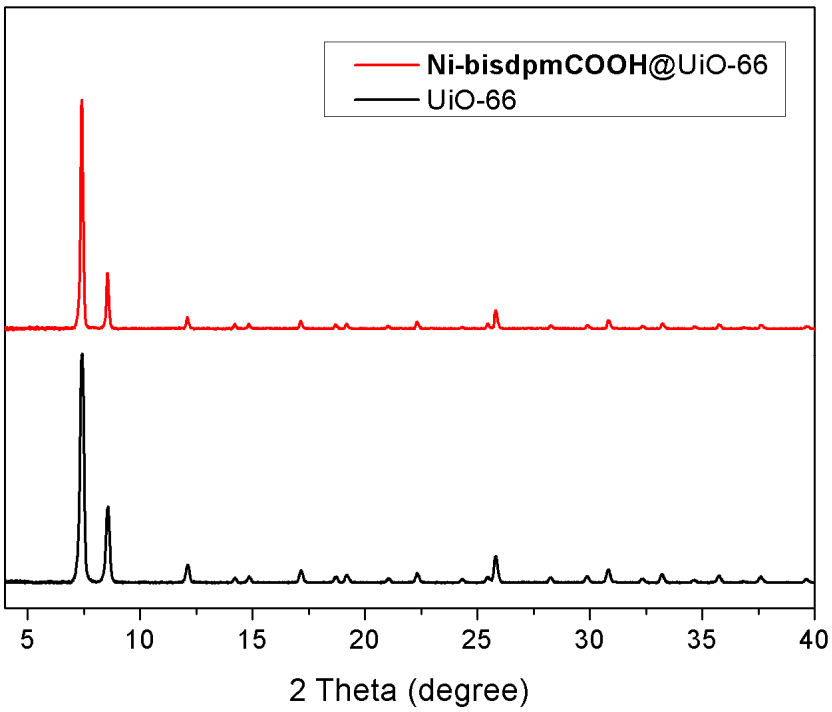

Figure 3.7. *XRPD pattern of Ni-bisdpmCOOH@UiO-66 (top) and of UiO-66 (bottom).*

A further evidence of the effective doping comes from the similar UV-vis absorption properties of Ni-bisdpmCOOH and Ni-bisdpmCOOH@UiO-66. As shown by their

diffuse reflectance spectra reported in Fig. 3.8, they both display comparable main absorption peaks at *ca.* 450 and 500 nm, with a broad absorption above 550 nm.

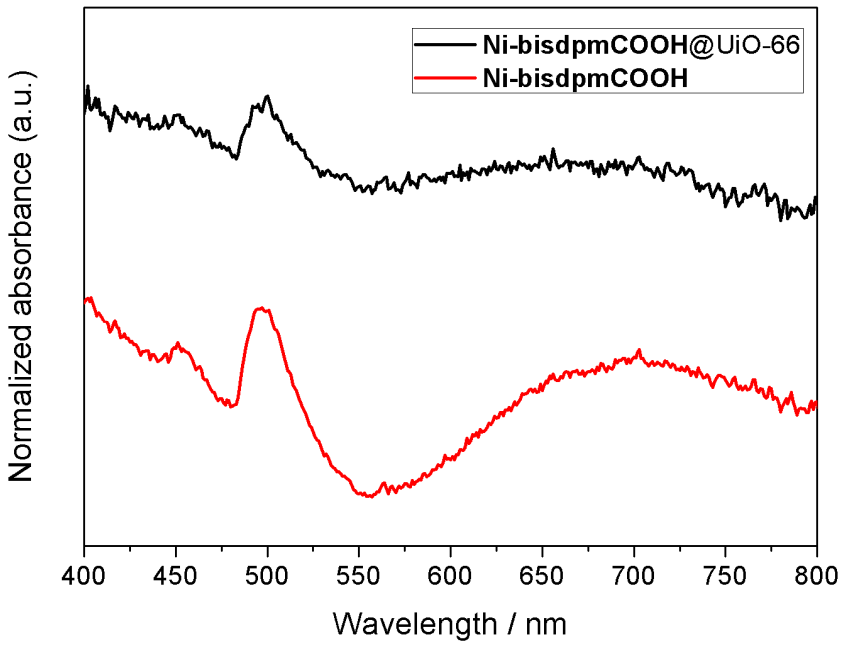

Figure 3.8. *Diffuse reflectance spectra of Ni-bisdpmCOOH (bottom) and of the doped framework (top).*

3.10 Conclusions

In conclusion, the photophysical and electrochemical properties of Ni-bisdpmCOOH, which was investigated as a representative example of an intriguing class of bisdipyrrin complexes, demonstrate its effective ability to act as a rather good sensitizer of TiO_2-based photoanodes, enabling photocurrent production up to 620 nm. Furthermore, the successful doping of the highly stable UiO-66 MOF with this visible light sensitizer has been achieved. This represents a preliminary, however necessary step towards the development of new multifunctional materials for photocatalytic applications. The successfully prepared Ni-bisdpmCOOH@UiO-66 MOF may be used for solar into chemical energy conversion applications.

REFERENCES

[1] Part of this chapter has been published on *New. J. Chem.*, **2017**, *41*, 12500.

[2] (a) Loudet A.; Burgess, K. *Chem. Rev.*, 2007, **107**, 4891. (b) Benstead, M.; Mehl, G. H.; Boyle, R. W. *Tetrahedron*, 2011, **67**, 3573. (c) Lu, H.; J. Mack, J.; Yang, Y.; Shen, Z. *Chem. Soc. Rev.*, 2014, **43**, 4778. (d) Kowada, T.; Maeda, H.; Kikuchi, K. *Chem. Soc. Rev.*, 2015, **44**, 4953.

[3] (a) Wood, T. E.; Thompson, A. *Chem. Rev.*, 2007, **107**, 1831. (b) Sakamoto, R.; Iwashima, T.; Tsuchiya, M.; Toyoda, R.; Matsuoka, R.; Kögel, J. F.; Kusaka, S.; Hoshiko, K.; Yagi, T.; Nagayama, T.; Nishihara, H.*J. Mater. Chem.* A, 2015, **3**, 15357. (c) Baudron, S. A. *Dalton Trans.*, 2013, **42**, 7498. (d) Baudron, S. A. *CrystEngComm.*, 2016, **18**, 4671.

[4] Hall, J. D.; McLean, T. M.; Smalley, S. J.; Waterland, M. R.; Telfer, S. G. *Dalton Trans.*, 2010, **39**, 447.

[5] X. Liu, X.; Nan, H.; Sun, Q.; Zhang, Q.; Zhan, M.; Zou, L.; Xie, Z.; Li, X.; Lu, C.; Cheng, Y. *Dalton Trans.*, 2012, **41**, 10199.

[6] Bronner, C. ; Baudron, S. A. ; Hosseini, M. W. ; Strassert, C. A. ; Guenet A. ; De Cola, L. *Dalton Trans.*, 2010, **39**, 180.

[7] (a) Hanson, K.; Tamayo, A.; Diev, V. V.; Whited, M. T.; Djurovich P. I.; Thompson, M. E. *Inorg. Chem.*, 2010, **49**, 6077. (b) Bronner, C.; Baudron, S. A.; Hosseini, M. W. *Inorg. Chem.*, 2010, **49**, 8659. (b) Bronner, C. ; Veiga, M. ; Guenet, A. ; Hosseini, M. W.; De Cola, L. ; Strassert, C. A. ; Baudron, S. A. *Chem. Eur. J.*, 2012, **18**, 4041.

[8] (a) Falk, H.; Neufingerl, F. *Monatsh. Chem.*, 1979, **110**, 987. (b) Sazanovich, I. V.; Kirmaier, K.; Hindin, E.; Yu, L.; Bocian, D. F.; Lindsey, J. S.; Holten, D. *J. Am. Chem. Soc.*, 2004, **126**, 2664. (c) Maeda, H.; Hashimoto, T.; Fujii, R.; Hasegawa, M. *J. Nanosci. Nanotechnol.*, 2009, **9**, 240. (d) Lee, S.; Seok, C.-H.; Park, Y.; Lee, A.; Jung, D. H.; Choi, S.-H.; Park, J. *Mol. Cryst. Liq. Cryst.*, 2010, **531**, 65. (e) Kusaka, S.; Sakamoto, R.; Kitagawa, Y.; Okumura, M.; Nishihara, H. *Chem. Asian J.*, 2012, **7**, 907. (f) Sakamoto, R.; Kusaka, S.; Kitagawa, Y.; Kishida, M.; Hayashi, M.; Takara, Y.; Tsuchiya, M.; Kakinuma, J.; Takeda, T.; Hirata, K.; Ogino, T.; Kawahara, K.; Yagi, T.; Ikehira, S.; Nakamura, T.; Isomura, M.; Toyama, M.; Ichikawa, S.; Okumura, M.; Nishihara, H. *Dalton Trans.*,

2012, **41**, 14035. (g) Yang, L.; Zhang, Y.; Yang, Q.; Chen, Q.; Ma, J. S. *Dyes Pigm.*, 2004, **62**, 27. (h) Hashimoto, T.; Nishimura, T.; Lin, J. M.; Khim, D.; Maeda, H. *Chem. Eur. J.*, 2010, **16**, 11653.

[9] Orłowsk, R.; Gryko, D.; Gryko, D. T. *Chem. Rev.*, 2017, **117**, 3102.

[10] (a) Johnson, A. W.; Price, R. *J. Chem. Soc.*, 1960, 1649. (b) Bröring, M. Beyond dipyrrins: Coordination interaction and templated macrocyclizations of open-chain oligopyrroles, in *Handbook of Porphyrin Science*, 2010, vol. 8, p. 343.

[11] (a) Struckmeier, G.; Thewalt, U.; Furhop, J.-H. *J. Am. Chem. Soc.*, 1976, **98**, 278. (b) Zhang, Y.; Thompson, A.; Rettig, S. J.; Dolphin, D. *J. Am. Chem. Soc.*, 1998, **120**, 13537. (c) Khoury, R. G.; Jaquinod, L.; Smith, K. M. *Tetrahedron*, 1998, **54**, 2339. (d) Bröring, M.; Link, S.; Brandt, C. D.; Cónsul Tejero, E. *Eur. J. Inorg. Chem.*, 2007, 1661. (e) Maeda, H.; Nishimura, T.; Akuta, R.; Takaishi, K.; Uchiyama, M.; Muranaka, A. *Chem. Sci.*, 2013, **4**, 1204. (f) Ruffin, H.; Baudron, S. A.; Salazar-Mendoza, D.; Hosseini, M. W. *Chem. Eur. J.*, 2014, **20**, 2449. (g) Baudron, S. A.; Ruffin, H.; Hosseini, M. W. *Chem. Commun.*, 2015, **51**, 5906. (h) Baudron, S. A.; Hosseini, M. W. *Chem. Commun.*, 2016, **52**, 13000.

[12] (a) Bröring, M.; Brandt, C. D.; Lex, J.; Humpf, H.-U.; Bley-Escrich, J.; Gisselbrecht, J.-P. *Eur. J. Inorg. Chem.*, 2001, 2549. (b) Bröring, M. ; Brandt, C. D.; Bley-Escrich, J.; Gisselbrecht, J.-P. *Eur. J. Inorg. Chem.*, 2002, 910. (c) Gill, H. S.; Finger, I.; Božidarević, I.; Szydlo, F.; Scott, M. J. *New J. Chem.*, 2005, **29**, 68. (d) Antina, E. V.; Kuznetsova, R. T.; Antina, L. A.; Guseva, G. B.; Dudina, N. A.; V'yugin, A. I.; Solomonov, A. V. *Dyes Pigments*, 2015, **113**, 664.

[13] (a) Halper, S. R.; Cohen, S. M. *Inorg. Chem.,* 2005, **44**, 486. (b) Murphy, D. L.; Malachowski, M. R.; Campana, C. F.; Cohen, S. M.; *Chem. Commun.*, 2005, 5506. (c) Halper, S. R.; Do, L.; Stork, J. R.; Cohen, S. M. *J. Am. Chem. Soc.*, 2006, **128**, 15255. (d) Baudron, S. A. *CrystEngComm.*, 2010, **12**, 2288. (e) Béziau, A.; Baudron, S. A.; Pogozhev, D.; Fluck, A.; Hosseini, M. W. *Chem. Commun.*, 2012, **48**, 10313. (f) Béziau, A.; Baudron, S. A.; Fluck, A.; Hosseini M. W. *Inorg. Chem.*, 2013, **52**, 14439. (g) A. Béziau, S. A. Baudron, G. Rogez and M. W. Hosseini, *Inorg. Chem.*, 2015, **54**, 2032.

[14] Artigau, M. Bonnet, C.; Ladeira, S.; Hoffmann, P.; Vigroux, A. *CrystEngComm.*, 2011, **13**, 7149.

[15] Due to solubility issues, the proton integration in the ^{1}H NMR spectrum is hampered.

[16] (a) Brückner, ; Zhang, Y.; Rettig, S. J.; Dolphin, D. *Inorg. Chim. Acta A*, 1997, **263**, 279. (b) Hall, J. D.; McLean, T. M.; Smalley, S. J.; Waterland, M. R.; Telfer, S. G. *Dalton Trans.*, 2010, **39**, 437. (c) Weston, M.; Reade, T. J.; Handrup, K.; Champness, N. R.; O'Shea, J. N. *J. Phys. Chem. C*, 2012, **116,** 18184.

[17] Dozzi, M. V. ; Marzorati, S. ; Longhi, M. ; Coduri, M. ; Artiglia, L ; Selli, E. *Appl. Catal. B: Environ.*, 2016, **186**, 157.

[18] Kumar, B.; Llorente, M.; Froehlich, J.; Dang, T.; Sathrum, A.; Kubiak, C. P. *Annu. Rev. Phys. Chem.*, 2012, **63**, 541.

[19] Imahori, H.; Hayashi, S.; Hayashi, H.; Oguro, A.; Eu, S.; Umeyama, T.; Matano, Y. *J. Phys. Chem. C*, 2009, **113**, 18406.

[20] (a) Zhang, T.; Lin, T. *Chem. Soc. Rev.*, 2014, **43**, 5982. (b) Silva, P.; Vilela, S. M. F.; Tome, J. P. C.; Almeida Paz, F. A. *Chem. Soc. Rev.*, 2015, **44**, 6774. (c) Furukawa, H.; Müller, U.; Yaghi, O. M. *Angew. Chem. Int. Ed.*, 2015, **54**, 3417. (d) Deng, H.; Doonan, C. J.; Furukawa, H.; Ferrerira, R. B.; Towne, J.; Knobler, C. B.; Wang, B.; Yaghi, O. M. *Science*, 2010, **327**, 846.

[21] Devic, T.; Serre, C. *Chem. Soc. Rev.*, 2014, **43**, 6097.

[22] He, J.; Wang, J.; Chen, Y.; Zhang, J.; Duan, D.; Wang, Y.; Zhiying, Y. *Chem. Commun.*, 2014, **50**, 7063.

[23] Sun, Y.; Sun, L.; Feng, D.; Zhou, H.-C. *Angew. Chem., Int. Ed.*, 2016, **55**, 6471.

Chapter 4

PORPHYRINS

4.1 Porphyrins as metalloligand

Porphyrins are an important class of naturally occurring macrocyclic compounds that play a very important role in the metabolism of living organisms. Examples include the iron-containing porphyrins found as heme (of haemoglobin) and the magnesium-containing reduced porphyrin in chlorophyll. Etymologically, the word porphyrin derives from the Greek πορφύρα (*porphyra*), which means purple: in fact, these molecules are a large class of deeply coloured pigments and were used since old times as dyes in the coloration of clothes.

As shown in Figure 4.1, a porphyrin is a macrocyclic tetra-pyrrolic system linked in the α-position by methane bridges. Their easiest and most common functionalization is generally carried out in their *meso*-position, even though in many biological systems such as the abovementioned haemoglobin and chlorophyll, the functionalities are

present in the β-position. The tetrapyrrolic compounds with no metal inside the core of the porphyrin itself are called free base porphyrin (H_2P). On the other hand, when a metal cation is inserted into the porphyrin core, the compound is called metalloporphyrin (MP), where M can be a variety of metals. When all four *meso* positions of the porphyrin are linked to phenyl groups, then the resulting compound is generally called tetraphenylporphyrin (TPP).

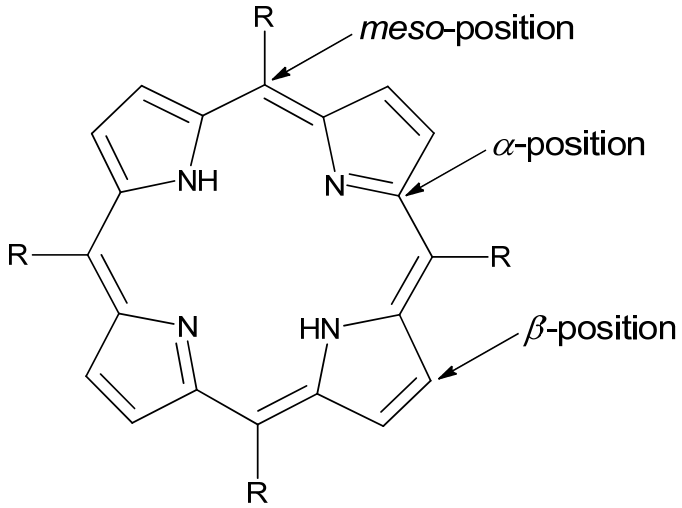

Figure 4.1. *The structure of a porphyrin.*

Porphyrins possess a delocalized system involving a total number of 22 π electrons and thus satisfy Hückel's rule of aromaticity (*i.e.*, $4n + 2\pi$ electrons). Their aromaticity induces a ring current effect in their ^1H NMR spectra so that the peripheral protons (*i.e.*, protons at *meso*- and *β*-positions) appear at lower field (typically in a range between 6 and 9 ppm, with respect to tetramethylsilane, TMS), while inner pyrrolic NH protons appear at high field (around -2.5 ppm respect to TMS). The aromaticity generated by this delocalized π-electrons system is responsible for the photophysical properties of porphyrins.

Porphyrin systems can be found in light-harvesting systems, anticancer drugs, catalysts, sensors, nonlinear optical materials and DNA binding or cleavage agents.[1] When referring to their application as light-harvesting moieties, their biggest limitation is due to π-stacking processes, which reduce both the emission properties and the solubility of the porphyrins.[2] However, when immobilized into MOFs, porphyrinic moieties can be used in any media without considering their solubility. Since the most used porphyrinic species feature carboxylate groups as coordinating units (that is, the tetrakis(4-carboxyphenyl)-porphyrin, or TCPP), the use of hard Lewis acidic species, such as Zr^{IV} and Al^{III}, has successfully expanded the range of working environments for porphyrinic-based MOFs, especially in aqueous media, and thus greatly diversified their applications.[3]

In order to target porphyrin-containing MOF structures, we selected two isoreticular MOFs, namely the MTCPP⊂UiO-66-X (X = –H or $–NH_2$)[4] and the PCN-222(M)[5] series. These two series were chosen as reference materials in which porphyrins are present in the supramolecular structure as "dopant" and as sole linker, respectively. In both cases, the MOF structures are Zr-based, since they offer a better and improved stability towards harsh chemical conditions with respect to Zn/Cu/Cd-based MOFs, as already discussed in Chapter 1 in terms of the HSAB theory. Detailed synthetic procedures of porphyrins and MOFs are reported in Appendix C.

4.2 The MTCPP⊂UiO-66-X series

As reported in the article by Sun *et. al.*,[4] the integration of multi-functionalities into MOFs is of great importance for extending the use of MOFs to a wide range of applications. To date, many strategies have been developed to incorporate multiple

functionalities into MOFs. Among them, the mixed-ligand approach is by far the most studied one. Pioneering studies by Yaghi and co-workers showed that up to eight functionalities can be introduced in MOF-5. However, this approach has two main limitations: (i) the use of soft Lewis acidic metal centres, such as M^{II}, so that the obtained frameworks suffer of poor stability under harsh chemical conditions which severely restrict their applications; (ii) the need of organic linkers as "auxiliary ligands" possessing the same geometry and connectivity of the "main linkers", which makes them "indistinguishable" during the formation of MOFs and prevents the formation of mixed phases.

In their work, Sun *et. al.*[4] managed to obtain the first example of mixed ligands MOF structures in which the auxiliary ligand has no structural homology with terephthalic acid, the primary ligand of the original MOF structure, the well-known UiO-66 (Figure 4.2).

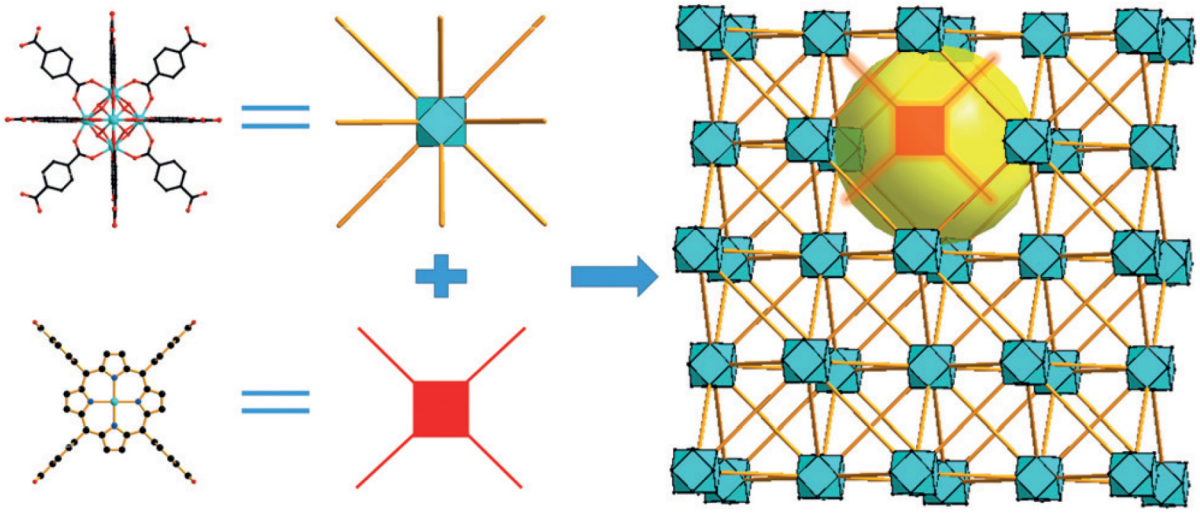

Figure 4.2. *Schematic illustration of UiO-66 incorporating TCPP (red) as well as the usual Zr_6 cluster (blue) and terephthalic linkers (brownish). Yellow sphere indicates the pore cavity.* [4]

In our aim to obtain porphyrin-based MOFs, we adopted the synthetic conditions reported in the work of Sun *et. al.*[4] to obtain the "doped" version of the UiO-66 framework. In the synthesis (Scheme 4.1), $ZrCl_4$, terephthalic acid, and tetrakis(4-carboxyphenyl)porphyrin (as metal-free, H_2TCPP, or metalated with Fe^{III}, Ni^{II}, Cu^{II} or Co^{II}, MTCPP) were mixed in *N,N*-dimethylformamide in the presence of large excess of benzoic acid as modulating agent and underwent solvothermal reaction at 130°C for 12 h, yielding powdery samples of MTCPP⊂UiO-66. These powders remained coloured after washings with *N,N*-dimethylformamide and acetone (Figure 4.3).

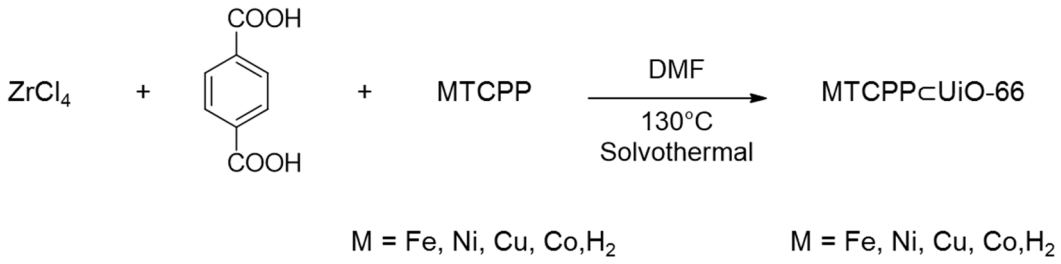

Scheme 4.1. *Synthetic route to the MTCPP "doped" UiO-66 frameworks.*

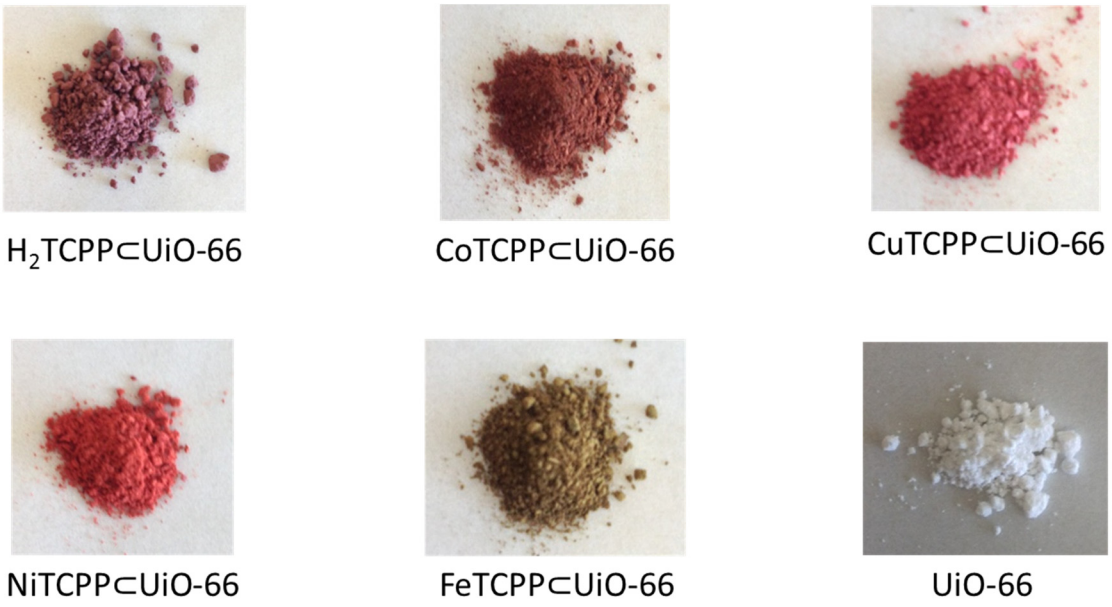

Figure 4.3. *Photographs of the different samples.*

The obtained MOF samples were analysed by means of XRPD and they proved to have diffraction patterns consistent with that of pure phase UiO-66, as shown in Figure 4.4. The absence of additional peaks in the diffraction patterns with respect to pure UiO-66 is an indication that, with the adopted synthetic conditions, no additional phase is formed during the solvothermal reaction.

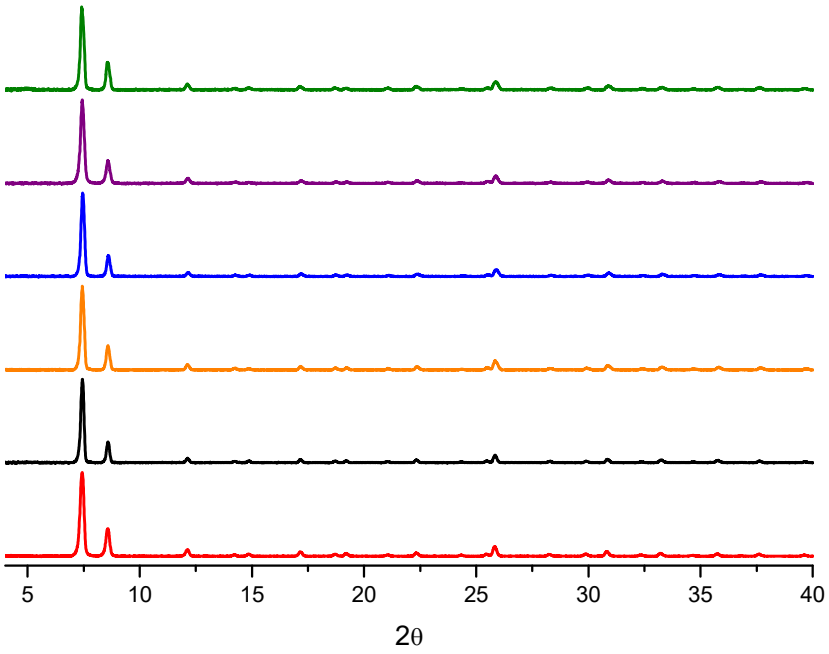

Figure 4.4. *Experimental XRPD pattern of (from top to bottom): H_2TCPP⊂UiO-66; CoTCPP⊂UiO-66; CuTCPP⊂UiO-66; NiTCPP⊂UiO-66; FeTCPP⊂UiO-66 and "undoped" UiO-66.*

The only conceptual limitation of this synthetic strategy is that there is no control over the distribution of the TCPP units inside the framework, and for this reason MTCPP⊂UiO-66 structures are indicated as "doped" structures. Therefore, the location of the TCPP units in the structure can be regarded as "statistically distributed". In fact, they are expected to be far enough from each other, since the original framework is maintained. In other words, as shown in Figure 4.2, the TCPP units can be regarded as *isolated units* in a framework made of terephthalic acid ligands.

Apart from modifying the nature of the metal inside of the porphyrin centre, another possible modification that can be done to the framework without modifying its topology, consists in the introduction of a second functionality on the BDC ligands. In the present work, we replaced the terephthalic acid with the 2-aminoterephthalic acid, since MOFs with amino groups proved to be very interesting, especially in terms of possible interactions with CO_2.[6] To obtain the parent MTCPP⊂UiO-66-NH_2 compounds, the synthetic strategy remains that shown in Scheme 4.1, with the only modification of 2-aminoterephthalic as main linker in place of terephthalic acid. The colour of the powders did not differ from that of the first series, since the effect that the amino group in the 2-aminoterephthalic ligand can have in the absorption spectra is negligible with respect to the contribution of the porphyrin units.[7] Figure 4.5 shows the XRPD patters of this MOF series.

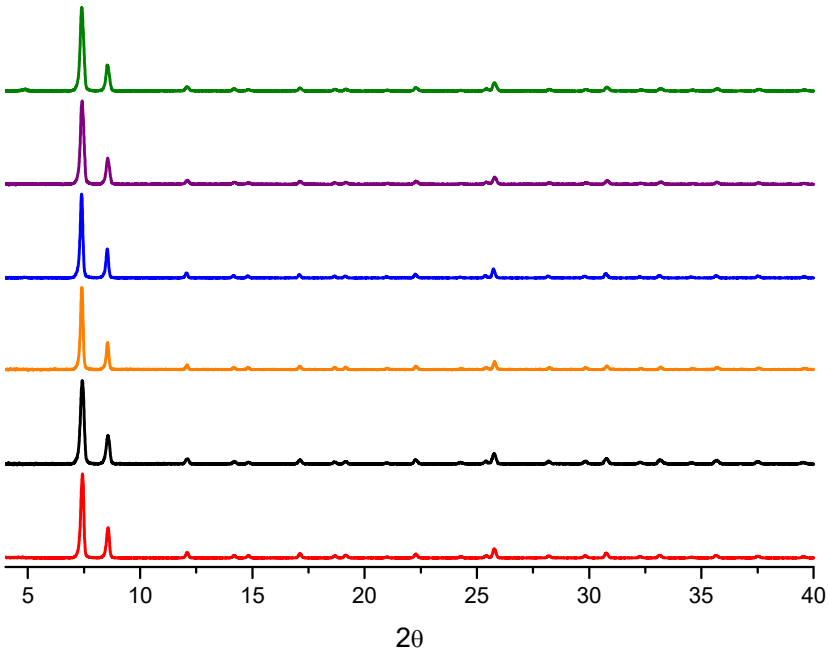

Figure 4.5. *Experimental XRPD pattern of (from top to bottom): H_2TCPP⊂UiO-66-NH_2; CoTCPP⊂UiO-66-NH_2; CuTCPP⊂UiO-66-NH_2; NiTCPP⊂UiO-66-NH_2; FeTCPP⊂UiO-66-NH_2 and "undoped" UiO-66-NH_2.*

Again, the diffraction patterns result to be in line with the one of the “undoped” structure, thus confirming the absence of additional phases in the framework, although the presence of the MTCPP units, which make them suitable for different applications, including photocatalysis.

4.3 The PCN-222(M) series

With the aim to obtain a sole porphyrin-based Zr-MOF structure, we targeted the PCN-222(M) series reported by Feng *et. al.*,[5] since it is known to be the thermodynamically more favoured product among the different Zr-TCPP-MOFs reported by Zhou and co-workers. [5,8] Moreover, this framework was recently reported to be photocatalytically active in the reduction of CO_2 to $HCOO^-$ anions.[9]

From a topological point of view, this framework is made of 8-connected Zr_6-clusters. Therefore, only eight TCPP units bridge the edges of the Zr_6 clusters, while the remaining positions are occupied by terminal hydroxo groups. Although the reduced connection of TCPP units around the Zr_6-cluster can affect the stability of the framework in harsh chemical conditions, on the other hand this opens up the chance to have additional “free space” around the Zr_6-clusters. Figure 4.6 shows the PCN-222 structure.

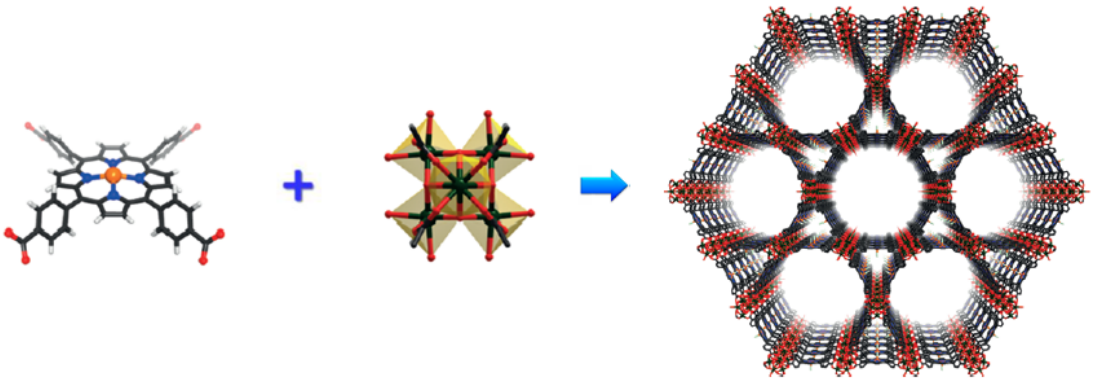

Figure 4.6. *Crystal structure of PCN-222 showing the large 1D channels of the framework.*[5]

The 3D framework of PCN-222 can be seen as Zr-carboxylate layers, which form a Kagome-type pattern in the *ab* plane, pillared by TCPP ligands. Remarkably, the 3D framework contains the largest known 1D hexagonal open channels, with a diameter of up to 3.7 nm along the *c* axis. This feature allows the frameworks to be classified as mesoporous material, since its N_2 adsorption isotherm is consistent with the type IV isotherm. This feature is of great importance whatever application is sought. Indeed, large channels facilitate the diffusion of reactants and product to/from the active centre of the structure, thus enhancing its catalytic activity.

In this work, we synthesized the isoreticular PCN-222(M) series with M = Fe, Ni, Cu, Co and H_2, in order to study the effect of the porphyrin metal centre on the catalytic properties of the framework, since the general catalytic mechanism can be modified by the type of the metal present in the structure and, in particular, in the porphyrin. Figure 4.7 reports a comparison between the experimental XRPD pattern for the isoreticular PCN-222(M) series and the simulated one, taken from ref [5]. The XRPD patterns of the isoreticular series do not differ one from the other (as expected) and there is good agreement with the simulated one.

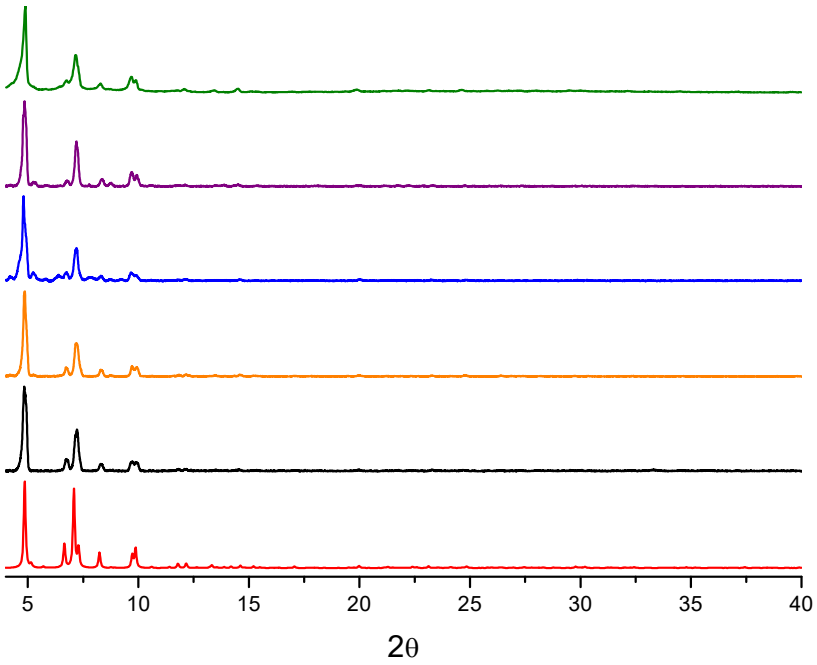

Figure 4.7. *Comparison between the experimental XRPD patter of (from top to bottom): PCN-222(no metal); PCN-222(Co); PCN-222(Cu); PCN-222(Ni) and PCN-222(Fe) with the simulated one.*

Since in the work of Zheng *et. al.*[10] it has been demonstrated that the nature of the metal centre in the porphyrin can affect the photocatalytic properties of a porphyrin-based MOF, our target was to study the dependence of the catalytic properties of the metalated framework towards CO_2 reduction.

REFERENCES

[1] (a) Bhugun, I.; Lexa, D.; Savéant, J.-M., *J. Phys. Chem.,* **1996**, *100*, 19981; (b) Hennig, H.; Luppa, D., J. *Prakt. Chem.*, **1999**, *341*, 757; (c) Sharghi, H.; Beyzavi, M. H.; Doroodmand, M.M., *Eur. J. Org. Chem.*, **2008**, *4126*; (d) Shinokubo, H.; Osuka, A., *Chem. Commun.*, **2009**, 1011; (e) Harriman, A., *J. Chem. Soc. Faraday Trans.*, **1981**, *77*, 369; (f) Harriman, A.; Porter, G.; Richoux, M.-C., J. *Chem. Soc. Faraday Trans*., **1981**, *77*, 833; (g) Knoer, G.; Vogler, A., *Inorg. Chem.*, **1994**, *33*, 314; (h) Tao, S. Y.; Li, G. T., *Colloid Polym. Sci.*, **2007**, *285*, 721; (i) Xie, Y. S.; Hill, J. P.; Charvet, R.; Ariga, K., *J. Nanosci. Nanotechnol.*, **2007**, *7*, 2969; (j) Di Natale, C.; Monti, D.; Paolesse, R., *Mater. Today*, **2010**, *13*, 37.

[2] (a) Lee, C. Y.; Farha, O. K.; Hong, B. J.; Sarjeant, A. A.; Nguyen, S. T.; Hupp, J. T., *J. Am. Chem. Soc.*, **2011**, *133*, 15858; (b) Son, H.-J.; Jin, S.; Patwardhan, S.; Wezenberg, S. J.; Jeong, M. S.; Wilmer, C. E.; Sarjeant, A. A.; Schatz, G. C.; Snurr, R. Q.; Farha, O. K.; Wiederrecht, G. P.; Hupp, J. T., *J. Am. Chem. Soc.*, **2013**, *135*, 862; (c) Xie, M.-H.; Yang, X.-L.; He, Y.; Zhang, J.; Chen, B.; Wu, C.-D., *Chem. Eur. J.*, **2013**, *19*, 14136; (d) Lu, K.; He, C.; Lin, W., *J. Am. Chem. Soc.*, **2014**, *136*, 16712.

[3] (a) Morris, W.; Volosskiy, B.; Demir, S.; Gándara, F.; McGrier, P. L.; Furukawa, H.; Cascio, D.; Stoddart, J. F.; Yaghi, O. M. Inorg. Chem. 2012, 51, 6443. (b) Fateeva, A.; Chater, P. A.; Ireland, C. P.; Tahir, A. A.; Khimyak, Y. Z.; Wiper, P. V.; Darwent, J. R.; Rosseinsky, M. J., *Angew. Chem., Int. Ed.*, **2012**, *51*, 7440. (c) Valenzano, L.; Civalleri, B.; Chavan, S.; Bordiga, S.; Nilsen, M. H.; Jakobsen, S.; Lillerud, K. P.; Lamberti, C., *Chem. Mater.*, **2011**, *23*, 1700. (d) Jakobsen, S.; Gianolio, D.; Wragg, D. S.; Nilsen, M. H.; Emerich, H.; Bordiga, S.; Lamberti, C.; Olsbye, U.; Tilset, M.; Lillerud, K. P., *Phys. Rev. B*, **2012**, *86*, 125429.

[4] Sun, Y.; Sun, L.; Feng, D.; Zhou, H.-C., *Angew. Chem. Int. Ed.*, **2016**, *55*, 6471.

[5] Feng, D.; Gu, Z.-Y.; Li, J.-R.; Jiang, H.-L.; Wei, Z.; Zhou, H.-C., *Angew. Chem. Int. Ed.*, **2012**, *51*, 10307.

[6] Arstad, B.; Fjellvåg, H.; Kongshaug, K.; Swang, O.; Blom, R., *Adsorption*, **2008**, *14*, 755.

[7] Long, J.; Wang, S.; Ding, Z.; Wang, S.; Zhou, Y.; Huang, L.; Wang, X., *Chem. Commun.*, **2012**, *48*, 11656.

[8] (a) Feng, D.; Jiang, H.-L.; Chen, Y.-P.; Gu, Z.-Y.; Wei, Z.; Zhou, H.-C., *Inorg. Chem.*, **2013**, *52*, 12661; (b) Feng, D.; Gu, Z.-Y.; Chen, Y.-P.; Park, J.; Wei, Z.; Sun, Y.; Bosch, M.; Yuan, S.; Zhou, H.-C., *J. Am.*

Chem. Soc., **2014**, *136*, 17714; (c) Feng, D.; Chung, W.-C.; Wei, Z.; Gu, Z.-Y.; Jiang, H.-L.; Chen, Y.-P.; Darensbourg, D. J.; Zhou, H.-C., *J. Am. Chem. Soc.*, **2013**, *135*, 17105; (d) Jiang, H.-L.; Feng, D.; Wang, K.; Gu, Z.-Y.; Wei, Z.; Chen, Y.-P.; Zhou, H.-C., *J. Am. Chem. Soc.*, **2013**, *135*, 13934.

[9] Xu, H.-Q.; Hu, J.; Wang, D.; Li, Z.; Zhang, Q.; Luo, Y.; Yu, S.-H.; Jiang, H.-L., *J. Am. Chem. Soc.*, **2015**, *137*, 13440.

[10] Zhang, H.; Wei, J.; Dong, J.; Liu, G.; An, P.; Zhao, G.; Kong, J.; Wang, X.; Meng, X.; Zhang, J.; Ye, J., *Angew. Chem. Int. Ed.*, **2016**, *55*, 14310.

Chapter 5

PHOTOPHYSICAL CHARACTERIZATION AND PHOTOCATALYTIC ACTIVITY OF PORPHYRIN-CONTAINING MOFs

5.1 Photophysical properties of porphyrins

Porphyrins are the strongest light absorbing materials in nature, also called pigments of life. Hence, the UV-Vis absorption spectroscopy is the most suitable analytical technique to investigate their electronic structure of porphyrins and their metal derivatives even at low concentration.[1] By monitoring the change in the intensity and wavelength of the absorption spectra of porphyrins, substantial information on their excited states and variation in the peripheral substituents of the porphyrin ring could be gained. The study of the photophysical properties, the electronic structure, excited

state and deactivation of porphyrins and their metal complexes is of prime importance for their applications. A brief explanation on the porphyrin spectra is given in the following.

The extended conjugation of the 22-π electrons in the frontier orbitals is responsible for their highly intense colour. Porphyrins possess characteristic UV-Vis spectra because of their fourfold symmetry and four nitrogen atoms directed towards the centre of the electronic heart. The characteristic absorption spectra of porphyrins undergo perturbation by different factors, such as the conjugation pathway, symmetry and other chemical variations.[2] They are helpful to distinguish between free-base porphyrins and their metal complexes. In fact, upon metalation, the D_{2h} symmetry of the porphyrin changes to D_{4h}.[3]

Most of the porphyrins show two sets of distinct region or bands in their electronic absorption spectrum, *i.e.* around 350-500 nm and 500-750 nm, respectively. The first sets of band are called Soret- or B-bands with molar absorption coefficients of 10^5 M^{-1} cm^{-1} and involve the electronic transition from the ground state to the second singlet excited state ($S_0 \rightarrow S_2$). The second set of band is called the Q-band with molar absorption coefficients of 10^4 M^{-1} cm^{-1} and involves the transition from the ground state to the first singlet excited state ($S_0 \rightarrow S_1$).

For a free-base porphyrin, the set of Q-band is composed by four absorption transitions, which are lowered when the system becomes more symmetric upon metalation of the porphyrin core. In particular, metalloporphyrins can be divided into two groups: *regular metalloporphyrins* and *hypsoporphyrins*. To the first group belong the metalloporphyrins containing closed-shell metal ions (d^0 or d^{10}), such as Zn^{II}, in which the *d* π (d_{xy}, d_{yz}) metal-based orbitals are relatively low in energy. These have

very little effect on the porphyrin π to π* energy gap in porphyrin electronic spectra. To the second group belong the metalloporphyrins containing metal cations of d_m-type, in which *m* = 6 – 9, having filled *d* π orbitals. In this group, there is a significant metal *d* π to porphyrin π* orbital interaction (metal to ligand π-backbonding). This results in an increased porphyrin π to π* energy separation causing the absorption to undergo a hypsochromic (blue) shift.

5.2 Photophysical characterizations

Since MOF materials are insoluble in any solvent, their photophysical characterization has to be carried out in the solid state. Because of self-absorption phenomena which arise from the bulk of materials, MOF materials were studied as a suspension in DMSO (solvent in which they demonstrated to be rather stable). Therefore, the corresponding MTCPP ligands were studied in the solid state too, as dispersion in solid matrix (while for MOF materials, the DMSO suspension can be addressed as *liquid dispersion*), *i.e.*, the MTCPP ligands were studied as 4% w/w dopant in a PMMA/toluene solution (100 mg mL^{-1}). In fact, we could not find a suitable solvent to obtain a liquid stable suspension for the MTCPP ligands, that is a solvent in which these molecules do not dissolve and the suspension remains stable over time.

5.2.1 DRS spectra

5.2.1.1 MTCPP ligands

The MTCPP ligands were investigated by means of DRS spectra as solid dispersion in order to confirm their effective metalation (Figure 5.1).[4]

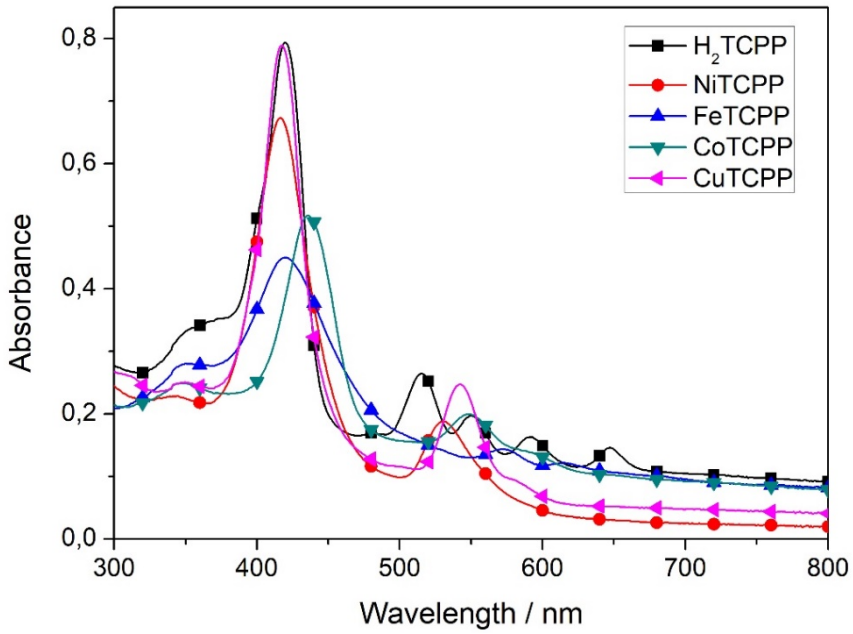

Figure 5.1. *DRS spectra of the porphyrin ligands.*

From the DRS spectra, the metalation of the porphyrin centre is confirmed by the reduction of the number of Q bands for the four metalloporphyrins with respect to H_2TCPP, due to their higher symmetry. Moreover, a shift in the position of the Soret band is observed. The exact positions of the Soret and Q bands for the examined samples are listed in Table 5.1.

Table 5.1. Soret and Q bands positions of the investigated metalloporphyrins.

	Soret band [nm]	Q bands [nm]
H_2TCPP	420	515, 550, 591, 647
NiTCPP	416	530
FeTCPP	420	571, 616
CoTCPP	436	549
CuTCPP	417	542

The reduction of the number of Q band from 4, as it is in the case of H_2TCPP, to 1, as it is in the cases of NiTCPP, CoTCPP and CuTCPP, is consistent with the symmetry transition from the D_{2h} to the D_{4h} group. For what concerns FeTCPP, its symmetry is C_{4v} due to the presence of the axial –Cl ligand for the Fe^{III} ion. Although the reported values are referred to solid state analysis, they agree with ones reported for liquid state analysis (in terms of number of bands).[5]

5.2.1.2 MTCPP⊂UiO-66-X series

For the MTCPP⊂UiO-66-X series, the powders were analysed as bulk material. The DRS spectra for the isoreticular MTCPP⊂UiO-66 and MTCPP⊂UiO-66-NH_2 series are shown in Figure 5.2 and 5.3, respectively.

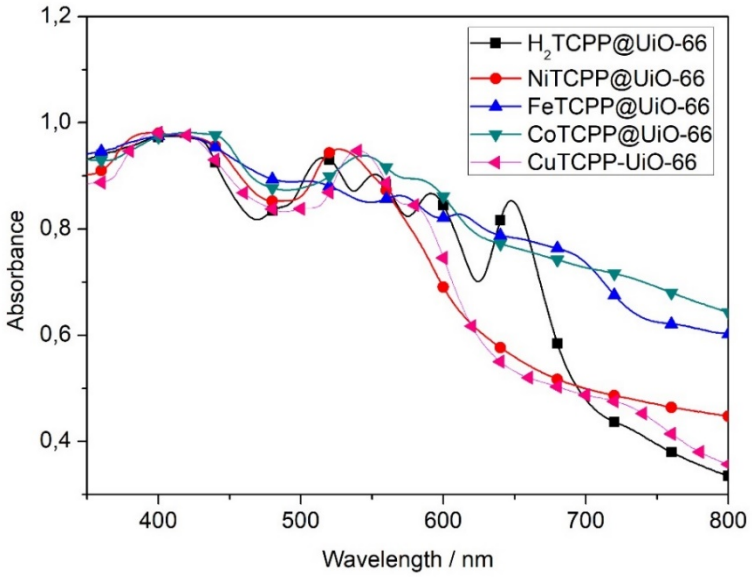

Figure 5.2. *DRS spectra of the MTCPP⊂UiO-66 series.*

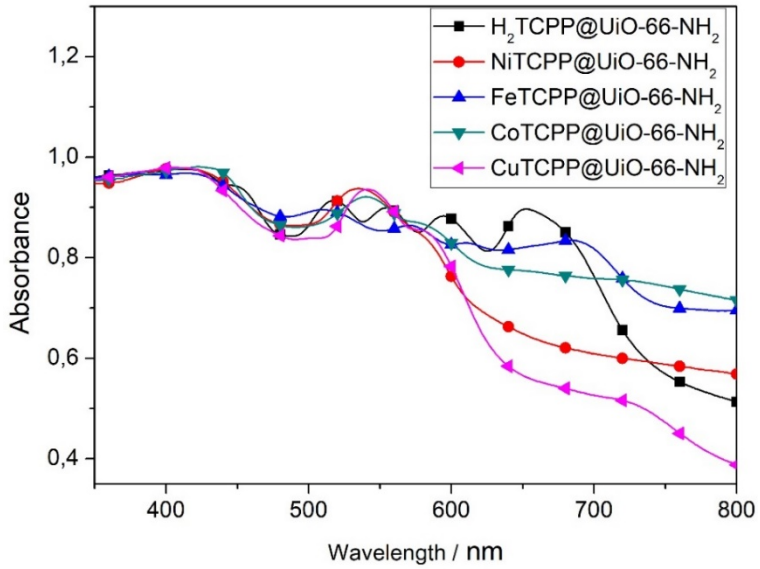

Figure 5.3. *DRS spectra of the MTCPP⊂UiO-66-NH_2 series.*

As shown in Figure 5.2 and 5.3, the broad absorption of all these structures make them suitable as light-harvesting materials, thanks to the porphyrin ligands, which act as dopant and light harvesting unit.

5.2.1.3 PCN-222(M) series

The PCN-222(M) series were analysed as powder dispersed in alumina matrix (*ca* 1 : 20 w/w), because of the high concentration of dyes in the framework, which hampered the analysis when analysed in bulk. The DRS analysis of the PCN-222(M) series is shown in Figure 5.4.

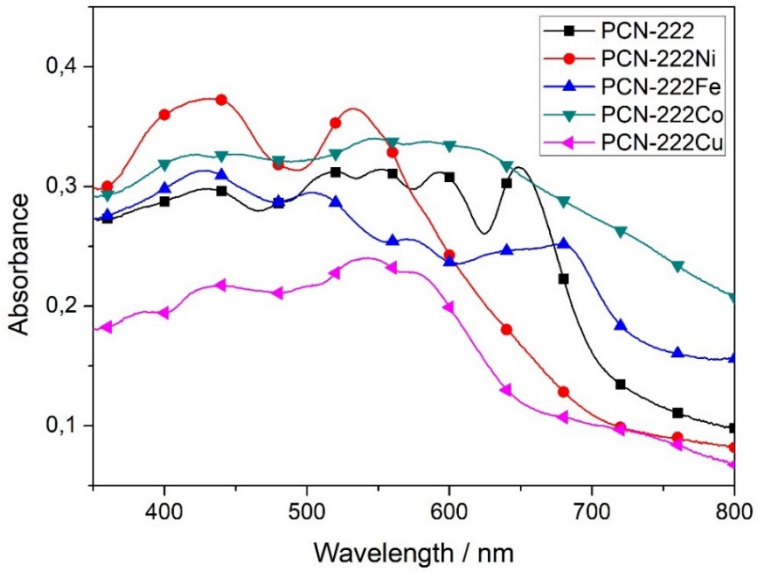

Figure 5.4. *DRS analysis for the PCN-222(M) series.*

Also in the case of PCN-222(M) the general vibronic structure of the MTCPP ligand is maintained, although PCN-222(Co) is more likely to show a broad absorption, rather than a defined structure as for PCN-222. Only for the latter sample a DRS spectrum is reported in the literature, and its shape is absolutely comparable with present results.[6] Also in this case, the broad signals, which extend up to 700 – 800 nm, indicate that these structures possess good light-harvesting properties, thanks to the presence of porphyrins in the framework.

5.2.2 Excitation and emission spectra

5.2.2.1 MTCPP ligands

The MTCPP ligands were also analysed in a PMMA matrix. The excitation spectra were recorded at a fixed emission wavelength of 650 nm. The spectra were normalized for the beamwidth used, to make the intensities of the signals directly comparable. The excitation scans of the MTCPP ligands in the extended range are reported in Figure 5.5 and zoomed in Figure 5.6 to observe the less intense signals of the metalated porphyrins.

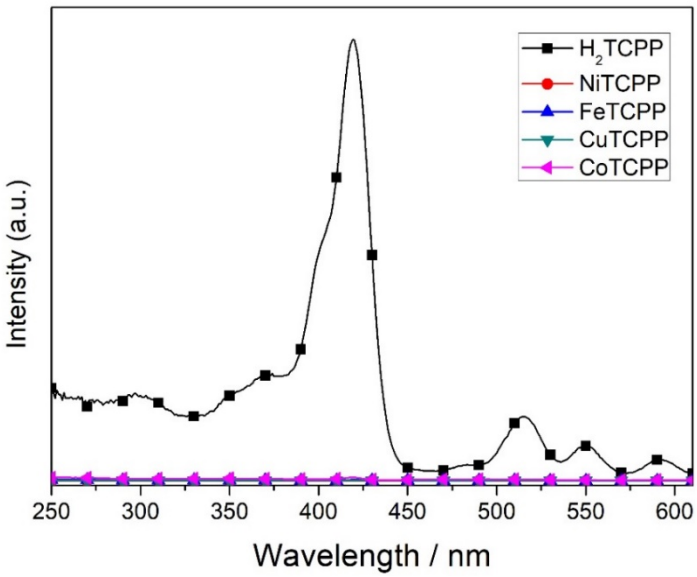

Figure 5.5. *Excitation spectra of MTCPP ligands.*

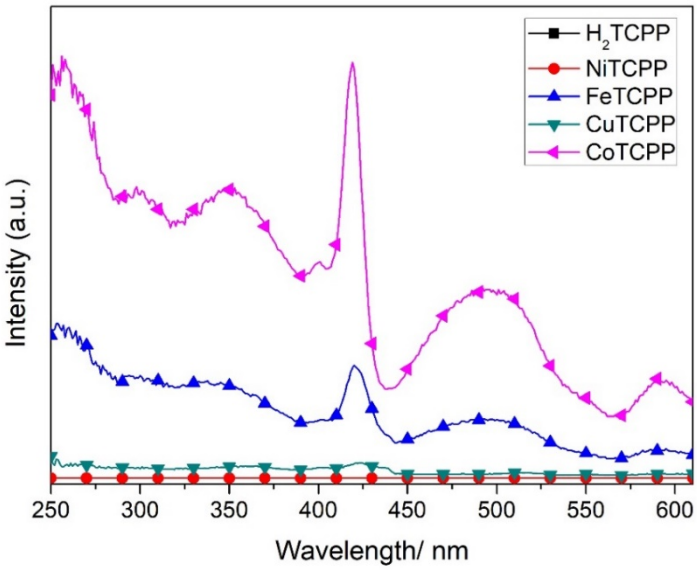

Figure 5.6. *Excitation spectra of MTCPP ligands (enlarged).*

As shown in Figure 5.5 and 5.6, H_2TCPP is the ligand which displays the most intense signal, with an intense Soret band plus the Q bands. For the other samples, the signal are very weak. For NiTCPP, in particular, its signal is practically at the same intensity as the background noise. Indeed, it was found that for NiTCPP is not even possible to record an excitation spectrum.[7]

The emission spectra were recorded keeping the excitation wavelength fixed at λ = 420 nm. Also in this case, the emission pattern of H_2TCPP is the most intense one, while for the other samples the intensities are extremely weak. For CoTCPP, there is the most intense signal among the metalated ones, although no fluorescence response was observed for a Co-porphyrin.[8] NiTCPP displays no fluorescence spectrum as expected,[9] while for CuTCPP the emission pattern is coherent with phosphorescence, with a peak centred around 780 nm.[10] The emission patterns are shown in Figure 5.7 and 5.8.

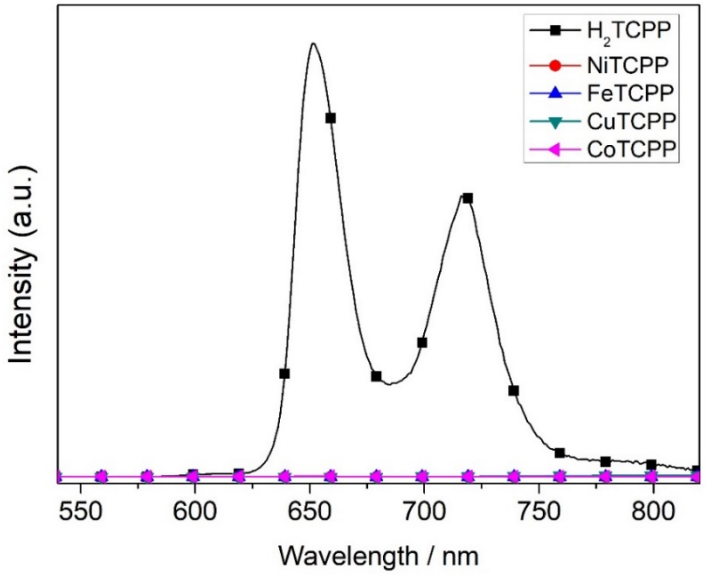

Figure 5.7. *Emission spectra for MTCPP ligands.*

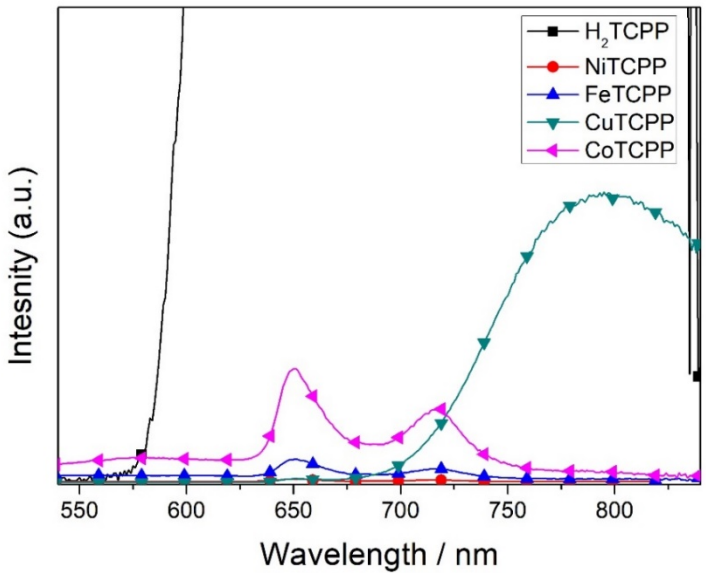

Figure 5.8. *Emission spectra for MTCPP ligands (enlarged).*

The phosphorescence, which arises from the CuTCPP, anyway, is not originated from an emission from a triplet state. In ref [10], in fact, it is stated that the phosphorescence from CuTCPP molecules is originated from the existence of thermally equilibrated triplet-doublet/triplet-quartet states, which cause the activation of long-lived phosphorescence. This assumption is supported by the evidence that,

upon addition of ethyl iodide (an external heavy atom provider), there is no change in the emission intensity. Even though the signals for the metalated porphyrins were much weaker than that of H_2TCPP, we managed to obtain data for the excited state lifetimes for all of them, apart from NiTCPP. The excited state lifetimes were obtained using a laser source with λ = 404 nm and monitoring the first emission peak of the MTCPP. The results are summarized in Table 5.2:

Table 5.2. *Excited state lifetimes for MTCPP ligands.*

	λ_{em} [nm]	τ [ns], (%)			χ^2	τ [ns]
		τ_1	τ_2	τ_3		
CuTCPP	795	28.79 (11.25)	173.28 (38.68)	683.30 (50.06)	1.075	412
CoTCPP	717	2.48 (54.25)	12.68 (45.75)		1.146	7.15
FeTCPP	716	2.25 (27.39)	10.83 (72.61)		1.200	8.48
H_2TCPP	717	4.89 (14.74)	11.98 (85.26)		1.030	10.9

Except for the case of CuTCPP, it is evident how metalation reduces the excited state lifetimes, as it can be seen by comparing the results obtained with Co- and FeTCPP with those obtained for H_2TCPP.

5.2.2.2 MTCPP⊂UiO-66 series

MOF samples were analysed as liquid dispersion, by suspending the powders in DMSO. By this way, self-quenching of the signals was avoided, which was observed when the powders were studied in the solid state. In this case, since the MTCPP ligands behave as dopants in the structure, the spectra of the undoped MOF is reported along the spectra of doped MOFs. The excitation spectra were recorded while keeping the emission wavelength fixed at the emission maximum of each MOF. They are shown in Figure 5.9 and 5.10 (enlarged and zoom section, respectively).

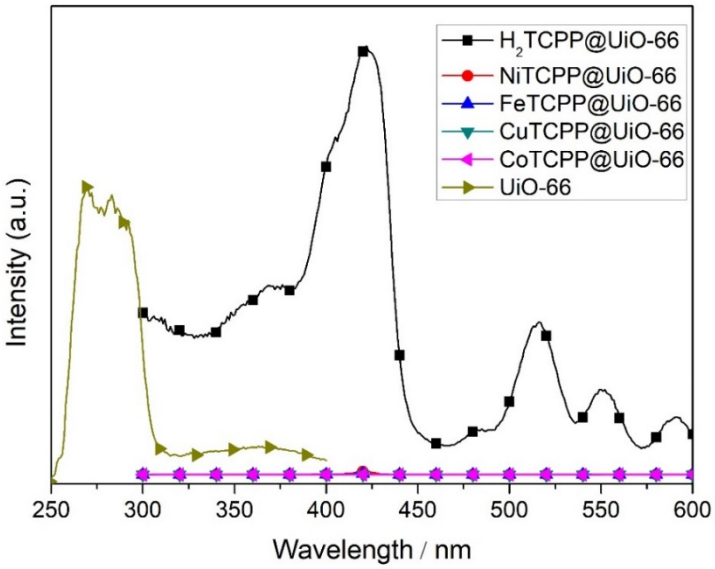

Figure 5.9. *Excitation spectra of MTCPP⊂UiO-66 samples.*

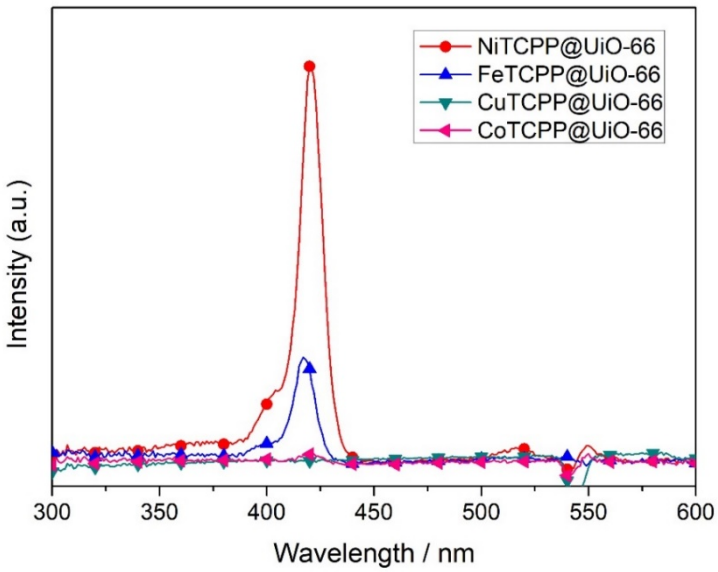

Figure 5.10. *Excitation spectra of MTCPP⊂UiO-66 samples (enlarged).*

As expected, also in this case the H_2TCPP-based MOF displays the most intense excitation spectrum, while terephthalic acid does not display any excitation spectrum in the visible. Regarding the metalated samples, counter-intuitively, the most intense excitation spectrum is that of the NiTCPP-based MOF, while in the case of CuTCPP- and CoTCPP-based MOFs, the signals are almost indistinguishable from the background noise. Regarding the background noise, an instrumental artefact related to the low intensity of the signal arose in the 535-555 nm window. This artefact was tentatively corrected by subtracting the signal obtained from a DMSO solution, but this correction left the signals related to the Q band affected anyway.

The emission spectra were recorded keeping fixed the excitation wavelength at the wavelength of maximum excitation for each MOF (Figures 5.11 and 5.12).

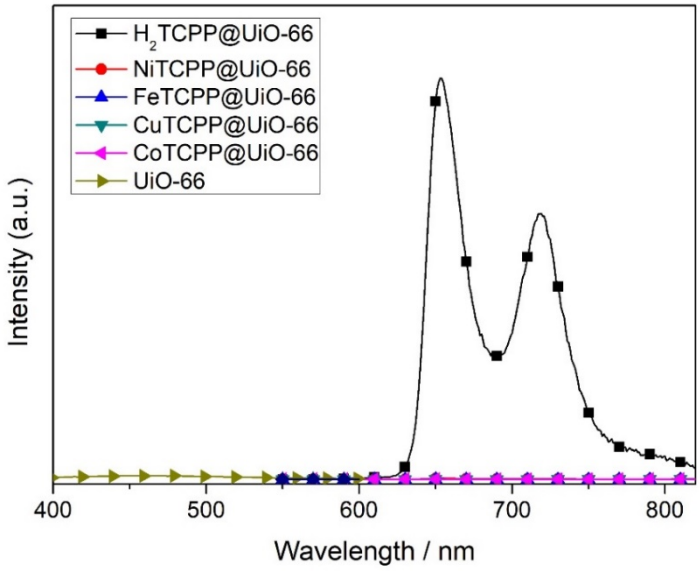

Figure 5.11. *Emission spectra of MTCPP⊂UiO-66 samples.*

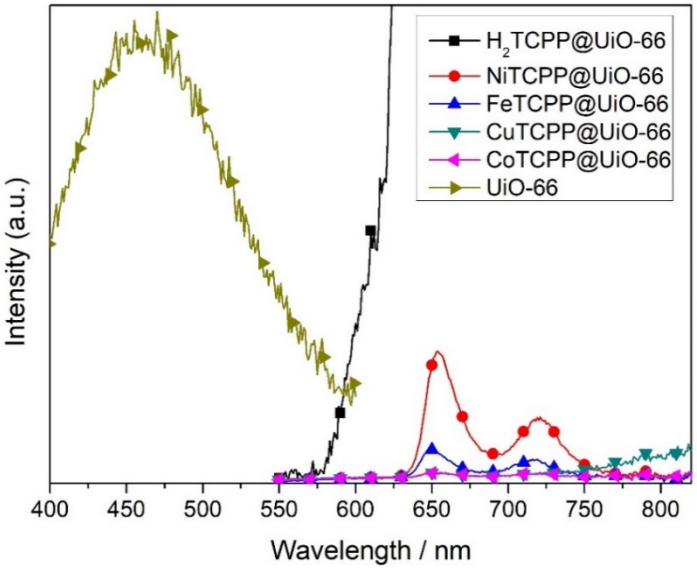

Figure 5.12. *Emission spectra of MTCPP⊂UiO-66 samples (enlarged).*

The H_2TCPP-based MOF sample displays the most intense emission signal and, by expanding the intensity scale, the NiTCPP-based MOF displays the most intense signal among the metalated porphyrins. The CuTCPP-based MOF still displays a phosphorescence signal, although its intensity is reduced with respect to the free ligand and a weak fluorescence signal appears at λ = 650 nm.

Due to the fact that the MTCPP units are very diluted in the framework, the excited state lifetimes were recorded only for the H_2TCPP-based MOF sample. Also in this case, the laser excitation source was used at λ = 404 nm. The results are summarized in Table 5.3.

Table 5.3. *Excited state lifetime for H_2TCPP⊂UiO-66.*

	λ_{em} [nm]	τ [nm]	χ^2
H_2TCPP⊂UiO-66	653	6.1	1.0

As shown in Table 5.3, the excited state lifetimes of the H_2TCPP-doped MOF structure is shorter respect than that of the free H_2TCPP ligand (11 ns). This suggests the activation of other non-radiative decay pathways as a consequence of the embedding of the TCPP unit in the MOF framework.

5.2.2.3 MTCPP⊂UiO-66-NH_2 series

MOF samples were investigated also in DMSO suspension. The excitation and emission spectra of the undoped structures are shown along the spectra of the doped materials, for sake of comparison. The excitation spectra were recorded keeping the emission wavelength fixed at λ = 660 nm in the case of the doped samples, while for the undoped one, the emission wavelength was fixed at λ = 439 nm. The spectra are shown in Figure 5.13 and 5.14.

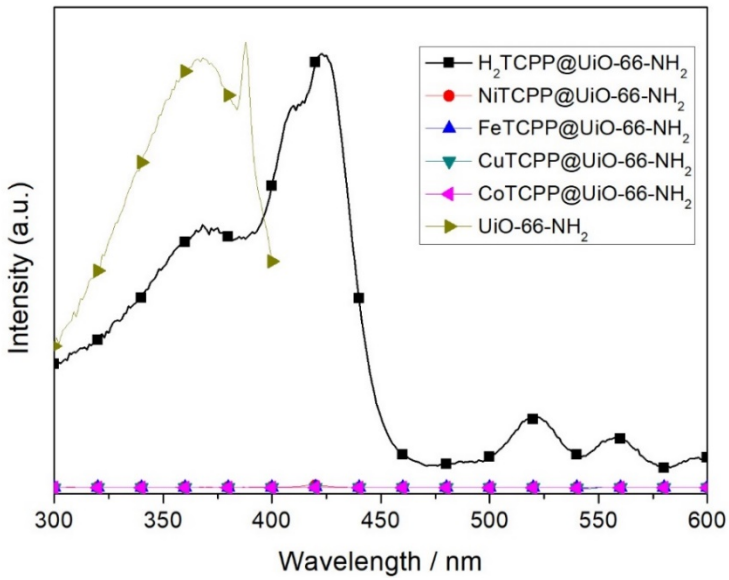

Figure 5.13. *Excitation spectra of MTCPP⊂UiO-66-NH₂ samples.*

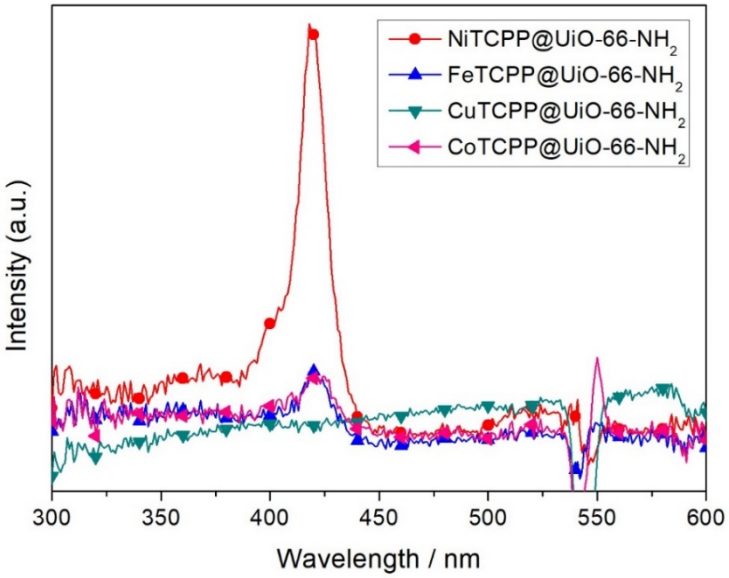

Figure 5.14. *Excitation spectra of MTCPP⊂UiO-66-NH₂ samples (enlarged).*

The H_2TCPP-based MOF displays the most intense signal among the doped materials, while the undoped exhibits a broad band centred at λ = 360 nm, up to the visible. The CuTCPP-based MOF displays a signal which does not differ substantially from the background noise, while the NiTCPP-based MOF exhibits the most intense signal among the doped (metalated) structures.

The emission spectra were recorded by keeping fixed the excitation wavelength at λ = 420 nm in the case of the doped structures and at λ = 325 nm for the undoped structure, as shown in Figure 5.15 and 5.16.

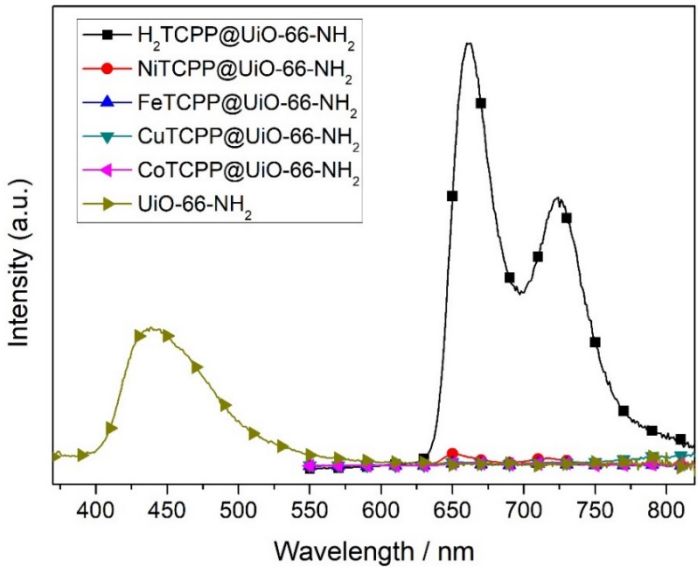

Figure 5.15. *Emission spectra of MTCPP⊂UiO-66-NH₂ samples.*

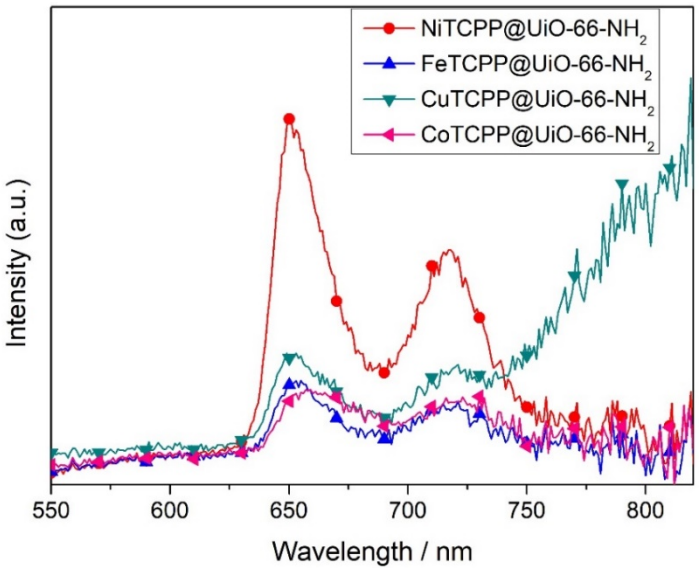

Figure 5.16. *Emission spectra of MTCPP⊂UiO-66-NH₂ samples (enlarged).*

Also in this case, the H_2TCPP-based doped MOF displays the most intense emission signal. The blue-shifted emission of the sole UiO-66-NH_2, in the range from

400 to almost 600 nm, perfectly overlaps the excitation spectrum of the TCPP moieties in the doped structures. For the metalated-doped structures, once again, the NiTCPP-based one displays the most intense signal, although the signal is less intense than in the previous series. Furthermore, the CuTCPP-based sample exhibits phosphorescence signal red-shifted compared to that of the free ligand and its fluorescence signal is more prominent and the second peak can be detected with respect to the previous series. This suggests that upon embedding the CuTCPP ligand in the structure, some kind of interaction between the porphyrin and the surroundings occurs, which modifies the thermally equilibrated triplet-doublet/triplet-quartet states of CuTCPP, originating the phosphorescence emission.

Because of the very weak signals of the doped structures, we could measure only the lifetime of the H_2TCPP-based structure (Table 5.4). The laser excitation was at λ = 404 nm.

Table 5.4. *Excited state lifetime for H_2TCPP⊂UiO-66.*

	λ_{em}	τ [ns], (%)		χ^2	τ [ns]
		τ_1	τ_2		
H_2TCPP⊂UiO-66-NH_2	661 nm	3.0 (45.5)	6.2 (54.5)	1.090	4.75

The average excited state lifetime is even shorter than that determined for the previous series (4.75 ns vs 6.1 ns) and the decay is bi-exponential instead of being mono-exponential, although the lifetime of the second component is practically identical to that of the previous series. Therefore, the only difference is the presence

of the first shorter component, possibly originated from the interaction between the H_2TCPP moiety and the 2-aminoterephthalic ligands, which can be excited at λ = 404 nm.

For the sole 2-aminoterephthalic MOF, there is an overlap between its emission spectrum and the excitation spectrum of the H_2TCPP-doped structure, possibly due to an energy transfer between the two moieties, so a Förster energy transfer,[11] acting as donor and acceptor moiety, respectively. To prove this hypothesis, the H_2TCPP-based MOF was excited at 325 nm, in order to avoid any direct excitation of H_2TCPP moiety, which does not emit when excited at this wavelength (this was proved by exciting the parent H_2TCPP⊂UiO-66 structure). The comparison between the emission pattern of H_2TCPP⊂UiO-66-NH_2 and UiO-66-NH_2 is shown in Figure 5.17.

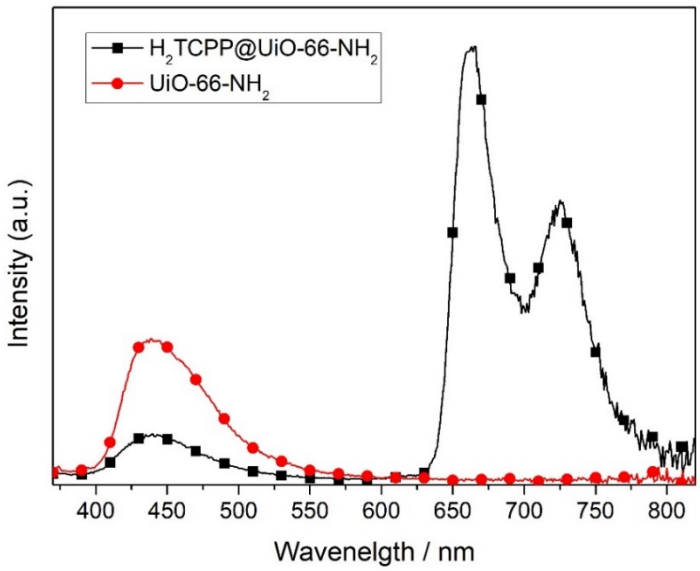

Figure 5.17. *Emission comparison between H_2TCPP⊂UiO-66-NH_2 and UiO-66-NH_2 samples.*

There is effectively an energy transfer between the 2-aminoterephthalic ligand and the porphyrin. In fact, the emission from the 2-aminoterephthalic ligand in the doped structure is lower than in the undoped structure, while the emission from the porphyrin

appears, thus demonstrating the energy transfer from the the 2-aminoterephthalic ligand to the porphyrin in the H_2TCPP⊂UiO-66-NH_2 structure.

5.2.2.4 PCN-222(M)

The MOF samples were characterized in a DMSO suspension. The excitation spectra were recorded keeping the emission wavelength fixed at λ = 720 nm. The spectra are normalized for the beamwidth used, so the intensities of the signals are directly comparable. In this case, the framework is composed by the sole porphyrin as organic linker, which is the only responsible for the luminescence properties.

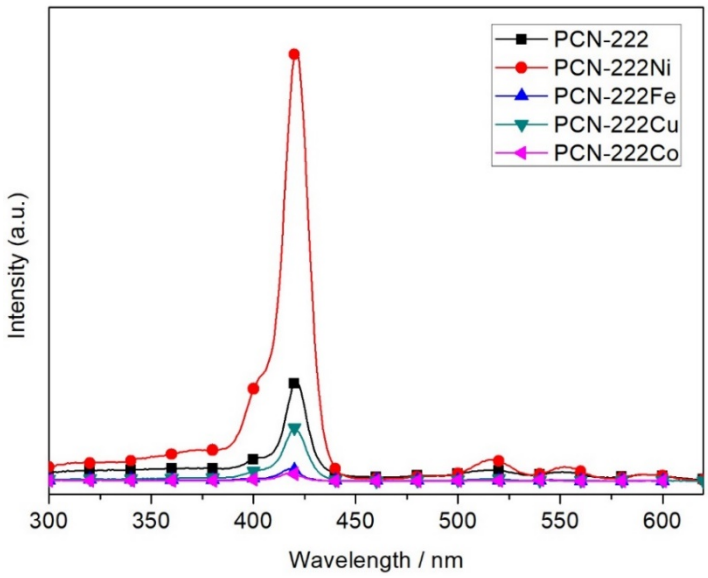

Figure 5.18. *Excitation spectra of PCN-222(M) samples.*

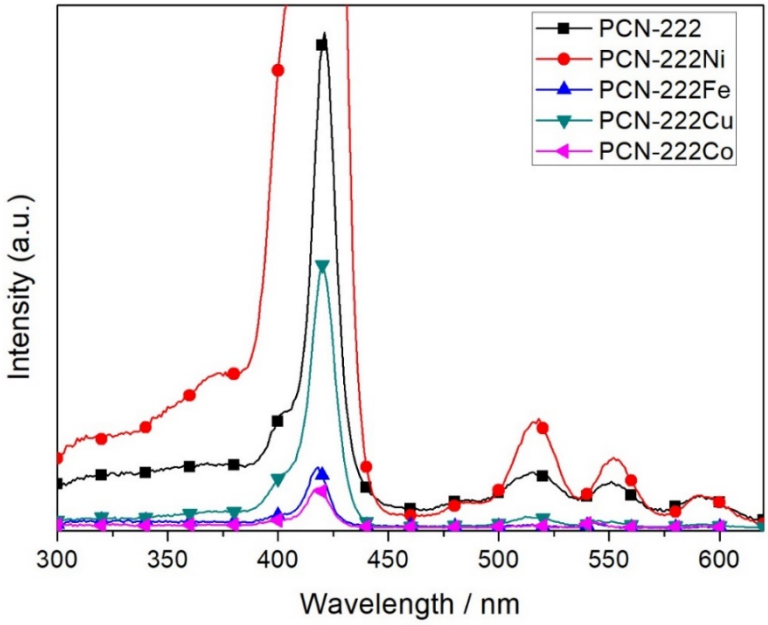

Figure 5.19. *Excitation spectra of PCN-222(M) samples (enlarged).*

All samples exhibit an excitation spectrum that significantly deviates from the background noise, due to the higher concentration of porphyrin linker in this series.

In this series the PCN-222(Ni) sample shows the highest excitation spectrum, which is surprising, since the sole ligand does not even display any excitation spectrum.

Also the CuTCPP-containing sample, which in the previous series did not display any appreciable excitation spectrum, in this series exhibits a relatively intense spectrum. Consequently, also the emission spectra are more intense.

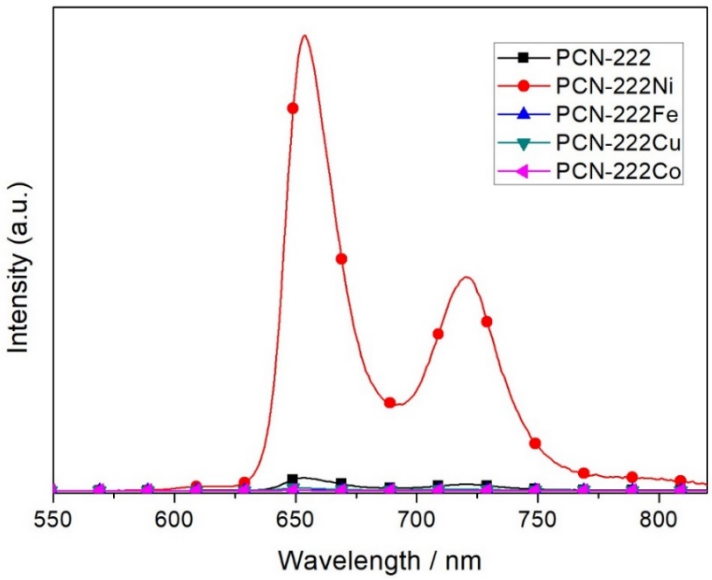

Figure 5.20. *Emission spectra of PCN-222(M) samples.*

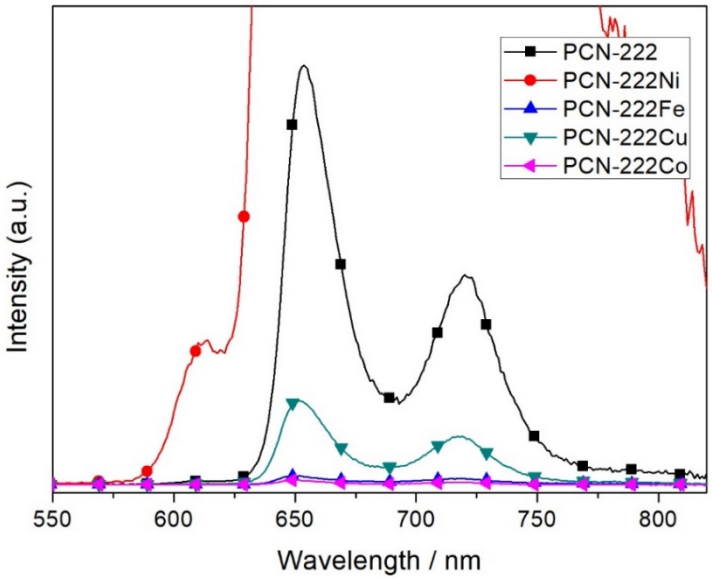

Figure 5.21. *Emission spectra of PCN-222(M) samples (enlarged).*

As shown in Figures 5.20 and 5.21, the NiTCPP-containing structure displays the most intense emission spectrum, as direct consequence of its very intense excitation spectrum. Furthermore, the CuTCPP-containing sample, which displays a phosphorescent emission centred at 800 nm as free ligand, shifted progressively towards a sole fluorescent-based signal in this series, whereas in the doped series,

the phosphorescent and fluorescent signals are mixed together. Since the phosphorescent signal in CuTCPP is generated by the existence of thermally equilibrated triplet-doublet/triplet-quartet states, the arrangement of the CuTCPP unit in the framework affects these thermally equilibrated states. In particular, in this series, the equilibrium is completely disrupted and so the phosphorescent signal is completely converted into fluorescent one.

The excited state lifetimes of PCN-222 and PCN-222(Ni) samples were obtained upon excitation at λ = 404 nm and are reported in Table 5.5.

Table 5.5. *Excited state lifetime for PCN-222 and PCN-222(Ni) samples.*

	λ_{em} [nm]	τ [ns], (%)		χ^2	τ [ns]
		τ_1	τ_2		
PCN-222	720	1.9 (59.0)	4.7 (41.0)	1.190	3.1
PCN-222(Ni)	720	11	/	1.115	11

In the case of PCN-222, the results are comparable to literature ones, *i.e.* there is a bi-exponential decay, although longer than that already reported.[6] Anyway, the porphyrin moieties inside the framework display a shorter decay signal with respect to that of the free ligand, as expected. Different is the case of PCN-222(Ni), which displays a long mono-exponential decay. In this case, since the free ligand does not display any measurable emission spectrum, no comparison is possible between the luminescence of the free ligand and that of the porphyrin-containing framework.

Clearly,by embedding the NiTCPP ligand inside the framework, there is an enhancement of luminescence, which is not seen in the other samples.

5.3 Summary of the obtained results

A recent paper by Zhang *et. al.*[12] reported an enhanced photocatalytic activity for a Co-implanted porphyrin MOF, compared to its non-metalated counterpart, which was related to the fact that, upon Co(II) addition, the luminescence properties of the MOF structure were quenched, with respect to the non-modified one. From our systematic analysis, it is evident that the quenching of the luminescent properties comes before the insertion of the Co(II) porphyrin inside the framework. In particular, the decrease of the luminescent properties of the porphyrin ligands is directly seen upon metalation of the porphyrin ring itself and then is further quenched upon insertion in a framework.

Thus, the luminescence decrease appears to be not an exclusive consequence of the implantation of the Co ion inside the porphyrin-based framework.

Therefore, the luminescent properties of the porphyrin-containing MOFs are directly driven by the luminescent properties of the free porphyrin ligands, with two major exceptions. Indeed, NiTCPP or CuTCPP porphyrins displayed intriguing deviation from the common trend.

In the case of the NiTCPP-containing structures, upon insertion of the ligand in the framework, the luminescent signal grew, becoming the most intense signal among the others, a phenomenon related to the amount of the porphyrin inside the framework. Indeed, from a moderate enhancement of the excitation and emission signal in the doped structures, the framework named PCN-222(Ni), containing only NiTCPP units as organic linkers, exhibits the most intense excitation and emission spectra.

In the same way, for the CuTCPP-containing structures there is a progressive shift from a pure phosphorescent emission signal in the free ligand to a pure fluorescent one in the PCN-222(Cu) structure.

Therefore, it is evident that the geometry disposition of the porphyrin ligands affects their electronic properties, although in two different ways.

5.4 Photocatalytic CO_2 reduction tests with the MTCPP⊂UiO-66-NH_2 series

In order to remove any trace of anions trapped inside the pores of the MOFs (typically formate anions deriving from the decomposition of DMF at the high temperatures of the synthesis), the samples were washed thoroughly with distilled water until no ions were detected through IC analysis. Then, the samples were dried in an oven at 80°C overnight and stored.

Photocatalytic carbon dioxide reduction tests were performed using a bench-scale apparatus connected to a liquid phase recirculating closed system. In a typical experiment, 20 mg of MOF sample was suspended in 44 mL of an acetonitrile solution containing 10% v/v of Triethanolamine (TEOA) as sacrificial electron donor[13] and sonicated to obtain a homogeneous suspension. The photoactive mixture was placed in a 45 mL cylindrical quartz vessel, which was magnetically stirred during the photocatalytic experiments. The photoreactor was connected to a closed stainless steel recirculation system, in which CO_2 was continuously fluxed by means of a bellow pump (Metal Bellows, MB41E). The gaseous species evolving from the aqueous suspension under irradiation accumulated in the gas phase, which was analyzed on line by sampling at regular time intervals and injection into an Agilent 6890N gas

chromatograph (GC), equipped with two capillary columns (MolSieve 5A and HP-Plot Q), a flame ionization detector (FID) and a thermoconductivity detector (TCD). CO_2 was used to saturate the solution and as carrier gas.

The GC response was first calibrated by injecting known volumes of H_2, CO_2, CO and CH_4 into the recirculation system through a six ways sampling valve.

A Lot Oriel, 300 W xenon lamp (emitting in the 200 – 1100 nm range) was used as light source, which was placed at 8 cm from the photoreactor. A 385 nm long-pass filter was used in all experiments.

Each sample was tested in a 6 hour long kinetic run, with sampling every hour. Prior to the beginning of irradiation, the system was purged with CO_2 for approximately 45 min, in order to eliminate any trace of oxygen and other undesired gaseous species.

The presence of products in the liquid phase (typically, formate ions) was determined by ion chromatography (IC), employing a Metrohm 761 Compact IC instrument equipped with an anionic Metrosep A column.

The UiO-66-NH_2 framework can reduce CO_2 to formate anion in a mixed solution of acetonitrile and TEOA.[14] The low formate production rate has been increased by the used of mixed ligands[14] and mixed metals in the node,[15] or both.[16]

Since the main limitation of the UiO-66-X frameworks lies in its poor light harvesting properties, the idea behind the use of the MTCPP⊂UiO-66-NH_2 series was to extend the light harvesting to a broader range of the visible spectrum. Moreover, the porphyrin units in MOF structures have been proved to act as catalytic centres towards carbon dioxide reduction,[6,12] thus potentially leading to an increased overall photocatalytic activity.

Despite these forewords, our photocatalytic tests displayed neither production of formate anions nor any gaseous products that significantly differed from those obtained in blank tests performed in the absence of photocatalyst. These results are obviously surprising, since the setup of photocatalytic tests was similar to those already employed.

Despite the absence of photocatalytic activity, the frameworks proved to be stable in the operating conditions ofthe photocatalytic tests (see for example Figure 5.22).

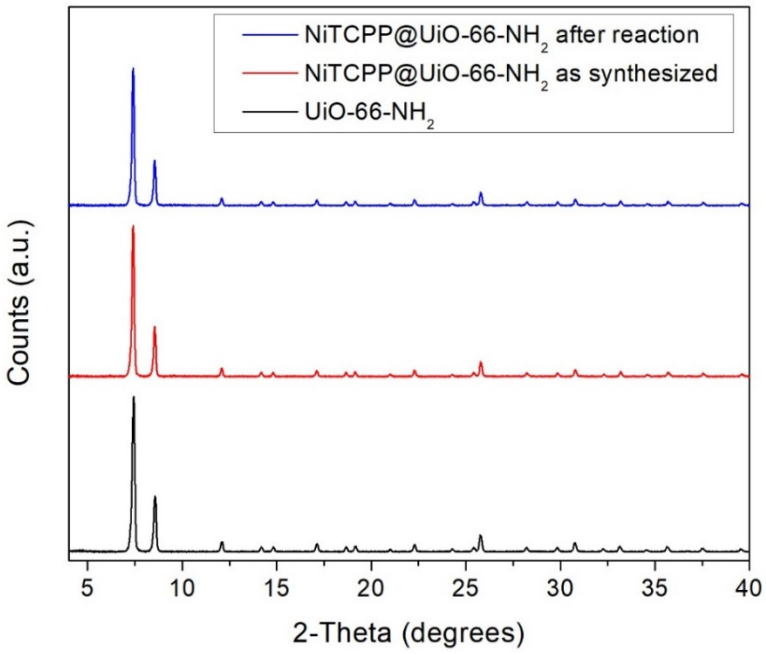

Figure 5.22. *Morphological analysis comparison before and after the photocatalytic test of NiTCPP⊂UiO-66-NH₂.*

Figure 5.23 shows that the framework retained its crystallinity after the reaction. The robustness of all samples was confirmed through their XRPD analysis.

5.5 Photocatalytic CO_2 reduction tests with the PCN-222(M) series

The photocatalytic tests were carried out in a closed 10 mL Pyrex vessel. In a typical procedure, 10 mg of MOF sample in 5 mL of a 20% v/v Triethanolamine (TEOA) – acetonitrile solution were degassed and bubbled with CO_2 for 30 min under stirring, in order to eliminate any trace of O_2. The CO_2 flow was set at 60 mL min^{-1} and forced to pass through a pure acetonitrile solution, before being bubbled into the reaction vessel. Then, the vessel was sealed and exposed to a simulated solar radiation with the aid of an Oriel Solar Simulator, with a power intensity of light, measured by means of a Thorlab PM200 power meter equipped with a S130VC power head with Si detector of 72 mW. Each sample was irradiated for 6 hours after which the suspension was decanted and 200 μL of it were diluted 10 times with distilled H_2O. The amount of formate anions was determined by ion chromatography (IC), employing a Metrohm 761 Compact IC instrument equipped with an anionic Metrosep A column.

Analysis in dark were subjected to the same procedure with the exception of light irradiation and the solutions were analysed 24 h after being saturated with CO_2.

Results in literature showed reduction from carbon dioxide to formate ions with this class of materials.[12] Since carbon dioxide is known to have particular affinity for some metals and their oxides,[17] we tested carbon dioxide affinity towards different metal ions inside the porphyrin ring. In fact, for example, the iron ion inside the eme-group can reversibly interact with carbon dioxide, while Liu *et. al.*[18] demonstrated the superior activity of a metal organic framework made of porphyrins by insertion of Cu(II) ions in the porphyrin ring.

In this perspective, the effect of different metals inside the porphyrin ring was evaluated in terms of formate ions production. The results are shown in Figure 5.24.

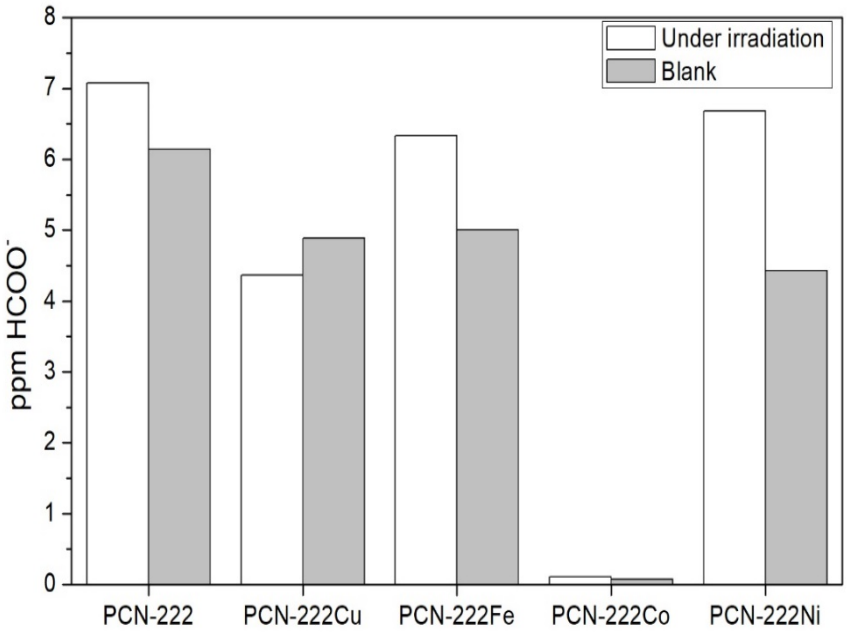

Figure 5.23. *Photocatalytic CO_2 reduction results of the PCN-222(M) series.*

With no sample, a significant difference, in terms of formate amount, from the blank analysis was obtained. The formate anions formed in the blank tests could originate from the framework itself as residues of the solvothermal synthesis (DMF decomposition at high temperature), although the samples were washed thoroughly with distilled water and dried prior to use.

Moreover, after the photocatalytic reactions, the suspension, once decanted, was not colourless: porphyrin leaching was evident for all the samples and also in the trials without irradiation. As an example, the comparison of the XRDP analysis of the PCN-222 sample is shown in Figure 5.25.

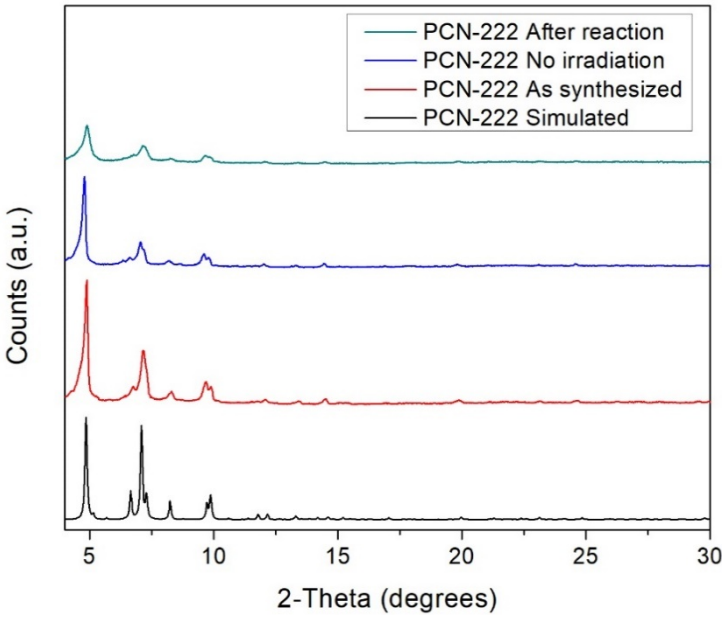

Figure 5.24. *XRPD analysis of PCN-222 sample.*

The framework underwent partial collapse after 24 hours in a 20% v/v TEOA – acetonitrile solution in the dark. Thus, the light colour of the decanted suspension of the blank experiment is due to the presence of some leached porphyrin. In the case of the irradiated sample, the framework underwent a substantial collapse and a major amount of porphyrin was leached into the solution. This evidence applies for all samples.

The framework collapse in the reaction media can be explained by recalling the structure of the Zr cluster of this series. In fact, from a topological point of view, this framework is made of 8-connected Zr_6-clusters. Therefore, only eight TCPP units bridge the edges of the Zr_6 clusters, while the remaining positions are occupied by terminal hydroxo groups. Therefore, there is a reduction of connectivity around the Zr cluster, which opens up the chance of nucleophilic substitution, especially in basic environments. The presence of TEOA might lead to a partial collapse of the framework, exasperated by the presence of irradiation.

Anyway, these results are in contrast with those obtained with for the PCN-222 framework by Ye and co-workers,[12] who reported the framework to be stable over the photocatalytic tests in the same media and able to effectively reduce carbon dioxide to formate anions, with no production in the dark. Repeated tests on the PCN-222 sample (freshly prepared) gave the same results, in term of chemical stability and production yield.

REFERENCES

[1] Kobayashi, N. *J. Porphyrins Phtalocyanines*, **2000**, *4*, 377.

[2] Hashimoto, T.; Choe, Y.-K.; Nakano, H.; Hirao, J. *J. Phys. Chem. A*, **1999**, *103*, 1984.

[3] Gouterman, M. *J. Chem. Phys.*, **1959**, *30*, 1139.

[4] The original %R values were converted into Abs values using the formula Abs = 1 – (%R/100). This conversion is valid for all the analysed samples.

[5] Zheng, W.; Shan, N.; Yu, L.; Wang, X., *Dyes and Pigments*, **2008**, *77*, 153.

[6] Xu, H.-Q.; Hu, J.; Wang, D.; Li, Z.; Zhang, Q.; Luo, Y.; Yu, S.-H.; Jiang, H.-L. *J. Am. Chem. Soc.* **2015**, *137*, 13440.

[7] Eastwood, D.; Gouterman, M., *J. Mol. Spectroscopy*, **1969**, *30*, 437.

[8] Zheng, W.; Shan, N.; Yu, L.; Wang, X. *Dyes and Pigments*, **2008**, *77*, 153.

[9] Harriman, A. *J. C. S. Faraday I*, **1980**, *76*, 1978.

[10] Guldi, D. M. *J. Phys. Chem. A* **2003**, *107*, 3215.

[11] Förster, T., *Ann. Phys.* (Weinheim, Ger.), **1948**, *437*, 55.

[12] Zhang, H.; Wei, J.; Dong. J.; Liu, G.; Shi, L.; An, P.; Zhao, G.; Kong, J.; Wang, X.; Meng, X.; Zhang, J.; Ye, J. *Angew. Chem. Int. Ed.* **2016**, *55*, 14310.

[13] Pellegrin, Y.; Odobel, F. *C. R. Chimie*, **2017**, *20*, 283.

[14] Sun, D.; Fu, Y.; Liu, W.; Ye, L.; Wang, D.; Yang, L.; Fu, X.; Li, Z *Angew. Chem. Int. Ed*, **2012**, *51*, 3364.

[15] Sun, D.; Liu, W.; Qiu, M.; Zhang, Y.; Li, Z. *Chem. Commun.* **2015**, *51*, 2056.

[16] Lee, Y.; Kim, S.; Kang, J. K.; Cohen, S. M. *Chem. Commun.* **2015**, *51*, 5735.

[17] Freund, H.-J.; Roberts, M. W. *Surface Science Reports*, **1996**, *25*, 225.

[18] Liu, Y.; Yang, Y.; Sun, Q.; Wang, Z.; Huang, B.; Dai, Y.; Qin, X.; Zhang, X. *ACS Appl. Mater. Interfaces*, **2013**, *5*, 7654.

Part 2

Photoelectrochemical water oxidation

Chapter 6

6.1 Semiconductor electrodes for energy conversion

Semiconductors possess band structures, which can explain their electronic, magnetic, and optical properties. A semiconductor has conducting properties in between those of an insulator and a conductor, and it forms a rectifying junction when immersed in an electrolyte solution.

Generally, in a semiconductor, the metal in its highest oxidation state, and thus its t_{2g} and e_g orbitals are unoccupied. The conduction band (CB) derives from these predominantly metal-based orbitals, while the valence band (VB) of an oxide is generally derived from the filled 2p orbitals of oxygen ligand. The band gap (E_g) is defined as the energy gap between the VB and CB. In d^0 oxides, such as TiO_2, this gap is rather wide (E_g > 3 eV), and therefore these materials are not intrinsic semiconductors. This means that without an imperfection or the presence of a dopant,

these materials are in fact insulators. Fortunately, metal oxides are never perfect and therefore their crystallographic defects lead to their semiconductor behaviour.

For example, the presence of oxygen vacancies in the crystalline structure allows a partial reduced state of some metal ions in the oxide structure itself. This, in turn, raises the Fermi level (E_F), locating the extra electron in the conduction band.[1] Since these electrons are responsible for conducting current, in this case the semiconductor is considered as *n*-type, in which, indeed, electrons are the majority carriers.

When a *n*-type semiconductor is placed in contact with an electrolyte, the interface between the two can be described in a way similar to that of a Schottky barrier.[2] In fact, when in contact, the Fermi levels of the two systems have to equilibrate, thus levelling the electrochemical potential of the solution and the Fermi level of the semiconductor oxide, as shown in Figure 6.1.

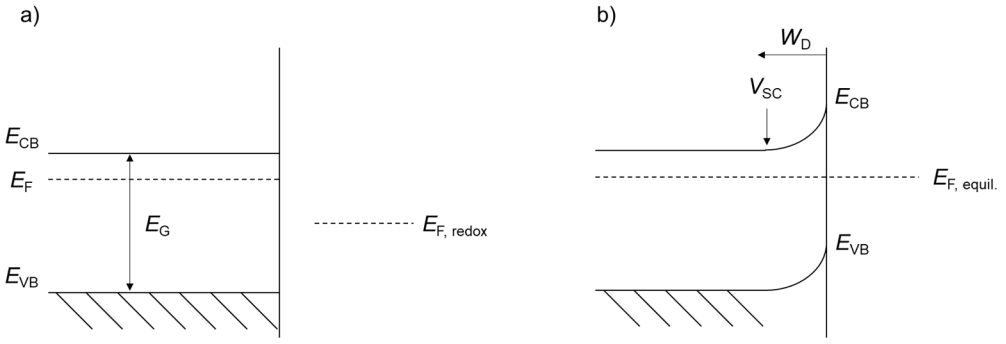

Figure 6.1.*The formation of a junction between an n-type semiconductor and an electrolyte solution: a) the separate system and b) after equilibration.*

Since the Fermi level in an *n*-type semiconductor is typically higher in energy than that of the solution, the electrons from the semiconductor "flow" into the solution, thus lowering the Fermi level and breaking the neutrality in the semiconductor itself. This charge transfer forms the so-called *built-in voltage* (V_{sc}), which is described as the difference in electrostatic potential between the semiconductor surface and its bulk.[3]

After reaching the equilibrium, the semiconductor surface is positively charged, since the majority carriers (*i.e.*, the electrons) have been depleted and a *depletion region* (W_D) is therefore formed.

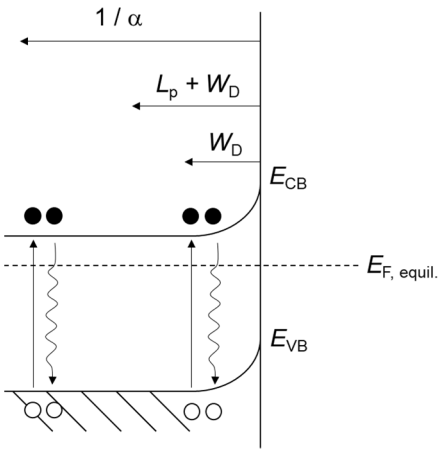

Figure 6.2. *Photogeneration of e^-/h^+ pairs in the bulk and depletion layer of an n-type semiconductor*

Generally, almost all electron-hole (e^-/h^+) pairs which are photogenerated in the bulk of a semiconductor tend to recombine and only those pairs which are photogenerated within the depletion region (W_D), or very close to it ($L_p + W_D$), have a chance to remain separated. In Figure 6.2, L_p is the carrier diffusion length, which depends on the material.[4]

Upon irradiation, these photogenerated pairs alter the equilibrium at the interface between the semiconductor and an electrolyte solution, thus creating a photovoltage. When an *n*-type semiconductor performs water oxidation, h^+ are collected at the surface to oxidize water (equation 1) and e^- flow to the external circuit to the counter electrode via the back contact, performing proton reduction (equation 2). This results in overall water splitting (equation 3):

$$H_2O + 4\ h\nu \rightarrow 2\ H^+ + ½\ O_2 + 2\ e^- \qquad E° = 1.23\ V\ vs\ RHE \qquad (1)$$

$2\ H^+ + 2\ e^- \rightarrow H_2$ $E° = 0$ V vs RHE (2)

$H_2O + 4\ hv \rightarrow ½\ O_2 + H_2$ $E° = –1.23$ V vs RHE (3)

6.2 Photoelectrochemical water splitting

The first example of photoelectrochemical (PEC) water splitting was reported by Fujishima and Honda using TiO_2 in 1972.[5] Since then, many efforts have been devoted to obtain a more efficient device employing TiO_2 as in a PEC system. The wide use of TiO_2 as photoanode can be ascribed to the fact that its valence band edge lies at an electrochemical potential more positive than that of the water oxidation (1.23 V_{RHE}) and because it is stable towards oxidative decomposition under illumination. In fact, non-oxide based semiconductors, such as CdS and GaP, undergo oxidative decomposition during water oxidation, a process that is known as *photocorrosion*. In this process, the photogenerated holes react preferentially with the anions (i.e., S^{2-} or P^{3-}) rather than with water.[6] Therefore, photostable metal oxide semiconductors, such as TiO_2, appear to be a judicious choice for water photo-oxidation.

Anyway, despite these positive features, common metal oxides such as TiO_2 possess valence band edges, which are too low in energy with respect to 1.23 V_{RHE}. Although this fact was preliminarily addressed as positive, it carries a potential drawback, which is the high overpotential required for the reaction to occur and the wide band gap of these materials, which makes them active only under UV light. Thus, many large band gap semiconductors[7] suffer from low efficiency, since the UV part of the sun emission spectrum contributes for about 4% of the total spectrum.

A general PEC system should possess a ca. 10% solar to hydrogen (STH) efficiency, be stable over a long period of time and be cost-competitive with fossil fuels.[8] As shown in Figure 6.3, when the bandgap of a certain semiconductor oxide decreases, the theoretical STH efficiency increases.

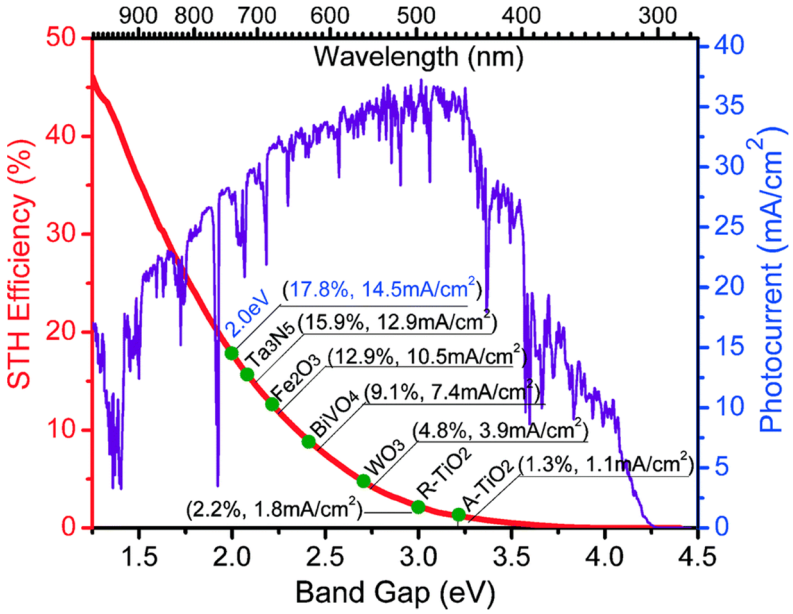

Figure 6.3. *STH efficiency and photocurrent maximum based on band gap and AM1.5G illumination.*[9]

This evidence is in line with the fact that, since the reaction relies on absorbed light, then the larger is the number of absorbed photons, the higher is the theoretical efficiency of the system. As shown in Figure 6.3, visible light has to be harvested in order to obtain a theoretical 10% STH value, although a quantitative conversion of photons into current (IPCE) and Faradic efficiency are assumed in this theoretical model, which unlike to be obtained.

6.3 Approaches to form visible-light absorbing oxides

In order to impart visible light absorption properties to common metal oxide semiconductors, a widely employed strategy is doping the crystal lattice with cations.[10] Although this strategy works well in the case of photocatalysts for organic dyes degradation,[11] the significant amount of dopant needed to harvest visible light becomes a drawback for photoelectrochemical applications, since it lowers the crystallinity of the oxide and increases the rates of carrier recombination.

Moreover, doping through metal cations does not produce a band shift, but new energy levels in the band gap, leading to absorption in the visible portion of the solar spectrum.[12] The formation of the so-called solid solutions is an efficient way to overcome the limits of metal cation doping.

According to the IUPAC definition, a solid solution is a "*solid in which components are compatible and form a unique phase*", which has a consequence the fact that the new phase possesses a mixed nature with respect to the original ones and, obviously, the properties of the final one can be tailored by varying the proportion with the starting ones. One example of a quaternary solid solution is the wurtzite phase $(Zn_{1-x}Ga_x)(O_{1-x}N_x)$, for which, by controlling the mole ratio of ZnO to GaN (which are both large band gap semiconductors), a significant decrease is band gap is realized.[13] This is possible because of the mixed state of the valence band, a hybrid between the metal d orbitals and the p orbitals of the anions, which raises the valence band energy towards less positive values.

A variation of the above-mentioned strategy is the formation of ternary phases (ABO_x), in which the valence band consists of metal based orbitals hybridized with

O(2p) ones, as shown in Figure 6.4. Also in the case of oxy-nitrides, such as TaON, the N(2p) and O(2p) states form the valence band.[14]

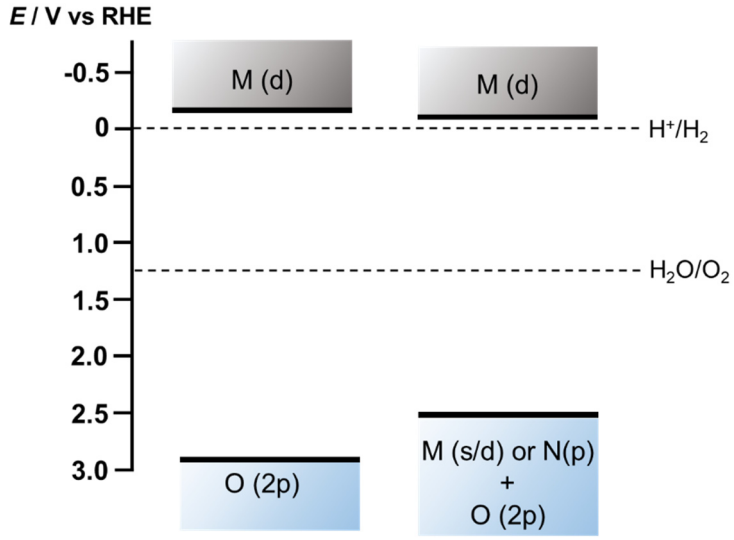

Figure 6.4. *Band structure of a semiconductor oxide comparing purely O (2p) to M (s/d) + O (2p) based valence band.*

In Figure 6.4, the metal based s or d orbitals hybridize with O(2p) orbitals, raising the overall energy of the valence band. This is a more useful methodology to narrow the band gap compared to lowering the conduction band energy. In fact, most oxides possess a conduction band edge that is very close to or below the H^+/H_2 redox couple, and lowering it shifts the open-circuit potential of the cell (V_{oc}) towards more positive values with respect to H^+/H_2. As V_{oc} becomes more positive, the required input of electric voltage required to drive water splitting will be greater as well.

Most ternary phase oxides are derived from oxyanions (BO_x^{n-}) in which the empty valence orbitals of the d^0/d^{10} metal component (B) form the conduction band. The valence band is typically formed from filled, or nearly filled, s or d orbitals of the metal cation (A^{n+}) of the ternary phase. One example of this type is $BiVO_4$: the Bi(6s) orbitals dominate the valence band maximum, forming a 2.5 eV band gap material.[15]

Ternary oxides and oxynitrides are becoming an attractive solution for research directed toward forming new visible light absorbing phases for PEC water splitting. This part of the thesis focuses on the 1st row transition metal tungstates (AWO_x), in particular copper-based tungstate ($CuWO_4$) because of the many advantageous PEC properties associated with WO_3 as a semiconductor for PEC water oxidation. The synthesis, characterization, and photoelectrochemistry of $CuWO_4$ thin films are the focus of the following chapter.

REFERENCES

[1] Dmochowski, J. E. *J. Phys.: Conference Series* **2007**, *79*, 12010.

[2] Gerischer, H. *J. Electroanal. Chem. And Interfacial Chem.*, **1975**, *58*, 263.

[3] Bisquert, J.; Cendula, P.; Bertoluzzi, L.; Gimenez, S *J. Phys. Chem. Lett.*, **2014**, *5*, 19840.

[4] Memming, R. "Electrochemical Decomposition of Semiconductors" in *Semiconductor Electrochemistry*, Wiley-VCH Verlag GmbH: 2007; pp. 16-18, p 373.

[5] Fujishima, A.; Honda, K. *Nature* **1972**, *238*, 37.

[6] Gerisher, M.; Mindt. W. *Electrochimica Acta*, **1968**, *13*, 1329.

[7] Osterloh, F. E. *Chem. Mater.* **2008**, *20*, 35.

[8] (a) Bard, A. J.; Fox, M. A. *Acc. Chem. Res.* **1995**, *28*, 141; (b) Pinaud, B. A.; Benck, J. D.; Seitz, L. C.; Forman, A. J.; Chen, Z.; Deutsch, T. G.; James, B. D.; Baum, K. N.; Baum, G. N.; Ardo, S.; Wang, H.; Miller, E.; Jaramillo, T. F. *Energy Environ. Sci.* **2013**, *6*, 1983.

[9] Li, J.; Wu, N. *Catal. Sci. Technol.*, **2015**, *5*, 1360.

[10] Martyanov, I. N.; Uma, S.; Rodrigues, S.; Klabunde, K. J. *Chem. Commun.* **2004**, 2476.

[11] Etacheri, V.; Seery, M. K.; Hinder, S. J.; Pillai, S. C. *Chem. Mater.* **2010**, *22*, 3843.

[12] Choi, W.; Termin, A.; Hoffman, M. R. *J. Phys. Chem* . **1994**, *98*, 13669.

[13] (a) Maeda, K.; Takata, T.; Hara, M.; Saito, N.; Inoue, Y.; Kobayashi, H.; Domen, K. *J. Am. Chem. Soc.* **2005**, *127*, 8286; (b) Maeda, K.; Teramura, K.; Lu, D.; Takata, T.; Saito, N.; Inoue, Y.; Domen, K. *Chem. Mater.* **2006**, *110*, 13753.

[14] (a) Fang, C. M.; Orhan, E.; de Wijs, G. A.; Hintzen, H. T.; de Groot, R. A.; Marchand, R.; Saillard, J.-Y.; de With, G. *J. Mater. Chem. A* **2001**, *11*, 1248; (b) Zhang, F.; Yamakata, A.; Maeda, K.; Moriya, Y.; Takata, T.; Kubota, J.; Teshima, K.; Oishi, S.; Domen, K. *J. Am. Chem. Soc.* **2012**, *134*, 8348.

[15] Walsh, A.; Yan, Y.; Huda, M. N.; Al-Jassim, M. M.; Wei, S.-H. *Chem. Mater.* **2009**, *21*, 547.

Chapter 7

UNDERSTANDING THE LIMITS: THE CASE OF $CuWO_4$

7.1 Introduction

As a potential way to produce clean O_2 and H_2 from water exploiting sunlight, photoelectrochemical water splitting has recently attracted great attention among researchers. In the frame of oxygen evolution reaction (OER), the initial interest was directed towards the development of binary metal oxide-based photoelectrodes, such as α-Fe_2O_3[1] and WO_3,[2] which proved to be the most promising ones. The choice of these binary metal oxide-based systems can be addressed to the ease of their synthesis and the limited cost. Among the two, WO_3 has shown longer hole diffusion length and higher mobility[3] than those of α-Fe_2O_3. Despite this, WO_3 suffers from poor

chemical stability in neutral or basic pH values and a rather wide bandgap (2.6 – 2.7 eV). Therefore, the developing of a W-based photoanode, which can account of the positive properties of WO_3 and, simultaneously addresses its drawback, is of paramount importance.

A promising W-based ternary oxide is $CuWO_4$, because of its narrower bandgap (2.2 – 2.3 eV), which allows it to harvest a larger portion of visible light than bare WO_3. Moreover, $CuWO_4$ has proven to be stable in neutral and slight basic pH values, thanks to the hybridization of Cu_d with O_p orbitals, thus creating metal-oxo bonds. Furthermore this hybridization leads to the negative shift of its VB with respect to the one of WO_3 and consequently to the band gap narrowing.[4] Although the photoelectrochemical properties of the $CuWO_4$-based photoelectrodes have already been tested both alone and in heterojunctions with WO_3 and $BiVO_4$,[4,5] the deep understanding of the factors which affect the photogenerated pairs have not been properly investigated yet.

In this study, we prepared multi-layered $CuWO_4$-based photoanodes thin films with a citrate-based aqueous solution method and we critically study them with the aim to better understand the limitations affecting the material itself. Therefore, we characterized the photoelectrodes under front and back-side illumination conditions and we tested their performance as a function of the light intensity. We used these experiments as diagnostic tools to extract information on the charge carrier transport properties of undoped $CuWO_4$. Interestingly, this material shows a non-linear photocurrent response by varying the light intensity. In particular, likewise $BiVO_4$, $CuWO_4$ shows higher efficiencies at low intensity, while under one sun irradiation (100 mW cm^{-2}) its efficiency markedly drops. On the other hand, differently from $BiVO_4$ photoanodes,[6] $CuWO_4$ does not display any drop of performance under light intensities

higher than one sun. This is in analogy with the good water oxidation properties of this material. Both Linear Sweep Voltammetry (LSV) and Incident Photon-to-Current Efficiency (IPCE) analyses show a drop of the photoelectrode performance from back- to front-side irradiation, while transient photocurrent shows stable photocurrent values. These evidences should enlighten the bulk recombination of photogenerated pairs as the main limitation of this photocatalytic material.

7.2 Materials

The following chemicals were employed in the present work: copper(II) nitrate trihydrate (99% purity, Sigma Aldrich), ammonium tungsten hydrate (99% purity, Fluka), Citric acid (99% purity, Sigma Aldrich), deionized water, boric acid (99.5% purity, Sigma Aldrich) and KOH (99.5% purity, Sigma Aldrich). All the chemicals were used as received with no further purifications.

7.3 Photoelectrodes preparation

The precursor solution of $CuWO_4$ was prepared as follows: 14 mmol of citric acid were dissolved in 5.3 mL of EtOH and 2.4 mL of deionized H_2O. This method allows to obtain 10 mL of a 0.5 M Cu and W solution. Then, under vigorous stirring, 5 mmol of $Cu(NO_3)_2 \cdot 3H_2O$ were dissolved, followed by the addition of a stoichiometric amount of $(NH_4)_6H_2W_{12}O_{40} \cdot xH_2O$ (ammonium metatungstate hydrate). Fluorine-doped tin oxide (FTO) glass (Pilkington Glass, TEC-7, thickness 2 mm) was coated with the solution by spin coating at 4000 rpm for 30 s. Prior to deposition, the FTO glass was cleaned under sonication for 30 min in a soap solution, rinsed thoroughly with water and then in EtOH for 30 min and then dried in air. Furthermore, prior to coat the first layer, the

FTO was soaked few seconds in isopropanol, then placed into the spin coater. This procedure lowers the light scattering at wavelengths longer than 550 nm. We found that it was unnecessary for depositing the successive layers. After being coated, the $CuWO_4$ film was pre-annealed at 250°C for 10 min and then annealed at 550°C for 1 h. To eliminate any possible trace of CuO phase, the photoanodes were treated for about 30 s in a 0.5 M HCl aqueous solution, washed with distilled water and then dried in air before any measurement. Multilayers of $CuWO_4$ were obtained by repeating the deposition, annealing and CuO removal up to six times.

7.4 Optical, morphological and photoelectrochemical characterization

The UV-Vis absorption spectra were recorded with a Jasco V-650 spectrophotometer. The crystalline phase of the materials were determined by XRD analysis on deposited thin films using a Philips PW 1830/40 X-ray Powder Diffractometer, equipped with a Cu sealed tube at 40 kV and 40 mA. Photoelectrochemical (PEC) measurements were performed using a home-made 3 arms cell and an Autolab PGSTAT 12 (EcoChemie, Utrecth, The Netherlands). The potentiostat was controlled by NOVA software (version 2.1). In a typical set up, the FTO/$(CuWO_4)_n$ electrode (where n stands for the number of layers of $CuWO_4$ deposited onto FTO, ranging from 1 to 6) was used as working electrode, a Pt wire was used as counter electrode and Ag/AgCl (3.0 M in NaCl) was used as reference electrode. The photoanodes were tested both under back side (through the FTO/$CuWO_4$ interface) and under front side illumination (through the $CuWO_4$/FTO

interface). The light source was provided by an Oriel, Model 81172 Solar Simulator equipped with an AM 1.5G filter. The light intensity was set to 100 mW cm^{-2} (1 Sun), unless otherwise specified. The intensity was measured by means of a Thorlab PM200 power meter equipped with a S130VC power head with Si detector. Photoelectrochemical experiments were carried out in a 0.1 M potassium borate (KBi) buffered at pH 9. The potential *vs*. Ag/AgCl was converted into the RHE scale using the following equation: $E_{RHE} = E_{Ag/AgCl} + 0.059\ pH + E°_{Ag/AgCl}$, with $E°_{Ag/AgCl\ (3.0\ M\ NaCl)}$ = 0.210 V at 25°C.

Incident photo-to-current efficiency (IPCE) measurements were carried out using a 300 W Lot-Oriel Xe lamp equipped with a Lot-Oriel Omni-λ 150 monochromator and a Thorlabs SC10 automatic shutter. A 1.23 V bias *vs*. RHE was applied and the current was measured with a 10 nm step, within the 300 to 600 nm wavelength range. The incident light power was measured at each wavelength. The IPCE was calculated using the following equation:

$$IPCE = \frac{[1240 \cdot j]}{P_\lambda \cdot \lambda} \cdot 100$$

where *j* is the photocurrent density (mA cm^{-2}) and P_λ (mW cm^{-2}) is the power of the monochromatic light at wavelength λ (nm).

The internal quantum efficiency (IQE) was calculated by combining the IPCE spectrum with the absorption (A) spectrum of the photoanode:

$$IQE = \frac{IPCE}{1 - 10^{-A}}$$

7.5 Characterization of $CuWO_4$ multilayer photoanodes

The electronic absorption spectra of $CuWO_4$ multilayer photoanodes thin films were collected in transmittance mode, thanks to the optical transparency obtained through the novel citrate-based synthetic procedure.

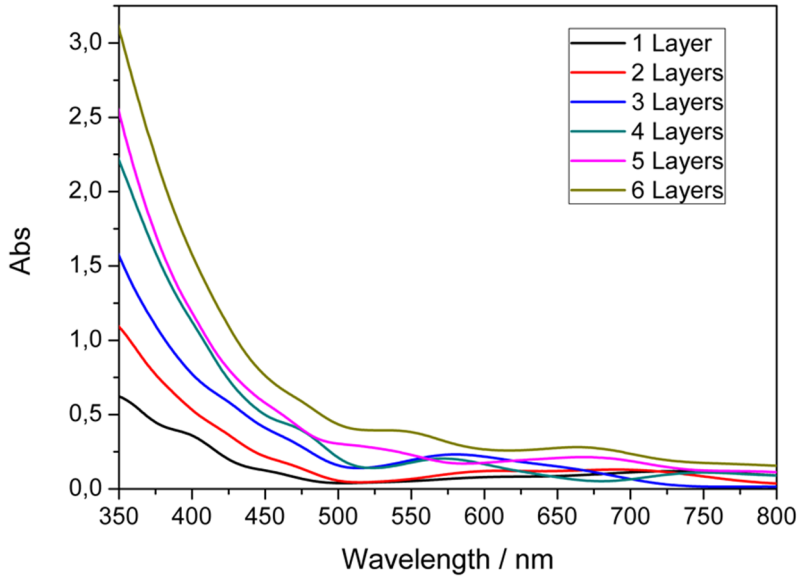

Figure 7.1. *Absorption spectra of $CuWO_4$ multilayer photoanodes.*

As shown in Figure 7.1, the absorbance linearly increases in the band gap excitation range together with the number of $CuWO_4$ layers, while at wavelengths longer than 500 nm the presence of scattering and of interference fringes due to the FTO thin film slightly enhance the absorbance (especially for two thickest films). The band-gap for this material is considered to be indirect,[7] and the main transition is assigned as the metal-to-metal charge transfer (MMCT) associated with hybridized O(2p) + Cu(3d) valence band and the W(5d) conduction band. In addition to the MMCT band and to the interference fringes, $CuWO_4$ photoanodes show low energy, localized *d-d* bands within the Jahn-Teller distorted Cu_6O octahedra over 700 nm, typical of

Cu(II) salts.[8] In our case, these bands are more pronounced at low number of layers and are anyway partially masked by interference fringes.

The phase purity of the $CuWO_4$ films was assessed through XRPD analysis and comparison with the Bragg reflections from JCPDF 72-0616, which revealed triclinic structure (Figure 7.2). The diffractogram lacks of any impurity signal, in particular those ascribed to CuO and WO_3 phases.

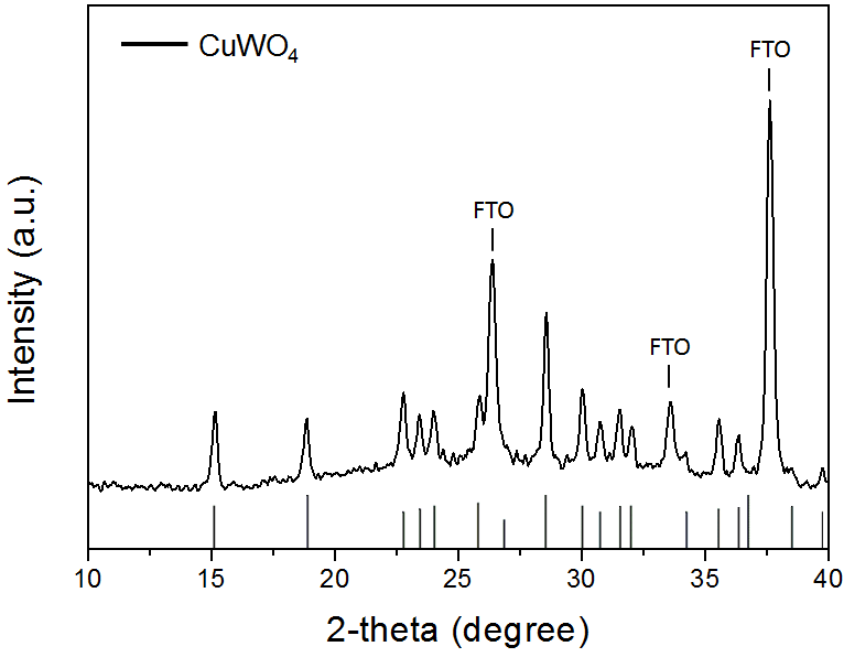

Figure 7.2. *XRD analysis of the $CuWO_4$ thin film coated onto FTO. Bragg reflections from JCPDF 72-0616 are indicated in grey.*

7.6 Photoresponse of $CuWO_4$ multilayer photoanodes

Figure 7.3a shows the IPCE analyses as a function of wavelength for the $CuWO_4$ multilayer photoelectrodes at an applied bias of 1.23 V_{RHE}. All samples show modest efficiencies in back-side irradiation mode, with a rapid decrease of the recorded values. The photoanodes still generate measurable currents up to 550-560 nm (a 500 nm cut

off filter was used to avoid interferences due to the second harmonic reflections of the grating monochromatic), implying that the photoactive material has a narrower band gap with respect to WO_3 (2.2-2.3 eV considering the photocurrent onset wavelength). The high film transparency allowed us to combine the absorption spectra of each film with the photocurrent generated in the monochromatic IPCE experiments and to calculate the internal quantum efficiency (IQE). This parameter takes into account the amount of absorbed photons which gives photocurrent, thus giving information on bulk recombination. The IQE reported in Figure 7.3b and calculated from the IPCE (Figure 3a) give moderate values, thus suggesting that only a modest fraction of the absorbed photons yields electrons in the outer circuit. Such low charge carrier collection efficiencies indicate that the photogenerated pairs quickly recombine in $CuWO_4$ and that bulk recombination is the main issue in these films. The efficiency of the $CuWO_4$ photoanodes increases with the thickness and the film obtained by repeating 6 times the coating procedure shows the best efficiency.

Figures 7.3c and 7.3d show the IPCE and the IQE analyses of the $CuWO_4$ multilayer photoanodes under front-side irradiation. Under such irradiation condition, most of the charge carriers are photogenerated close to the electrode/electrolyte interface and the conduction band electrons, in order to reach the extraction site at the FTO, need to travel longer than under to backside irradiation mode. Therefore, we expect considerable wavelength dependent differences when testing the photoanodes in the two irradiation modes. Indeed, under front side irradiation the films obtained by repeating 5 times the coating procedure is the best performing one. This result is in contrast with that obtained in backside mode (see Figures 7.3a and b). Furthermore, the IQE values obtained under front side irradiation with each electrodes are lower with

respect to the values obtained in backside mode (see Figure D1). These results indicate that the overall photoresponse is limited by the electron transport properties of the material.[9] The IPCE and the IQE values obtained in front side irradiation at wavelengths longer than 370 nm exceed those recorded in back side mode since $CuWO_4$ has low extinction coefficients at these wavelengths. Therefore, in front side irradiation mode, long wavelength photons are absorbed closer to the FTO than in backside irradiation mode (Figure D1).

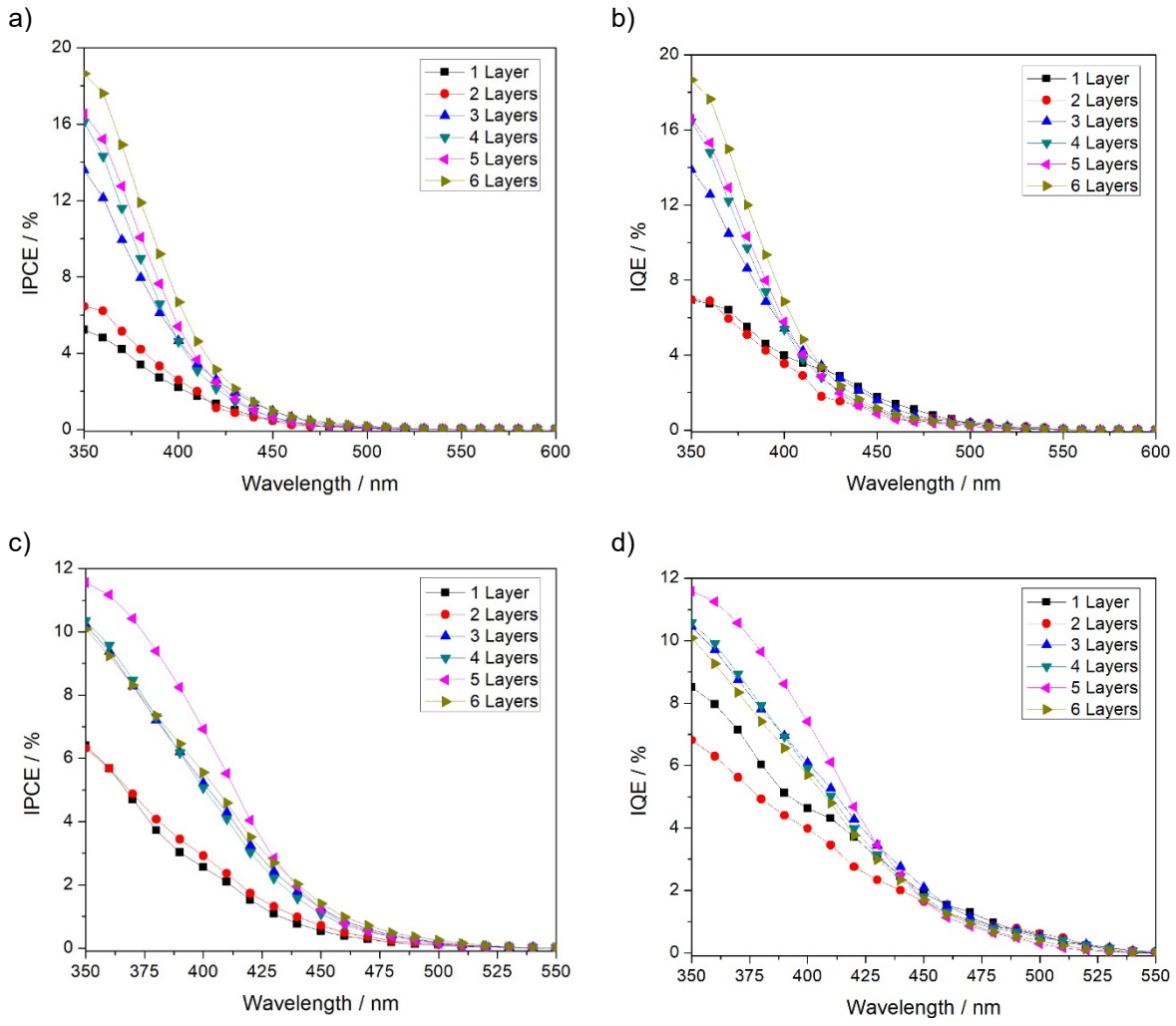

Figure 7.3. *IPCE and IQE analyses of $CuWO_4$ multilayer photoanodes under back-side (a-b) and front-side (c-d) irradiation mode.*

It is worth noting that the IQE values (especially for the backside irradiation mode) practically matches the IPCE ones. This is due to the absorption profile of our photoanodes, which stays above the unit in most of the cases, in particular from the 3rd layer, over the active wavelength range.

The photoelectrodes were tested in linear sweep voltammetry experiments both under AM 1.5G simulated solar light (with an intensity of 100 mW cm^{-2}) in back and front-side illumination with the electrodes contacted with a 0.1 M KBi buffer solution at pH 9 and the results are reported in Figure 7.4.

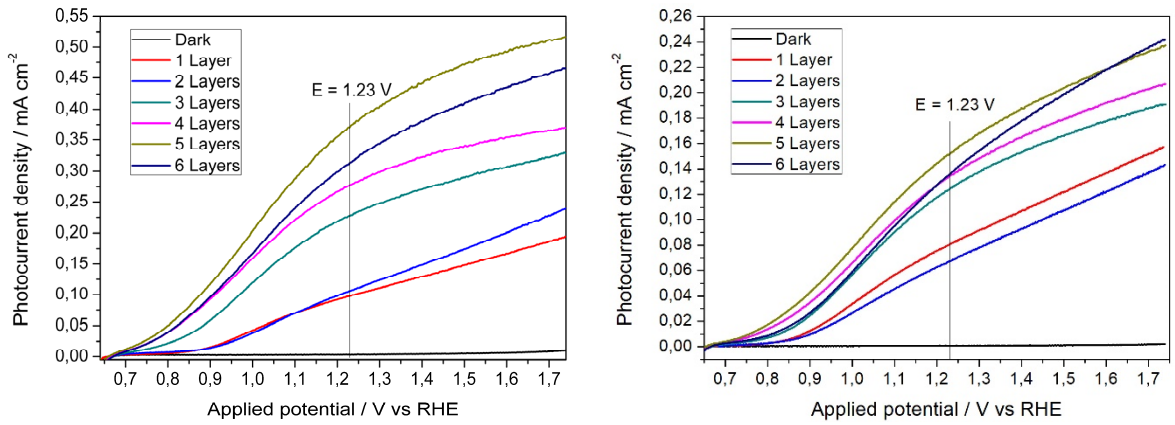

Figure 7.4. *Linear sweep voltammetry of $CuWO_4$ multilayer photoanodes under different irradiation geometries: backside irradiation (left) and front side irradiation (right).*

The 5-layer photoanode outputs the highest photocurrent response under linear potential scan in both the irradiation configurations. This result is apparently in contrast with the results of back side irradiation IPCE measurements. However, this discrepancy can be explained by considering the different light intensity employed in simulated solar light (100 mW cm^{-2}) scans and in IPCE experiments. In fact, by assuming poor electron transport as the main cause of photogenerated pairs recombination, it is reasonable that at low light intensity, with less photogenerated

electron-hole pairs, the efficiency of the 6-layered photoanode overcomes that of the 5-layered one, especially under backside irradiation condition. Moreover, by comparing the photocurrent response under back- and front-side irradiation configuration, one may conclude that photogenerated pairs recombination is a consequence of the poor electron transport properties, given the difference in terms of photocurrent, ranging from 20 to 60% for the 1-layered and the 5-layered specimens, respectively.

By integrating the IPCE values within the reference AM 1.5G solar spectrum,[6] it is possible to calculate the fraction of photons absorbed by the selected material. In Figure 7.5, the red area corresponds to the calculated value for the 5-layered photoanode.

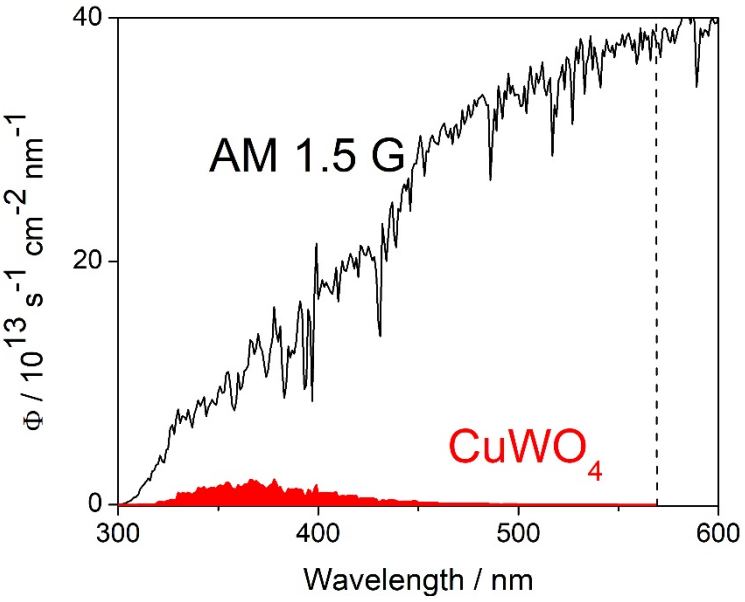

Figure 7.3. *Product of the IPCE of $CuWO_4$ (5^{th} layer) under back-side illumination configuration with the AM1.5 solar spectrum. The dashed vertical line represents the absorption edge of the material found through IPCE analysis.*

By assuming unitary internal quantum efficiency values over the absorption range of the material (up to 550-560 nm), it is possible to calculate the theoretical maximum photoresponse value under 1 sun illumination, which is, for the 5-layered film, approximatively 5.6 mA cm^{-2}. As reported in Figure 7.4, the actual measurement reveals a lower photocurrent than the theoretical limit: at 1.23 V_{RHE}, the photocurrent density is 0.37 mA cm^{-2}, which is roughly 6.6% of the predicted value.

In order to assess whether the photogenerated pairs recombination occurs in the bulk or on the surface, transient photocurrent profiles were examined. As shown in Figure 7.6, the transient photocurrent response at 1.23 V_{RHE} of the $CuWO_4$ photoanode 5^{th} layer (black line) shows no photocurrent peak at the beginning of irradiation and, over time, the photocurrent output remains stable.

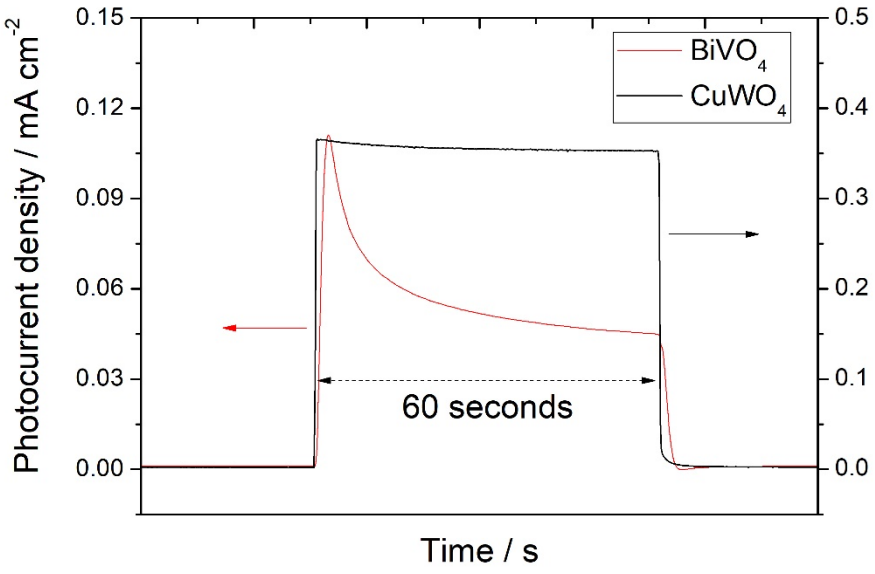

Figure 7.4. *Chopped AM1.5 chronoamperometry plots of $CuWO_4$ 5^{th} layer (black line) and typical $BiVO_4$ under backside illumination configuration at 1.23 V_{RHE}.*

By contrast, the same measurement on $BiVO_4$ electrode (red line) shows a completely different transient photocurrent profile. In fact, the decrease in photocurrent

shortly after the light is turned on is due to recombination of the photogenerated electrons with the accumulated holes. When the light is switched off, the accumulated holes at the surface of the photoelectrode react with free electrons in the conduction band. This causes electrons to be withdrawn from the external circuit, thus generating a cathodic transient photocurrent response. Such transient photocurrent behaviour in $BiVO_4$ originates from the fact that the material is characterized by slow water oxidation, which means slow hole transfer across the semiconductor/electrolyte interface. This, in turn, causes photogenerated holes to accumulate near the surface, which increases the chance of recombination with the electrons.

Therefore, the different behaviour of the two materials enlightens the different nature of photogenerated pairs recombination: while in $BiVO_4$ recombination occurs at the interface between the semiconductor and the electrolyte, *i.e.*, it is *superficial*, in $CuWO_4$ appears to occur inside the material, *i.e.* in *bulk*.

Another consequence is the fact that $CuWO_4$ does not suffer from slow water oxidation kinetic. In order to effectively rule out such an effect as the origin of the poor photoresponse of the material, H_2O_2 was added to the electrolyte as a hole scavenger. Hydrogen peroxide possesses a much higher oxidation rate constant than water, thanks to its more cathodic reduction potential (+0.68 V_{RHE} versus 1.23 V_{RHE} for water) and to the fact that only two holes are needed for its oxidation, in contrast with water, which needs four holes.[10]

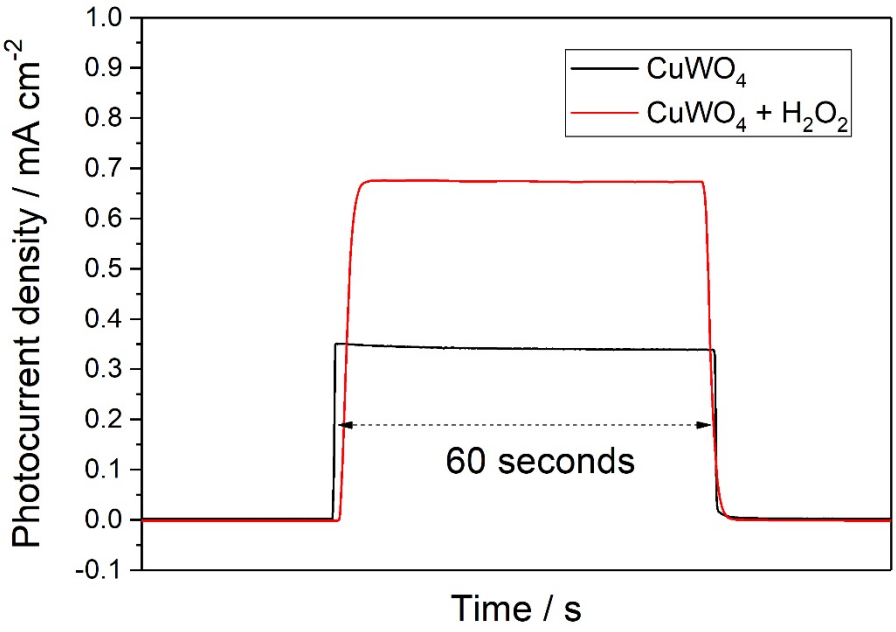

Figure 7.7 *Chopped AM1.5 chronoamperometry plots of $CuWO_4$ with (red line) and without (black line) addition of 0.5 M H_2O_2.*

Figure 7.7 shows an AM1.5 photocurrent density of 0.67 mA cm^{-2} at 1.23 V_{RHE} after adding H_2O_2, which corresponds to almost 2-fold increase of the original photocurrent value of 0.37 mA cm^{-2} obtained for the 5-layered photoanode. This doubled value agrees with the so-called *current doubling* effect,[11] in which the oxidised form of H_2O_2 undergoes further oxidation by injection of an electron into the conduction band of the semiconductor. The schematic representation of the current doubling effect is depicted in Scheme 7.1 and is described by the following reactions:

$$H_2O_2 + h^+{}_{CuWO_4} \rightarrow 2H^+ + O_2{}^{\cdot -} \quad (1)$$

$$O_2{}^{\cdot -} \rightarrow O_2 + e^-{}_{CB} \quad (2)$$

Giving the fact that the photocurrent output for the $CuWO_4$ photoanode only doubles its value in the presence of H_2O_2 as hole scavenger, one can conclude that

the water oxidation step does not affect the performance of the material and, therefore, the photogenerated pairs undergo recombination in the bulk, not at the interface between the photoelectrode surface and the electrolyte.

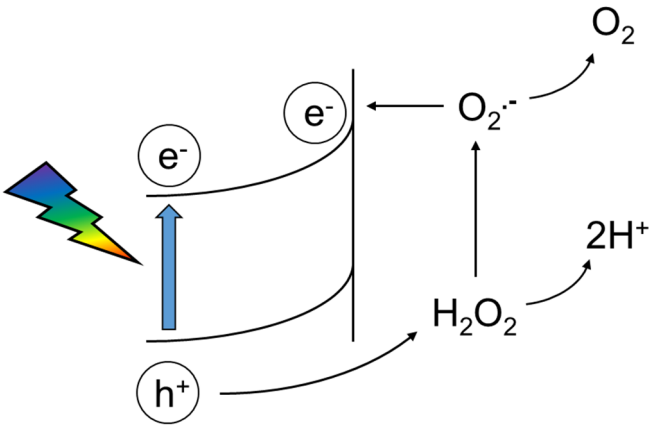

Scheme 7.1. *Schematic representation of the current doubling effect in the presence of H_2O_2, in which its oxidised form (a superoxide anion) is further oxidised by electron injection into the conduction band of $CuWO_4$.*

7.7 Light intensity dependence

In order to probe the charge separation efficiency of our materials, we evaluated the effect of the light intensity on the material in backside irradiation configuration. Therefore, we recorded the photocurrent response of the 5-layered photoanode at different power intensities ranging from 0.25 to 2 suns (from 25 to 200 mW cm^{-2} AM 1.5G light respectively).

As shown in Figure 7.8, upon increasing the power intensity, the photocurrent response of the $CuWO_4$ photoelectrode increases, although this increment is not proportional to the light intensity increase.

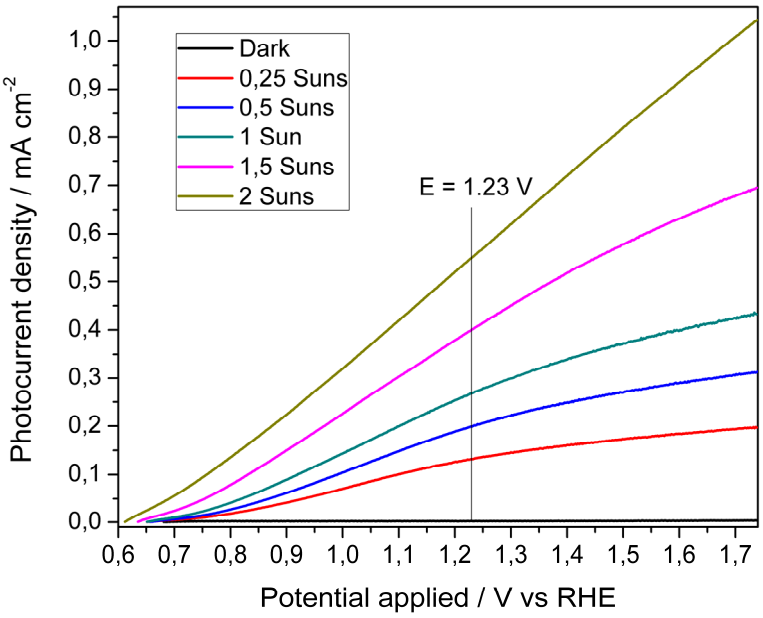

Figure 7.8. *LSV analysis of the multilayer $CuWO_4$ photoelectrode as a function of the irradiation power.*

In the previous section, a theoretical maximum photocurrent value under 1 sun illumination of 5.6 mA cm^{-2} was estimated by integrating the IPCE values over the solar spectrum. In the same way, an estimated maximum photocurrent value at each power intensities (*i.e.* fraction of the solar spectrum) can be easily derived as well. By dividing the experimental values for the theoretical ones, one can obtain an indication of how close the experimental value is to the theoretical one. This estimation is somehow correlated to the internal quantum efficiency (IQE) at different light intensities. The resulting IQE values as a function of the number of absorbed photons (which is proportional to the number of photogenerated charge carriers and the light intensity) are shown in Figure 7.9.

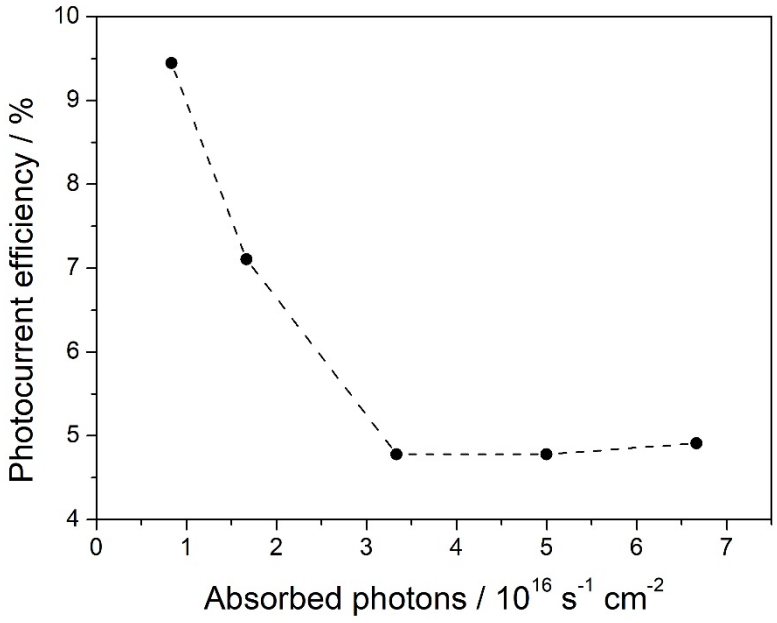

Figure 7.9. *Photocurrent efficiency dependence (IQE) with respect to absorbed photons at 1.23 V_{RHE}.*

The overall IQE decreases with increasing the light intensity up to 1 sun, then the value stabilizes for illumination intensities greater than this value. The increased photocurrent efficiency at low light intensity correlates with the IPCE analyses (*i.e.* at very low light intensity and thus with low number of photogenerated pairs), and so the 6-layered photoanode performed best. Moreover, the H_2O_2 experiment gave no positive effect to the photoresponse other than the current doubling effect, and this implies that each hole that reaches the electrode surface combines with water. Therefore, no improvement can be obtained by the use of water oxidation catalysts (WOC). In accordance to this statement, a single layer photoanode was treated hydrothermally with aqueous solution containing Ni^{2+} and Fe^{3+} sources in order to grow Ni/Fe oxidation catalyst as reported elsewhere for BiVO4.[12] Monochromatic LSV analysis at λ = 420 nm showed no photocurrent enhancement for the WOC-treated $CuWO_4$ photoanode (Figure 7.10).

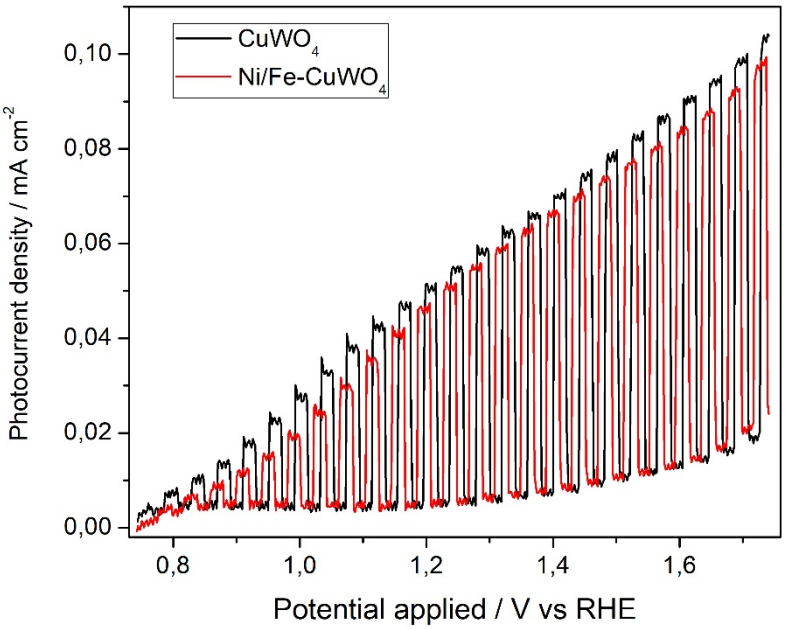

Figure 7.10. *LSV comparison between bare (black line) and Ni/Fe-treated (red line) $CuWO_4$ photoanodes. The LSV scans were recorded at power intensity of 2 mW cm^{-2} at λ = 400 nm.*

Therefore, further efforts to improve $CuWO_4$ should be directed toward improving charge separation in the bulk by doping the structure with metal ions.[13]

Other than recombination at bulk defects, other possible factors affecting the charge separation efficiency in $CuWO_4$ photoanodes are: (i) charge trapping at the interface with the back-contact and (ii) the presence of a Schottky barrier at the back contact. The first issue has been already addressed for $BiVO_4$ with the aid of a thin SnO_2 layer, which serves as "*hole mirror*", thus preventing the hole to move toward the back-contact.[14] Although this simple treatment gave a 3-fold enhancement of IPCE in the reported example, this is valid only for semiconductors with a conduction band (CB) negative enough to be able to transfer electrons to the back-contact without being blocked by the SnO_2 layer itself. In other words, the SnO_2 layer should not act as an *electron mirror*. Since the CB of $CuWO_4$ is more positive with respect to the CB of SnO_2 one, SnO_2 cannot be used for this purpose. On the other hand, the formation of

Schottky barrier is likely to occur, because low light intensities the internal quantum efficiencies of the photoanodes are quite low.

Therefore, by summarizing the findings, $CuWO_4$ photoanodes are affected by poor electron transport and they suffer from bulk recombination of photogenerated charges, although at very high light intensities, *i.e.* greater than 1 sun, the photocurrent efficiency does not suffer from further drops. No improvements can be achieved by depositing additional water oxidation catalysts on the surface, since the recombination of the charges occurs in the bulk.

In the frame of energy conversion devices, the here developed optically transparent $CuWO_4$ photoanodes should operate in a tandem cell configuration. In fact, the bias voltage in such a device is generated by a photovoltaic (PV) cell placed behind the photoanode, using the unabsorbed light that passes through. Under the hypothesis that a PV cell that generates 1.23 V from the light transmitted by $CuWO_4$ photoanodes, solar-to-hydrogen conversion efficiencies of 0.4% (1.23 V × 0.37 mA cm^{-2} / 100 mW cm^{-2}) can be obtained with the 5-layered $CuWO_4$ photoanode.

7.8 Conclusions

In conclusion, the limiting factors of optically transparent $CuWO_4$ photoanodes have been successfully identified. In particular, through a combination of different analysis, we demonstrated that $CuWO_4$ photoanodes suffer from poor electron transport and high recombination at bulk defects. Despite this, the optically transparent material is able to generate a photocurrent density of 0.37 mA cm^{-2} under simulated AM1.5 illumination and does not display water oxidation kinetic issue, as demonstrated by the absence of photocurrent enhancement by the deposition of Ni/Fe water oxidation

catalyst on the photoanode surface. Further efforts on this material should be therefore oriented to the improvement of charge separation in the bulk through metal ions, as in the case of $BiVO_4$ photoanodes, with which $CuWO_4$ shares some of its limiting factors.

REFERENCES

[1] Tilley, S. D.; Cornuz, M.; Sivula, K.; Grätzel, M. *Angew. Chem., Int. Ed*. **2010**, *49*, 6405.

[2] Solarska, R.; Krolikowska, A.; Augustynski, J. *Angew. Chem., Int. Ed*. **2010**, *49*, 7980.

[3] (a) Reyes-Gil, K. R.; Wiggenhorn, C.; Brunschwig, B. S.; Lewis, N. S. *J. Phys. Chem. C*, **2013**, *117*, 14947; (b) Wang, H.; Lindgren, T. He, J.; Hagfeldt, A.; Lindquist, S.-E. *J. Phys. Chem. B*, **2000**, *104*, 5686.

[4] Yourey, J. E.; Bartlett, B. M. *J. Mater. Chem.*, **2011**, *21*, 7651.

[5] (a) Pilli, S. K.; Deutsch, T. G.; Furtak, T. E.; Brown, L. D.; Turner, J. A.; Herring, A. M. : *Phys. Chem. Chem. Phys.*, **2013**, *15*, 3273; (b) Ye, W.; Chen, F.; Zhao, F.; Han, N.; Li, Y. *ACS Appl. Mater. Interfaces*, **2016**, *8*, 9211.

[6] Abdi, F. F.; van de Krol, R. *J. Phys. Chem. C*, **2012**, *116*, 9398.

[7] Lacomba-Perales, R.; Ruiz-Fuertes, J.; Errandonea, D.; Martìnez-Garcìa, D.; Segura, A. *Europhys. Lett.*, **2008**, *83*, 37002.

[8] Ruiz-Fuertes, J.; Sanz-Ortiz, M. N.; Gonzàlez, J.; Rodrìguez, F.; Segura, A.; Errandonea, D. *J. Phys.: Conf. Ser.*, **2010**, *215*, 012048/1

[9] (a) Liang, Y. Q.; Tsubota, T.; Mooij, L. P. A.; Van de Krol, R. *J. Phys. Chem. C,* **2011**, *115*, 17594; (b) Lindquist, S. E.; Finnstrom, B.; Tegner, L. *J. Electrochem. Soc*., **1983**, *130*, 351.

[10] Dotan, H.; Sivula, K.; Grätzel, M.; Rothschild, A.; Warren, S. C. *Energy Environ. Sci.*, **2011**, *4*, 958.

[11] Fujishima, A.; Kato, T.; Maekawa, E.; Honda, K. *Bull. Chem. Soc. Jpn.,* **1981**, *54*, 1671.

[12] Cai, L.; Zhao, J.; Li, H.; Park, J.; Cho, I. S.; Han, H. S.; Zheng, X. *ACS Energy Lett.*, **2016**, *1*, 624.

[13] Zhong, D. K.; Choi, S.; Gamelin, D. R. *J. Am. Chem. Soc.*, **2011**, *133*, 18370.

[14] Liang, Y. Q.; Tsubota, T.; Mooij, L. P. A.; Van de Krol, R. *J. Phys. Chem. C*, **2011**, *115*, 17594.

Part 3

Temperature-assisted photocatalytic methanol steam reforming

Chapter 8

8.1 TiO_2 in photocatalysis

Nowadays, with the rapid depletion of fossil fuels (coal, natural gas, and petroleum oil), the development of renewable energies based on sufficient energy sources with sustainable supply for the long-term in a large quantity is in high demand. Ever increasing attention has been paid to explore novel methods for developing renewable energy technologies. Conversion of solar energy into chemical energy in the form of so-called “solar fuels”, such as H_2, methanol, methane, etc., is considered one of the most perspective strategies to solve the energy and environmental problems in the future. H_2 is an excellent energy carrier for the development of low-carbon emission economy. To develop hydrogen economy, extensive research has been carried out on photocatalytic or photoelectrochemical (PEC) splitting of water into H_2 and O_2 since the first report of the photoelectrochemical water splitting reaction on TiO_2 electrode by Fujishima and Honda.[1]

As one of the earliest studied *n*-type semiconductor photocatalysts, TiO_2 has been widely used in environmental purification,[2] self-cleaning, H_2 production, photosynthesis, CO_2 reduction,[3] organic synthesis,[4] solar cells, etc.[5] Being cheap, stable, nontoxic, and environmentally friendly, TiO_2 is an idea model of semiconductor photocatalyst to investigate. Therefore, the number of publications on TiO_2 has increased exponentially in recent decades. As a versatile material, TiO_2 is extensively applied in various fields. Nevertheless, as a photocatalyst, the most challenging and meaningful application of TiO_2 should be the photocatalytic fuel generation reactions, mainly including H_2 production. In this perspective, the following chapter illustrates modified TiO_2-based photocatalysts, which are employed to produce hydrogen from water in gaseous phase.

8.2 Basic properties of TiO_2 semiconductor photocatalysts

Semiconductor is a kind of material with electrical conductivity between conductor (such as metals) and insulator (such as ceramic). The unique electronic property of a semiconductor is characterized by its valence band (VB) and conduction band (CB). There is no electron state between the top of the VB and the bottom of CB. The energy range between CB and VB is called bandgap, which is usually denoted as E_g. The band structure, including the bandgap and the positions of VB and CB, is one of the important properties for a semiconductor photocatalyst, because it determines the light absorption behaviour as well as the redox capability of a semiconductor. As shown in Figure 8.1, the photocatalytic reaction initiates from the generation of electron−hole pairs upon light irradiation. When a semiconductor photocatalyst absorbs photons with

energy equal to or greater than its E_g, the electrons in VB will be excited to CB, leaving the holes in the VB.

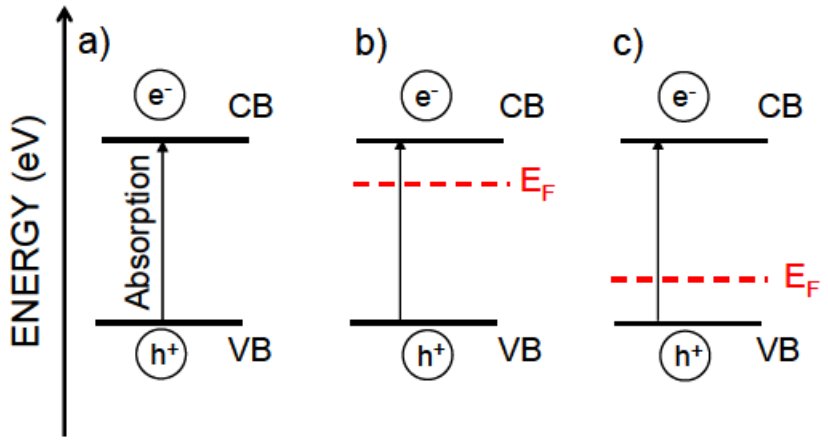

Figure 8.1. *Schematic representation of semiconductor activation: (a) general semiconductor, (b) n-type semiconductor and (c) p-type one. Taken from ref [6].*

Another aspect has to be considered when discussing the band structure of a semiconductor, which is the Fermi level, generally labelled as E_F. According to its definition, the Fermi level represents the energy level at which the probability of occupation by an electron is equal to ½.[6] For an intrinsic semiconductor (which means that it has no impurities) E_F lies exactly in between the VB and the CB. As can be seen from Figure 8.1, the position of E_F can be modified through doping. In particular, in an *n*-type semiconductor, where the major charge carriers are electrons, E_F lies just below the CB, whereas in a *p*-type semiconductor, in which the major charge carriers are holes, E_F lies just above the VB.

When a semiconductor is in contact with another phase (that is, the electrolyte in solution), a charge redistribution occurs. From the energy level viewpoint, this implies that the electrochemical potentials of the two species must be the same.

In most of *n*-type semiconductor materials, the Fermi level lies at more negative energies (generally referred as “more cathodic”) than the redox potential of the electrolyte. Therefore, in order to achieve equilibrium, the E_F of the semiconductor has to lower its energy in order to match the potential energy of the electrolyte. This causes an upward band bending of the band edges (Figure 8.2) and a net flow of electrons will be created from the semiconductor to the electrolyte, thus forming the so-called depletion layer at the interface between the semiconductor and the electrolyte.[7]

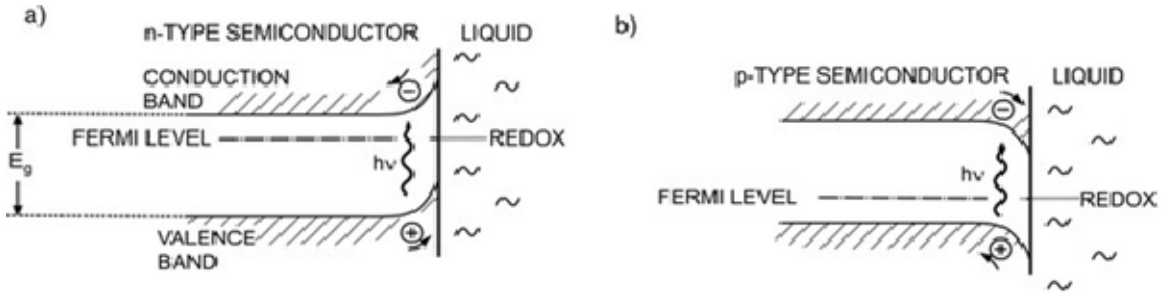

Figure 8.2. *Band bending for (a) an n-type semiconductor and (b) a p-type semiconductor, both in equilibrium with a solution. Taken from ref [7].*

Conversely, for a *p*-type semiconductor, where the Fermi level possesses more anodic character than the redox potential of the electrolyte, the system equilibration is achieved when the E_F of the semiconductor “increases” its energy to match the electrolyte one. Therefore, in this case there is a downward band banding with and, consequently, a net flow of holes towards the electrolyte will be created, together with the formation of a depletion layer.

Besides these fundamental structural features, the most important factor that determines the activity of a photocatalyst is the efficiency of charge separation. Because of its high importance, different strategies have been examined to improve it. Once the charge separation has taken place, the successive step is the surface

catalytic reaction. The electron photopromoted in the CB are responsible of the reduction reaction and their reduction capability is determined by the position of the CB itself. Conversely, the photoproduced holes in the VB are responsible for the oxidation reaction and their oxidation capability is determined by the VB position itself. In the case of the water splitting reaction, the CB position of a photocatalyst has to be more negative (more cathodic) than the redox potential of the proton reduction reaction (0 V_{RHE}), while the energy level of VB has to be more positive than the redox potential of water oxidation (1.23 V_{RHE}).

In most cases, efficient photocatalytic reactions (*i.e.* involving efficient charge separation processes) proceed only after loading noble metal and oxide co-catalysts on semiconductors.

8.3 Loading co-catalysts on TiO_2

Because of fast recombination of photogenerated electrons and holes or lack of appropriate reaction sites, single semiconductor-based photocatalysts usually do not show high efficiency in photocatalysis. To improve their photocatalytic efficiencies, it is necessary to develop composite photocatalysts by loading proper oxidation and/or reduction co-catalysts on the oxide surface. In such system, the roles of co-catalysts include: *i*) to provide trapping sites for the photogenerated charges and promote the charge separation, thus enhancing the quantum efficiency; *ii*) to improve the photostability of the catalysts by consuming the photogenerated electrons and holes; and *iii*) to catalyse the reactions by lowering the activation energy. Various kinds of co-catalysts have been applied to TiO_2 to improve the photocatalytic activity of H_2 evolution reactions, including metal co-catalysts, metal oxide/sulfide co-catalysts, and

hydrogenase-mimic co-catalysts. In this part of the thesis, the attention have been devoted to the modification of the TiO_2 surface with noble metal nanoparticles. Because the work function of a noble metal is usually larger than that of most semiconductors, electron transfer from CB of semiconductor to metal readily happens. In fact, the higher is the work function, the stronger is the electron trapping ability of the metal. Platinum, in particular, possesses the largest work function (5.12−5.93 eV)[8] among the noble metals. Anyway, the photocatalytic activity of Pt/TiO_2 also largely depends on the way the nanoparticles are loaded on the surface of TiO_2. That is, the size and distribution of noble metal nanoparticles (NM NPs) effectively affects the photocatalytic performances of a NM NPs loaded semiconductor photocatalyst.

Au is also an efficient H_2 evolution co-catalyst for TiO_2.[9] Moreover, since it possesses a plasmonic band set at wavelength around 540 nm, its plasmonic effect has also been investigated on Au/TiO_2, which is quite different from being a co-catalyst.[10] Besides Pt and Au, other metal co-catalysts including Pd, Rh, Ru, Ir, Ag, Ni, Co, etc., were also investigated for H_2 production on TiO_2-based photocatalysts.[11] By the way, considering the availability and cost of noble metals, the development of non-noble metal co-catalysts is of paramount importance.

8.4. Hydrogen generation on TiO_2 photocatalyst through photo-steam reforming of methanol

The main motivation of the photocatalytic research is to develop efficient photocatalysts to drive thermodynamically uphill reactions by overcoming the energy barrier/overpotential through a relatively low energy reaction pathway. Also, because a photocatalytic reaction on a semiconductor photocatalyst involves light absorption,

charge separation, carrier migration and surface catalytic reactions, a large part of photocatalysis research is also about the engineering of photocatalysts aiming at improving the efficiencies of these key processes. Water splitting is an energetically uphill reaction (*i.e.* requires at least 1.23 eV energy input) involving four electron transfer processes. The H_2 production by overall water splitting using solar energy, that is, photocatalytically split water into H_2 and O_2 in 2 : 1 stoichiometric ratio, is the true "solar fuel" production reaction, because the net solar energy to chemical energy conversion by this reaction is achieved.

On the other hand, half reactions of photocatalytic water splitting in the presence of sacrificial reagents have been extensively studied to evaluate the H_2 production possibility with different photocatalysts. Until now, several typical systems for photocatalytic H_2 production have been developed, with the aid of inorganic anions. These inorganic anions can be easily oxidized by the photogenerated holes and promote the H_2 production reaction. For example, the highest quantum yield of ~93% for H_2 production at 420 nm was achieved with S^{2-}/SO_3^{2-} as the sacrificial reagent using Pt−PdS/CdS as the photocatalyst.[12] Adapting the concept of these H_2 production reactions in the presence of sacrificial reagents, photocatalytic steam reforming of methanol is also a valuable choice.

Methanol, indeed, with one hydroxide function group and one carbon atom, is the simplest alcohol. The research on photocatalytic methanol reforming is regarded as the model reaction for biomass reforming, which can provide some basic understandings on the mechanism of photocatalytic biomass reforming. In the photocatalytic H_2 production system, methanol is usually used as a sacrificial reagent to promote the activity. Although, the photo-steam reforming reaction did not receive

much attention, it has been intensively studied in our group.[13] In these studies, methanol was found to undergo oxidation up to carbon dioxide through the formation of formaldehyde and formic acid as intermediate species, which are involved in a series of parallel and competitive reactions. Moreover, carbon monoxide, methane, dimethyl ether and acetaldehyde were identified as additional side products.

In the following chapter, the synergistic effect of Au NPs loaded onto the TiO_2 surface and the contribution of external heat will be discussed in the frame of methanol photo-steam reforming reaction, in order to evaluate their effect on the oxidation products selectivity.

REFERENCES

[1] Fujishima, A.; Honda, K. *Nature,* **1972**, *238*, 37.

[2] Frank, S. N.; Bard, A. J. J. *Am. Chem. Soc.,* **1977**, *99*, 303.

[3] Koci, K.; Obalova, L.; Lacny, Z. *Chem. Pap.,* **2008**, *62*, 1.

[4] Kraeutler, B.; Bard, A. J. *J. Am. Chem. Soc.*, **1978**, *100*, 4317.

[5] Wang, R.; Hashimoto, K.; Fujishima, A.; Chikuni, M.; Kojima, E.; Kitamura, A.; Shimohigoshi, M.; Watanabe, T. *Nature*, **1997**, *388*, 431.

[6] Bott, A. W. *Current Separ.* **1998**, *17*, 87.

[7] Bäuerle, D. in "Laser Processing and Chemistry", 4th edition, 2011, Chapter 15, page 361.

[8] Lide, D. R. *CRC Handbook of Chemistry and Physics*; CRC Press: Boca Raton, FL, 2005; p 12.

[9] (a) Greaves, J.; Al-Mazroai, L.; Nuhu, A.; Davies, P.; Bowker, M. *Gold Bull.*, **2006**, *39*, 216; (b) Feil, A. F.; Migowski, P.; Scheffer, F. R.; Pierozan, M. D.; Corsetti, R. R.; Rodrigues, M.; Pezzi, R. P.; Machado, G.; Amaral, L.; Teixeira, S. R.; Weibel, D. E.; Dupont, J. *J. Braz. Chem. Soc.*, **2010**, *21*, 1359; (c) Wu, G. P.; Chen, T.; Su, W. G.; Zhou, G. H.; Zong, X.; Lei, Z. B.; Li, C. *Int. J. Hydrogen Energy,* **2008**, *33*, 1243; (d) Primo, A.; Corma, A.; Garcia, H. *Phys. Chem. Chem. Phys.*, **2011**, *13*, 886.

[10] Gomes Silva, C.; Juarez, R.; Marino, T.; Molinari, R.; Garcia, H. *J. Am. Chem. Soc.,* **2011**, *133*, 595.

[11] (a) Kim, J.; Monllor-Satoca, D.; Choi, W. *Energy Environ. Sci.*, **2012**, *5*, 7647; (b) Chiarello, G. L.; Aguirre, M. H.; Selli, E. *J. Catal.*, **2010**, *273*, 182; (c) Gu, Q.; Long, J.; Zhou, Y.; Yuan, R.; Lin, H.; Wang, X. *J. Catal.*, **2012**, *289*, 88; (d) Ma, Y.; Chong, R. F.; Zhang, F. X.; Xu, Q.; Shen, S.; Han, H. X.; Li, C. *Phys. Chem. Chem. Phys.,* **2014**, *16*, 17754.

[12] Yan, H. J.; Yang, J. H.; Ma, G. J.; Wu, G. P.; Zong, X.; Lei, Z. B.; Shi, J. Y.; Li, C. *J. Catal*. **2009**, *266*, 165.

[13] (a) Chiarello, G. L.; Aguirre, M. H; Selli, E. *J. Catal.*, **2010**, *273*, 182; (b) Chiarello, G. L.; Ferri, D.; Selli, E., *J Catal.*, **2011**, *280*, 168; (c) Bernaregi, M.; Dozzi, M. V.; Bettini, L. G.; Ferretti, A. M.; Chiarello, G. L.; Selli, E., Catalysts, 2017, 7, 301.

Chapter 9

TEMPERATURE-DEPENDENT METHANOL PHOTO-STEAM REFORMING

9.1 Introduction

Titanium dioxide, TiO_2, has attracted widespread interest in the field of heterogeneous photocatalysis since the discovery of Fujishima and Honda who reported the photoelectrochemical water splitting back in 1972.[1] Although its ubiquitous use in photocatalytic (PC) reaction systems, three main drawbacks still affect this material. The first one is the wide bandgap of about 3.2 eV (for the anatase form), which corresponds to absorption at a wavelength below 390 nm, to efficiently photopromote an electron from the valence band (VB) into the conduction band (CB). Therefore, TiO_2 only utilizes the UV part of the solar spectrum, which accounts for about 5% of the entire solar radiation. The second drawback is related to the low quantum efficiency in photocatalytic reactions due to the fast electron-hole

recombination. The third drawback derives from the deactivation of the photocatalyst, due to the formation of stable by-products on its surface, which hampers the photocatalytic performance, especially for the degradation of volatile organic compounds (VOCs).[2] The latter issue can be partly addressed through increased temperature together with photocatalysis, thus exploiting the possible synergistic effect of the so-obtained thermo-photocatalysis (TPC). This coupled system has been employed in the degradation of benzene[3] and other industrial plants pollutants.[4] Furthermore, the coupled thermo-photocatalysis approach has been used to investigate the role of temperature in the production of hydrogen from water, although controversial results have been obtained, some experiments having enlightened beneficial effects of temperature, while others showed negative effects.[5] In all these investigations, TiO_2 has always been modified with metal nanoparticles in order to boost its thermo- and photocatalytic properties. The role of the metal deposited onto TiO_2 and the use of temperature in the methanol photo steam reforming reaction has never been investigated so far.

The possibly synergistic effect of gold nanoparticles deposited onto TiO_2 by means of the deposition-precipitation (DP) method, and the effect of temperature have been thus investigated. Results show that the selectivity in the oxidation products of methanol depends on temperature and this suggests that temperature plays an important role on the equilibria involving the oxidation reaction.

9.2 Photocatalysts preparation

All photocatalysts were home-prepared, apart from P25 TiO_2 from Evonik, which is frequently employed as benchmark in photocatalytic studies.

The Au/TiO_2_DP photocatalysts series with nominal Au amount of 0.3 and 1% was prepared following a slight variation of the original Haruta's method,[6] *i.e.* involving the use of $NaBH_4$ as reducing agent. The TiO_2 support was dispersed in water (about 10 g L^{-1}) and the required amount of gold, in the form of $HAuCl_4$ solution (0.1 g L^{-1} of Au), was added under vigorous stirring. The pH was then adjusted to 10 by dropwise addition of a 1 M NaOH solution. The suspension, thermostated at 80 °C, was firstly vigorously stirred for 3 h and then centrifuged. The recovered powder was re-suspended in water and reduced by addition of a large excess of $NaBH_4$, under stirring. The suspension color turned from white to purple, indicating the reduction of Au(III) to metallic NPs. The so-obtained powder was repeatedly washed with water until the content of chloride ions in the supernatant was below 1 ppm and finally dried at 70 °C overnight and grounded in an agate mortar.

The Au/TiO_2_C photocatalysts series with nominal Au amount of 0.3 and 1% was synthesised by the deposition of surfactant-stabilised preformed gold nanoparticles on TiO_2, adopting a reverse micelle method similar to that described by Liu *et. al*.[7] Chloroauric acid was used as gold precursor. Proper amounts of this precursor were dissolved in 95 mL of a n-dodecyltrimethylammonium chloride aqueous solution to obtain a 40 : 1 surfactant to gold precursor molar ratio. The gold colloidal suspension was then obtained by adding 5 mL of a $NaBH_4$ aqueous solution (4 : 1 $NaBH_4$ to gold precursor molar ratio) under vigorous stirring. The colour turned from yellowish to deep dark, as a consequence of gold reduction. The proper amount of TiO_2 powder, dispersed in water (50 mL) in an ultrasonic bath, was then added to the gold colloidal suspension under vigorous stirring. When stirring was stopped, a coloured powder precipitated, while the supernatant liquid was perfectly clear, indicating the total

deposition of the gold colloids on the TiO_2 surface. Finally, the powder was recovered after at least four cycles of precipitation, supernatant separation and washing with water. The final wet powder was centrifuged to minimise its water content and dried overnight in oven at 70°C.

The Au/TiO_2_P photocatalysts series with nominal Au amount of 0.1 and 1% was synthesised from 6% v/v methanol/water suspensions containing 3 g L^{-1} of TiO_2 and the required amount of Au(III) acetate as gold precursor, preliminary dissolved in an acidic aqueous medium. Gold photoreduction to metallic gold nanoparticles deposited onto TiO_2 was achieved by irradiating the suspensions for 2 h under nitrogen atmosphere. An immersion fluorescent low pressure mercury arc lamp (Jelosil) was employed as irradiation source, emitting in the 300-400 range, with a maximum emission peak centred at 360 nm. Gold-modified TiO_2 powders were recovered after at least five centrifugation and washing cycles, in order to achieve the complete removal of residual ions and organic precursors. The final wet precipitated powder was dried overnight in oven at 70°C. All chemicals were purchased from Aldrich and used as received.

9.3 Characterisation details

UV-Vis diffuse reflectance (DR) spectra were recorded using a Lambda 19, Perkin-Elmer spectrophotometer equipped with an RSA-PE-20 integrating sphere assembly, using a calibrated SRS-99-010 Spectralon Reflectance Standard, produced by Labsphere, as a reference material.

HR-TEM analysis was carried out with a JEOL JEM 2010 electron microscope, equipped with a LAB6 electron gun operating at 200 keV and a Gatan CCD camera

allowing high-resolution imaging. Specimens for HRTEM analysis were sonicated in 2-propanol and then transferred as a suspension to a copper grid covered with a holey carbon film.

X-Ray diffraction analysis was performed employing a Philips PW 1820 powder diffractometer, operating at 40 kV and 40 mA, using filtered Cu K_α radiation (λ = 1.54056 Å).

9.4 Photocatalytic tests

The photocatalysts were tested in the methanol photo-steam reforming reaction. For the tests, a recirculating stainless steel system, reported in the sketch in Figure 9.1, was employed.[8]

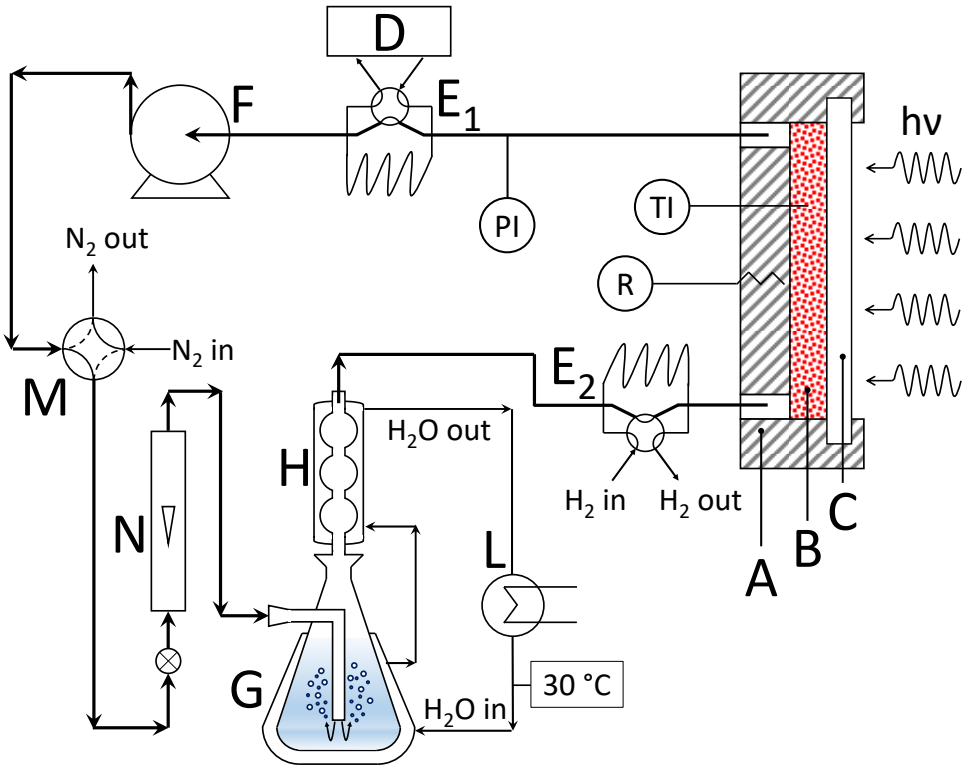

Figure 9.1. *Sketch of the recirculating gas phase system employed for the photocatalytic tests.*

The photoreactor (A) was a flat stainless steel cell with central cylindrical, 4 mm thick and 63.5 mm in diameter round hollow (B) frontally closed by a Pyrex glass optical window (C). The temperature of the photocatalytic bed was controlled by a thermocouple inserted behind the cell, while the temperature was varied with the aid of four heating cartridges (R) inserted on the sides of the thermocouple and controlled by an OMRON E5CC PID controller. The photoreactor was connected to a closed stainless steel circuit, where the gas phase was recirculated at a constant rate by means of a bellow pump (F) and forced to pass through a bubbling system (G), containing 55 mL of a 20% v/v methanol – water solution held at 30°C, surmounted by a refrigerator-condenser element (H). The photocatalytic bed, which was fitted in the hollow of the cell (B), was prepared by mixing 15 ± 1 mg of photcatalysts with 20-40 mesh quartz beads and a 1 mL of distilled water in a Petri dish, followed by drying in oven at 70°C for 1 h. The amount of quartz beads was 7.10 ± 0.05 g.

Prior to any analysis, the system was purged with nitrogen for about 45 min, in order to eliminate any trace of oxygen. The photocatalytic tests were performed in two different ways: in continuum and in recirculating mode. In the first case, the photocatalytic bed was continuously fed with a stream of N_2 saturated with the methanol-water solution vapour at 9 mL min^{-1} with the 4 way-ball valve (M) in the position of the dashed line in Figure 9.1, in order to avoid accumulation of gas phase in the system. In the second case, the methanol-water vapour mixture was fluxed at 60 mL min^{-1} with the 4 way-ball valve in the position of the solid line, in order to accumulate gaseous products inside the system. In the continuum mode, the heat ramp was of 1 °C min^{-1}, while in the recirculation mode 4 different temperatures (40, 100, 150 and 200°C) were selected. The recirculating/flowing gas was analysed on-

line by sampling it every 20 min by means of a pneumatic sampling valve placed at the exit of the photoreactor.

Gas samples were automatically injected into an Agilent 6890N gas chromatograph (GC), equipped with two columns (HP-PlotU and Molesive 5Å), two detectors (D) (thermoconductivity and flame ionization detectors) and a Ni-catalyst kit for CO and CO_2 methanation. N_2 was used as carrier gas. The GC response was first calibrated by injecting known volumes of H_2, CO_2, CO and CH_4 into the recirculation system through the loop of a six ways sampling valve. The amount of formic acid accumulated in the liquid solution during the photocatalytic tests was determined by ion chromatography (IC) after the runs, employing a Metrohm 761 Compact IC instrument equipped with an anionic Metrosep A column.

The irradiation source was a Xenon lamp (Lot Oriel, 300 W), placed at 6 cm from the photoreactor, emitting in the 200–1100 nm wavelength range. The relative pressure was 0.25 bar at the beginning of the recirculating runs and increased during irradiation, as a consequence of the accumulation of products in the gas phase. Three consecutive irradiation cycles were always performed in the case of recirculation tests, in order to check their reproducibility, with 30-min long N_2 purging in the dark between each irradiation cycle. The rate of products formation is given as the average of the values in three photocatalytic runs.

9.5 Photocatalysts characterization

The deposition of gold nanoparticles on TiO_2 was confirmed by the colour change of the modified oxide powder, turning from white into purple of different intensity, originating from the surface plasmon resonance of nanocrystalline Au(0) particles. All

gold-containing samples display the typical plasmon resonance absorption band, with an absorption maximum around 550 nm. This absorption is observed when the wavelength of the incident light is larger than the nanoparticle size and is originated by light in resonance with the surface plasmon oscillation, causing the free electrons in the metal to oscillate in resonance with the frequency of light.[9] The intensity of the plasmon resonance band clearly increases with increasing the gold loading, without any appreciable difference in the absorption maximum, indicating a progressive increase in particle density without marked variation of their size (see Appendix E).

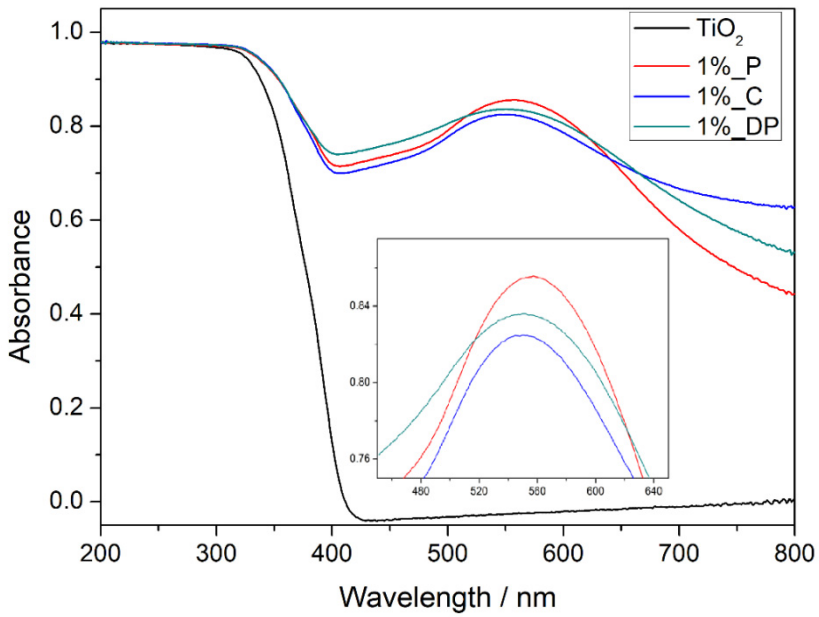

Figure 9.2. *Diffuse reflectance spectra (DRS) of TiO_2 and TiO_2 modified powders with nominal 1% Au nanoparticles loading, obtained by the three different methodologies. In the inset, the magnification of the plasmonic band evidences the red shift in the absorption maximum for the P sample.*

By comparing the absorption bands of the different Au-loaded TiO_2 series (Figure 9.2), some differences can be noticed in relation to the properties of gold nanoparticles, depending on the deposition method. In particular, the longer is the wavelength of the plasmon resonance band maximum, the larger are the gold nanoparticles. The trend

is confirmed by the UV-Vis DRS analysis, for which the plasmon resonance band maximum is red-shifted on going from the DP-method-modified TiO_2 to the P-method modified one, thus indicating that smaller sized nanoparticles are obtained with the DP method.

Gold deposition on TiO_2 was also verified by HRTEM analysis, yielding valuable, direct information on the dimension and the distribution of Au nanoparticles on the TiO_2 surface, as reported in Figure 9.3.

Ongoing from top to bottom in Figure 9.3, increasing size in the gold nanoparticle diameter can be seen. In particular, the nanoparticles generated by the modified DP method are in the 2 – 4 nm mean diameter range, while those obtained by the colloidal method are in the 3 – 8 nm range on average, together with some rare bigger particles up to 20 nm. Finally, the photodeposition method afforded the biggest nanoparticles, with mean diameter around 20 nm.

No variation in XRD patterns was expected after gold deposition by the adopted procedures, not implying any heat treatment, as already verified in previous studies.[10]

a)

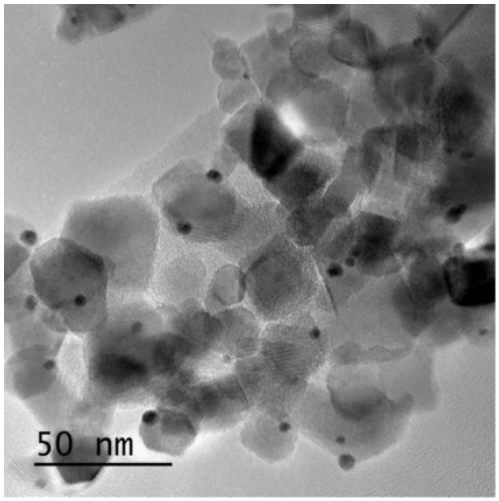

b)

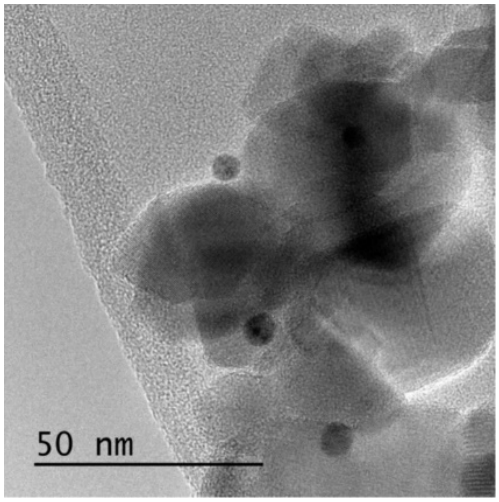

c)

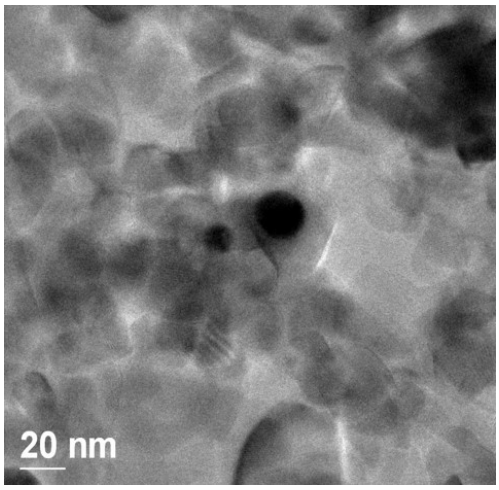

Figure 9.3. *HRTEM images of: a) 1%Au/TiO_2_DP, b) 1%Au/TiO_2_C and c) 1%Au/TiO_2_P samples.*

9.6 Effects of gold deposition method and nominal amount

A comparison between the performances of the different gold-containing photocatalysts is reported in Figure 9.4. Although a deep investigation of the effects of the metal deposition method and nominal loading was beyond the aim of the work, one can notice that the best results in terms of hydrogen production rate are obtained with the DP series. The lower hydrogen production rate attained with Au/TiO_2_P series with respect to the other photocatalysts could be partially ascribed to larger Au nanoparticles in this series. In fact, the plasmonic band maximum was red-shifted by ca. 10 nm, with respect to the other samples, being at 557 nm in comparison with 548 nm for 1%Au/TiO_2-DP, for example. This should indicate an average particles diameter larger than expected, with a consequent lowering in the activity of the photocatalyst.

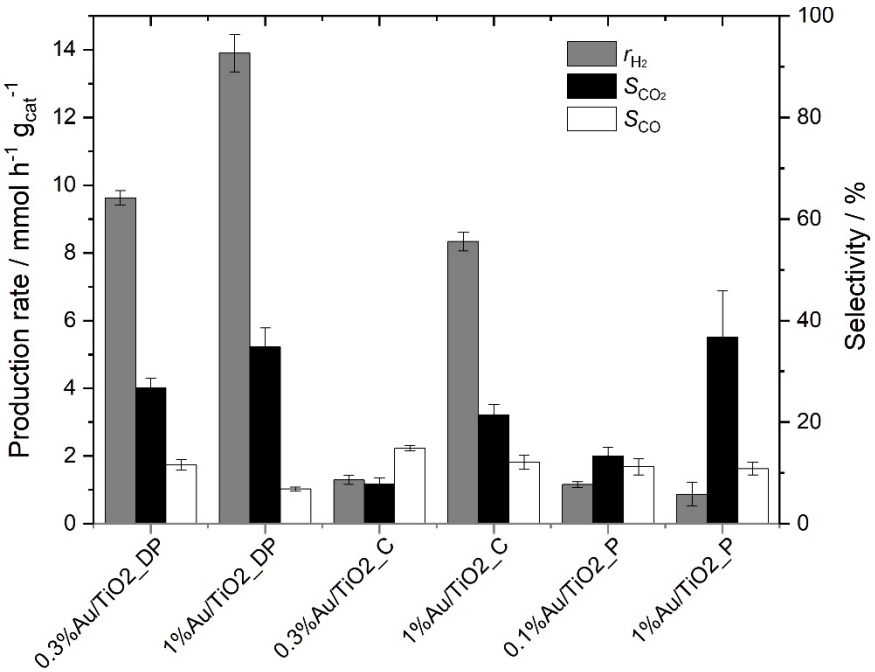

Figure 9.4. *Overview of the rate of hydrogen production and per cent selectivity to CO_2 and CO obtained with the investigated photocatalysts. Specific reaction conditions: 0.014 g of photocatalyst fed in recirculation mode with 40 mL min^{-1} of 2% CH_3OH/3% H_2O/N_2 (balance) gas mixture.*

Because of the better results, both in terms of hydrogen production rate and selectivity towards CO_2 and CO, 1%Au/TiO_2_DP was chosen as reference sample to test the synergistic effect of temperature and light in the methanol steam reforming reaction.

9.7 Determination of products and intermediate species

Besides the main products of the methanol photo-steam reforming, *i.e.* hydrogen, carbon dioxide and carbon monoxide, other gaseous products such as formaldehyde, methane, dimethyl ether and ethane were detected as side-products of the reaction during all photocatalytic tests. Taking 1%Au/TiO_2_DP sample at 40°C as reference, its composition *vs*. time profiles of the recirculating gas during irradiation is displayed in Figure 9.5.

Because of the steady-state conditions, water and methanol do not vary significantly in the course of the photocatalytic test. The concentrations of H_2, CO_2 and CO increase practically linearly with irradiation time, because these products accumulate in the recirculating gas phase, according to a pseudo-zero order rate law, due to the high excess of reactants (water and methanol). By contrast, the amounts of formaldehyde, acetic acid and methyl ether in the gas mixture outcoming from the photoreactor rapidly increase at the beginning of irradiation and then remains practically constant during irradiation. In fact, these species are continuously produced at almost constant rate in the photoreactor, as a consequence of adsorbed methanol oxidation, followed by desorption, and are continuously trapped in the liquid solution by the subsequent gas phase bubbling into it. Formic acid, another intermediate species, is detected in the liquid solution by IC analysis at the end of the runs.

a)

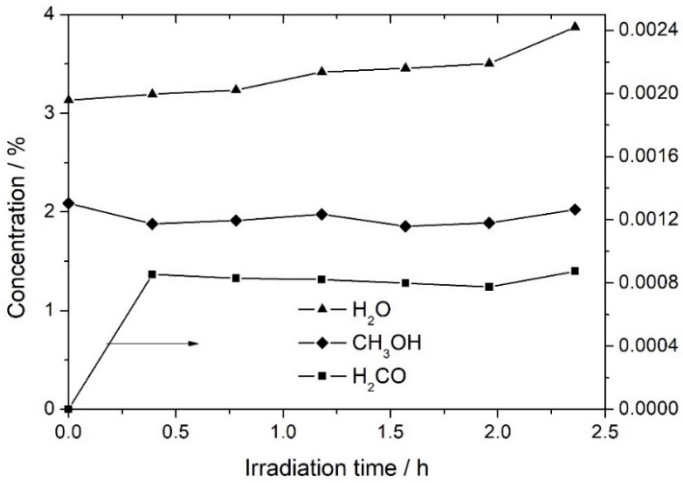

b)

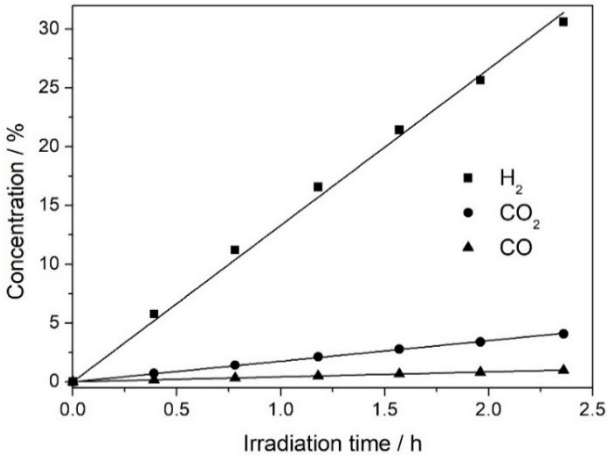

c)

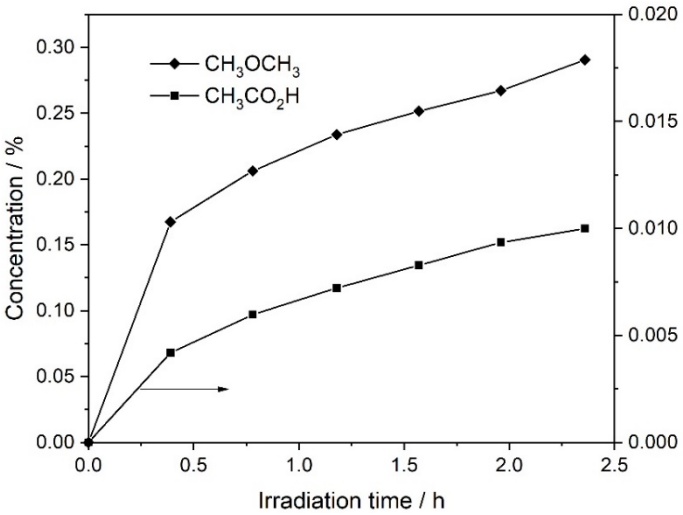

Figure 9.5. *Typical gas-phase composition profiles (concentration expressed in mole percent) during irradiation, in the methanol photo-steam reforming reaction.*

On the basis of the main final oxidation products, by products and intermediate species detected in both gas and liquid phase, the following reaction scheme should be considered:[11,12]

$$CH_3OH \xrightarrow{h\nu,\ TiO_2} H_2CO + H_2 \quad (1)$$

$$H_2CO + H_2O \xrightarrow{h\nu,\ TiO_2} HCO_2H + H_2 \quad (2)$$

$$H_2CO \xrightarrow{h\nu,\ TiO_2} CO + H_2 \quad (3)$$

$$HCO_2H \xrightarrow{h\nu,\ TiO_2} CO_2 + H_2 \quad (4)$$

$$HCO_2H \xrightarrow{h\nu,\ TiO_2} CO + H_2O \quad (5)$$

$$2\,CH_3OH \xrightarrow{h\nu,\ TiO_2} CH_3COOH + H_2 \quad (6)$$

$$2\,CH_3OH \xrightarrow{h\nu,\ TiO_2} CH_3OCH_3 + H_2O \quad (7)$$

According to reaction (7), the formation of dimethyl ether does not contribute to hydrogen production.

The results of the photocatalytic tests performed with different gold-modified TiO_2 photocatalysts are reported in Table 9.1. The rates of H_2, CO_2 and CO production were taken as the slope of the straight lines of the produced amount (normalised per unit catalyst weight) vs. irradiation time plots (see Figure 9.5). The rate of formaldehyde production, r_{H_2CO}, was estimated as the average GC peak area recorded in gas samples collected during irradiation at the exit of the photoreactor, taking into account the flow rate in the recirculating gas. The average rate of formic acid production was estimated as the overall amount accumulated into the liquid solution, determined by IC at the end of the runs, divided by the overall irradiation time and the weight of catalyst, thus assuming a constant production rate during irradiation also for intermediate species.

The selectivity in hydrogen production was also calculated from the rates of H_2CO, HCO_2H, CO or CO_2 formation, as the ratio between the rate of H_2 production from methanol to give one of the four products, by taking into account the stoichiometric coefficients of reactions (1) – (4), and the overall rate of H_2 photoproduction. For example, the selectivity to CO_2 in H_2 production, S_{CO_2}, was calculated as follows:

$$S_{CO_2} = \frac{3 \cdot r_{CO_2}}{r_{H_2}} \cdot 100$$

On the basis of equations (1) – (5), it is possible to define a possible model for methanol oxidation, which is expressed by equation (8).

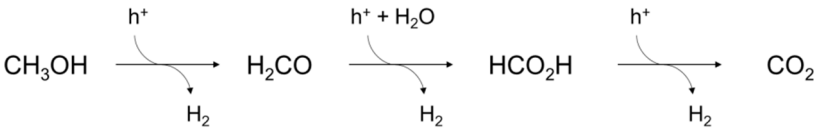

(8)

In this model,[11,12] methanol oxidation occurs through a series of consecutive reactions, obtained by taking into account equations (1), (2) and (4). The remaining reactions (3) and (5) have to be taken into account as parallel reactions with respect to the model expressed in equation (8), in order to explain the production of CO in the gas mixture. Therefore, the proposed mechanism for the methanol oxidation reaction can be expressed as follows:

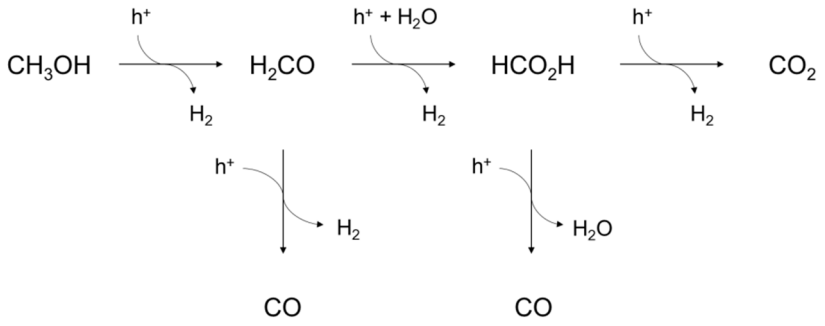

(9)

Therefore, CO is formed either upon formaldehyde dehydrogenation or through formic acid dehydration. Since methanol and water are known to adsorb competitively on the oxide surface, with the formation of surface hydroxyl and methoxy groups, the products of formaldehyde oxidation depend on the probability to have an adsorbed water molecule close to one adsorbed formaldehyde molecule. In any case, whether the oxidation reaction of formaldehyde is parallel (*i.e.* leading to the formation of CO) or consecutive (*i.e.* leading to the formation of HCO_2H), formaldehyde needs to be adsorbed on the oxide surface. In fact, since adsorbed methanol is oxidized through a series of consecutive surface reactions, under steady-state conditions the surface concentration of intermediate species is constant and a competition is established at each step between further oxidation and desorption of the adsorbed intermediate species. In particular, the higher is the desorption rate with respect to the oxidation rate, the higher is the accumulation rate of that intermediate in the gas phase and consequently the lower is the selectivity to CO_2.

9.8 Effects on selectivity of temperature and of deposited Au nanoparticles

Figure 9.6 compares the results of photothermocatalytic methanol steam reforming obtained with 1%Au/TiO_2_DP under dark and under illumination conditions. This figure reports the amounts of hydrogen, carbon dioxide, carbon monoxide and formaldehyde detected in the effluent over the 50-380°C temperature range with a heating ramp of 1°C min^{-1} and flow rate of 9.3 mL min^{-1}. Sampling of the effluent was made in continuum, in order to avoid accumulation of products in the gas phase, so as to investigate the gas phase composition at any time.

No appreciable reaction under dark conditions occur below 250°C, except for a very small production of CO_2, which starts slightly below 200°C. Under irradiation, the concentration profiles change dramatically, as follows: (i) hydrogen content tends to slightly decrease up to around 300°C, and dramatically decreases over this temperature, the same one at which the sole thermal reaction takes place; (ii) the carbon dioxide content decreases up to about 200°C; at this temperature, the thermal process starts and the production under illumination becomes more pronounced; (iii) carbon monoxide production decreases almost linearly up to 220°C; above this temperature, the thermal reaction takes place. Interestingly, its content in the gas phase increases exponentially (following the dark thermal process) up to 300°C and, at higher temperatures, the production rate becomes slower; (iv) formaldehyde production increases up to 270°C, and it decreases at higher temperatures with almost no contribution from the dark thermal process.

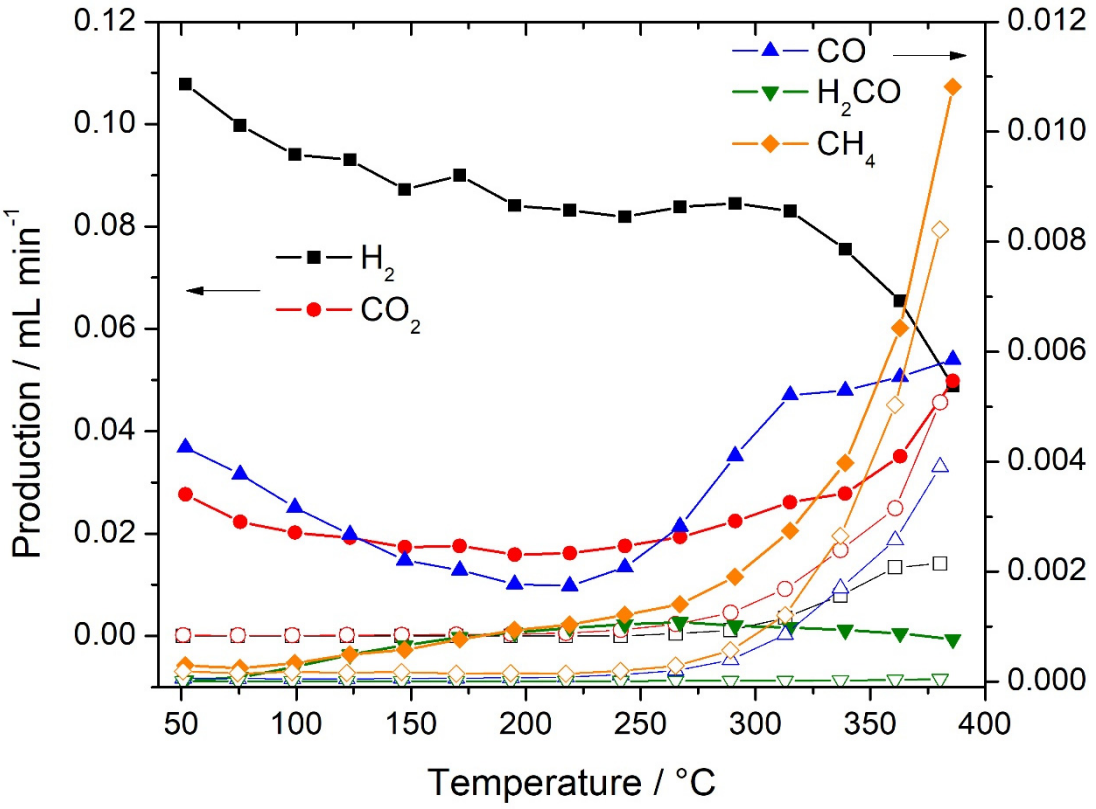

Figure 9.6. *Production trend of the gaseous products at different temperatures. Solid lines with filled symbols represent analysis under irradiation, while dashed lines with open symbols represent analysis in absence of irradiation.*

Clearly, there is a transition from a photothermal-catalysed reaction to a thermal-catalysed one, which occurs close to the inflection point of the hydrogen, carbon monoxide and formaldehyde production. In particular, these trends are opposite with respect those observed under dark conditions, indicating that under irradiation at such high temperature the reaction follows a completely different path.

Table 9.1 reports the selectivity trends for the photocatalyst in continuum under irradiation. Although the mass balance does not take into account formic acid production (which accumulates in the liquid phase), it can be seen that the selectivity towards CO_2 is enhanced, with a 2.2-fold increase. This can be ascribed to the low

flow rate adopted in continuum (9.3 mL min^{-1}), which increases the contact time between the methanol/water solution and the photocatalyst.

Table 9.1. *Methanol oxidation selectivity trends as a function of temperature.*

Temperature [°C]	S_{CO_2} [%]	S_{CO} [%]	S_{H_2CO} [%]
51.8	76.8	7.9	0.0
75.6	67.2	7.6	0.1
99.5	64.4	6.7	0.3
123.4	61.9	5.8	0.5
147.3	59.6	5.1	0.8
171.2	58.5	4.5	0.9
195.1	56.7	4.2	1.1
219.1	58.2	4.2	1.2
243.1	64.4	5.1	1.3
267.1	69.0	6.7	1.3
291.1	79.6	9.7	1.2
315.0	94.4	12.6	1.2
339.0	110.4	14.0	1.2
362.9	160.9	16.9	1.3
385.9	306.4	24.0	1.6

Moreover, S_{CO_2} over 300°C exceeds the limit of 100%. This could imply the fact that there is an accumulation of carbonaceous species on the photocatalyst surface, which are released above 300°C.

The methanol steam reforming reaction under photothermocatalytic conditions at fixed temperature was investigated in the recirculation mode, *i.e.* by accumulating the products in the gas phase. For this study, four different temperatures, *i.e.* 40, 100, 150 and 200°C were selected. Results, in terms of production rates of hydrogen, carbon dioxide and carbon monoxide, as well as in terms of selectivity towards methanol oxidation with respect to hydrogen production, are given in Figure 9.7 and Table 9.2.

Table 9.3. *Photocatalytic performance of 1%Au/TiO_2_DP photocatalyst in methanol photo-steam reforming at different temperatures, in terms of production rate and per cent selectivity with respect to hydrogen production. Reaction conditions: 0.015 g of photocatalysts fed in recirculation mode with 60 mL min^{-1} of a 2% CH_3OH/3% H_2O/N_2 (balance) gas mixture.*

Sample	Production rate [mmol h^{-1} g_{cat}^{-1}]					Selectivity with respect to H_2 production [%]			
	H_2	CO_2	CO	H_2CO	HCO_2H	CO_2	CO	H_2CO	HCO_2H
40°C	20.84	2.91	0.70	5.14	1.40	42.0	6.8	24.6	13.4
100°C	20.62	1.75	0.37	11.67	0.63	25.4	3.6	56.5	6.1
150°C	18.87	0.88	0.15	13.89	0.35	14.0	1.7	73.7	3.7
200°C	14.37	0.37	0.07	12.83	0.19	7.7	1.0	89.3	2.6

The rate of hydrogen production, r_{H_2}, tends to decrease as the temperature increases, as reported in Figure 9.7a. At the same time, the amounts of carbon dioxide and carbon monoxide in the gas phase decrease, although at this stage a precise evaluation cannot be done.

The selectivity results in methanol oxidation reported in Figure 9.7b, confirm the results obtained in continuum mode. In fact, the selectivity towards formaldehyde increases with increasing temperature, while the selectivity towards carbon monoxide and carbon dioxide decreases.

Bare P25 TiO_2 was found to have low performance at 40°C, with a very high S_{CO} value, even higher than S_{CO_2} (18% vs. 11%),[11] while 1%Au/TiO_2_DP, under the same conditions, exhibits a S_{CO} value which is 2.6 times lower than that of P25 TiO_2 (see Table 9.2). At the same time, S_{CO_2} is higher for 1%Au/TiO_2_DP, with a 3.8 times higher selectivity towards CO_2 with respect to P25 TiO_2. Therefore, the presence of gold nanoparticles on TiO_2 enhances the separation between the photopromoted charges in the photocatalyst, and this is reflected not only in the reduction path leading to hydrogen production, but also in the photocatalytic methanol oxidation to CO_2.

a)

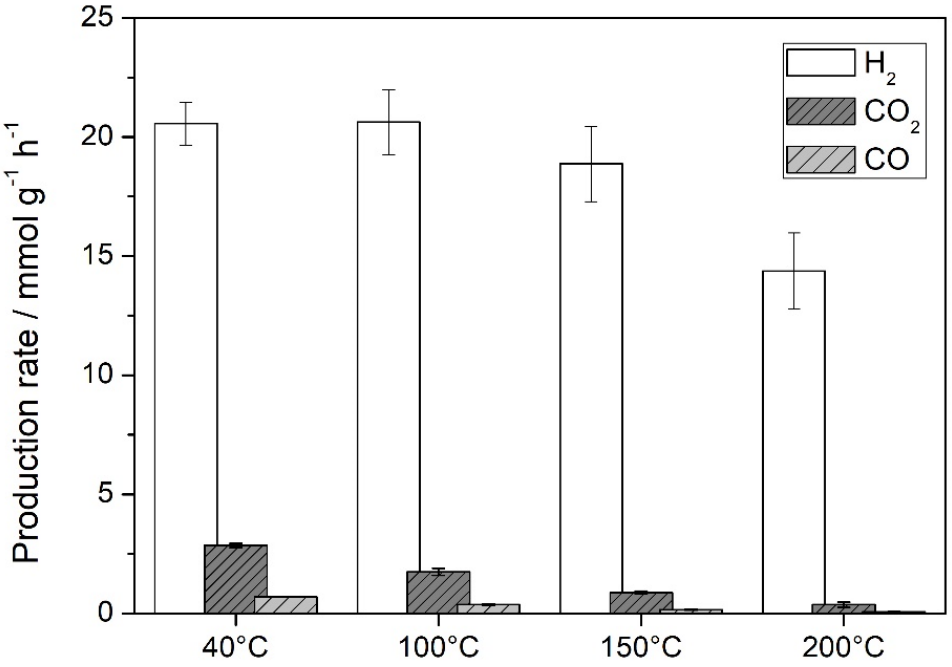

b)

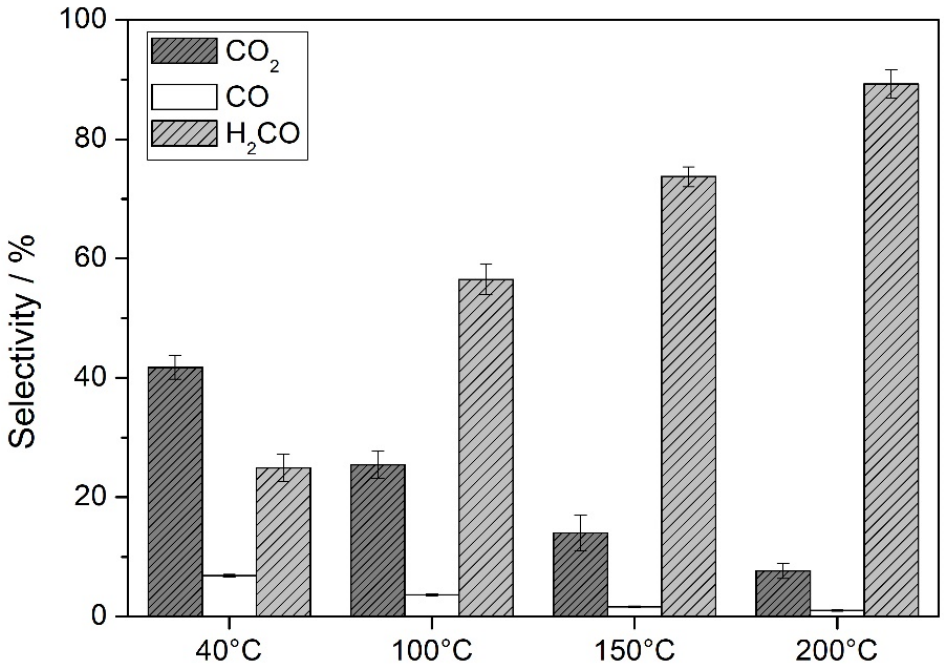

Figure 9.7 *Production rate (a) and selectivity (b) to oxidation products with respect to hydrogen production vs. temperature.*

With increasing temperature, both S_{CO_2} and S_{CO} decrease reaching minimum values of 7.7% and 1.0%, respectively, at 200°C, while S_{H_2CO} constantly increases up

to almost 90%. These evidences imply that methanol oxidation is far from being complete. At the same time, the parallel reactions producing CO either from H_2CO or from HCO_2H are inhibited as well. Moreover, the selectivity towards H_2CO increases, while S_{HCO_2H} drops 5 times from 40°C to 200°C.

These evidences can be explained in the light of the mechanism reported in equation 9 and of the adsorption/desorption equilibria involving intermediate species. In particular, H_2CO, which is the first oxidation product of methanol, at higher temperature tends to desorb easier from the oxide surface, thus limiting the amount of formaldehyde that can be successively oxidized on the photocatalyst surface. Under the reasonable assumption that the main reaction pathway for CO production is the one expressed by equation 5, *i.e.* through formic acid dehydration,[12] the drop of S_{CO} can be easily explained, since also S_{HCO_2H} is dramatically reduced with increasing temperature. Therefore, the temperature increase leads to an incomplete methanol oxidation to CO_2, but at the same time lowers the CO content, which could be beneficial for fuel cells applications. Indeed, CO is the most undesired by-product, since it is well recognized that it poisons the Pt-based catalysts, largely employed in this technology.

Since the production rate of hydrogen tends to decrease with increasing temperature in the recirculation mode, a stability test of freshly prepared materials was performed at two different temperatures under continuum mode, in order to rule out any contribution from the accumulation of by-products in the photoreactor.

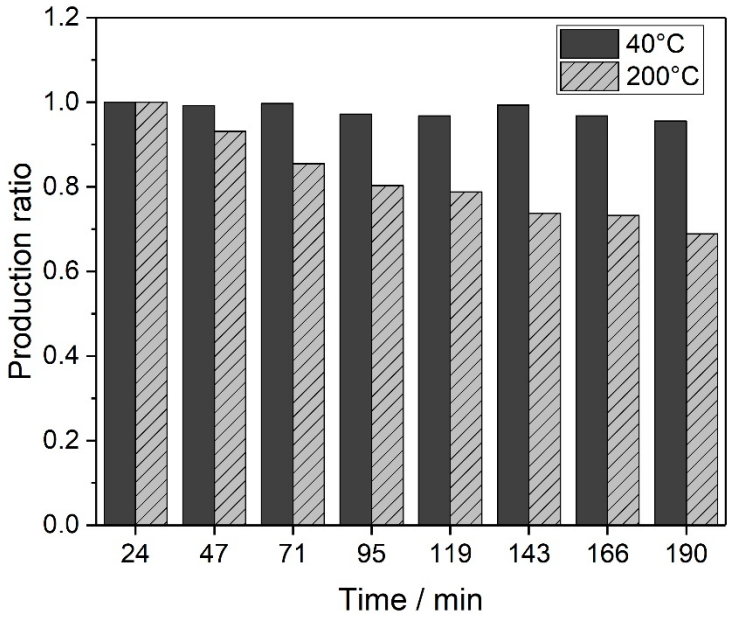

Figure 9.8. *Hydrogen production ratio over time at different temperatures.*

As shown in Figure 9.8, the photoactivity towards hydrogen production decreases at 200°C while it remains reasonably stable over 3 hours. A possible explanation for the photocatalyst performance drop could be the accumulation of carbonaceous species, which tend to poison the photocatalyst, unless they are removed with high temperature treatment (see section 9.8 and table 9.1). Another possible explanation could be the sintering of the gold nanoparticles, although this can hardly occur at this relatively low temperature. A possible confirmation analysis could be provided by electronic microscopy analysis, such as SEM and TEM, of the used photocatalyst. Unfortunately, this could not be done, because the photocatalyst dispersion on quartz grains is irreversible.

9.9 Conclusions

Among different gold modified TiO_2 photocatalysts, the DP-made ones with a 1% nominal amount of gold nanoparticles resulted to be best performing in photo-steam

reforming of methanol, in terms of both hydrogen production rate and selectivity to CO and CO_2. With increasing temperature, the selectivity towards CO and CO_2 dropped, whereas the selectivity towards H_2CO increased, due to the high desorption rate of formaldehyde from the oxide surface, which limits its further oxidation on the photocatalyst surface. Even though an incomplete methanol oxidation is attained under high temperature, the decrease of CO content of the gas phase could be beneficial when hydrogen is photocatalytically produced for fuel cell applications.

REFERENCES

[1] Fujishima, A.; Honda, K. *Nature* **1972**, *238*, 37.

[2] Wu, W.-C.; Yang, S.-J.; Ho, C.-H; Lin, Y.-S.; Liao, L.-F.; Lin, J.-L. *J. Phys. Chem. B*, **2006**, *110*, 9627.

[3] Wang, X.; Zeng, D.; Xie, C., *Mat. Lett.*, **2015**, *139*, 336.

[4] Zheng, Y., Wang, W.; Jiang, D.; Zhang, L. *Chem. Eng. J.*, **2016**, *284*, 21.

[5] Tan, T. H.; Ng, Y. H.; Taylor, R. A.; Auguey-Zinsou, K.-F.; Amal, R. ACS catal., 2016, 6, 1870.

[6] Haruta, M. *Catal. Today*, **1997**, *36*, 153.

[7] Liu, J. H.; Wang, A. Q.; Chi, Y. S.; Lin, H. P.; Mou, C. Y. *J. Phys. Chem. B*, **2005**, *109*, 40.

[8] Bernareggi, M; Dozzi, M. V.; Bettini, L. G.; Ferretti, A. M.; Chiarello, G. L.; Selli, E. *Catalysis*, **2017**, *7*, 301.

[9] Alvarez, M. M.; Khoury, J. T.; Schaaff, T. G.; Shafigullin, M. N.; Vezmar, I.; Whetten, R. L. *J. Phys. Chem. B*, **1997**, *101*, 3706.

[10] Dozzi, M. V.; Prati, L.; Canton, P.; Selli, E. *Phys. Chem. Chem. Phys.*, **2009**, *11*, 7171.

[11] Chiarello, G. L.; Ferri, D.; Selli, E. *J. Catal.*, **2011**, *280*, 168

[12] Chiarello, G. L.; Aguirre, M. H.; Selli, E. *J. Catal.*, **2010**, *273*, 182.

Chapter 10

10.1 Conclusions

The aim of this work was to explore the photocatalytic properties of new materials (Chapters 3, 5 and 7) and to evaluate the effect of temperature in a photocatalytic reaction (Chapter 9). In all cases, important results were achieved and the following conclusions were drawn.

10.2 The Ni-bisdipyrrinato complex as potential sensitizer

A Ni-based bisdipyrrin metalloligand was synthesized and, for the first time in literature, it has been thoroughly characterized from a spectroscopic, electrochemical and photoelectrochemical point of view. Moreover, this molecule proved to be suitable to act as a photosensitizer for TiO_2-based systems. This was made possible by the high energy LUMO of the synthesized, in contrast to similar complexes carrying single dipyrrin ligand moieties. The functional aspects of this molecule were investigated

through electrochemical and photoelectrochemical studies. These investigations provided ample evidence for the usability of the metalloligand as photosensitizer, albeit the typical dependence from surface-adsorption conditions were discussed as well. This is indeed the first report on the use of bisdipyrrin complexes in a functional set-up and the obtained data from this first-principle study as well as the now good availability of such sophisticated metal complexes may well impact future developments of these compounds in the topical fields of photoelectrocatalysis and small molecule activation.

The photosensitizer was also successfully implanted into the UiO-66 framework with the aid of the mixed ligands one pot synthetic technique, which was preceded by just one report in the literature with hard Lewis acid metal cation (*i.e.* Zr^{IV}).

10.3 The porphyrin-containing Zr-based MOF series

Two series of isoreticular porphyrin-containing Zr-based MOFs have been investigated as potential photocatalysts for carbon dioxide reduction. The results show that carbon dioxide reduction is not a feasible process employing the tested materials. In the case of the UiO-66-NH_2 doped series, no reduction product has been detected through GC analysis, but the framework proved to be stable under the adopted photocatalytic conditions. In the case of the PCN-222(M) series, the framework underwent collapse in the photocatalytic conditions. All samples have been systematically characterized spectroscopically, in order to better understand the dynamics of the excited states. The intriguing result that has been obtained from this analysis is that the geometry disposition of the porphyrin ligands in the framework affects their electronic properties. In particular, with NiTCPP, there is a growth in the luminescence signal upon insertion of the ligand in the frameworks. Indeed, from a

non-luminescence behaviour as free ligand, the PCN-222(Ni) MOF proved to have the most intense excitation and emission spectra. On the other hand, in the case of CuTCPP, there is a progressive shift from a pure phosphorescence emission signal as a free ligand to a pure fluorescent one in the PCN-222(Cu) structure. It is worth noting that this behaviour has never been reported in any porphyrin-based MOF before.

10.4 $CuWO_4$ as water oxidation photocatalyst

A W-based photoanode, $CuWO_4$, has been thoroughly investigated as potential candidate for water oxidation reaction. Although this material has been known since the ‘80s, few reports are present in the literature and a systematic analysis of its photocatalytic properties and performances still misses. In our investigation, we successfully synthesized multilayers of optically transparent thin film of $CuWO_4$ by a citrate-based solution method. These photoelectrodes were tested under front- and backside irradiation and their performance as a function of the light intensity was evaluated as well. Similarly to $BiVO_4$, this material showed higher efficiencies at low light intensity and showed electron transport as limiting factor. On the other hand, differently from $BiVO_4$, this W-based photoanode did not display any drop of performance at high light intensities and showed excellent water oxidation kinetics with almost square transient photocurrent response in the absence of a hole scavenger in the solution. Indeed, experiments either with H_2O_2 or with WOC, did not display any enhancements of photoactivity, thus revealing the bulk recombination of photogenerated carriers as main critical issue of the material.

10.5 The effects of Au nanoparticles and temperature in methanol photosteam reforming reaction

The possible synergistic effect of gold nanoparticles deposited onto TiO_2 and temperature on the methanol photosteam reforming reaction have been investigated. Three different methodologies for nanoparticles deposition onto TiO_2 were compared and the best sample, in terms of hydrogen production rate and carbon dioxide selectivity, has been tested at different temperature. From the kinetic tests performed in continuum and in the recirculation mode, it is evident that the selectivity towards carbon dioxide and carbon monoxide decreases with increasing temperature, while the selectivity towards formaldehyde increases. These results are in line with the proposed methanol oxidation reaction mechanism, in which temperature plays a role on the equilibria of the intermediate species. Although the oxidation at high temperature is incomplete because of the lower carbon dioxide selectivity, at the same time the carbon monoxide content in the effluent gas phase is decreased. This, in turn, could be beneficial when hydrogen is photocatalytically produced for fuel cell application.

10.6 Future perspectives

Although Metal Organic Frameworks are compounds of remarkable interest, they still need a deep investigation in order to gain further insight in their potential photocatalytic action. In fact, although this class of materials is able to harvest a significant part of the solar spectrum, the yield of thermodynamically up-hill reactions such as carbon dioxide and water reduction is still around one order of magnitude lower

than that of “classical” semiconductor photocatalysts. Therefore, this field is not fully explored yet, and surely deserves more attention.

Regarding $CuWO_4$, a successful strategy to improve its photocatalytic activity may consist in modifying its crystal structure through metal ion doping, in order to reduce bulk recombination of photogenerated charges. Moreover, since the electron transport is a limiting factor, heterojunction systems in which electron transport is enhanced, for example with WO_3, are a valuable choice, as preliminary results in literature already report.

The study of the effect of temperature over the methanol photosteam reforming reaction could be performed with other noble metal nanoparticle-modified TiO_2. In fact, although Au has proved to be “innocent” towards temperature effect, other metals, such as Pt and Ag, may have a different behaviour at high temperature, thus modifying the oxidation pathway.

APPENDIX A
SUPPLEMENTARY INFORMATION FOR CHAPTER 2

SYNTHESIS OF dpmCOOMe

Ligand **dpmCOOMe** was synthesized in a two-steps synthesis, as shown below.

STEP 1

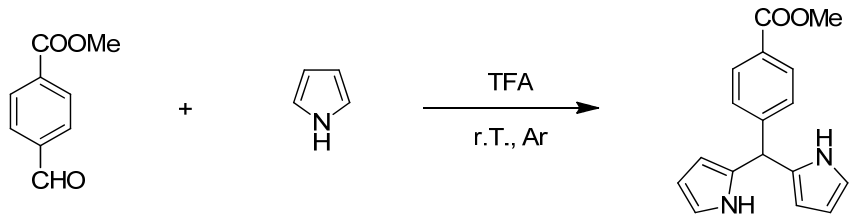

A B C

Chemicals	MW (*g/mol*)	m (m*g*)	n (*mmol*)	Equiv.	d (*g/mL*)	V (*mL*)
A	164.16	4000.0	24.37	1		
B	67.09	67.69	1000.0	41	0.967	70
C	280.32	2900.0	10.35			

Lit. Ref. *Inorg. Chim. Acta, 1997, 263, 279-286 (modified)*

Procedure:

Pyrrole (70 mL, 1 mol, 41 equiv., prior filtered over Al_2O_3 pad)was introduced in a 2-neck 250 mL round bottomed flask and then reagent A (4.0 g, 24.37 mmol, 1 equiv.).

The flask was flushed continuously with Ar. After covering the flask with an Al foil, few drops of TFA were added.

The reaction mixture was left under stirring at room temperature for about 3 h.

The excess of pyrrole was distilled off and the crude suspended in Et_2O and filtered.

The white solid was then dried via Schlenk line to remove any trace of Et_2O and pyrrole.

Yield = 42.5 % (2.90 g)

Characterization:

^1H NMR (300 MHz, $CDCl_3$) d: 3.91 (s, 3H); 5.53 (s, 1H); 5.89 (m, 2H); 6.17 (dd, J = 2.8, 6.0 Hz, 2H); 6.72 (td, J = 1.6, 2.6, 2H); 7.29 (d, J = 8.2, 2H); 7.98 (m, 4H).

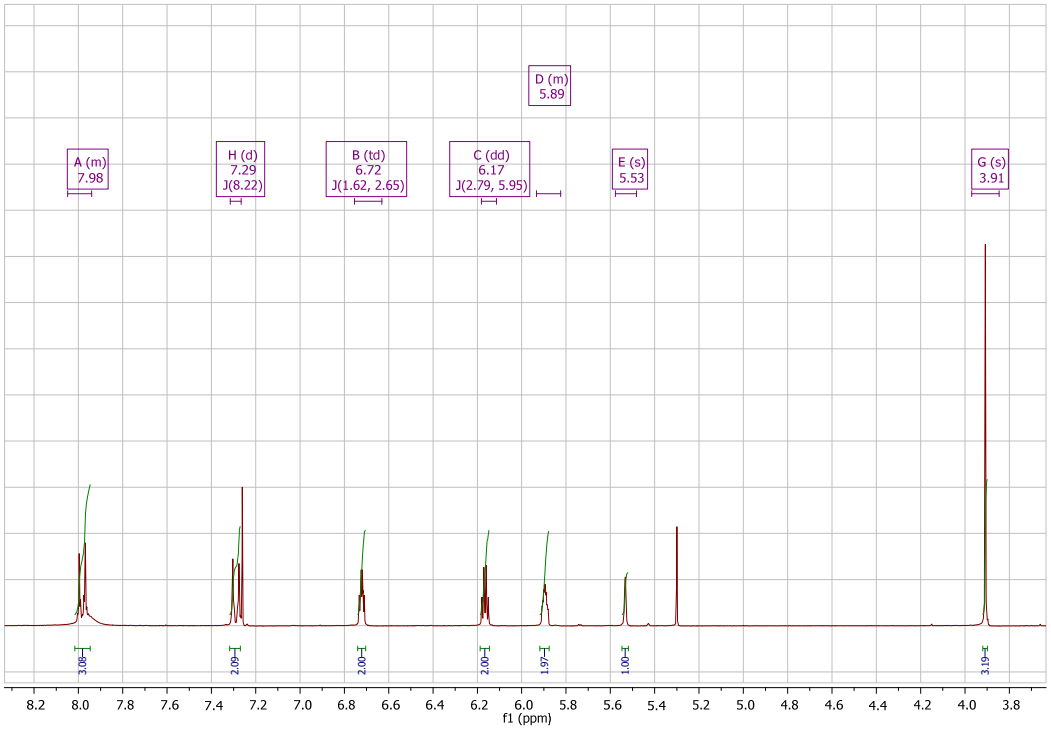

Figure A1. *^1H NMR of the intermediate product.*

STEP 2

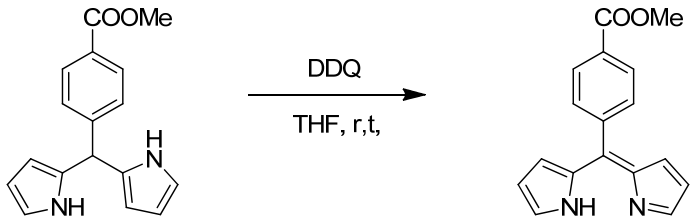

A B

Chemicals	MW (*g/mol*)	m (m*g*)	n (*mmol*)	Equiv.	d (*g/mL*)	V (*mL*)
A	280.32	2900.0	10.35	1		
DDQ	227.00	2590.0	11.38	1.1		
B	278.31	2360.5	8.48			
Solvents						
THF						450 + 250

Lit. Ref. *Inorg. Chim. Acta, 1997, 263, 279-286 (modified)*

Procedure:

In a 2 L flask, reagent A (2.90 g, 10.35 mmol) was dissolved in 450 mL of THF. Then, a solution of 2,3-Dichloro-5,6-dicyano-1,4-benzoquinone (DDQ, 2.59 g, 11.38 mmol) in 250 mL of THF was added dropwise. Reaction mixture was left to react overnight at room temperature. The crude was purified by means of column chromatography (SiO_2, $CHCl_3$ + 1% Et_3N).

Yield = 2.36 g (82%)

Characterization:

^{1}H NMR (300 MHz, $CDCl_3$), δ: 8.12 (d, J = 8.4 Hz, 2H), 7.66 (t, J = 1.3 Hz, 2H), 7.57 (d, J = 8.4 Hz, 2H), 6.53 (dd, J = 1.1, 4.2 Hz, 2H), 6.40 (dd, J = 1.5, 4.2 Hz, 2H), 3.97 (s, 3H).

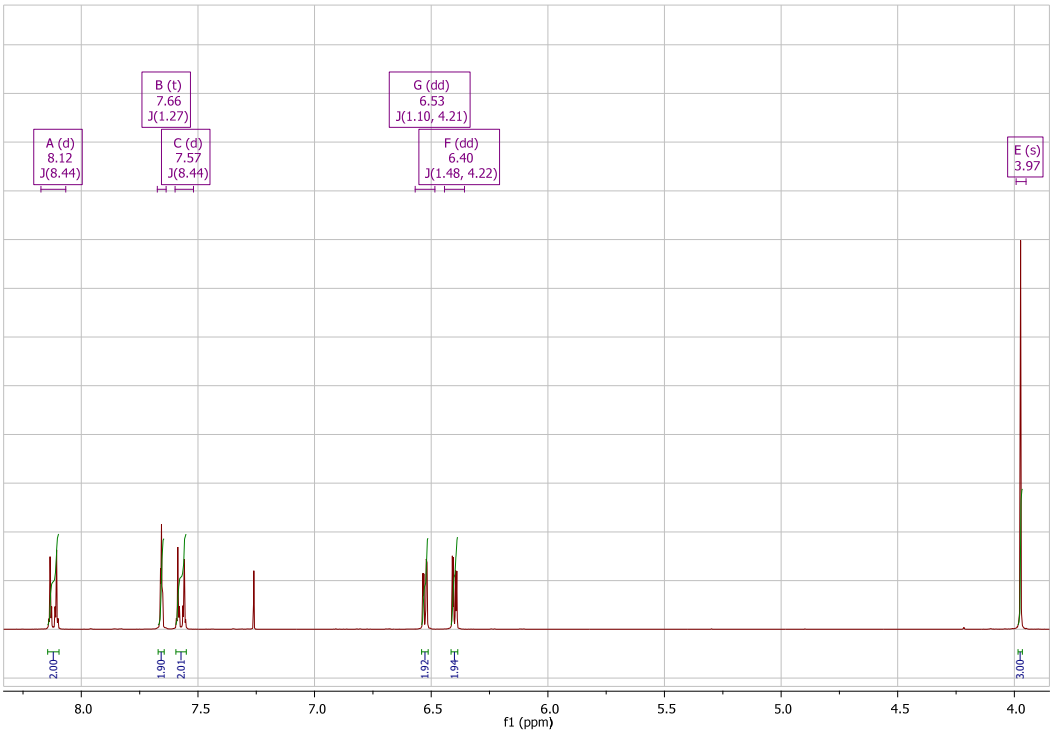

Figure A2. *^{1}H NMR of Ligand dpmCOOMe.*

SYNTHESIS OF Pd(dpmCOOMe)$_2$

A C

Chemicals	MW (*g/mol*)	m (mg)	n (*mmol*)	Equiv.	d (*g/mL*)	V (*mL*)
A	278.31	559.0	2.009	2		
B	224.51	225.0	1.002	1		
TEA						0.5
C	661.01	572.0	0.865			
Solvents						
MeOH						160

Lit. Ref. *Dalton Trans. 2010, 39, 437-445 (modified)*

Procedure:

Reagent A (559.0 mg, 2 mmol), $Pd(OAc)_2$ (225.0 mg, 1 mmol) and TEA (0.5 mL) were combined in MeOH (160 mL) and stirred at room temperature for 3 h.

The suspension was then filtered and washed with cyclohexane.

Yield = 572.0 mg (86.5%)

Characterization:

^{1}H NMR (300 MHz, $CDCl_3$) δ: 8.17 (d, J = 8.4 Hz, 4H), 7.66 (d, J = 8.3 Hz, 4H), 7.41 (t, J = 1.4 Hz, 4H), 6.65 (dd, J = 1.2, 4.35 Hz, 4H), 6.38 (dd, J = 1.6, 4.4 Hz, 4H), 3.99 (s, 6H)

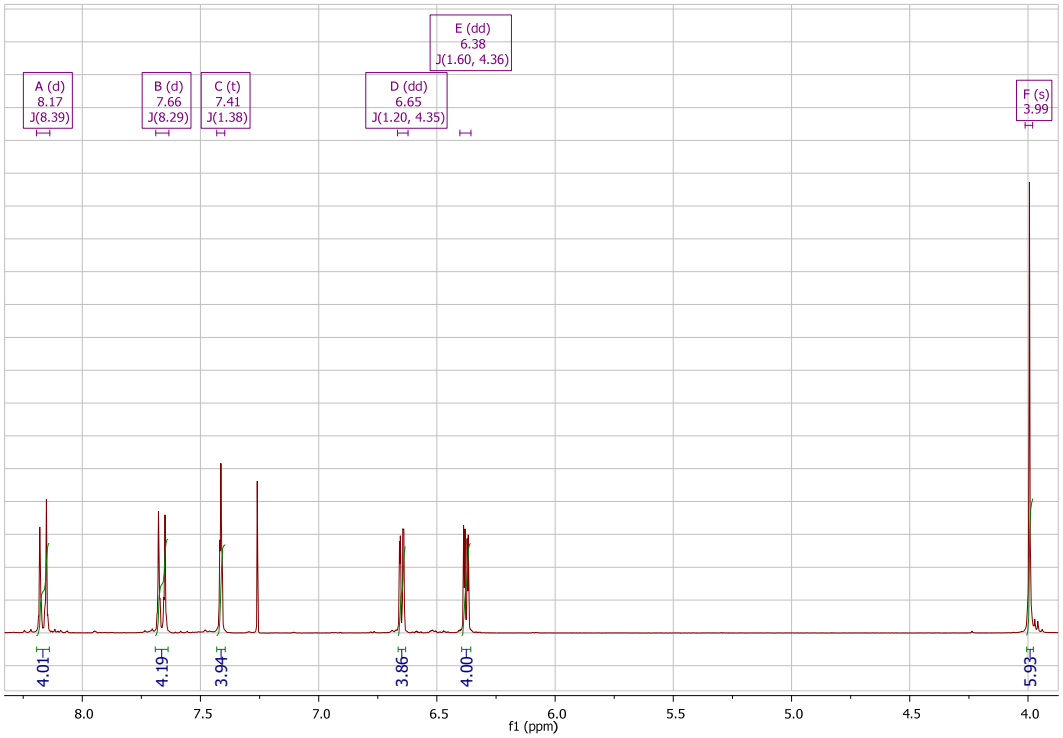

Figure A3. *^{1}H NMR of metalloligand $Pd(dpmCOOMe)_2$.*

SYNTHESIS OF $Pd(dpmCOOH)_2$

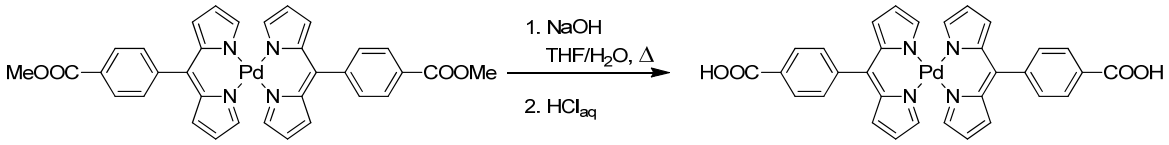

A B

Chemicals	MW (*g/mol*)	m (mg)	n (*mmol*)	Equiv.	d (*g/mL*)	V (*mL*)
A	661.01	250	0.378			
NaOH 1M						50
B	632.96	237.0	0.374			
Solvents						
THF						50

Lit. Ref. *Dalton Trans. 2010, 39, 437-445*

Procedure:

Reagent A (250.0 mg, 0.378 mmol) was suspended in a mixture of THF and aqueous NaOH (50 mL each). The reaction mixture was refluxed overnight.

After cooling down to room temperature, the mixture was acidified with HCl until no further precipitate was detected.

The product was filtered, washed with water and dried.

Since in the ^1H NMR spectrum there were some impurities, the product was refluxed again in the solvent mixture for additional 4 h. After cooling down, the mixture was filtered and the solid discarded. The filtrate was then acidified and solid collected.

Yield almost quantitative.

Characterization:

1H NMR (300 MHz, DMSO-d_6) δ: 13.18 (bs, 2H), 8.10 (d, J = 8.2 Hz, 4H), 7.70 (d, J = 8.25 Hz, 4H), 7.38)s, 4H), 6.63 (dd, J = 1.0, 4.3 Hz, 4H), 6.49 (dd, J = 1.5, 4.4 HZ, 4H).

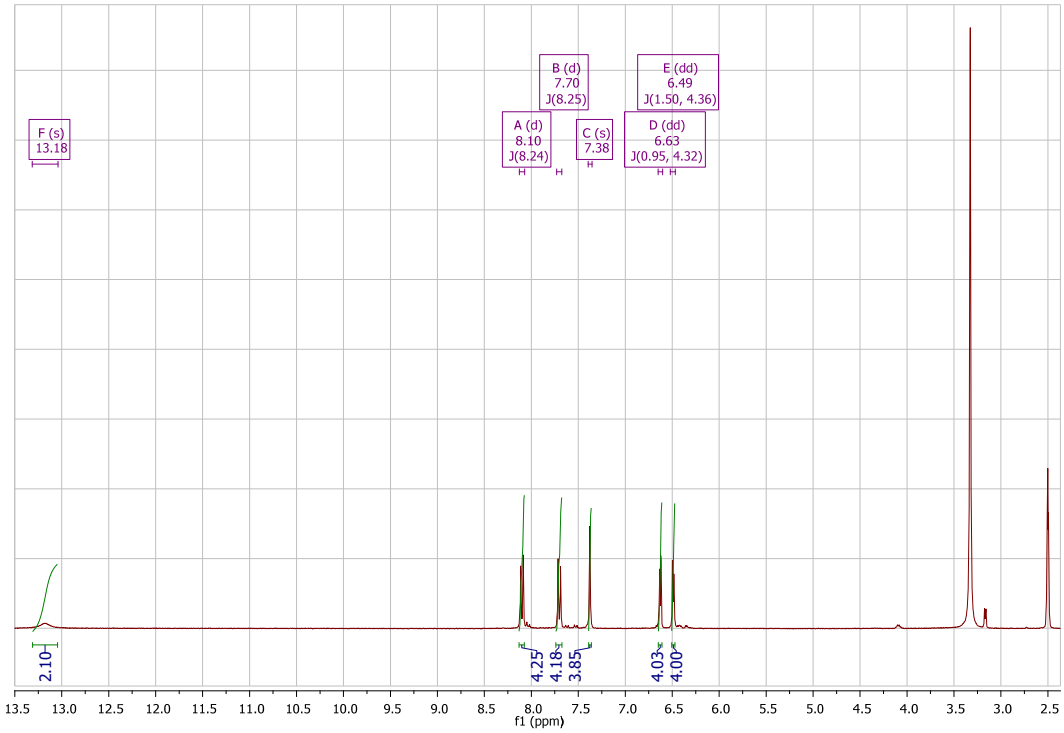

Figure A4. *^{1}H NMR of metalloligand Pd(dpmCOOH)$_2$.*

SYNTHESIS OF Ni(dpmCOOMe)$_2$

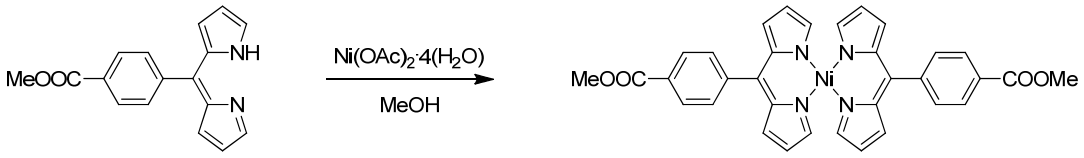

A B

Chemicals	MW (*g/mol*)	m (mg)	n (*mmol*)	Equiv.	d (*g/mL*)	V (*mL*)
A	278.31	300.0	1.08	1		
$Ni(OAc)_2{\cdot}4H_2O$	248.84	140.0	0.56	0.5		
B	613.29	182.0	0.297			
Solvents						
MeOH						230

Lit. Ref. *Cryst. Eng. Comm., 2011, 13, 7149*

Procedure:

$Ni(OAc)_2{\cdot}4H_2O$ (140.0 mg, 0.56 mmol) was added to a solution of A (300.0 mg, 1.08 mmol) in MeOH (230 mL) and the mixture was magnetically stirred at room temperature overnight.

The solvent was evaporated and the crude dissolved in the minimum amount of $CHCl_3$. MeOH was added and $CHCl_3$ was evaporated at reduced pressure, thus obtaining green dichroic microcrystals with metallic lustre, which were filtered and dried.

Yield = 182.0 mg (53%)

Characterization:

^{1}H NMR (300 MHz, $CDCl_3$), δ: 10.25 (s, 4H), 8.07 (d, J = 8.1 Hz, 4H), 7.93 (d, J = 3.6 Hz, 4H), 7.45 (d, J = 8.1 Hz, 4H), 6.69 (d, J = 4.0 Hz, 4H), 3.96 (s, 6H)

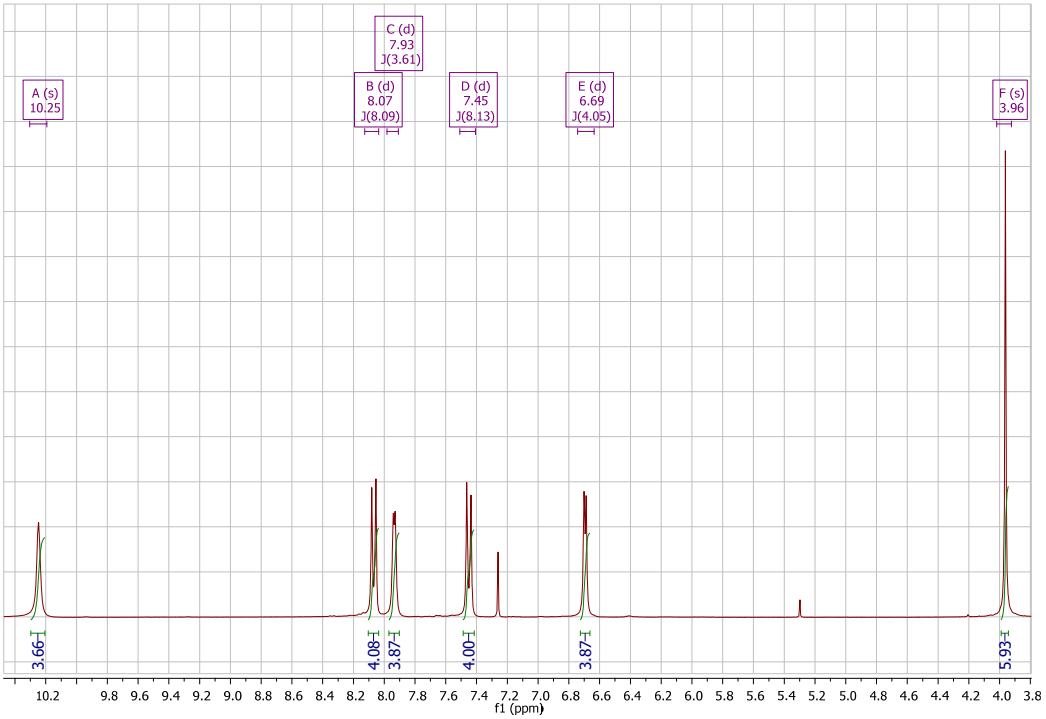

Figure A5. *^{1}H NMR of metalloligand Ni(dpmCOOMe)$_2$.*

SYNTHESIS OF Ni-bisdpmCOOMe

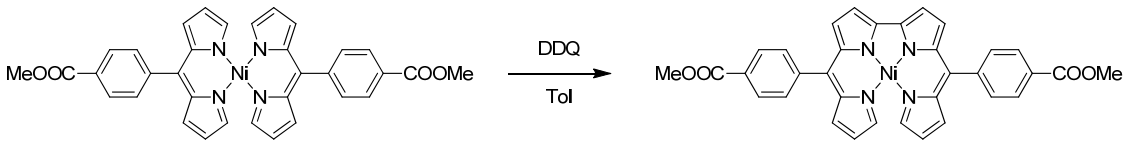

A C

Chemicals	MW (*g/mol*)	m (m*g*)	n (*mmol*)	Equiv.	d (*g/mL*)	V (*mL*)
A	613.29	306.0	0.50	1		
DDQ	227.0	125.3	0.55	1.1		
C	611.27	232.0	0.38			
Solvents						
Tol						90

Lit. Ref. *Chem. Comm. 2015, 51, 5906-5909*

Procedure:

DDQ (125.3 mg, 0.55 mmol) was added in small portions to a toluene solution of complex A (306.0 mg, 0.50 mmol in 90 mL). Upon heating at reflux overnight, mixture turned from red to brown.

TCL showed that the reaction was not complete after one night, therefore 10% more of DDQ was added and the reaction was kept under reflux for additional 5 h.

After cooling down, the solvent was evaporated and the crude purified by means of column chromatography (SiO_2, $CHCl_3$).

Yield = 232.0 mg (76%)

Characterization:

^{1}H NMR (300 MHz, $CHCl_3$) δ: 8.15 (d, J = 8.3 Hz, 4H), 7.64 (d, J = 8.3 Hz, 4H), 6.74 (dd, J = 1.1 Hz, 4.4 Hz, 2H), 6.68 (d, J = 4.4 Hz, 2H), 6.64 (d, J = 4.4 Hz, 2H), 6.45 (dd, J = 1.5 Hz, 4.4 Hz, 2H), 5.96 (t, J = 1.2 Hz, 2H), 3.99 (s, 6H)

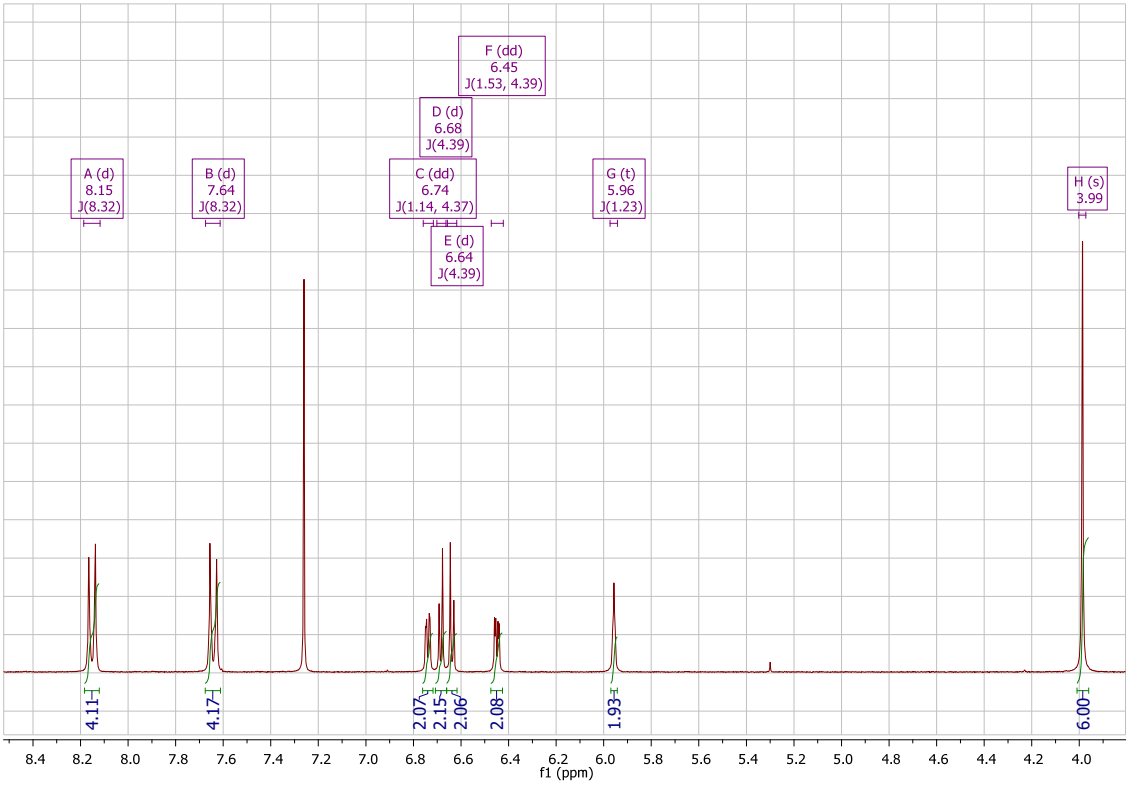

Figure A6. *^{1}H NMR of metalloligand Ni-bisdpmCOOMe.*

SYNTHESIS OF Ni-bisdpmCOOH

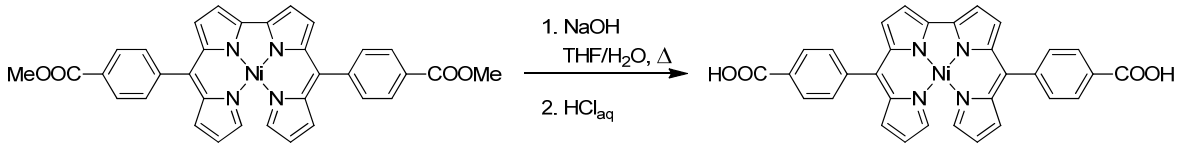

A C

Chemicals	MW (*g/mol*)	m (m*g*)	n (*mmol*)	Equiv.	d (*g/mL*)	V (*mL*)
A	611.27	100.0	0.164			
NaOH 1M						15
C	583.22	69.6	0.119			
Solvents						
THF						15
H_2O						5

Lit. Ref. *Tetrahedron Lett. 2010, 51, 1269-1272 (modified)*

Procedure:

Reagent A (100.0 mg, 0.164 mmol) was dissolved in a mixture of THF, NaOH 1 M and H_2O (15 + 15 + 5 mL, respectively) and refluxed overnight.

After cooling down to room temperature, THF was removed at reduced pressure and H_2O phase carefully acidified with diluted HCl until neutral pH (actually pH = 6.5 or 6). The suspension was filtered and the powder recovered and washed with H_2O and dried in the oven.

Yield = 69.6 mg (72.5%)

Characterization:

^{1}H NMR (300 MHz, DMSO-d_6) δ: 8.09 (d, J = 8.1 Hz, 5H[1]), 7.69 (d, J = 8.1 Hz, 5H), 6.83 (d, J = 4.2 Hz, 2H), 6.74 (d, J = 4.4 Hz, 2H), 6.71 (d, J = 4.2 Hz, 2H), 6.56 (d, J = 4.2 Hz, 2H), 6.02 (s, 2H)

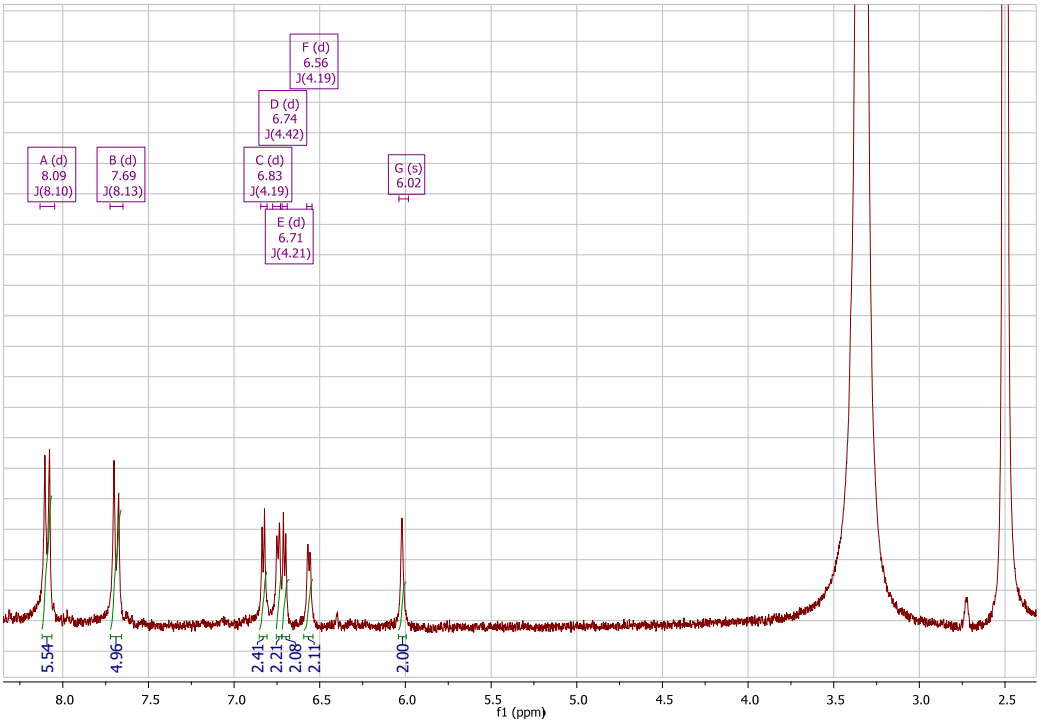

Figure A7. *^{1}H NMR of metalloligand Ni-bisdpmCOOH*

[1] Since the solution is very diluted due to solubility issues of the compound, the proton integration is hampered. Anyway, the absence of the peak of the ester and the reduced solubility are a proof of the fact that Ni(II) is preserved inside the free-acid structure.

MOF STRUCTURES

UiO-66

$ZrCl_4$ (30 mg, 0.129 mmol), terephthalic acid (BDC, 30 mg, 0.180 mmol) and benzoic acid (500 mg, 4.094 mmol) were ultrasonically dissolved in 3 mL of DMF in a Pyrex vial. The mixture was heated in an oven at 85°C for 24 h. After cooling down to room temperature, a white powder was collected by centrifugation. The solid was washed with DMF three times to remove unreacted precursors, and then solvent-exchanged with acetone three times. The resulting white powder was obtained by centrifugation, and dried in an oven at 80°C.

$Pd(dpmCOOH)_2$⊂UiO-66

$ZrCl_4$ (30 mg, 0.129 mmol), terephthalic acid (BDC, 30 mg, 0.180 mmol), $Pd(dpmCOOH)_2$ (10 mg, 0.016 mmol) and benzoic acid (500 mg, 4.094 mmol) were ultrasonically dissolved in 3 mL of DMF in a Pyrex vial. The mixture was heated in an oven at 85°C for 24 h. After cooling down to room temperature, a dark powder was collected by centrifugation. The solid was washed with DMF three times to remove unreacted precursors, and then solvent-exchanged with acetone three times. The resulting white powder was obtained by centrifugation, and dried in an oven at 80°C.

UiO-66-NH_2

$ZrCl_4$ (30 mg, 0.129 mmol), 2-aminoterephthalic acid (BDC-NH_2, 20 mg, 0.110 mmol) and benzoic acid (500 mg, 4.094 mmol) were ultrasonically dissolved in 3 mL of DMF in a Pyrex vial. The mixture was heated in an oven at 120°C for 12 h. After

cooling down to room temperature, a yellow powder was collected by centrifugation. The solid was washed with DMF three times to remove unreacted precursors, and then solvent-exchanged with acetone three times. The resulting white powder was obtained by centrifugation, and dried in an oven at 80°C.

$Pd(dpmCOOH)_2$⊂UiO-66-NH_2

$ZrCl_4$ (30 mg, 0.129 mmol), 2-aminoterephthalic acid (BDC-NH_2, 20 mg, 0.110 mmol), $Pd(dpmCOOH)_2$ (10 mg, 0.016 mmol) and benzoic acid (500 mg, 4.094 mmol) were ultrasonically dissolved in 3 mL of DMF in a Pyrex vial. The mixture was heated in an oven at 120°C for 12 h. After cooling down to room temperature, a dark powder was collected by centrifugation. The solid was washed with DMF three times to remove unreacted precursors, and then solvent-exchanged with acetone three times. The resulting white powder was obtained by centrifugation, and dried in an oven at 80°C.

UiO-66-$(OH)_2$

$ZrOCl_2{\cdot}8H_2O$ (60 mg, 0.019 mmol), 2,5-dihydroxobenzenedicarboxylic acid (DOBDC, 60 mg, 0.303 mmol) and benzoic acid (500 mg, 4.094 mmol) were ultrasonically dissolved in 4 mL of H_2O and AcOH (1 :1 in volume) in a Pyrex vial. The mixture was heated in an oven at 120°C for 24 h. After cooling down to room temperature, a yellow powder was collected by centrifugation. The solid was washed with DMF three times to remove unreacted precursors, and then solvent-exchanged with acetone three times. The resulting white powder was obtained by centrifugation, and dried in an oven at 80°C.

$Pd(dpmCOOH)_2$⊂UiO-66-$(OH)_2$

$ZrOCl_2 \cdot 8H_2O$ (30 mg, 0.093 mmol), 2,5-dihydroxobenzenedicarboxylic acid (DOBDC,30 mg, 0.151 mmol), $Pd(dpmCOOH)_2$ (10 mg, 0.016 mmol) and benzoic acid (500 mg, 4.094 mmol) were ultrasonically dissolved in 4 mL of H_2O and AcOH (1 :1 in volume) in a Pyrex vial. The mixture was heated in an oven at 120°C for 24 h. After cooling down to room temperature, a dark powder was collected by centrifugation. The solid was washed with DMF three times to remove unreacted precursors, and then solvent-exchanged with acetone three times. The resulting white powder was obtained by centrifugation, and dried in an oven at 80°C.

Ni-bisdpmCOOH⊂UiO-66

$ZrCl_4$ (30 mg, 0.129 mmol), terephthalic acid (BDC, 20 mg, 0.120 mmol), Ni-bisdpmCOOH (5 mg, 0.0086 mmol) and benzoic acid (600 mg, 4.918 mmol) were ultrasonically dissolved in 2 mL of DMF in a Pyrex vial. The mixture was heated in an oven at 120°C for 12 h. After cooling down to room temperature, a shiny black powder was collected by centrifugation. The solid was washed with DMF three times to remove unreacted precursors, and then solvent-exchanged with acetone three times. The resulting black powder was obtained by centrifugation, and dried in an oven at 80°C.

APPENDIX B

SUPPLEMENTARY INFORMATION FOR CHAPTER 3

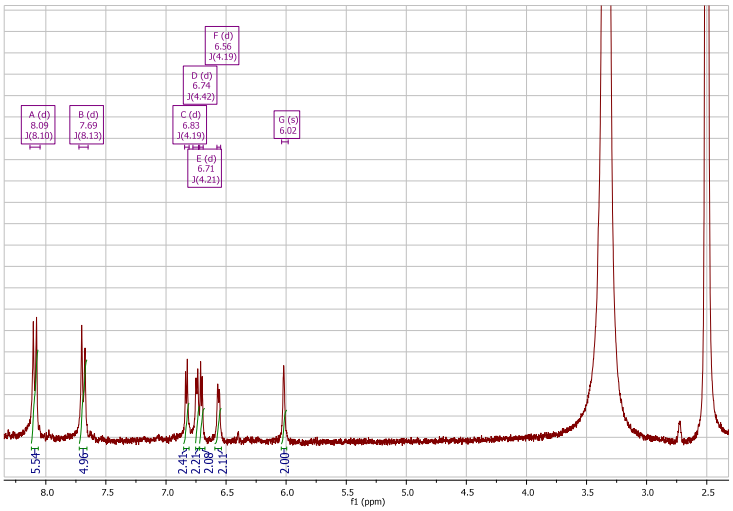

Figure B1. *^{1}H NMR spectrum of complex Ni-bisdpmCOOH.*

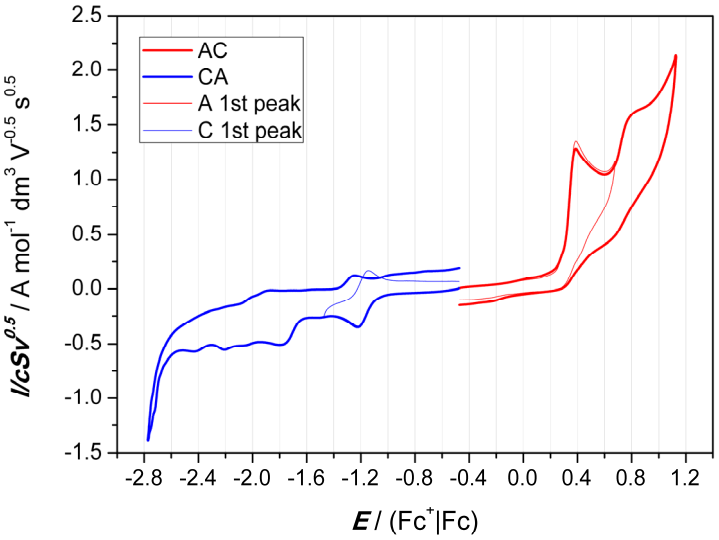

Figure B2*. Anodic (AC) and cathodic (CA) scans (bold lines) of the Ni-bisdpmCOOH complex. Overimposed (thin lines), anodic scan around the first oxidation peak (A) and cathodic scan around the first reduction peak (C).*

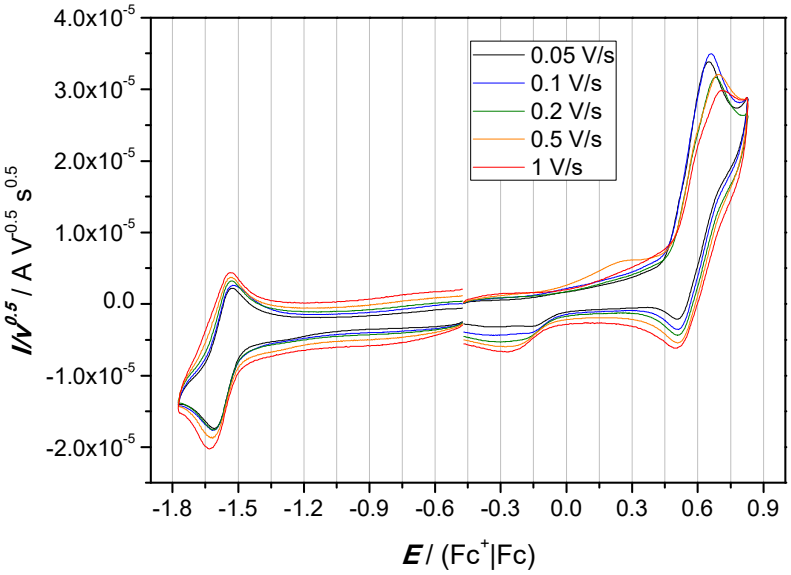

Figure B3. *Effect of the scan rate on the first oxidation peaks of NiTCPP.*

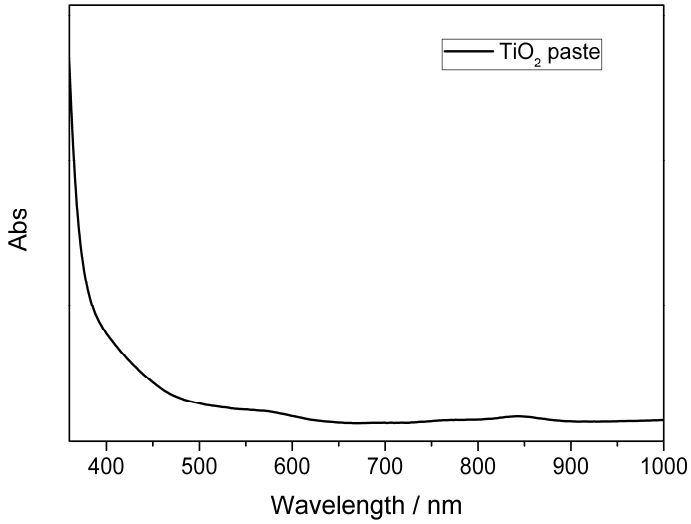

Figure B4. *UV-Vis-NIR absorption spectrum of the TiO_2 paste.*

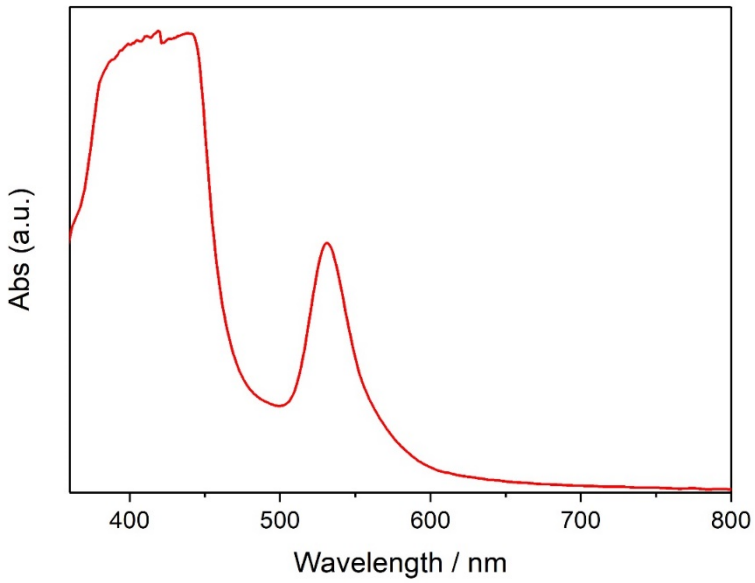

Figure B5. *Absorption spectrum (difference) of NiTCPP adsorbed onto the TiO_2 paste.*

APPENDIX C

SUPPLEMENTARY INFORMATION FOR CHAPTER 4

PORPHYRINS SYNTHESIS

Except for ligand tetrakis(4-carboxyphenyl)porphyrin (H_2TCPP), which was purchased from TCI Europe, the other metal-involved MTCPP ligands were synthesized in a three-steps route as shown below

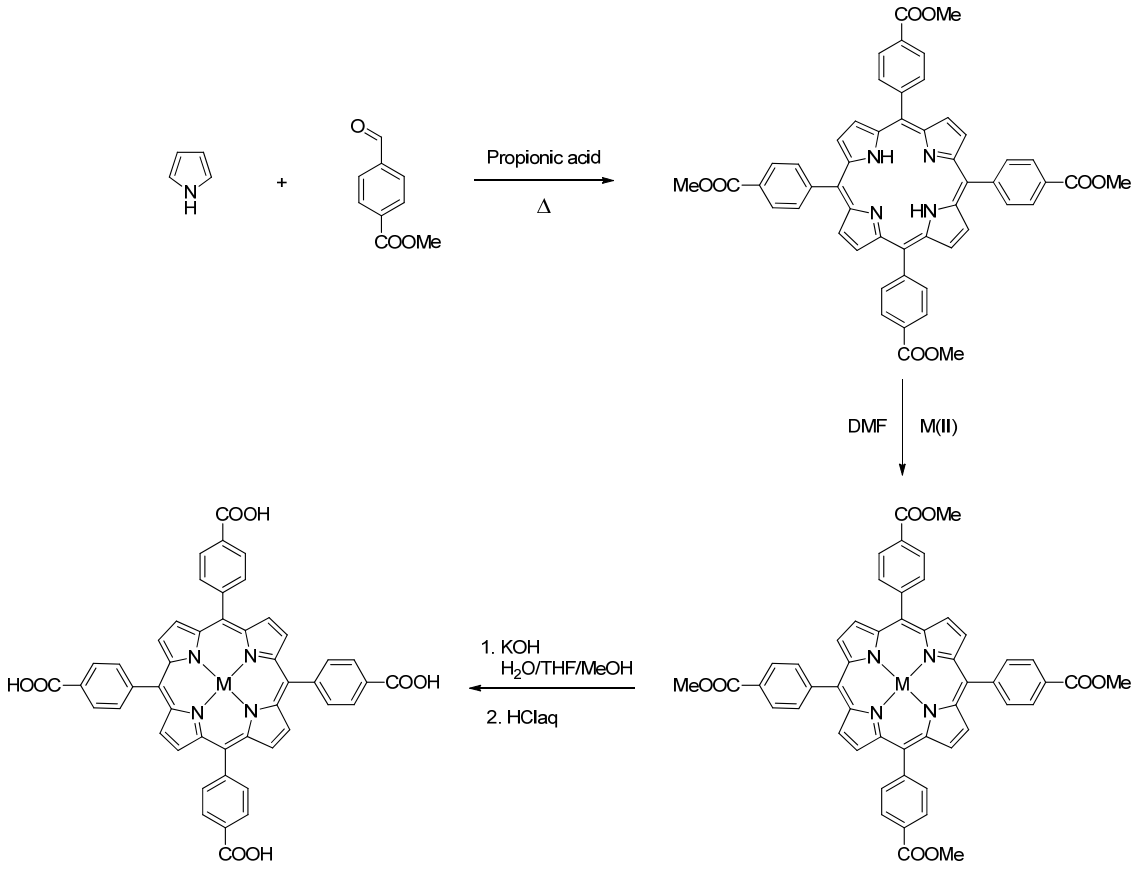

Scheme C1. *Three step synthetic route to MTCPP ligand.*

[5,10,15,20-Tetrakis(4-methoxycarboxyphenyl)porphyrin] (TPPCOOMe)

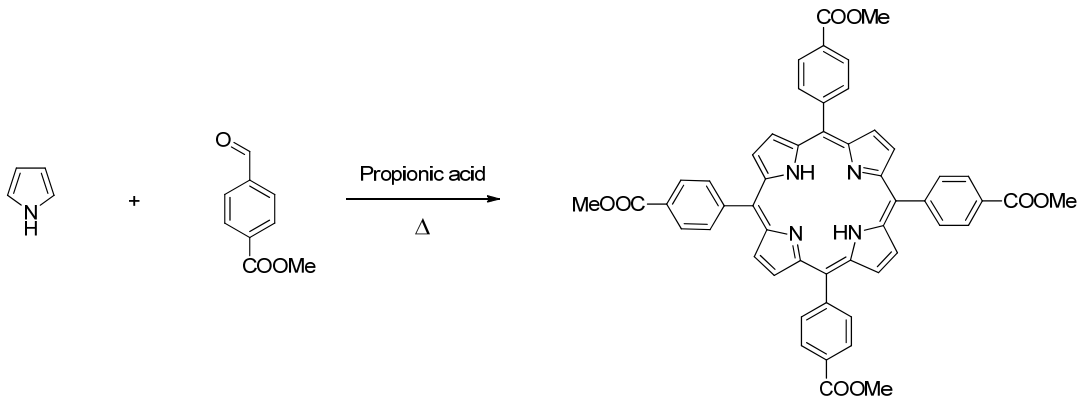

A B C

Chemicals	MW (*g/mol*)	m (*g*)	n (*mol*)	Equiv.	d (*g/mL*)	V (*mL*)
A	164.16	6.9	0.042	1		
B	67.09	2.9	0.043	1	0.967	3.0
C	846.88	2.5				
Solvents						
Propionic acid						100

Lit. Ref. *Angew. Chem. Int. Ed. 2012, 51(41), 10307-10310*

Procedure:

reagent B (3.0 mL, 0.043 mol) and reagent A (6.9 g, 0.042 mol) were added to a refluxed propionic acid (100 mL), in a 500 mL 3-necked flask and the solution was refluxed overnight in darkness.

After cooling down to room temperature, crystals were collected by vacuum filtration, washed with propionic acid, water and then dried in the oven.

Yiled = 2.5 g (17.5%)

Characterization:

^{1}H NMR (300 MHz, $CDCl_3$) δ: 8.82 (s, 8H), 8.45 (d, J = 8.3 Hz, 8H), 8.29 (d, J = 8.25 Hz, 8H), 4.11 (s, 12H), -2.81 (bs, 2H).

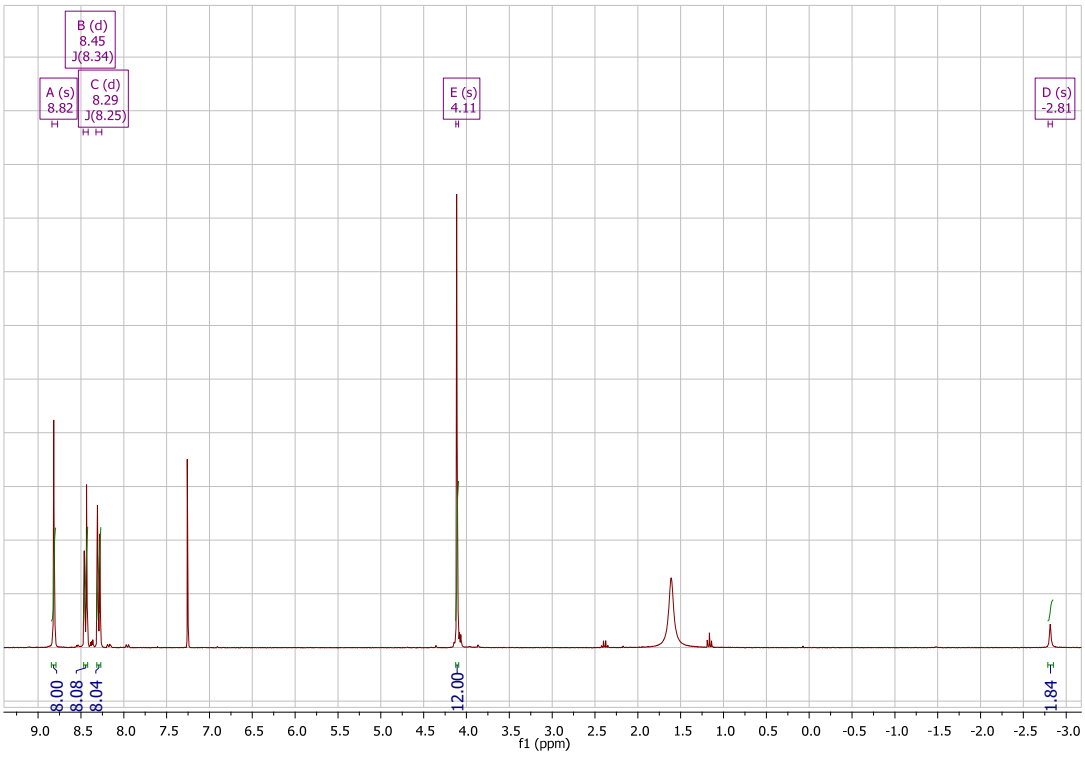

Figure C1. *^{1}H NMR of the TPPCOOMe ligand.*

[5,10,15,20-Tetrakis(4-methoxycarbonylphenyl)porphyrin-M] series (MTPPCOOMe)

[5,10,15,20-Tetrakis(4-methoxycarbonylphenyl)porphyrinato]-Fe(III) Chloride

A solution of TPPCOOMe (500.0 mg, 0.59 mmol) and $FeCl_2$ (1.36 g, 10.7 mmol) in 60 mL of DMF was refluxed for 5 h ca. After cooling down to room temperature, ca 150 mL of water were added. The resultant precipitate was washed with water, then with 1 M HCl and then again with water until the filtrate was colourless. The obtained crystalline powder (in quantitative yield) was dried in oven and directly used in the following step without further purification.

[5,10,15,20-Tetrakis(4-methoxycarbonylphenyl)porphyrinato]-Co(II)

A solution of TPPCOOMe (470.0 mg, 0.55 mmol) and $CoCl_2{\cdot}4H_2O$ (1.80 g, 7.57 mmol) in 60 mL of DMF was refluxed for 5 h ca. After cooling down to room temperature, ca 150 mL of water were added. The resultant precipitate was washed with water, then with 1 M HCl and then again with water until the filtrate was colourless. The obtained crystalline powder (in quantitative yield) was dried in oven and directly used in the following step without further purification.

[5,10,15,20-Tetrakis(4-methoxycarbonylphenyl)porphyrinato]-Ni(II)

A solution of TPPCOOMe (500.0 mg, 0.59 mmol) and $NiCl_2{\cdot}6H_2O$ (1.80 g, 7.57 mmol) in 60 mL of DMF was refluxed for 5 h ca. After cooling down to room temperature, ca 150 mL of water were added. The resultant precipitate was washed with water, then with 1 M HCl and then again with water until the filtrate was colourless.

The obtained crystalline powder (in quantitative yield) was dried in oven and directly used in the following step without further purification.

[5,10,15,20-Tetrakis(4-methoxycarbonylphenyl)porphyrinato]-Cu(II)

A solution of TPPCOOMe (500.0 mg, 0.59 mmol) and $CuCl_2 \cdot 2H_2O$ (1.30 g, 7.63 mmol) in 60 mL of DMF was refluxed for 5 h ca. After cooling down to room temperature, ca 150 mL of water were added. The resultant precipitate was washed with water, then with 1 M HCl and then again with water until the filtrate was colourless. The obtained crystalline powder (in quantitative yield) was dried in oven and directly used in the following step without further purification.

[5,10,15,20-Tetrakis(4-carbonylphenyl)porphyrinato]-M series (MTCPP)

[5,10,15,20-Tetrakis(4-carboxyphenyl)porphyrinato]-Fe(III) Chloride

FeTPPCOOMe was stirred in a mixture of THF and MeOH (25 mL each), to which a solution of NaOH (2.4 g, 60 mmol) in water (25 mL) was added. This mixture was refluxed overnight.

After cooling down to room temperature, THF and MeOH were removed and more water was added. The mixture was refluxed for ca 30 min in order to obtain a homogeneous solution, which was acidified with 1 M HCl until no further precipitate was detected. The solid was then filtered, washed with water until the filtrate was colourless and dried in oven.

[5,10,15,20-Tetrakis(4-carboxyphenyl)porphyrinato]-Co(II)

CoTPPCOOMe was stirred in a mixture of THF and MeOH (25 mL each), to which a solution of NaOH (2.4 g, 60 mmol) in water (25 mL) was added. This mixture was refluxed overnight.

After cooling down to room temperature, THF and MeOH were removed and more water was added. The mixture was refluxed for ca 30 min in order to obtain a homogeneous solution, which was acidified with 1 M HCl until no further precipitate was detected. The solid was then filtered, washed with water until the filtrate was colourless and dried in oven.

[5,10,15,20-Tetrakis(4-carboxyphenyl)porphyrinato]-Ni(II)

NiTPPCOOMe was stirred in a mixture of THF and MeOH (25 mL each), to which a solution of NaOH (2.4 g, 60 mmol) in water (25 mL) was added. This mixture was refluxed overnight.

After cooling down to room temperature, THF and MeOH were removed and more water was added. The mixture was refluxed for ca 30 min in order to obtain a homogeneous solution, which was acidified with 1 M HCl until no further precipitate was detected. The solid was then filtered, washed with water until the filtrate was colourless and dried in oven.

[5,10,15,20-Tetrakis(4-carboxyphenyl)porphyrinato]-Cu(II)

CuTPPCOOMe was stirred in a mixture of THF and MeOH (25 mL each), to which a solution of NaOH (2.4 g, 60 mmol) in water (25 mL) was added. This mixture was refluxed overnight.

After cooling down to room temperature, THF and MeOH were removed and more water was added. The mixture was refluxed for ca 30 min in order to obtain a homogeneous solution, which was acidified with 1 M HCl until no further precipitate was detected. The solid was then filtered, washed with water until the filtrate was colourless and dried in oven.

FeTCPP⊂UiO-66

$ZrCl_4$ (30 mg, 0.129 mmol), terephthalic acid (BDC, 30 mg, 0.180 mmol), FeTCPP (10 mg, 0.011 mmol) and benzoic acid (500 mg, 4.094 mmol) were ultrasonically dissolved in 2 mL of DMF in a Pyrex vial. The mixture was heated in an oven at 130°C for 12 h. After cooling down to room temperature, the powder was collected by centrifugation. The solid was washed with DMF three times to remove unreacted precursors, and then solvent-exchanged with acetone three times. The resulting white powder was obtained by centrifugation, and dried in an oven at 80°C.

NiTCPP⊂UiO-66

$ZrCl_4$ (30 mg, 0.129 mmol), terephthalic acid (BDC, 20 mg, 0.120 mmol), NiTCPP (10 mg, 0.012 mmol) and benzoic acid (600 mg, 4.918 mmol) were ultrasonically dissolved in 2 mL of DMF in a Pyrex vial. The mixture was heated in an oven at 130°C for 12 h. After cooling down to room temperature, the powder was collected by

centrifugation. The solid was washed with DMF three times to remove unreacted precursors, and then solvent-exchanged with acetone three times. The resulting white powder was obtained by centrifugation, and dried in an oven at 80°C.

CuTCPP⊂UiO-66

$ZrCl_4$ (30 mg, 0.129 mmol), terephthalic acid (BDC, 30 mg, 0.180 mmol), CuTCPP (10 mg, 0.012 mmol) and benzoic acid (500 mg, 4.094 mmol) were ultrasonically dissolved in 2 mL of DMF in a Pyrex vial. The mixture was heated in an oven at 130°C for 12 h. After cooling down to room temperature, the powder was collected by centrifugation. The solid was washed with DMF three times to remove unreacted precursors, and then solvent-exchanged with acetone three times. The resulting white powder was obtained by centrifugation, and dried in an oven at 80°C.

CoTCPP⊂UiO-66

$ZrCl_4$ (30 mg, 0.129 mmol), terephthalic acid (BDC, 30 mg, 0.180 mmol), CoTCPP (10 mg, 0.012 mmol) and benzoic acid (500 mg, 4.094 mmol) were ultrasonically dissolved in 2 mL of DMF in a Pyrex vial. The mixture was heated in an oven at 130°C for 12 h. After cooling down to room temperature, the powder was collected by centrifugation. The solid was washed with DMF three times to remove unreacted precursors, and then solvent-exchanged with acetone three times. The resulting white powder was obtained by centrifugation, and dried in an oven at 80°C.

H_2TCPP⊂UiO-66

$ZrCl_4$ (30 mg, 0.129 mmol), terephthalic acid (BDC, 30 mg, 0.180 mmol), H_2TCPP (10 mg, 0.013 mmol) and benzoic acid (500 mg, 4.094 mmol) were ultrasonically dissolved in 2 mL of DMF in a Pyrex vial. The mixture was heated in an oven at 130°C for 12 h. After cooling down to room temperature, the powder was collected by centrifugation. The solid was washed with DMF three times to remove unreacted precursors, and then solvent-exchanged with acetone three times. The resulting white powder was obtained by centrifugation, and dried in an oven at 80°C.

FeTCPP⊂UiO-66-NH_2

$ZrCl_4$ (30 mg, 0.129 mmol), 2-aminoterephthalic acid (BDC-NH_2, 30 mg, 0.166 mmol), FeTCPP (10 mg, 0.011 mmol) and benzoic acid (500 mg, 4.094 mmol) were ultrasonically dissolved in 2 mL of DMF in a Pyrex vial. The mixture was heated in an oven at 120°C for 12 h. After cooling down to room temperature, the powder was collected by centrifugation. The solid was washed with DMF three times to remove unreacted precursors, and then solvent-exchanged with acetone three times. The resulting white powder was obtained by centrifugation, and dried in an oven at 80°C.

NiTCPP⊂UiO-66-NH_2

$ZrCl_4$ (30 mg, 0.129 mmol), 2-aminoterephthalic acid (BDC-NH_2, 20 mg, 0.110 mmol), NiTCPP (10 mg, 0.012 mmol) and benzoic acid (600 mg, 4.918 mmol) i were ultrasonically dissolved n 2 mL of DMFin a Pyrex vial. The mixture was heated in an oven at 120°C for 12 h. After cooling down to room temperature, the powder was collected by centrifugation. The solid was washed with DMF three times to remove

unreacted precursors, and then solvent-exchanged with acetone three times. The resulting white powder was obtained by centrifugation, and dried in an oven at 80°C.

CuTCPP⊂UiO-66-NH_2

$ZrCl_4$ (30 mg, 0.129 mmol), 2-aminoterephthalic acid (BDC-NH_2, 30 mg, 0.166 mmol), CuTCPP (10 mg, 0.012 mmol) and benzoic acid (500 mg, 4.094 mmol) were ultrasonically dissolved in 2 mL of DMF in a Pyrex vial. The mixture was heated in an oven at 120°C for 12 h. After cooling down to room temperature, the powder was collected by centrifugation. The solid was washed with DMF three times to remove unreacted precursors, and then solvent-exchanged with acetone three times. The resulting white powder was obtained by centrifugation, and dried in an oven at 80°C.

CoTCPP⊂UiO-66-NH_2

$ZrCl_4$ (30 mg, 0.129 mmol), 2-aminoterephthalic acid (BDC-NH_2, 20 mg, 0.110 mmol), CoTCPP (10 mg, 0.012 mmol) and benzoic acid (600 mg, 4.918 mmol) were ultrasonically dissolved in 2 mL of DMF in a Pyrex vial. The mixture was heated in an oven at 120°C for 12 h. After cooling down to room temperature, the powder was collected by centrifugation. The solid was washed with DMF three times to remove unreacted precursors, and then solvent-exchanged with acetone three times. The resulting white powder was obtained by centrifugation, and dried in an oven at 80°C.

H_2TCPP⊂UiO-66-NH_2

$ZrCl_4$ (30 mg, 0.129 mmol), 2-aminoterephthalic acid (BDC-NH_2, 30 mg, 0.166 mmol), H_2TCPP (10 mg, 0.013 mmol) and benzoic acid (500 mg, 4.094 mmol) were

ultrasonically dissolved in 2 mL of DMF in a Pyrex vial. The mixture was heated in an oven at 120°C for 12 h. After cooling down to room temperature, the powder was collected by centrifugation. The solid was washed with DMF three times to remove unreacted precursors, and then solvent-exchanged with acetone three times. The resulting white powder was obtained by centrifugation, and dried in an oven at 80°C.

PCN-222(Fe)

$ZrCl_4$ (50 mg), FeTCPP (50 mg) and benzoic acid (2700 mg) in 8 mL of *N,N*-dimethylformamide (DEF) were ultrasonically dissolved and then transferred in a 20 mL Teflon-lined bomb. The mixture was heated in 120 ºC oven for 48 h and then 130 ºC oven for 24 h. After cooling down to room temperature, the crystalline material was harvested by filtration.

To activate the sample, the obtained as-synthesized PCN-222(Fe) was suspended in a solution of 8 mL of 1 M HCl in 60 mL DMF and stirred at 120 ºC overnight. Then, the powder was centrifuged and washed with DMF three times and acetone three times. After removal of acetone by decanting, the sample was dried in an oven at 85°C.

PCN-222(Ni)

$ZrCl_4$ (50 mg), NiTCPP (50 mg) and benzoic acid (2700 mg) in 8 mL of *N,N*-dimethylformamide (DEF) were ultrasonically dissolved and then transferred in a 20 mL Teflon-lined bomb. The mixture was heated in 120 ºC oven for 48 h and then 130 ºC oven for 24 h. After cooling down to room temperature, the crystalline material was harvested by filtration.

To activate the sample, the obtained as-synthesized PCN-222(Ni) was suspended in a solution of 8 mL of 1 M HCl in 60 mL DMF and stirred at 120 ºC overnight. Then, the powder was centrifuged and washed with DMF three times and acetone three times. After removal of acetone by decanting, the sample was dried in an oven at 85°C.

PCN-222(Cu)

$ZrCl_4$ (50 mg), CuTCPP (50 mg) and benzoic acid (2700 mg) in 8 mL of *N,N*-dimethylformamide (DEF) were ultrasonically dissolved and then transferred in a 20 mL Teflon-lined bomb. The mixture was heated in 120 ºC oven for 48 h and then 130 ºC oven for 24 h. After cooling down to room temperature, the crystalline material was harvested by filtration.

To activate the sample, the obtained as-synthesized PCN-222(Cu) was suspended in a solution of 8 mL of 1 M HCl in 60 mL DMF and stirred at 120 ºC overnight. Then, the powder was centrifuged and washed with DMF three times and acetone three times. After removal of acetone by decanting, the sample was dried in an oven at 85°C.

PCN-222(Co)

$ZrCl_4$ (50 mg), CoTCPP (50 mg) and benzoic acid (2700 mg) in 8 mL of *N,N*-dimethylformamide (DEF) were ultrasonically dissolved and then transferred in a 20 mL Teflon-lined bomb. The mixture was heated in 120 ºC oven for 48 h and then 130 ºC oven for 24 h. After cooling down to room temperature, the crystalline material was harvested by filtration.

To activate the sample, the obtained as-synthesized PCN-222(Co) was suspended in a solution of 8 mL of 1 M HCl in 60 mL DMF and stirred at 120 ºC overnight. Then, the

powder was centrifuged and washed with DMF three times and acetone three times. After removal of acetone by decanting, the sample was dried in an oven at 85°C.

PCN-222

$ZrCl_4$ (50 mg), H_2TCPP (50 mg) and benzoic acid (2700 mg) in 8 mL of *N,N*-dimethylformamide (DEF) were ultrasonically dissolved and then transferred in a 20 mL Teflon-lined bomb. The mixture was heated in 120 ºC oven for 48 h and then 130 ºC oven for 24 h. After cooling down to room temperature, the crystalline material was harvested by filtration.

To activate the sample, the obtained as-synthesized PCN-222 was suspended in a solution of 8 mL of 1 M HCl in 60 mL DMF and stirred at 120 ºC overnight. Then, the powder was centrifuged and washed with DMF three times and acetone three times. After removal of acetone by decanting, the sample was dried in an oven at 85°C.

APPENDIX D

SUPPLEMENTARY INFORMATION FOR CHAPTER 7

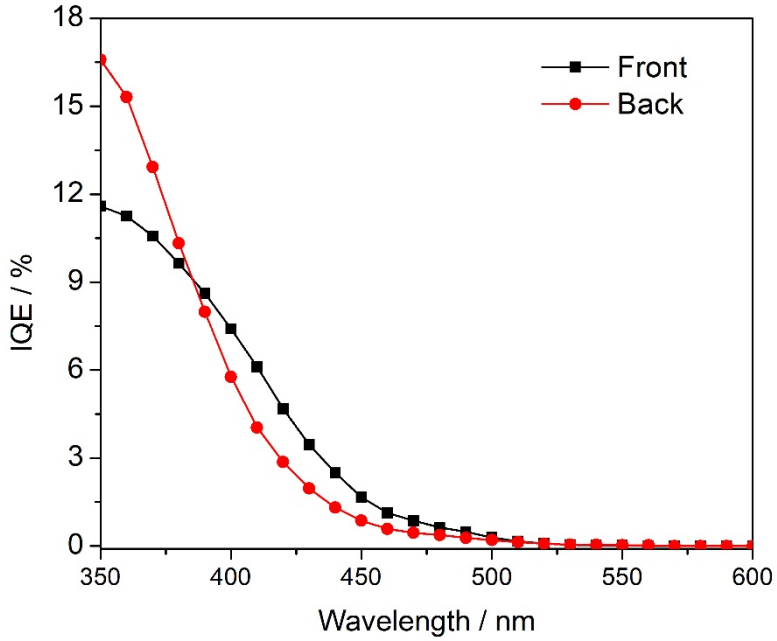

Figure D1. *Comparison of IQE analyses for front- and backside irradiation of CuWO4 photoanode (5th layer).*

APPENDIX E

SUPPLEMENTARY INFORMATION FOR CHAPTER 9

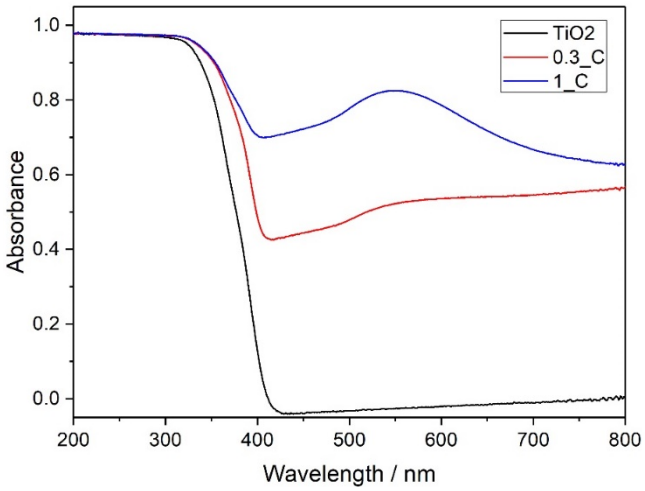

Figure E1. *Diffused reflectance spectra the Au/TiO_2_C photocatalysts series.*

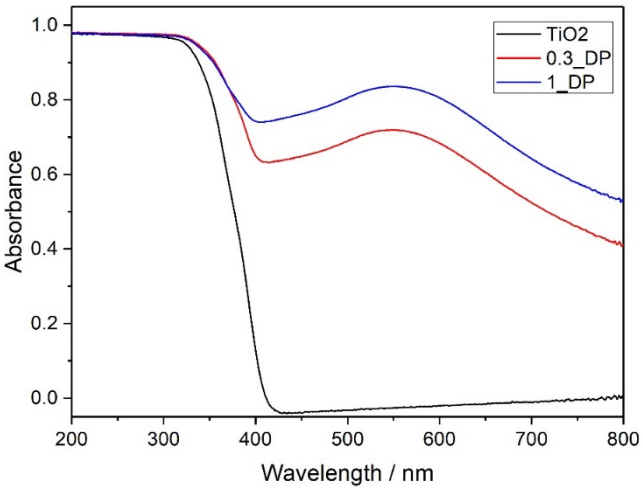

Figure E2. *Diffused reflectance spectra of the Au/TiO_2_DP photocatalysts series.*

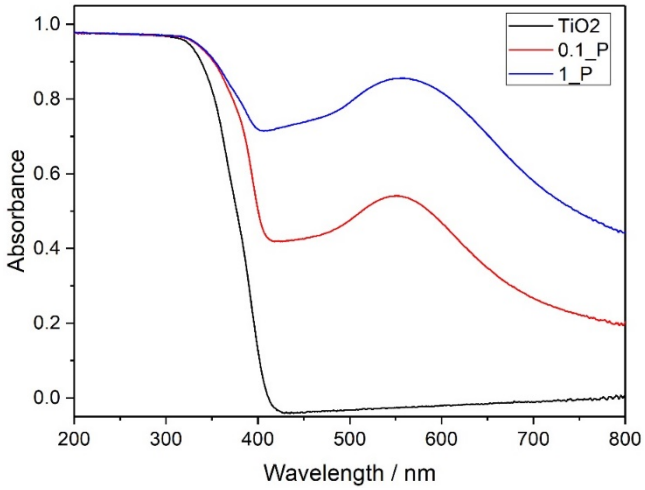

Figure E3. *Diffused reflectance spectra of the Au/TiO_2_P photocatalysts series.*

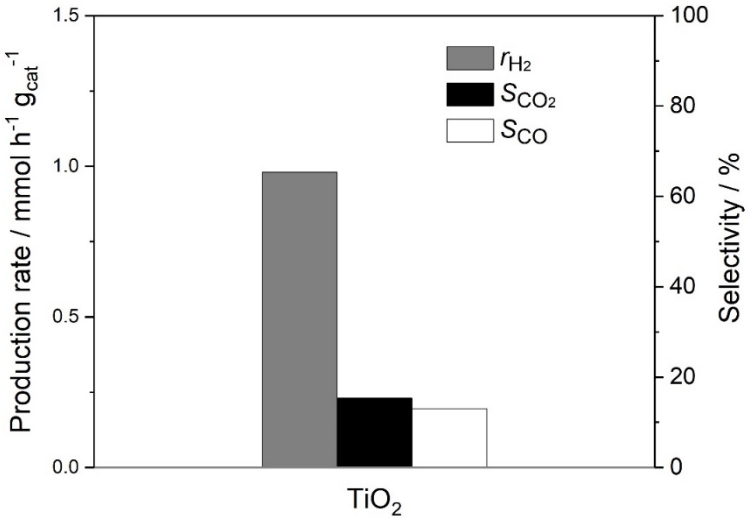

Figure E4. *Hydrogen production rate and selectivity for bare P25 TiO_2.*